Fall 2012

Expansions of supramolecular chemistry: nanocrystals, pharmaceutical cocrystals, imaging, and decorated olefins

John Roy George Sander
University of Iowa

EXPANSIONS OF SUPRAMOLECULAR CHEMISTRY: NANOCRYSTALS, PHARMACEUTICAL COCRYSTALS, IMAGING, AND DECORATED OLEFINS

by

John Roy George Sander

An Abstract

Of a thesis submitted in partial fulfillment
of the requirements for the Doctor of
Philosophy degree in Chemistry
in the Graduate College of
The University of Iowa

December 2012

Thesis Supervisor: Professor Leonard MacGillivray

ABSTRACT

Crystal engineering has matured into a design-driven field based on the exploitation of reliable interactions between the functional groups of molecules so as to achieve desired properties. The utility of crystal engineering has been realized in a breadth of fields and, as a microcosm of crystal engineering, this thesis will explore the application of crystal engineering in the pharmaceutical sciences, nanotechnology, synthetic chemistry, materials science, and biomedical imaging.

As the trend in drug development continues to skew towards molecules with poor aqueous solubility the ability improve the physicochemical properties of a pharmaceutical agent, especially *via* non-covalent means, has become crucial. One method to impart improved physiochemical properties to pharmaceutical agents is through cocrystallization. A portion of this thesis will focus on the design-driven development of pharmaceutical cocrystals so as to impart improved mechanical properties to acetaminophen. As part of our investigation, we observed unexpected intermolecular interactions between the constituents of our cocrystals, which will contribute to the continued development of crystal engineering. In addition, we are interested in developing a methodology for the reliable fabrication of organic nanocrystals based on multi-component solids. Whereas the field of inorganic nanocrystals has blossomed, organic nanocrystals have remained largely underdeveloped. To expand the field of organic nanocrystals we turned to the synthesis of pharmaceutical nano-cocrystals. Specifically, we determined a sonochemical approach combined with multiple solvents and a surfactant could effectively synthesize pharmaceutical nano-cocrystals. As part of our desire to synthesize complex, multi-component, organic nanocrystals we also investigated the ability of a sonochemical approach to synthesize host-guest nanocrystals. In particular, the results demonstrated that sonochemistry successfully fabricates nano-

and micrometer sized crystals of a host-guest solid and affords rhombic-dodecahedral crystals of a hollow topology.

This thesis will also examine [2+2] photodimerizations in the solid-state. Previous work has successfully established the application of a template-directed solid-state approach to the photodimerization of olefins in the solid-state. However, these studies have largely focused on the reactivity of symmetric bipyridines. Thus, we have expanded the functional group diversity associated with [2+2] photodimerizations to include the cyano moiety. We have shown the template approach successfully aligns our targeted cyano-substituted olefins to enable photodimerizations in the solid-state.

In addition, we have investigated the ability to synthesize cocrystals based on iodinated contrast agents. We believe the cocrystal approach could afford contrast agents with tailored properties based on the selected cocrystal former. The results of our investigation include five cocrystals and five salts composed of iodinated contrast agents. The results help to establish a knowledge base to be exploited in the design of future contrast agent based cocrystals with tailored properties.

Abstract Approved: _____
Thesis Supervisor

_____
Title and Department

_____
Date

EXPANSIONS OF SUPRAMOLECULAR CHEMISTRY: NANOCRYSTALS, PHARMACEUTICAL COCRYSTALS, IMAGING, AND DECORATED OLEFINS

by

John Roy George Sander

A thesis submitted in partial fulfillment
of the requirements for the Doctor of
Philosophy degree in Chemistry
in the Graduate College of
The University of Iowa

December 2012

Thesis Supervisor: Professor Leonard MacGillivray

Graduate College
The University of Iowa
Iowa City, Iowa

CERTIFICATE OF APPROVAL

_____

PH.D. THESIS

_____

This is to certify that the Ph.D. thesis of

John Roy George Sander

has been approved by the Examining Committee
for the thesis requirement for the Doctor of Philosophy
degree in Chemistry at the December 2012 graduation.

Thesis Committee: _____
Leonard R. MacGillivray, Thesis Supervisor

_____
F. Christopher Pigge

_____
Daniel M. Quinn

_____
Alexei V. Tivanski

_____
Geoff G. Z. Zhang

To my parents, grandparents, and brother.

Not all those who wander are lost.
J. R. R. Tolkien
The Fellowship of the Ring

ACKNOWLEDGMENTS

I have to concede the idea of encapsulating the immense amount of gratitude I feel in a categorized one page summary is quite daunting. First of all, I want to express my gratitude towards my advisor Professor Leonard R. MacGillivray for taking on a graduate student with no prior research experience and helping to mold me into a scientist. I'm truly grateful for the time, effort, and countless hours you have dedicated to making me a supramolecular chemist.

I am also indebted to Dr. Geoff G. Z. Zhang for his role as a second advisor both through our collaboration and my two summers spent at Abbott Laboratories. I'm gracious for all the fruitful conversations we've had.

I also want to take the opportunity to thank Dr. Dale C. Swenson and Roger F. Henry who were an immense amount of help with crystallographic studies. Both of you were always willing to take the time to answer any questions I may have had.

I owe a special debt of gratitude towards Dr. Dejan-Krešimir Bučar who is as much a mentor as he is a friend. To group members past and present I will always remember the special moments we've shared. In addition, I want to thank Dr. Charles A. Liberko for the opportunity to work together.

Last but certainly not least I have to thank my family. My parents, grandparents, and brother have played a vital role in helping me reach this point in my life. I would never have made it this far without them. To Lindsay, without your daily support we both know I would have fallen apart a long time ago.

ABSTRACT

Crystal engineering has matured into a design-driven field based on the exploitation of reliable interactions between the functional groups of molecules so as to achieve desired properties. The utility of crystal engineering has been realized in a breadth of fields and, as a microcosm of crystal engineering, this thesis will explore the application of crystal engineering in the pharmaceutical sciences, nanotechnology, synthetic chemistry, materials science, and biomedical imaging.

As the trend in drug development continues to skew towards molecules with poor aqueous solubility the ability improve the physicochemical properties of a pharmaceutical agent, especially *via* non-covalent means, has become crucial. One method to impart improved physiochemical properties to pharmaceutical agents is through cocrystallization. A portion of this thesis will focus on the design-driven development of pharmaceutical cocrystals so as to impart improved mechanical properties to acetaminophen. As part of our investigation, we observed unexpected intermolecular interactions between the constituents of our cocrystals, which will contribute to the continued development of crystal engineering. In addition, we are interested in developing a methodology for the reliable fabrication of organic nanocrystals based on multi-component solids. Whereas the field of inorganic nanocrystals has blossomed, organic nanocrystals have remained largely underdeveloped. To expand the field of organic nanocrystals we turned to the synthesis of pharmaceutical nano-cocrystals. Specifically, we determined a sonochemical approach combined with multiple solvents and a surfactant could effectively synthesize pharmaceutical nano-cocrystals. As part of our desire to synthesize complex, multi-component, organic nanocrystals we also investigated the ability of a sonochemical approach to synthesize host-guest nanocrystals. In particular, the results demonstrated that sonochemistry successfully fabricates nano-

and micrometer sized crystals of a host-guest solid and affords rhombic-dodecahedral crystals of a hollow topology.

This thesis will also examine [2+2] photodimerizations in the solid-state. Previous work has successfully established the application of a template-directed solid-state approach to the photodimerization of olefins in the solid-state. However, these studies have largely focused on the reactivity of symmetric bipyridines. Thus, we have expanded the functional group diversity associated with [2+2] photodimerizations to include the cyano moiety. We have shown the template approach successfully aligns our targeted cyano-substituted olefins to enable photodimerizations in the solid-state.

In addition, we have investigated the ability to synthesize cocrystals based on iodinated contrast agents. We believe the cocrystal approach could afford contrast agents with tailored properties based on the selected cocrystal former. The results of our investigation include five cocrystals and five salts composed of iodinated contrast agents. The results help to establish a knowledge base to be exploited in the design of future contrast agent based cocrystals with tailored properties.

TABLE OF CONTENTS

LIST OF TABLES

LIST OF FIGURES

LIST OF SCHEMES

CHAPTER 1. INTRODUCTION

1.1. Supramolecular chemistry

The term *supramolecular chemistry* has been defined by Nobel laureate Jean-Marie Lehn as "the chemistry of molecular assemblies and of the intermolecular bond".[1] Research in the field of supramolecular chemistry was originally inspired by a desire to understand the creation of electrical events *via* sodium and potassium ion transport in the nervous system.[2] Then in 1967 Pedersen made a seminal contribution to this are of interest in his report on a series of macrocyclic polyethers capable of binding metal cations (*e.g.* potassium).[3] The discovery was followed by a groundswell of research on synthetic receptors capable of 'host-guest' type behavior. In addition to the work done by Pedersen, seminal contributions by Lehn[4] on cryptands and Cram[5] on spherands developed the concepts of molecular recognition and self-assembly as an area of scientific research. Modern day supramolecular chemistry has evolved into an interdisciplinary field that bridges biology, chemistry, and physics.[6] In general, the goal of supramolecular chemistry is the design-driven fabrication of 'supermolecules' that are assembled by a series molecular recognition events that involve intermolecular interactions between the constituent components.[7] Whereas molecules are built with covalent bonds supramolecular compounds, or supermolecules, are built by joining molecules *via* intermolecular interactions (Fig. 1).

Paramount to the construction of supermolecules is a detailed understanding of intermolecular interactions, or supramolecular interactions. Supramolecular interactions can be characterized by their ability to participate in directional or nondirectional forces. While directional forces are particularly useful in the geometric and spatial alignment of constituent molecules, nondirectional interactions play a vital role in the spacing and conformation of supramolecular components.[6, 8-10] Herein, both forms of supramolecular

interactions will be described with a particular focus on the forces that are utilized in the original research disseminated in this dissertation.[6, 8-10]

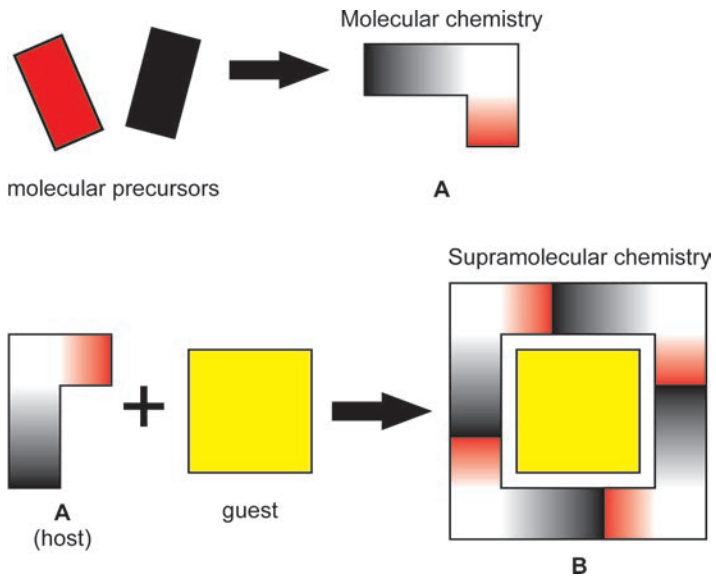

Figure 1 Perspective view of the X-ray crystal structure that depicts ion-ion interactions between ammonium moieties and $Fe(CN)_6^{3-}$. Reprinted with permission of John Wiley and Sons, copyright 2011.

With respect to nondirectional, supramolecular interactions, ion-ion and van der Waals forces are the most commonly encountered nondirectional interactions, albeit, of vastly different energies. Attractive van der Waals forces are generated when an approaching nucleus induces a fluctuation in the polarization of a molecular electron cloud.[11] The weak, nondirectional, nature of van der Waals forces precludes exclusively using these interactions in the design of a supramolecular assembly. However, in the solid-state van der Waals forces have a pronounced role in crystal packing, which will help determine the final configuration of molecules within structure.[8] The prototypical example of ion-ion interactions is inorganic salts. The coulombic interactions between the cations and anions of inorganic salts (*e.g* $ZnCl_2$) dictates the distance between the

components and the lack of geometric constraints is often evident in the ability of these systems to pack in isotropic crystalline lattices. To impart directionality to ion-ion interactions, charged functionalities can be incorporated into host-guest systems wherein the host framework and guest molecule have opposite charges.[12-14]

Ion-dipole and dipole-dipole interactions are largely electrostatic interactions, akin to ion-ion forces, but the anisotropic nature of dipoles provides a degree of directionality. For example, ion-dipole interactions have been exploited in host-guest chemistry with the family of cucurbit[n]urils.[15, 16] The molecules consist of a hydrophobic cavity and two portals lined with carbonyl groups. The interaction between the carbonyl groups and ammonium cations has been well documented for their prominent role in self-assembly and molecular recognition processes (Fig. 2).[15, 16] For dipole-dipole interactions, and more specifically bond dipole-bond dipole interactions, carbonyl and cyano groups are commonly investigated.[17-19] The dipole-dipole interactions adopt three commonly observed motifs: antiparallel, perpendicular, or sheared parallel.[17] However, analyses of these interactions have resulted in a mixture of opinions wherein these interactions are viewed as "feeble" or possessing strengths comparable to hydrogen bonds.[17-19]

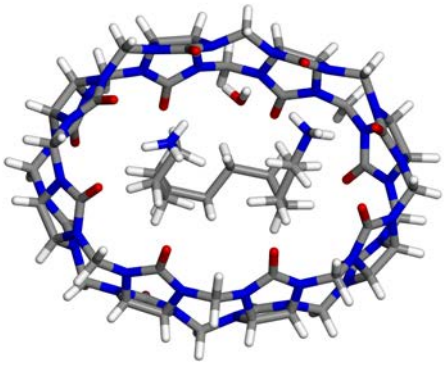

Figure 2 Perspective view of the X-ray crystal structure wherein cucurbit[8]uril encapsulates an α,ω-alkane diammonium ions.

Interactions between π-surfaces and neighboring π-surfaces, cations, and anions play a role in supramolecular chemistry and critical biological processes. Specifically, π···π interactions are evident in base pair stacking within the DNA helix and in binding events between proteins and DNA.[20, 21] Efforts to delineate π···π interactions have been pursued by both theoretical and experimental studies.[21-24] As a reference point, computational studies investigated the assembly and intermolecular interactions within benzene dimers.[23] The study identified at least three structures for the benzene dimer, namely offset parallel, T-shaped edge-to-face, and tilted-T structure.[22] Fig. 3 provides insight into the interactions between π-atoms with respect to orientation and distance.[22]

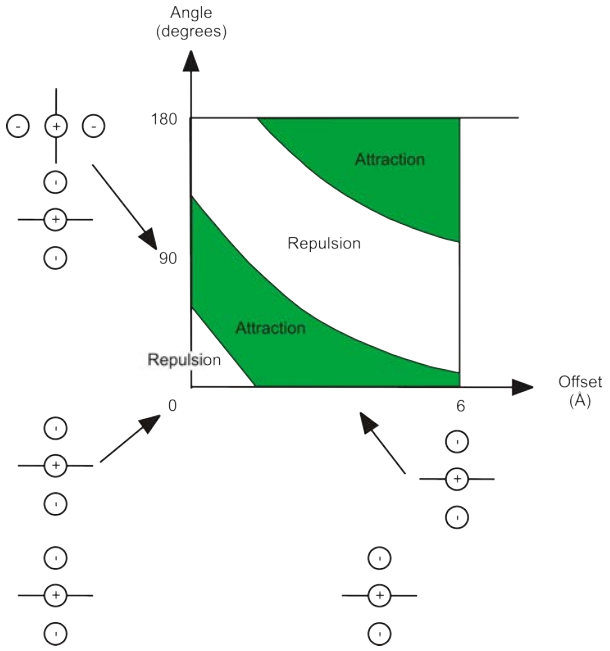

Figure 3 Interaction between idealized π–atoms at various distances and geometries. (Adapted from 22, © American Chemical Society, 1990)

The major contributions to the interaction energy between benzene rings originates from columbic and van der Waals term components, with the former depending on relative charge distribution and the latter on contact surface area.[22] The directionality of π···π

interactions is manifested in the desire of aromatics to adopt these energetically favorable conformations. Consequently, all three conformations, parallel, T-shaped edge-to-face, and tilted-T, have been reported as part of the complexation of aromatics within structurally-diverse hosts in which complementary electrostatic interactions also play a role.[22, 25-27]

Further insight into the organization of π-surfaces has also been acquired in solid-state studies. Desiraju and Gavezzoti investigated the packing of 32 aromatic compounds and showed the solid-state arrangement of the molecules was based on the ability to participate in C···C and C···H interactions.[28] Consequently, the number and positioning of C- and H-atoms within a molecule has an impact on the final packing arrangement. In total, the results showed π-surfaces tend to pack in herringbone, sandwich-herringbone, γ (parallel), and β (graphite sheets) arrangements (Fig. 4).[28]

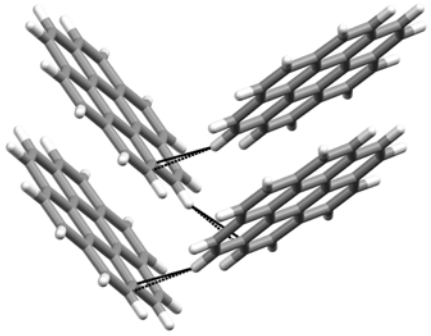

Figure 4 X-ray crystal structure of coronene viewed along the *c*-axis to reveal the γ packing sustained by C-H···π and π···π.

Supramolecular interactions based on cation- or anion-π binding fall at the extreme polls of intuition. Whereas a cation can be expected to participate in favorable coulombic interactions with the negatively charged region of a π-surface the approach of an anion would be expected to only encounter repulsive forces. In 1981, experimental

support for cation-π interactions was established in mass spectrometry and ion cyclotron resonance studies involving alkali-metal cations and simple aromatic compounds.[29] The results revealed the fundamental nature of cation-π interactions and that the strength of this interaction is comparable to even the strongest supramolecular interactions (*ca.* 10-40 kcal/mol).[6, 29] Later, Deakyne and Meot-Ner showed that organic ions (*e.g.* alkylammoniums) display 'unconventional ionic hydrogen bonds' with aromatic molecules.[30] However, interest in cation-π interactions is considered to have remained stagnant until a series of reports describing cation-π interactions within protein crystals and encapsulated within synthetic receptors (*i.e.* cyclophanes).[31, 32] Subsequent work by Dougherty *et al.* established cation-π interaction models that have been exploited in the design and implementation of a variety of synthetic receptors.[31-36] Moreover, Gokel *et al.* have studied cation-π interactions with a series of lariat ethers. The crown ether moiety binds a metal cation (*e.g.* sodium) and an appropriately positioned sidearm with an aromatic functionality (*e.g.* indole) is able to participate in cation-π interactions that reinforce the binding of the cation (Fig. 5).[37-39]

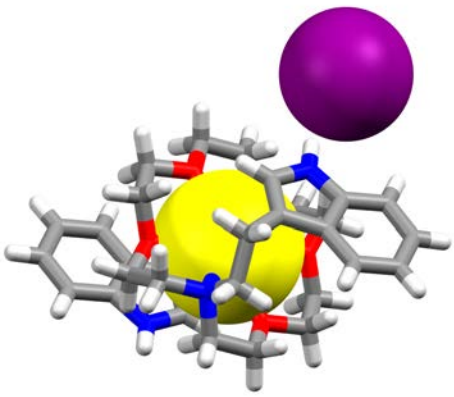

Figure 5 X-ray crystal structure of a lariat crown ether which binds a sodium cation and contains an indole substituted appendage which participates in cation-π interactions to strength the binding interaction (color scheme: Na-yellow and I-purple). Reprinted with permission of John Wiley and Sons, copyright 2011.

More recently, anion-π interactions have been the focus of theoretical and computational studies.[40, 41] The interaction consists of electrostatic and polarization components with the former being correlated with the quadrupole moment of an electron-deficient ring (*e.g* hexafluorobenzene) and the latter case a result of the approaching anion. Theoretical studies support the concept of electron deficient aromatics exhibiting favorable interactions towards anions with binding energies comparable to hydrogen bonds (*i.e.* 5-12 kcal/mol).[42-46] Generally, experimental support of anion-π interactions has been derived from crystallographic studies on organic and metal-organic receptors synthesized for anion binding (Fig. 6).[47, 48] However, a recent analysis of the Cambridge Structural Database by Hay and Custelcean refutes the previous assignment of anion-π interactions within crystals.[49] Examples of anion-π interactions with uncharged, and positively charged, arenes were deemed "extraordinary" with only a small number of structures meeting the theoretical spacial requirements for anion-π interactions.

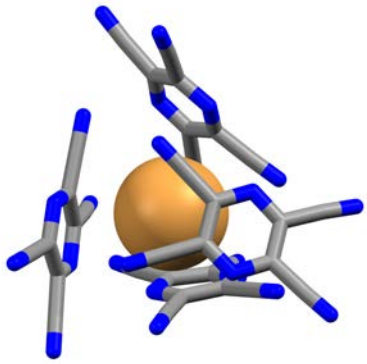

Figure 6 X-ray crystal structure which reveals the formation of anion-π interactions between a Br^- anion tetracyanopyrazine molecules (color scheme: Br-brown). Reprinted with permission of John Wiley and Sons, copyright 2011.

The attractive forces between closed-shell metal cations of d^8-d^{10} systems (*e.g.* Au(I)) have been utilized in the fabrication of supramolecular materials such as host-

guest systems.[50] The cation-cation interaction is of comparable strength to hydrogen bonds and within ligand-supported complexes can exhibit directionality *via* intermolecular interactions (*e.g.* van der Waals, π···π, dipole-dipole) between the molecular scaffolds.[51, 52] The utility of closed-shell forces in templated photoreactions that employ Ag(I) ions will be discussed in greater detail in the subsequent sections. Alternatively, the utility of aurophillic interactions has been realized in the construction of a [2]rotaxane. The cyclic trinuclear gold complex was shown to complex $Au(PMe_3)_2^+$ at sufficient strength to maintain the interaction even in solution (Fig. 7).[52]

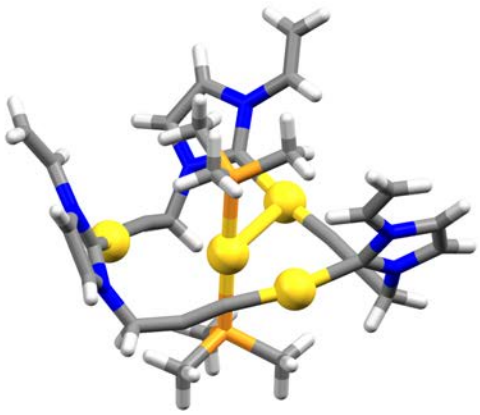

Figure 7 X-ray crystal structure of a [2]rotaxane that encapsulates $Au(PMe_3)_2^+$ *via* Au···Au forces between the host and guest (color scheme: Au-bright yellow).

Coordination bonds have found widespread application in supramolecular chemistry owing to their intermediate strength, reversibility, and inherent ability to impart geometric constraints based on the principles of inorganic chemistry.[53-55] The selection of an inert or labile coordination bond is crucial to the assembly of supramolecular structures as the dynamic nature of the latter allows the components of a supramolecular structure to undergo a series of "error corrections" until the thermodynamically favored product is achieved.[56] Once a stable structure is obtained the

labile coordination bonds are capable of showing remarkable cooperativity to impart enhanced ligand stability.[56] Coordination bonds also offer the panoply of tools supplied by the field of inorganic chemistry (*e.g.* coordination number, chelation) to impart function into supramolecular structures. Consequently, coordination bonds offer a unique and attractive means to modify the properties of supramolecular structures and materials *via* both metal ions and ligands (*e.g.* magnetism, optical).[57-62]

The use of, and understanding of, halogen bonding in supramolecular chemistry has been pioneered by Resnati and Metrangolo.[63-66] The halogen bond can be described as an attractive interaction between an electron poor halogen atom (*i.e.* the donor) and an electron rich atom (*i.e.* the acceptor).[63] With respect to organizing molecules within a supramolecular assembly, experimental and theoretical studies have shown halogen bonding offers an intermolecular interaction with a strong tendency towards linearity.[67] The resulting halogen bond can cause an elongation of the covalent bond that links the halogen atom to the donor molecule.[64] Although computational and gas-phase studies have suggested that halogen bonds can adopt a considerable range of strengths, the forces typically encountered in the solid-state range between *ca.* 2-12 kcal/mol.[68]

Commonly, the constituents of a supramolecular assembly sustained by halogen bonding will employ a halogen bond donor wherein the donating halogen atom is covalently linked to a molecule with electron-withdrawing substituents (*e.g.* fluorine) and paired to a halogen-bond-acceptor that has moderate electronegativity (*e.g.* N-atom is preferred over an O-atom).[64] The utility of halogen-bonding with perfluorinated constituents can be exemplified in a study of α,ω-diiodoperfluoroakanes by Resnati and Metrangolo.[65] By utilizing a series of bis(trimethylammonium) alkane diiodides the researchers were able to selectively encapsulate α,ω-diiodoperfluoroakanes based on the formation of $I^-\cdots I$ forces (Fig. 8). Interestingly, the process is highly selective for the α,ω-diiodoperfluoroakane that matches the alkyl chain length of the bis(trimethylammonium) alkane diiodides so that the components can form $I^-\cdots I$ halogen

bonds. Additional examples of halogen bonding in supramolecular materials includes work with 1,3,5-triiodotrifluorbenzene wherein cocrystallization with ammonium, sulfonium, and phosphonium iodides resulted in a honeycomb framework.[69]

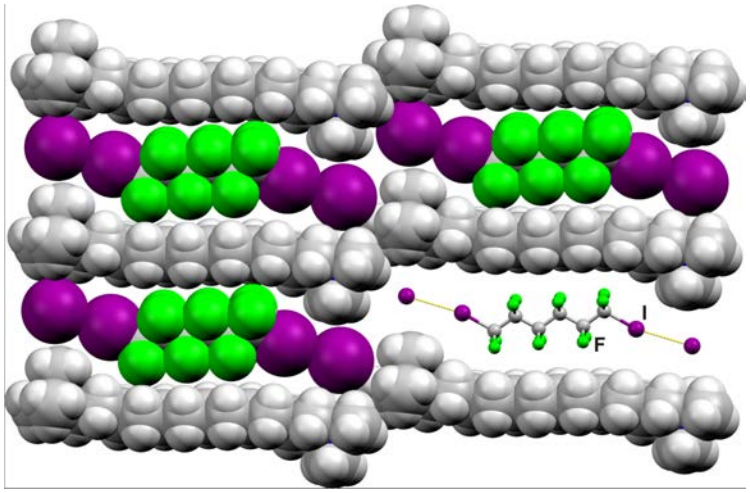

Figure 8 X-ray crystal structure that exemplifies the ability to selectively encapsulate α,ω-diiodoperfluoroakanes *via* interactions with the hosts I^- anions. Reprinted with permission of John Wiley and Sons, copyright 2011.

Hydrogen bonds, the final supramolecular interaction to be described in this survey, are considered the 'master-key' of anisotropic interactions.[70] The concept of the hydrogen bond can be attributed to Huggins and, despite objections by Huggins, also to Latimer and Rodebush for their independent research.[71] Then in 1931, in a paper describing the nature of the chemical bond, Pauling first used the descriptor 'hydrogen bond'.[72] As described by Pauling, a hydrogen bond may be formed when the electronegativity of A relative to hydrogen in an A-H covalent bond is sufficient to cause deshielding of the hydrogen.[73] The hydrogen bond then forms with an acceptor atom B that comprises lone-pair electrons or polarizable π-electrons resulting in an A-H···B arrangement. Hydrogen bonds have the flexibility to exist between a variety of

functionalities with various lengths, geometries, and strengths that lie in a continuum from strong (*e.g.* HF_2^-) to weak (*e.g.* C-H···O) in strength (total range *ca.* 1-30 kcal/mol).[6, 71, 74, 75]

Hydrogen bonds are ubiquitous in science and, as one would expect, the prominence of hydrogen bonds is also reflected in the number of supramolecular assemblies that utilize hydrogen bonding. While supramolecular interactions provide a plethora of construction options, consideration must be given to the molecular recognition process and manner in which the components undergo self-assembly to yield the final supermolecule. Molecular recognition is the process by which molecules select each other *via* favorable intermolecular interaction to yield a well-defined structure.[6] Molecular recognition is observed across biochemistry in events such as enzymatic processes where an enzyme selectively binds a substrate or in the high fidelity matching of DNA base pairs *via* hydrogen bonds and π···π interactions. With respect to synthetic systems, the fundamental understanding of molecular recognition can be traced back to the pioneering work on host-guest systems performed by Nobel laureates Pedersen, Lehn, and Cram.[2, 3, 5] Specifically, their results elucidated the demands, and utility, of molecular recognition in the systematic study of cationic binding with molecular hosts. The results demonstrated an ability to selectively bind cations by tuning the size of the molecular receptor to coincide with the size of the desired metal cation. A logical expansion of molecular recognition is to utilize the knowledge gained in constructing simple complexes (*e.g.* 1:1 host-guest assemblies) and apply that knowledge to the construction of larger supramolecular architectures wherein a series of molecular recognition events operate in a coherent, cooperative, manner to construct a supermolecule in a process referred to as self-assembly

Akin to molecular recognition, self-assembly is readily observed across a wide spectrum of biological processes. Nature has shown a remarkable ability to exploit the reversible nature of intermolecular interactions as part of an error correction process to

construct complex supramolecular molecules (*e.g.* proteins). This process is exemplified in a study of the denaturation and renaturation of ribonuclease A by Anfinsen.[76] The results showed ribonuclease A is readily denatured in a solution with a high concentration of urea to disrupt hydrogen-bonding interactions and mercaptoethanol to cleave the four disulfide bonds of riboculease A. The process leaves the polypeptide in an unfolded state. Remarkably, when urea is removed and the conditions are adjusted to allow disulfide bonds to form and break in an equilibrium process, the protein refolds to the original state with full restoration of catalytic activity. With respect to supramolecular chemistry, Whitesides has defined self-assembly as "the spontaneous assembly of molecules into structured, stable, noncovalently joined aggregates."[77] The success of arranging molecules into supramolecular aggregates in the liquid phase has provided a vast array of architectures, which have been thoroughly reviewed elsewhere.[6, 27, 78] However, it is worth noting the fundamental difference between self-assembly in solution versus the solid-state. Solution self-assembly is a thermodynamically driven process that utilizes the reversible nature of supramolecular interactions to undergo a series of error corrections until the most stable form is obtained.[6] In contrast, crystal self-assembly is a non-equilibrium process where the opportunity to undergo a shuffling of intermolecular interactions is limited. While the final structure certainly possesses intermolecular interactions the arrangement, and strength, of these interactions is subject to the crystallization conditions. For example, rapid nucleation can trap molecules in a kinetic arrangement (*i.e.* metastable polymorph) that fails to maximize the potential for strong intermolecular interactions. Thus, the construction of a supermolecule *via* crystal self-assembly requires consideration of nucleation thermodynamics in addition to the necessary intermolecular interactions to place molecules in a desired arrangement.[6]

1.2. Crystal engineering

Crystal engineering, as defined by Desiraju is 1989, is "the understanding of intermolecular interactions in the context of crystal packing and in the utilization of such understanding in the design of new solids with desired physical and chemical properties."[8] In relation to supramolecular chemistry, Dunitz expressed the idea that the crystal is a supermolecule par excellence.[7] The term crystal engineering was originally introduced by Pepinsky in 1955 but the idea of 'engineering' a crystal was not implemented until 1971.[79] At that time, Schmidt *et al.* first proposed the idea of engineering photochemical reactions in the solid-state *via* favorable intermolecular interactions.[80] The idea of controlling intermolecular interactions to orient molecules in a desired arrangement further evolved upon the introduction of synthon theory.[81] Synthon theory in crystal engineering strives to establish reliable intermolecular interactions between functionalities to control the architecture of molecular solids to impart a desired property. The term "synthon" was originally introduced by Corey as a tool in the retrosynthetic analysis of complex synthetic targets.[82] In crystal engineering, Desiraju describes a supramolecular synthon as "structural units within supermolecules which can be formed and/or assembled by known or conceivable synthetic operations involving intermolecular interactions."[81] Supramolecular synthons are classified as homosythons, intermolecular interaction sustained by two identical moieties, or heterosynthons wherein the functionalities of the synthon are chemically distinct, yet complementary. The synthon-based approach has been widely successful in the design-driven construction of solids with one-, two-, and three-dimensional networks. This strategy is exemplified in the construction of diamondoid networks.[83] For example, Wuest *et al*. utilized a tetra-arylcore decorated with pyridone subunits capable of forming two-point homosynthons with neighboring pyridone moieties, which directs the formation of a diamondoid network (Fig. 9).[83] Although the field of crystal engineering consists of a little over 40 years of experience the field has matured into an application driven discipline. In part,

owing to the design-driven approach synthon theory affords, crystal engineering has contributed to a vast array of fields such as pharmaceutics,[84-87] synthetic chemistry,[88] and semiconductors.[89, 90]

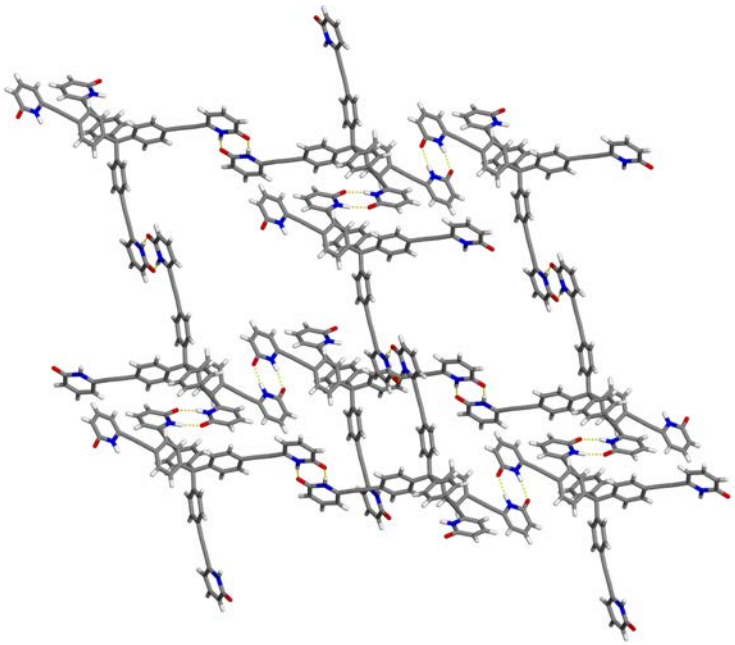

Figure 9 X-ray crystal structure of a diamondoid network constructed *via* intermolecular interactions between pyridone functionalities. Reprinted with permission of John Wiley and Sons, copyright 2011.

1.3. Crystal engineering applications

1.3.1. Pharmaceutical cocrystals

The impetus for pharmaceutical cocrystals can be connected to the current state of pharmaceutical agents (PAs) in development. Estimates place the percentage of PAs in development that exhibit poor aqueous solubility at 60%.[91] Traditionally, to improve the aqueous solubility of a PA the molecule would be subjected to extensive salt, polymorph, and hydrate/solvate screening with the goal of discovering a new phase with desirable properties.[92] However screening for a polymorph or hydrate/solvate that exhibits

improved physicochemical properties relies of a serendipitous event and lacks any preconceived design strategies that may affect the final arrangement of molecules in the new solid form. Meanwhile, salt formation relies on the composition of a PA agent to include an ionizable functionality.[84] In addition, salts are largely based on coulombic forces (*i.e.* ion-ion interactions) that lack the directionality inherent to other supramolecular interactions (*e.g.* hydrogen bonds).[84] Recently, Zaworotko and Almarrson introduced the concept of pharmaceutical cocrystals as a means to alter the physicochemical properties of a PA.[93] Pharmaceutical cocrystals are multi-component solids that exist as a stoichiometric ratio of a PA and a cocrystal former wherein both constituents are solid at ambient conditions. The design of pharmaceutical cocrystals is based on a retrosynthetic analysis that identifies complementary functional groups for the assembly of supramolecular synthons between a PA and a cocrystal former. With respect to improved physicochemical properties, a series of cocrystals with itraconazole exemplify the pharmaceutical cocrystals approach.[94] Specifically, itraconazole was cocrystallized with a series of dicarboxylic acids that assembles to form a heterosynthon between the triazole moiety of itraconazole and the carboxy group of the cocrystal formers (Fig. 10). The dissolution profile of itraconazole, Sporanox (an amorphous form of itraconazole on the market), and three cocrystals were compared. The results showed that in all cases the cocrystals exhibited improved solubility over itraconazole and, in the case of a *L*-malic acid itraconazole cocrystal, the cocrystal rivaled the dissolution of Sporanox. Subsequent research on pharmaceutical cocrystals has proven a wide array of physicochemical properties can be adjusted *via* cocrystallization. Specifically, the utility of pharmaceutical cocrystals has been realized with respect to structure determination, isolation of elusive intermediates, solubility/dissolution rate, bioavailability, hygroscopicity, and mechanical compaction.[84-87, 95-97]

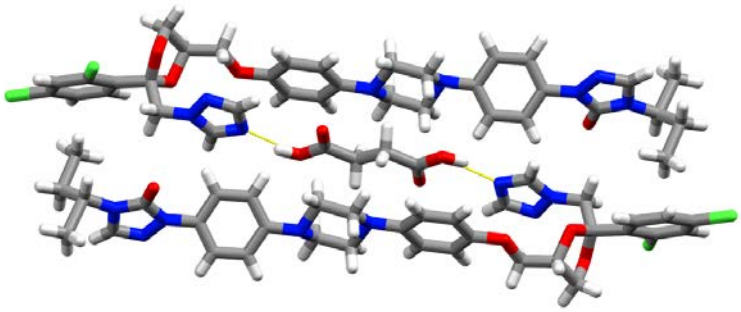

Figure 10 Perspective view of the X-ray crystal structure of itraconazole and *L*-malic acid that reveals a heterosynthon interaction between the cocrystal components.

A reflection of the utility of pharmaceutical cocrystals has been an increase in the screening methods used to discover pharmaceutical cocrystals. Cocrystals can be prepared *via* slow-solvent evaporation, melt crystallization, sublimation, mechanochemistry, sonochemistry, or solution-mediated phase transformation (SMPT).[84, 98] While each technique has merits the focus will be on the screening method employed in our group, SMPT. Originally introduced by Zhang *et al*., the slurry technique was based on an understanding of the thermodynamic driving force behind hydrate/solvate formation.[98] The results of their study suggest for pharmaceutical cocrystals one can expect cocrystal nucleation to occur when the activity of each cocrystal component exceeds a critical value. To ensure the activity of each component surpasses a critical value, a slurry is prepared such that an excess amount of solid is present as a physical mixture of the cocrystal components. In this environment, the activity values of both cocrystal components are held at one, which provides a thermodynamic driving force for cocrystal nucleation. Upon nucleation, the physical mixture is converted to cocrystal *via* a SMPT process until the activity of one of the cocrystal components decreases below the critical value. The efficiency of the SMPT screening method was originally demonstrated in a study of 16 known cocrystals. Subsequent research has not only

utilized SMPT as a means to discover wealth of new cocrystals[99-101] but has even identified a cocrystal composed of caffeine and adipic acid which was previously missed in screening procedures that utilized mechanochemistry.[102]

1.3.2. Organic nanocrystals based on multi-component solids

Despite the immense amount of research dedicated to nanometer scale materials, nanoscience largely comprises the study of the synthesis and size-dependent properties of inorganic-based nanocrystals.[103] Then in 1992, Nakanishi *et al*. introduced a reprecipitation method capable of fabricating organic nanocrystals in the absence of the harsh conditions (*e.g.* high temperature) commonly used to prepare inorganic nanocrystals.[104] Subsequent research has demonstrated organic nanocrystals exhibit interesting size-dependent properties (*e.g.* blue-shifted fluorescence).[105, 106] These properties have found applications in areas such as liquid crystal displays and organic field effect transistors, however, the studies were limited to single components systems.[107] Then in 2006 MacGillivray introduced a sonochemical method for the preparation of nanometer-scale cocrystals.[108] Nano-cocrystals are inherently more challenging to synthesize from a fabrication technique, such as the reprecipitation method, owing to the inherent solubility difference between the cocrystal components. The solubility difference arises from the necessity of cocrystal components to have orthogonal functionalities (*i.e.* hydrogen-bond-donors and –acceptors), which can be assembled into a supramolecular synthon.[109] The inability to achieve a desired concentration may have a detrimental impact on cocrystal nucleation and growth. In fact, in a study on the cocrystal, (resorcinol)·(*trans*-1,2-bis(4-pyridyl)ethylene) (**RES**)·(**BPE**), an attempt to use the reprecipitation method by dissolving the cocrystal components in a common high solubility solvent (*i.e.* ethanol) resulted in predominantly micron sized crystals. To overcome the solubility difference and achieve nanometer-scale cocrystals

ultrasonic irradiation was employed. Specifically, the cocrystal components were separately dissolved in a high solubility solvent (*i.e.* ethanol) then injected into an anti-solvent during exposure to ultrasonic irradiation. The coupling of rapid precipitation and ultrasonic irradiation resulted in a decrease in size to the nanoscale. Importantly, the reduction in size enabled the nano-cocrystals to undergo a single-crystal-to-single-crystal (SCSC) [2+2] photodimerization whereas macro-sized cocrystals cracked upon exposure to UV irradiation. The ability to impart SCSC reactivity through a reduction in size has widespread materials science applications (*e.g.* 3D data storage).

The ability to synthesize a nano-cocrystal *via* sonochemistry enabled additional investigations into the mechanical properties of nano-cocrystals. Specifically, the goal was to better understand the mechanical properties of crystals that undergo SCSC transformations. To achieve this goal, (5-cyanoresorcinol)·(**BPE**), (**5-CN-res**)·(**BPE**) was utilized owing to an ability to undergo a SCSC photodimerization in crystals of macro- or nanometer-scale dimensions.[110] Using atomic force microscopy nanoindentation analysis, the study determined macro-sized crystals of (**5-CN-res**)·(**BPE**) are comparatively soft and become 40% softer after the cycloaddition reaction. When (**5-CN-res**)·(**BPE**) was nanosized the cocrystal exhibited an 85% increase in stiffness and became 40% harder following the [2+2] photodimerization. The findings of this report suggest significant materials science application for multi-component nanocrystals. Specifically, the ability to modify the properties of a cocrystal by substituting one of the cocrystal components or through nanocrystallization offers the potential of materials with highly tailored properties.

1.3.3. Template-directed [2+2] photodimerizations in the solid-state

The design of solid-state systems capable of undergoing photo-induced reactions lies at the foundation of crystal engineering. Pioneered by Schmidt *et al.*, a study of

substituted cinnamic acids identified the conditions in which olefins can be expected to undergo a [2+2] photodimerization in the solid-state.[80, 111, 112] The requirements, known as the topochemical postulate, state olefins are expected to undergo a [2+2] photodimerization when the olefins are parallel and separated by < 4.2 Å. [80, 107, 108] The reactivity of olefins in the solid-state is exemplified by the three polymorphs of *o*-ethoxy-*trans*-cinnamic acid. The α- and β-polymorphs crystallize with olefins that lie parallel and within 4.2 Å, however, the molecules that comprise the α-form are arranged in a head-to-tail arrangement while the molecules of the β-form are oriented in a head-to-head fashion. Upon exposure to UV irradiation, both polymorphs undergo a cycloaddition reaction. A third polymorph of *o*-ethoxy-*trans*-cinnamic acid, namely the γ-form, also crystallizes in a head-to-tail arrangement but the olefins are separated by 5.3 Å, which results in photostability when exposed to UV irradiation.

In the work of Schmidt, photoreactive species were achieved by screening with multiple functional groups and crystallization conditions to isolate a form in which the olefins are topochemically aligned. In 2000, MacGillivray *et al.* introduced a cocrystallization method to impart control over the arrangement of olefins in the solid-state.[113] Specifically, **BPE** was cocrystallized with an equimolar amount of **RES**, which juxtaposes two **BPE** molecules in a discrete four-component assembly wherein the olefins of **BPE** are topochemically aligned. Subsequent research has shown **RES**-based molecules can successfully template the cycloaddition reaction of di- and tri-olefins with terminal pyridine functionalities. Remarkably, the template approach has proven to be modular with respect to a change in the template (*i.e.* substituted resorcinols), the molecular structure of the pyridyl-based moieties, and in an inversion of the hydrogen-bonding roles wherein the reactive olefin (*e.g.* fumaric acid) is a hydrogen bond donor.[88]

The modularity of the template approach is exemplified in an investigation of the solid-state photodimerization of 1,4-bis(4-pyridylethenyl)benzene (**BPEB**). Cocrystallization of **BPEB** with 5-methoxyresorcinol results in a discrete four-

component assembly in which the resorcinol-based template juxtaposes **BPEB** molecules.[114] In this arrangement, the olefins of **BPEB** are topochemically aligned, however, exposure to UV radiation results in only 60% of the targeted paracyclophane product owing to the formation of byproducts that are the result of cycloaddition reactions between neighboring assemblies. The modularity of the template approach was observed when **BPEB** was cocrystallized with 4-benzylresorcinol. In this cocrystal, the components again form a discrete four-component assembly with olefins that are favorably aligned but the packing of neighboring assemblies arranges the olefins at 5.8 Å, which is unsuitable for a photoreaction. As a result of the template switching, the byproducts were eliminated and the desired paracyclophane product was able to form in a 100% yield.

As previously noted, the template approach can be extended to include olefins with functionalities such as carboxylic acids. Specifically, cocrystals of fumaric acid and 2,3-bis(4-methylenethiopyridyl)naphthalene (**MTPN**) were synthesized in which the cocrystal components form a four-component assembly sustained by a carboxy···pyridine heterosynthon (Fig. 11).[115]

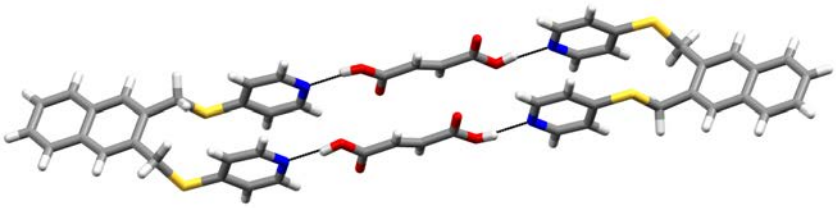

Figure 11 Perspective view of the X-ray crystal structure of fumaric acid and **MTPN** wherein the template approach is shown to align olefins based on the carboxylic acid group.

In this arrangement, the olefins of fumaric acid are aligned and undergo a SCSC transformation to yield the *rctt*-1,2,3,4-cyclobutanetetracarboxylic acid photoproduct.

The ability to instill functional group diversity not only extends the generality of the template approach but also affords cyclobutane photoproducts that are amenable to post-synthetic modifications.

The ability to template [2+2] photoreactions with coordination bonds has also been realized. Initially, the self-assembly of olefins was investigated using a dinuclear Schiff-base complex $[Zn_2\mathbf{L}(OH)]^{2+}$ (**L** = 2,6-bis[N-2(pyridylethyl)formimidoyl]-4-methylphenol) which arranges metal ions at a separation distance of *ca.* 3.2 Å.[116] Crystallization of $[Zn_2\mathbf{L}(OH)]^{2+}$ with **BPE** results in a complex that stacks **BPE** molecules at a distance suitable [2+2] photodimerization. UV irradiation of the metal complex results in a cycloaddition reaction involving the **BPE** molecules *via* a SCSC process. Interestingly, this solid provided the first example of a metal-organic solid that exhibits fluorescence based on the status of a photoreaction. The solid emitted a blue emission at 464 nm before photodimerization while the photoproduct has a green emission at 520 nm.

Although the Schiff-base complex afforded a framework suitable for arranging pyridine-substituted olefins interest remained in a metal-organic systems, akin to substituted resorcinols, amenable to template switching. A notable candidate for templated metal-organic photoreactions was the Ag(I) ion owing to a preference to adopt a linear coordination geometry and participate in argentophilic interactions at *ca.* 3.4 Å.[117-119] In an initial investigation, Ag(I) ions were crystallized with *trans*-1-(4-pyridyl)-2-(phenyl)ethylene (**4STBZ**).[51] Structural analysis *via* revealed the Ag(I) ions coordinate **4STBZ** molecules in a transoid arrangement that assembles into a dinuclear assembly sustained by Ag···Ag forces (Fig. 12). Within the assembly, the **4STBZ** molecules are arranged in a head-to-head fashion that places olefins at a distance suitable for a [2+2] photodimerization, however, the olefins exhibited a criss-cross arrangement.

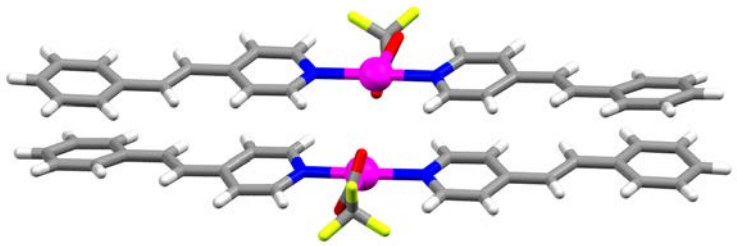

Figure 12 Perspective view of the discrete four-component assembly that forms with Ag(I) ions and **4STBZ** (disorder omitted for clarity).

Despite this arrangement, upon exposure to UV irradiation the complex undergoes a SCSC photodimerization to yield a cyclobutane photoproduct. The reactivity of the olefins in this instance was attributed to a pedal-like motion that occurs in the solid-state.[120] Interestingly, the SCSC process converted the dinuclear assembly 1D coordination network. To accommodate this transformation, the Ag(I) move apart *ca.* 1.2 Å which eliminates the previously observed argentophilic interactions but enables the formation of cation-π interactions. The photodimerization represents the first example of a finite complex undergoing a conversion to an infinite network and again highlights the surprising flexibility of the solid-state. In total, the template approach has afforded synthetically challenging products in quantitative and stereospecific yields. Products such as cyclophanes, ladderanes, and unsymmetrical cyclobutanes have a range of applications in materials science, natural products chemistry (*e.g.* ladderane lipids), the fabrication of self-assembled capsules, and metal-organic frameworks.[88]

1.3.4. Metal-organic frameworks and biomedical imaging

Coordination polymers and metal-organic frameworks (MOFs) have utilized the directional nature of coordination bonds to construct a vast collection of functional, self-assembled, networks. In seminal work, Robson described the synthesis of 3D coordination polymers based on the assembly of tetrahedral and octahedral metal

cyanides with linear organic molecules.[53] The diamondoid structures contained very-large adamantane-like cavities capable of performing ion exchange. Subsequent research, notably by Yaghi, on MOFs developed linear carboxylate bridges and metal clusters as nodes for the construction of 3D networks (Fig. 13).[121, 122]

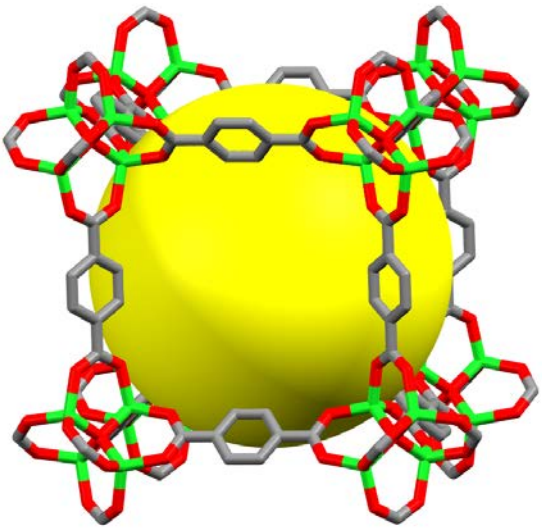

Figure 13 X-ray crystal structure of MOF-5 (color scheme: Zn-green) (solvent and counterions omitted for clarity). Reprinted with permission of John Wiley and Sons, copyright 2011.

A form of isoreticular synthesis has been described that enables the extended structures of MOFs to be retained and readily-modified to tune the pore structure, size, and connectivity.[122] In fact, recent reports have shown the ability to incorporate a diverse range of functional groups into the pores of MOFs.[59, 123-127] The frameworks have experienced applications in areas such as catalysis, gas storage, and bioimaging.[122, 128-130] For instance, Lin *et al.* have utilized MOFs to overcome the large dosage requirements of molecular contrast agents.[129] Specifically, Cu(II) and Zn(II) were crystallized with 2,3,5,6-tetraiodo-1,4,-benzenedicarboxylic acid to afford a series of coordination

polymers. The resulting solids are biodegradable and capable of delivering high iodine payloads that provide X-ray attenuation comparable to molecular contrast agents.

1.4. Dissertation overview

The focus of this dissertation will be on the development of multi-components solids with specific applications in the pharmaceutical industry, organic synthesis, materials science, and biomedical imaging. Specifically, chapter two will focus on the design-driven synthesis of pharmaceutical cocrystals. The aim our investigation was to develop cocrystals based on acetaminophen wherein the cocrystal components are arranged in a layered topology, which is expected to improve the mechanical properties of acetaminophen. The study employed the cocrystal formers 2,4-pyridinedicarboxylic acid and **BPE** and in both cases we observed unique synthon behavior between the cocrystal components. In the acetaminophen 2,4-pyridinedicarboxylic acid cocrystal the diacid surprisingly underwent an intramolecular proton transfer to afford a red, zwitterionic, cocrystal. The cocrystals composed of acetaminophen and **BPE** resulted in a series of cocrystals with 'masked synthons' wherein there is a lack of direct hydrogen-bonding between the cocrystal components owing to injected water molecules.

Chapter three will focus on the sonochemical preparation of multi-component organic nanocrystals. Specifically, we explore the experimental conditions necessary to synthesize a range of pharmaceutical nano-cocrystals based on caffeine, acetaminophen, carbamazepine, and itraconazole. We believe pharmaceutical nano-cocrystals offer the unique opportunity to combine the beneficial physicochemical properties of cocrystals and nanocrystals. The second portion of this chapter presents our results on the sonochemical preparation of nano- and micrometer sized crystals of a host-guest system. The resulting sonochemical procedure afforded crystals of a hollow rhombic-dodecahedral morphology attributed to a reversed crystal growth process.

Chapter four will focus on increasing the functional group diversity in solid-state [2+2] photodimerizations. The study investigates the ability to reliable align cyano-substituted olefins in the solid-state using templates based on resorcinol and Ag(I) ions. In the case of 4-pyridineacrylonitrile, both templates topochemically align the olefins however only the metal-organic solids underwent a photodimerization. Continued investigations with Ag(I) ions demonstrated the ability to reliable align cyano-substituted stilbazoles and dienes for solid-state [2+2] photodimerizations.

Chapter five describes the first examples of cocrystals based on iodinated contrast agents. In total, we successfully characterized five cocrystals and five salts that contain iodinated contrast agents. The results establish a library of cocrystals composed of contrast agents and a knowledge base of intermolecular interactions to be exploited in the design of future cocrystals with tailored properties.

CHAPTER 2. PREPARATION AND PROPERTIES OF ACETAMINOPHEN COCRYSTALS

A portion of this chapter was published as a communication and is adapted with permission from the *Journal of Pharmaceutical Sciences* [Sander, Bučar, Henry, Baltrusaitis, Zhang, and MacGillivray (2010) A red zwitterionic co-crystal of acetaminophen and 2,4-pyridinedicarboxylic acid, *99*, pp. 3676-3683].

2.1. Introduction

Acetaminophen (**APAP**) was first prepared by Morse in 1878 and has since become one of the most widely used antipyretic and analgesic drugs in the world.[131] There exist two well-characterized forms of **APAP**, a monoclinic Form I and an orthorhombic Form II (Fig. 14).[132, 133] The thermodynamically stable phase of **APAP**, Form I, exhibits corrugated layers sustained by hydrogen bonds between **APAP** molecules. Generally, the preferred method of drug formulation is the compression of a thermodynamically stable form of a pharmaceutical agent (PA) (*e.g.* **APAP** Form I) into an excipient-free tablet.[134] However, **APAP** Form I exhibits poor compressibility.[135-137] In fact, Form I is often used as a model compound to test the applicability of new compaction techniques.[138]

Researchers have investigated methods of simultaneously retaining the stability of **APAP** Form I while improving the mechanical properties of the solid. For example, a desolvated form of **APAP** crystallized from dioxane yields a sintered solid amenable to compression, however, residual solvent has precluded industrial applications.[134, 139-141] Akin to the dioxane crystallization studies, modifications to the crystal habit of Form I have been shown to improve the mechanical properties.[142-145] In particular, a comparison of prismatic and plate-like crystals of **APAP** Form I demonstrated small plate-like crystals exhibit better tableting properties than small prismatic crystals.[142] Indeed, the

benefits of small plate-like crystals were sustained in excipient formulations.[142] Although the APAP concentration becomes reduced when incorporating excipients (*e.g.* methylcellulose) the technique has successfully improved the mechanical properties of Form I.[134, 138, 146] In fact, the utility of such a strategy was further realized when the tableting procedure of **APAP**-excipient mixtures incorporated a precompression followed by a main compression. The resulting tablets exhibit of a higher tensile strength owing to the ductile nature of the heated solids generated during precompression.[146]

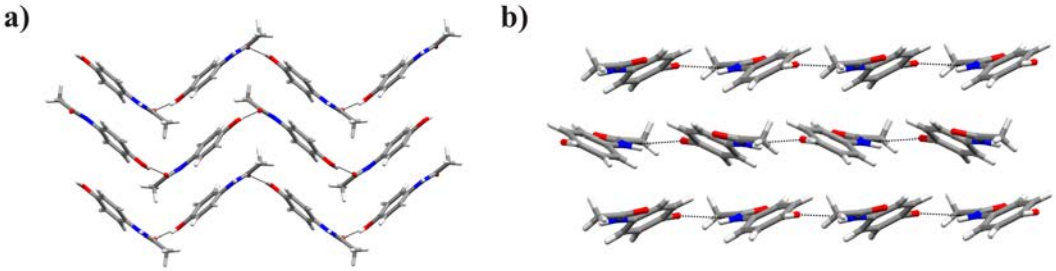

Figure 14 Solid-state packing of APAP (a) Form I and (b) Form II.

Computational studies attribute the poor mechanical properties of Form I to a stiff crystalline structure that resists shearing along the axial planes.[140] In contrast, the parallel planes of Form II lack strong intermolecular interactions between layers, which allows for facile slippage of the planes.[140] Compaction studies on Form II support the hypothesis that the parallel topology enables direct compression into a tablet.[141] Several methods describe the crystallization of Form II from ethanol, aqueous solutions, aqueous solutions with polymer heteronuclei, melt, and high-pressure environments.[132, 147-150] Despite the established crystallization techniques and potential industrial applications of Form II, the phase transformation of Form II to Form I occurs in the presence of residual crystallization solvent, high relative humidity, heating, or Form I impurities.[151-156]

Consequently, there exists great interest in the design of a thermodynamically stable form of **APAP** that exhibits parallel packing of flat hydrogen-bonded layers akin to Form II.

Across the pharmaceutical industry, the majority of drugs on the market or in development are in the solid dosage. However, the current trend in drug discovery is towards molecules that exhibit poor physicochemical properties.[91] **APAP** exemplifies a fundamental formulation challenge in the pharmaceutical industry; the physical properties of a molecular solid are dependent on the molecular arrangement within crystals.[157] To rectify inferior physicochemical properties, while retaining the biological activity of drug molecules, pharmaceutical scientists routinely employ non-covalent means to modify solid-state packing.

Cocrystals have emerged as a means to modify the solid-state arrangement of PAs *via* non-covalent means. Cocrystallization employs a retrosynthetic analysis to select molecular components that contain complementary functional groups capable of assembling *via* supramolecular synthons.[93] Synthons composed of hydrogen bonds can utilize the directional nature of hydrogen bonds to impart partial control over molecular solids to achieve desired properties.[81] In a recent report, Sun *et al.* utilized the directionality of hydrogen bonds to construct a cocrystal that comprises parallel 2D sheets of caffeine and methyl gallate.[96] A comparison was made between the tensile strength of the individual cocrystal components and the 1:1 caffeine methyl gallate cocrystal. Methyl gallate resisted compression under various compaction pressures while caffeine exhibited acceptable tensile strength with compression pressures < 180 MPa. Alternatively, the layers of the caffeine methyl gallate cocrystal provide slippage upon shearing that results in a solid with plasticity similar to an excipient based solid.

Encouraged by the improved tensile strength imparted to caffeine *via* cocrystallization, Jones and coworkers investigated cocrystallization as a means to improve the mechanical properties of **APAP**.[95] **APAP** was screened for cocrystallization with a series of CCFs selected on the basis of size, planarity, and the presence of

complementary functional groups for the assembly of supramolecular synthons with **APAP**. During their investigations, three cocrystals based on varied supramolecular arrangements, (**APAP**)·(theophylline), 2(**APAP**)·(naphthalene), and (**APAP**)·(oxalic acid), resulted in layered topologies (Fig. 15).

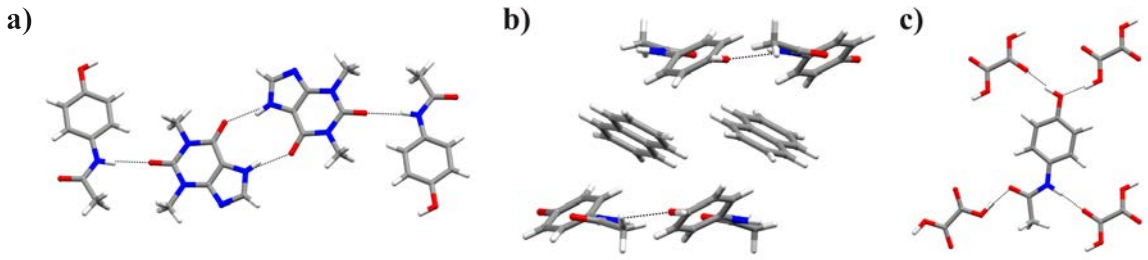

Figure 15 X-ray crystal structures of (a) (**APAP**)·(theophylline), (b) 2(**APAP**)·(naphthalene), and (c) (**APAP**)·(oxalic acid).

The components of the (**APAP**)·(oxalic acid) cocrystal each act as two-fold hydrogen-bond-donors and -acceptors to produce a layered 0D motif. Crystallization of **APAP** and theophylline results in **APAP** chains that pack with theophylline dimers through N-H(amide)···O(carbonyl) hydrogen bonds to give a 2D sheet. The third layered cocrystal, 2(**APAP**)·(naphthalene), involves a serendipitous fit of molecular shapes and sizes.[158] The alternating layers of **APAP** and naphthalene results in layers of **APAP** that resembling the hydrogen-bonding interactions of **APAP** Form II. Although each cocrystal exhibits a different 2D tiling, measurements and calculations verified the layered topology imparts compression properties superior to Form I of **APAP**.

The rectification of mechanical properties through cocrystallization offers an example, among the multitude of reports, wherein the assembly of supramolecular synthons has modified the arrangement of molecular solids.[159] Supramolecular synthons serve as the backbone of a crystal structure by providing a conceptually-coherent

description of the entire structure.[160] In this context, Desiraju has recognized that hydrogen-bonded arrays sustained by targeted synthons can be slightly modified by interjecting crystallization solvent molecules (*e.g.* water).[161] The modification of a synthon has, thus, been classified as a 'moderate success' in synthon theory (Scheme 1).

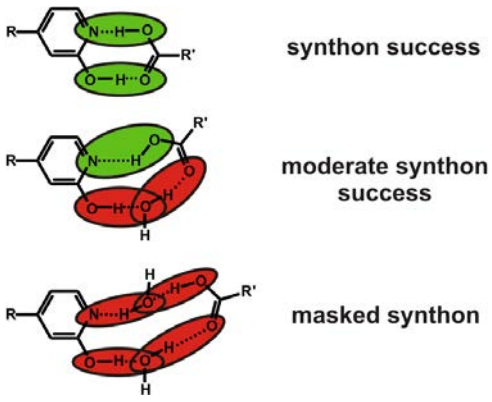

Scheme 1 Supramolecular synthons with levels of masking.

As in the case of moderate synthon success, an interjected solvent molecule can also be responsible for a *complete lack of direct interaction* between the components of a cocrystal. We tentatively classify this third case as 'masked synthons'. Incidences of masked synthons in cocrystallizations *via* interjected solvent molecules are quite rare in spite of the ubiquitous nature of water.

Water hydrogen bonding has maintained a prominent role in scientific research for over seventy years.[71] Water is essential for life processes; the literature describing the vital role of water is vast but can be exemplified wherein the molecule actively participates in the molecular recognition of DNA bases.[162] The pervasive nature of water is attributed to the size of the molecule and a surface area that is entirely capable of participating in hydrogen bonding. The unique properties of water manifest themselves in molecular crystals. A recent survey of the Cambridge Structural Database (CSD)

reported a high frequency (8.1%) of hydrated molecular crystals.[163] Within organic hydrates, water adapts eight different coordination environments capable of hydrogen bonding itself to form water clusters of discrete rings, chains, infinite tapes, or layered structures. Also, water can hydrogen bond to organic molecules of the crystal as a host, guest, combination of host or guest, or as an integral part of the structure.[164-167] Despite many rationalizations, correlations, and examples, the hydration of molecular crystals remains unpredictable.[161]

The intense research into pharmaceutical cocrystals has increased the incidence of reported cocrystals owing to improved protocols, cocrystallization techniques, and high-throughput screening. In parallel, reports of cocrystal polymorphs, hydrates and solvates have also increased. These structures can provide insight into the robust nature of supramolecular synthons in the assembly of cocrystals. For example, an analysis of 39 cocrystal polymorphs revealed 35 of those pairs maintained their supramolecular synthon with only slight changes to the overall packing.[168] The report also identified 12.4% of all reported cocrystals are cocrystal hydrates. Although the sample sizes vary by orders of magnitude, a comparison of the incidence of hydration in molecular crystals (8.1%) to cocrystals (12.4%) suggests cocrystals may have a greater propensity towards hydration. In addition, despite a determination of the incidence of hydrated cocrystals, a close examination of the hydrogen-bonding patterns exhibited by cocrystal hydrates has yet to be completed.

Our interests lie in the design driven discovery of pharmaceutical cocrystals that, in this case, utilize planar CCFs to direct the formation of a layered cocrystal with **APAP**. The design of the cocrystals consists of forming either a O-H(phenol)···N(pyridyl) or a N-H(amide)···N(pyridyl) heterosynthon. Reported **APAP** cocrystals show an ability of **APAP** to cocrystallize with CCFs containing aromatic N-atoms. Parsons has reported a cocrystal of **APAP** and 4,4'-bipyridine that comprises **APAP** chains sustained by O-H(phenol)···O(amide) hydrogen bonds (Fig 16a).[169]

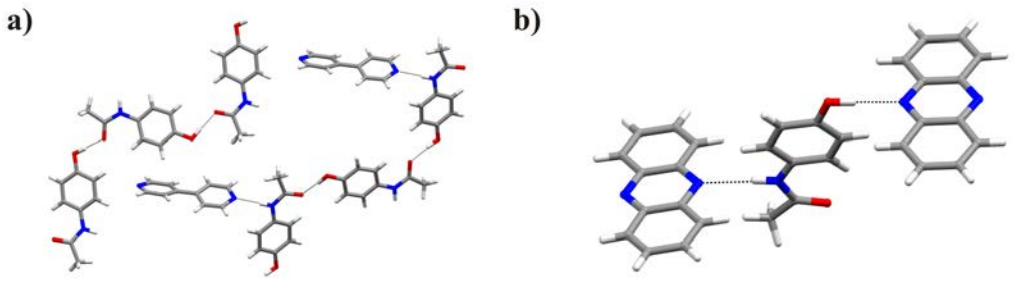

Figure 16 X-ray structures of (a) (**APAP**)·(4,4'-bipyridine) and (b) (**APAP**)·(phenazine) wherein **APAP** cocrystallizes with CCFs containing an aromatic N-atom.

The **APAP** chains orient N-H groups towards the pyridine functionality to form the N-H(amide)···N(pyridyl) heterosynthon. Jones cocrystallized **APAP** and phenazine to yield a solid that contains both potential heterosynthons between the components (Fig 16b).[95] The structure involved a Z-shaped supramolecular assembly wherein **APAP** acts as a dual hydrogen-bond donor to a pair of phenazine molecules through O-H(phenol)···N(pyridyl) and N-H(amide)···N(pyridyl) hydrogen bonds. Both examples demonstrate the reliability of forming **APAP** cocrystals with the O-H(phenol)···N(pyridyl) or the N-H(amide)···N(pyridyl) heterosynthon.

2.2. Materials and methods

2.2.1. Materials

Acetaminophen (98.0%) was purchased from Acros Organics while *trans*-1,2,-bis(4-pyridyl)ethylene (**BPE**) (97.0%) and 2,4-pyridinedicarboxylic acid (**PDA**) monohydrate (98.0%) were purchased from Aldrich. Ethanol (100%) was purchased from Decon Labs and methanol (ACS Reagent, ≥99.8%) was purchased from Sigma-Aldrich. All materials were used as received.

2.2.2. Survey of the Cambridge Structural Database

The CSD (version 5.31, updated November 2009) was searched for entries involving either **PDA**. The search was performed using ConQuest (version 1.12) and restricted to only organic compounds. A CSD survey revealed one entry involving **PDA** in the form of a cocrystal.

A survey of the CSD (version 5.32, update 5, November 2011) was performed with ConQuest30 (version 1.13) to investigate cocrystal hydrates. The structures must satisfy the following criteria: (a) crystallographic R factor < 0.10, (b) no ions, (c) 3D coordinates fully determined, (d) and purely organic components.[164] Searching for entries that contain the structure H-O-H retrieved molecular hydrates. The results were refined to those entries that contain 3, 4, 5, or 6 chemical units. Next, the entries were individually examined for solids containing at least two components that are solid at ambient conditions. Within the pool of remaining entries, a cocrystal was deemed to contain masked synthons when the components comprise functionalities capable of assembly into supramolecular synthons but lack any direct hydrogen bonding. The hydrogen-bonding interactions between components were limited to only those interactions less than the sum of the van der Waals radii.[167] To identify those structures comparable to **APAP** cocrystals we excluded host-guest/clathrate systems and structures formed in the strict absence of crystal engineering precepts.

2.2.3. Cocrystal screening

To explore cocrystal formation between **APAP** and CCFs that comprise sp^2-hybridized, or aromatic, N-atoms we employed the solution-mediated phase transformation (SMPT) based screening procedure. In a typical screening experiment with **APAP** and **BPE**, solid **APAP** was combined with an equimolar amount of BPE (99 mg total) and suspended in a low volume of solvent (700 μL) (*i.e.* 4:1 (v/v) water ethanol, 2:1 (v/v) ethanol water, aqueous ethanol, or 1:1 (v/v) ethanol methanol). Screening

experiments that comprise **APAP** and **PDA** consisted of solid **APAP** (1.0 mmol) combined with an equimolar amount of **PDA** and suspended in ethanol (2 mL). Solvents were selected based on an ability to solubilize both cocrystal components. The resulting suspensions were sonicated for 5 min using an ultrasonic cleaning bath (Branson 2510R-DTM; frequency: 42kHz ± 6% at 100W) to facilitate SMPT then equilibrated at ambient conditions for one week. Each solid was then filtered and analyzed *via* powder X-ray diffraction (PXRD). Those solids that exhibited a powder pattern different from the starting cocrystal components were further studied using single crystal X-ray diffraction.

2.2.4. Single crystal preparation

Single crystals of composition (**APAP**)·1.5(**BPE**)·4(H_2O) (**APAP1**), (**APAP**)·1.5(**BPE**)·2(H_2O) (**APAP2**), (**APAP**)·(**BPE**)·2(H_2O) (**APAP3**), and 2(**APAP**)·(**BPE**)·(ethanol) (**APAP4**) were achieved *via* slow-solvent evaporation. **APAP1**, **APAP3**, **APAP4** were prepared from a 1:1 molar ratio (33 mg total) of the cocrystals components whereas **APAP2** was prepared from a 1:1.5 molar ratio (42 mg total) of **APAP** to **BPE**. Single crystals of **APAP1-APAP4** were obtained by dissolving the polycrystalline solids using the corresponding solvents, 4:1 (v/v) water ethanol, 2:1 (v/v) ethanol water, aqueous ethanol, or 1:1 (v/v) ethanol methanol, respectively. The solutions were left to slowly evaporate at ambient conditions until suitable single crystals were obtained.

Single crystals of composition (**APAP**)·(**PDA**) (**APAP5**) were grown by slow-solvent evaporation. **APAP** (45 mg) and **PDA** monohydrate (54 mg) were separately dissolved in ethanol upon heating. The hot solutions were filtered through a cotton plug and simultaneously combined in a vial. The resulting solution was allowed to slowly evaporate at ambient conditions over the course of one month. Single crystals of (**PDA**)·(H_2O) (**PDA1**) were obtained *via* dissolution of **PDA** (25 mg) in boiling ethanol.

The solution was filtered through a cotton plug then allowed to slowly evaporate over the course of one week.

2.2.5. Powder X-ray diffraction measurements

PXRD data for **APAP** and **BPE** screening experiments were obtained from samples mounted on glass slides by a Siemens D5000 X-ray diffractometer using $CuK_{\alpha 1}$ radiation (λ = 1.54056 Å). The diffractometer was equipped with a Bruker Sol-X energy-sensitive detector (scan type: locked coupled; scan mode: continuous; step size: 0.02^{o}; scan time: 2s/step). PXRD data for **APAP** and **PDA** screening experiments were collected using an Inel G3000 diffractometer equipped with a curved position sensitive detector and parallel beam optics. Samples were loaded into aluminum sample holders and flattened with a glass slide. The diffractometer was operated with a copper anode tube (1.5 kW fine focus) at 40 kV and 30 mA. An incident beam germanium monochromator provided monochromatic $CuK_{\alpha 1}$ radiation. The diffractometer was calibrated using the attenuated direct beam at one-degree intervals. Calibration was checked using a silicon powder line position reference standard (NIST 640c). The program Symphonix[170] controlled the diffractometer the data was analyzed using Jade[171].

2.2.6. Single crystal X-ray diffraction measurements

Single crystals of **APAP1-APAP4** were individually mounted on glass fibers. Intensity data were collected on a Bruker APEX2 system. Data were collected at 100 K with graphite-monochromated MoK_{α} radiation (λ = 0.71073 Å). Data were collected in four sets using omega-phi scans with omega steps of 0.5° and phi steps of 90°. A total of 1464 frames were collected. Data were processed using *SaintPlus*.[172] Corrections for Lorentz-polarization effects were applied. Absorption was negligible. All structures were solved using direct methods that yielded the non-hydrogen atoms. All presented hydrogen atoms were located in Fourier-difference electron density maps. All non-hydrogen atoms were refined anisotropically. Hydrogen atoms associated with carbon

atoms were refined in geometrically constrained riding positions. Hydrogen atoms associated with oxygen atoms were included in the located positions. Refinement was achieved with the use of SHELX-97.[173]

Crystallographic analysis of **APAP5** and **PDA1** were performed on a Bruker SMART diffractometer equipped with an APEX1 CCD camera. The single crystals were mounted on a glass pin using epoxy glue. X-ray diffraction data sets were collected using graphite-filtered MoK_α radiation (λ = 0.71069 Å) at 100 K, processed using *SaintPlus*[174], and corrected for Lorentz-polarization effects. The data sets were collected performing omega scans with 0.5° steps. Structure solution and refinement were accomplished using *XSHELL*.[173] All non-hydrogen atoms were refined anisotropically and all hydrogen atoms bonded to carbon atoms were located in the Fourier-difference electron density map, fixed in geometrically constrained riding positions, and refined isotropically on the basis of corresponding C-atoms [U(H) = 1.2 U_{eq}(C)]. Hydrogen atoms associated with oxygen and nitrogen atoms were included in the located positions. The single crystal of **PDA1** exhibited pseudo-merohedral twinning. The program PLATON was used to identify a twofold rotation axis about a^* as twin law that is described by the matrix [1,0,1/0, -1,0,0/0, -1]. The implementation of the determined twin law in the structure refinement procedure resulted in a drop in the R-value from R = 0.121 to R = 0.044. The ratio of the fractional contributions of both twin domains was refined to be 0.456(2):0.544(2).

2.2.7. Mechanochemistry

Liquid-assisted grinding (LAG) experiments were performed manually with a mortar and pestle or mechanically with a mill. Manual grinding consisted of milling an equimolar amount of **APAP** and **BPE** (132 mg total) for 20 min with aliquots of hexanes (7 x 1 mL) added throughout the course of the experiment. The mechanical grinding used a stainless steel cell and two stainless steel balls. Physical mixtures of equimolar

amounts of **APAP** and **BPE** (200 mg total) were ground at 30 Hz for a total of 30 min. Hexanes (V = 200 μL) was used to facilitate cocrystal formation while limiting the amount of water introduced into the system.

2.2.8. Optical microscopy

Single crystals of **APAP5** were examined using a Wild-Heerbrugg M3Z (Leica Microsystems) optical microscope. Images were captured with a Nikon DXM1200F, (Nikon Inc.) digital camera using Nikon Act-1 software (version 2.62).

2.2.9. Density functional theory calculations

Crystal structure optimization followed by the band structure calculations were performed with the CRYSTAL'06 program.[175] Geometry optimization was performed using the PBE functional[176] and all electron basis sets 6-31G(d) for O, N, C and H atoms with H atom having outer shell exponents of 0.1613 and 1.1 bohr^{-2}. Atom positions were optimized while the unit cell parameters were kept fixed. Space groups used were $P2_1/c$ for **PDA1**, $P2_1/a$ for **APAP**,[133] and $P2_1/c$ for **APAP5**. The shrinking factors were set to 4 in all calculations. Truncation criteria for bielectronic integrals were set to 7, 7, 7, 7 and 14. Default convergence criteria were used to determine the optimized geometry. The B3LYP hybrid functional[177, 178] was used for band structure calculations, while other parameters were kept the same as in geometry optimization. Input for 165(3) band structure calculations was prepared and visualized using DL Visualize software.[179] Symmetry unique k points *Z*, *Γ*, *Y*, *A*, B, *D*, *E* and *C* for **PDA** and cocrystal whereas *Γ*, *Z*, *T*, *Y*, *S*, *X*, *U* and *R* for **APAP**. The total densities of states (TDOS) for all states were calculated for all structures using atom projected densities of states based on a Mulliken population analysis.

2.3. Results and discussion

Cocrystallization of **APAP** with CCFs that contain an aromatic N-atom were first investigated using **BPE**. The symmetrical bipyridine **BPE** contains two pyridyl groups capable of forming either O-H(phenol)···N(pyridyl) or N-H(amide)···N(pyridyl) heterosynthons with **APAP**.[88, 180] A new crystalline phase between **APAP** and **BPE** was first discovered utilizing the SMPT screening technique. Specifically, the initial SMPT study consisted of an ethanol suspension containing a 1:1 stoichiometric ratio of **APAP** and **BPE**. A comparison of the powder pattern exhibited by the SMPT solid to the powder pattern of the individual cocrystal components revealed the presence of a new solid phase (Fig. 17).

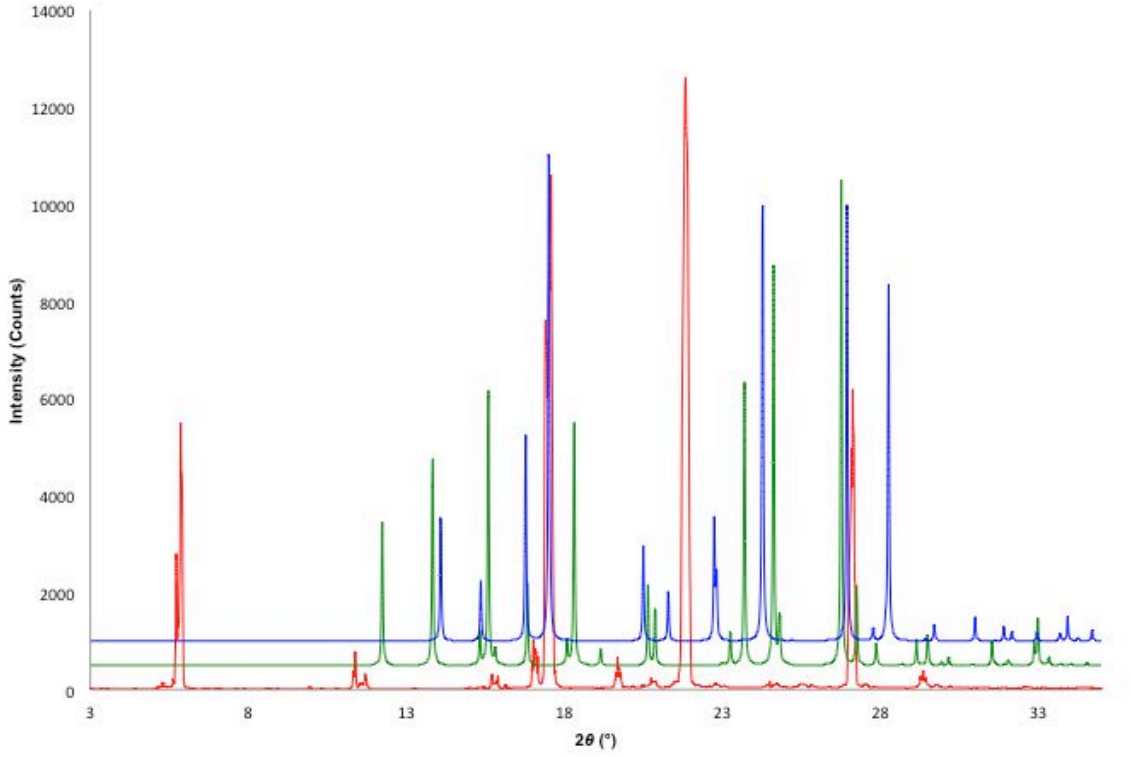

Figure 17 Comparison of the PXRD pattern obtained from the SMPT solid to the individual cocrystal components. The patterns arranged from top to bottom are calculated **BPE**, calculated **APAP** Form I, and the SMPT solid.

To determine the composition of the new crystalline phase single crystals were generated *via* slow-solvent evaporation. Herein, we report a series of cocrystals of **APAP** and **BPE** that exhibit varied synthon behavior. In particular, we discovered solids, **APAP1** and **APAP2**, wherein water molecules mask all direct hydrogen-bonding interactions between **APAP** and **BPE** molecules (Scheme 2).

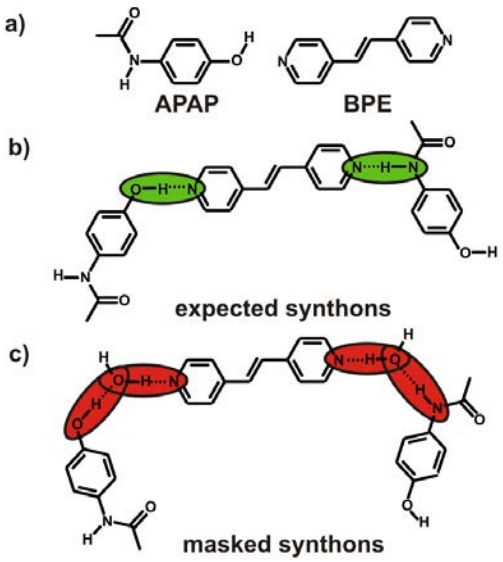

Scheme 2 (a) Selected cocrystal components **APAP** and **BPE**, (b) expected heterosynthons, and (c) masked synthons generated by injected water molecules.

We are unaware of a series of solids wherein the masking of a supramolecular synthon has been observed. We demonstrate that an expected O-H(phenol)···N(pyridyl) heterosynthon between **APAP** and **BPE** is achieved in hydrated/solvated cocrystals of composition **APAP3** and **APAP4**. The promiscuous synthon behavior within **APAP1**-**APAP4** prompted an investigation into an anhydrous cocrystal composed of **APAP** and **BPE**. Owing to the predominance of hydrated/solvated cocrystals *via* slow-solvent evaporation we employed mechanochemical techniques. The utilization of neat and

liquid-assisted grinding afforded a new solid phase which does not correspond to **APAP1**-**APAP4** or the individual cocrystal components. In addition, a survey of the CSD revealed over 550 cocrystals hydrates. Analysis of those entries revealed 30 cocrystal hydrates wherein the water molecules mask the hydrogen-bonding interactions between the cocrystal components, akin to **APAP1** and **APAP2**.

Whereas previous work demonstrated the utility of synthon theory in the assembly of **APAP** and CCFs based on aromatic N-atoms, masked synthons were unexpectedly realized in **APAP1**. Solid **APAP1** crystallized in the triclinic space group $P\bar{1}$ with an asymmetric unit that contains one **APAP**, one complete **BPE**, one half **BPE** that lies on a center of inversion and is unequally disordered over two orientations, and four water molecules. The crystal structure comprises acyclic chains of four water molecules that form O-H(water)···N(pyridyl) (O···N: 2.773(2) Å, 2.818(2) Å, 2.743(2) Å), O-H(water)···O(carbonyl) (O···O: 2.707(2) Å), N-H(amide)···O(water) (N···O: 2.777(2) Å), and O-H(phenol)···O(water) (O···O: 2.621(2) Å) hydrogen bonds. In this arrangement, the water chains effectively bridge alternating columns of **APAP** and stacked **BPE** molecules in a 2D sheet (Fig. 18a). The **BPE** columns alternate planar **BPE** molecules with molecules that have pyridyl rings slightly twisted at 3.5^{o}. The assemblies stack in a parallel manner with **BPE** molecules separated by 3.89 Å and 4.46 Å. A water chain terminus acts as a single molecule bridge by accepting a hydrogen bond from the amide group of **APAP** molecules and by donating a hydrogen bond to the pyridine ring of **BPE** molecules (Fig. 18b). Indeed, the second potential heterosynthon between **APAP** and **BPE** has two injected water molecules bridging the phenol and pyridine functionalities. The layers of **APAP1** connect *via* hydrogen bonds between the internal water molecules (O···O: 2.749(2) Å) of neighboring water chains to form a tetrameric water ring. The arrangement of the water tetramer results in a maximized hydrogen-bonding environment for each water molecule in the ring. The layers of **APAP1** stack in

an ABAB manner that enables weak C-H···O and C-H···π interactions between **APAP** and **BPE** to compliment the water tetramers.

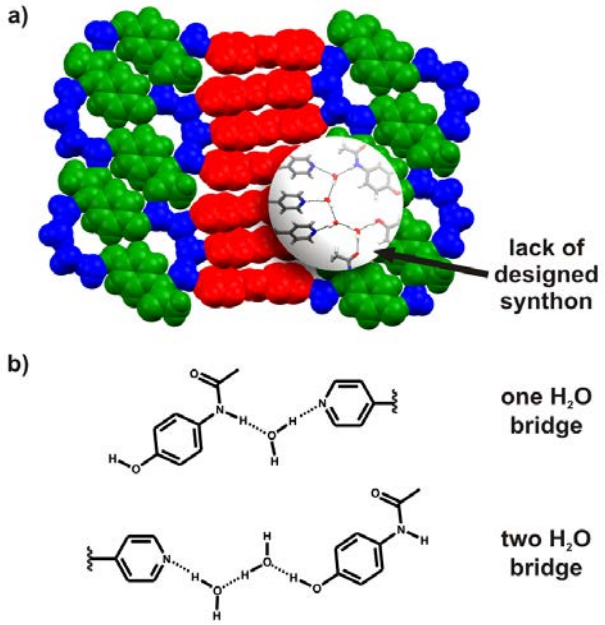

Figure 18 X-ray structure of **APAP1**: (a) 2D network viewed along the *a*-axis and (b) supramolecular synthons with bridging water molecules.

The predominance of masked synthons was evident in **APAP2**. As was observed in **APAP1**, the components of **APAP2** cocrystallize in the triclinic space group $P\bar{1}$ with an asymmetric unit composed of one **APAP**, one complete **BPE**, one half **BPE** that lies on a center of inversion and is unequally disordered over two orientations, and two water molecules. The cocrystal components assemble to form chains that involve intermolecular N-H(amide)···O(water) (N···O: 2.819(1) Å), O-H(phenol)···O(water) (O···O: 2.603(1) Å), O-H(water)···N(pyridyl) (O···N: 2.802(1) Å, 2.797(1) Å), O-H(water)···O(phenol) (O···N: 2.885(1) Å), and O-H(water)···O(carbonyl) (O···O: 2.722(1) Å) interactions. Adjacent chains pack to form alternating columns of **APAP** and **BPE** molecules that propagate to form, akin to **APAP1**, a 2D network (Fig. 19a). The **BPE**

columns comprise a pair of unique **BPE** molecules wherein the pyridine rings are either parallel or twisted at 16.6°. The molecules are separated by 3.73 Å and rotated to 6.2°. Akin to **APAP1**, the water molecules of **APAP2** act as a single molecule bridge, or insulation, between the phenol-to-pyridine and amide-to-pyridine interactions (Fig. 19b). The 2D networks stack in an ABAB arrangement to facilitate weak C-H···X interactions (X = O, N). In total, each water molecule hydrogen bonds to two **APAP** molecules and one **BPE** molecule in an arrangement which does not maximize hydrogen bonding but instead leaves a free pyridyl group similar to the (**APAP**)·(4,4,'-bipyridine) cocrystal. The hydrogen-bond array can be considered a unique occurrence considering the availability of a strong hydrogen-bond accepting group despite hydration increasing the availability of hydrogen-bond donors.[181, 182]

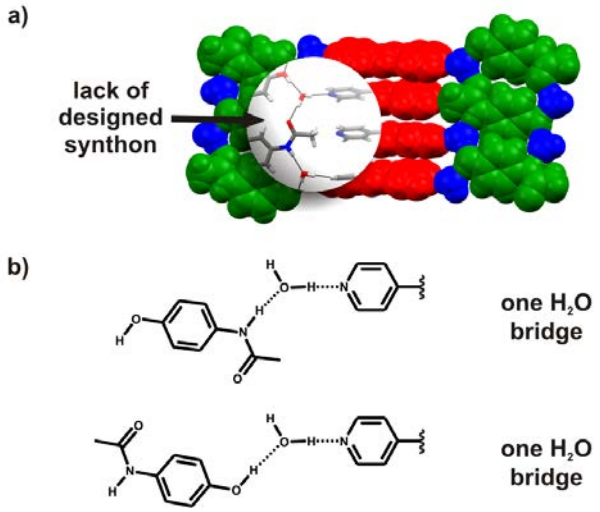

Figure 19 (a) X-ray structure of **APAP2** viewed along the *a*-axis to reveal a 2D network and (b) the single water bridges that comprise the masked synthons.

Whereas synthon breakdown was observed in the hydrated cocrystals **APAP1** and **APAP2**, the O-H(phenol)···N(pyridyl) heterosynthon was achieved when aqueous ethanol

was employed in the slow-solvent evaporation procedure. **APAP3** crystallized in a monoclinic space group $P2_1/c$ with an asymmetric unit that comprises one **APAP**, one **BPE**, and two water molecules. The components form a wave-like chain along the *b*-axis based on the phenol-pyridine heterosynthon (O···N: 2.714(2) Å) and a water dimer that participates in O-H(water)···N(pyridyl) (O···N: 2.840(2) Å) and O-H(water)···O(water) (O···O: 2.815(2) Å) hydrogen bonds (Fig. 20a). The water dimer bridges the amide and pyridine functionalities of the expected heterosynthon in a manner similar to **APAP1**, wherein, two water molecules bridge the phenol-to-pyridine interaction (Fig. 20b).

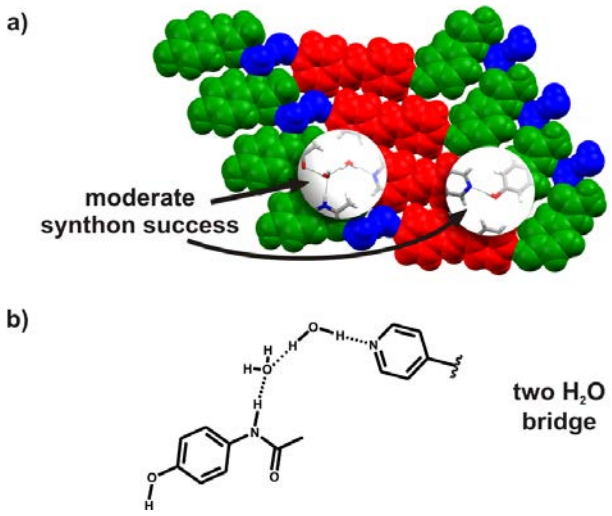

Figure 20 (a) Crystal structure of **APAP3** viewed along the *c*-axis to reveal 2D sheets composed of wave-like chains and (b) water dimer that bridges the amide-to-pyridine interaction.

Given that a single pyridyl group of the BPE molecules participates in a direct hydrogen bond with APAP, the synthon behavior of **APAP3** can be regarded as a unique form of a moderate synthon success.[161] The chains stack along the *a*-axis to form a 2D sheet that cross-links **APAP** molecules *via* N-H(amide)···O(water) (N···O: 2.874(1) Å) and O-H(water)···O(carbonyl) (O···O: 2.726(1) Å) hydrogen bonds. The **BPE** molecules

between chains are separated by 6.72 Å with the plane of each pyridyl ring twisted at a 12.9° angle. Similar to **APAP1**, The sheets stack ABAB being held together by O-H(water)···O(water) (O···O: 2.810(2) Å) hydrogen bonds and weak C-H···O and C-H···π forces.

The ability to achieve synthon success by forming a two-fold O-H(phenol)···N(pyridyl) heterosynthon between **APAP** and **BPE** was realized in **APAP4**. The solid crystallized in the triclinic space group $P\bar{1}$ with an asymmetric unit that comprises two **APAP**, one **BPE**, and one ethanol molecule. The phenol-pyridine heterosynthon (O···N: 2.773(2) Å, 2.704(2) Å) between **APAP** and **BPE** extends into a 1D ladder through N-H(amide)···O(carbonyl) (N···O: 2.887(2) Å) hydrogen bonds between APAP molecules and ethanol molecules that participate in O-H(hydroxy)···O(carbonyl) (O···O: 2.784(2) Å) and N-H(amide)···O(hydroxy) (N···O: 2.910(2) Å) hydrogen bonds (Fig. 21).

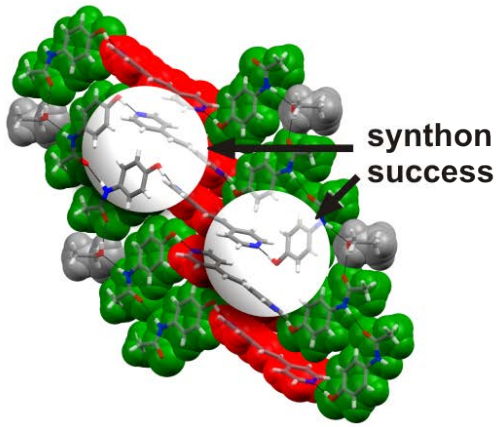

Figure 21 X-ray structure of **APAP4** exhibiting a 1D ladder along the *c*-axis.

BPE molecules serve as the rungs of the supramolecular ladder separated by 5.16 Å and 6.72 Å with the plane of each pyridyl ring twisted at a 28.90° angle. The ladders form a

2D sheet *via* hydrophobic packing with adjacent layers participating in C-H···O and C-H···π interactions.

The promiscuous hydrogen-bonding between **APAP** and **BPE** in cocrystals **APAP1**-**APAP4** prompted an investigation into the behavior of these components upon suspension in a range of solvents. The SMPT study would simultaneously aid in assessing the thermodynamic stability of **APAP1**-**APAP4** and the discovery of additional cocrystals. The SMPT experiments suspended of an equimolar amount of **APAP** and **BPE** in a range of solvents and allowed one week for equilibration before analysis *via* PXRD (Fig. 22).

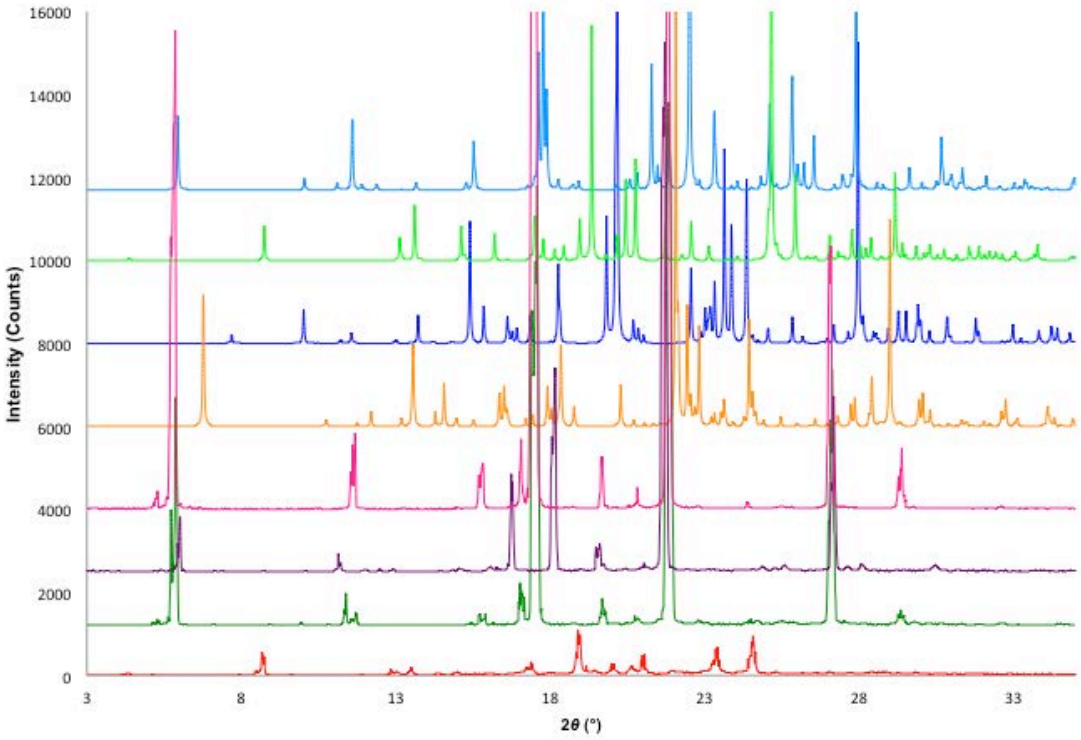

Figure 22 PXRD patterns arranged from bottom to top: SMPT with 4:1 (v/v) water ethanol, SMPT with aq. ethanol, SMPT with 1:1 (v/v) ethanol methanol, SMPT with 1:1 (v/v) toluene ethanol, calculated pattern for **APAP1**, calculated pattern for **APAP2**, calculated pattern for **APAP3**, and the calculated pattern for **APAP4**.

A comparison of the powder patterns obtained from the SMPT solids and the calculated powder patterns for **APAP1**-**APAP4** did not match. The differences suggest three likely scenarios. First, the crystals grown *via* slow-solvent evaporation represent kinetic forms whereas the SMPT trials crystallized thermodynamically stable cocrystals. Second, the equilibration time of one week may be insufficient for complete conversion to thermodynamically stable cocrystals. Third, the additional SMPT screening isolated new cocrystals composed of **APAP** and **BPE** in potentially hydrated or solvated forms. These results suggest the need for further solution-based investigations into **APAP** and **BPE** cocrystals with a focus on using the SMPT solids as seeds for the growth of single crystals.

The consistent formation of **APAP** and **BPE** cocrystal hydrates/solvates from solution-based techniques impelled us to investigate an anhydrous cocrystal *via* mechanochemistry. Mechanochemical processes are capable of yielding products that differ from the product obtained *via* solution-based techniques.[183] Our initial study employed neat grinding of an equimolar amount of **APAP** and **BPE** to limit solvent participation to atmospheric water. An analysis of the solid *via* PXRD suggested the resulting solid was amorphous. To increase crystallinity we turned to LAG which has been reported to improve crystallinity and catalyze cocrystal formation.[184-186] Specifically, we utilized hexanes in our LAG experiments owing to a lack of hydrogen-bonding groups and low water content. A comparison of experiments performed by hand using a mortar and pestle against automated milling show both LAG techniques successfully formed a new solid phase (Fig. 23). The LAG experiments employed an equimolar amount of **APAP** and **BPE**, however, the powder patterns suggest residual **APAP** after milling. The presence of **APAP** can be attributed to **BPE** impurities, which can be remedied through recrystallization or an adjusted component ratio (*i.e.* 1:1.2 molar ratio). Attempts to fully characterize this solid phase are ongoing.

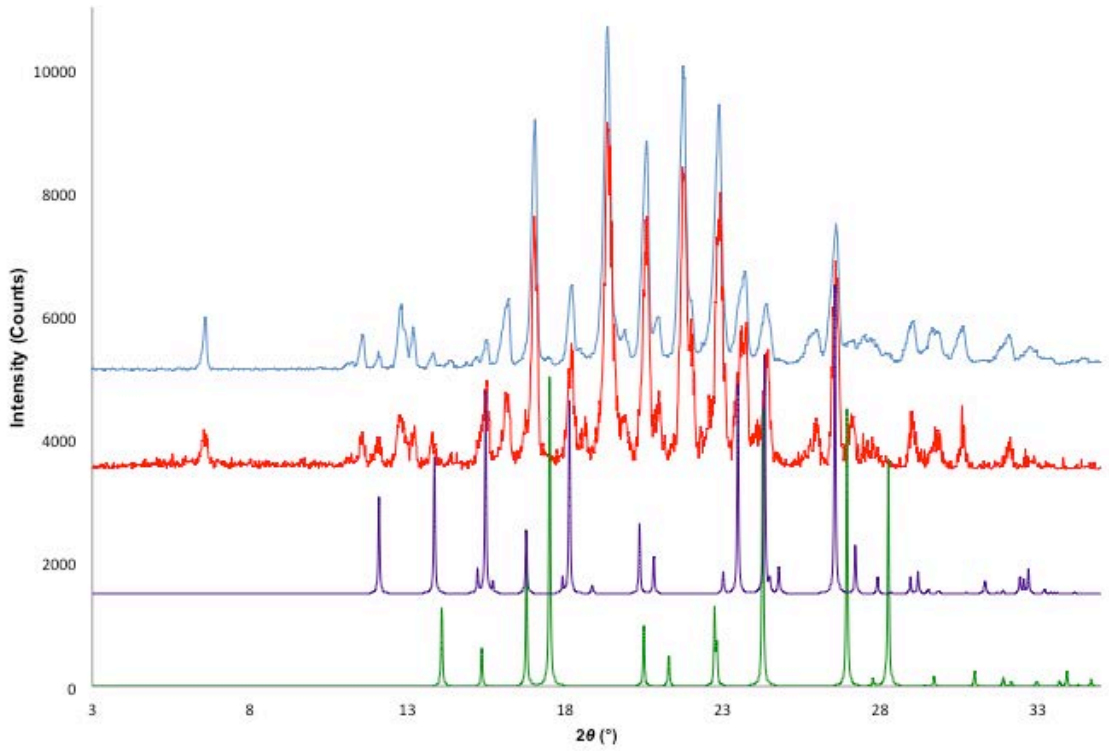

Figure 23 PXRD patterns arranged from top to bottom: solid from automated LAG, solid from manual LAG, calculated powder pattern for **APAP** Form I, and calculated powder pattern for **BPE**.

To determine the prominence of masked synthons in cocrystal hydrates we turned to the CSD. A survey of the CSD revealed over 550 cocrystal hydrates among those we excluded host-guest/clathrate systems and those structures crystallized in the absence of strict crystal engineering precepts. Of the remaining structures, there are 30 cocrystal with complementary components for the assembly of supramolecular synthons yet exhibited masked synthons (Table 1). Whether implicitly or explicitly stated, the design of 30 cocrystal hydrates was predicated on the formation of robust heterosynthons. Four cocrystal hydrates employed two-point recognition synthons (*e.g.* carboxylic acid dimer) while the remaining solids, similar to our goal involving **APAP** and **BPE**, involved single-point forces. We also note that the level of hydration, or water affinity, varies in the cocrystal hydrates from hemihydrate to tetrahydrate.[164]

Table 1 Functional group composition of hydrated cocrystals that contain masked synthons.

Entry	CSD Reference Code	Donor	Acceptor	Single water bridge	'Unmasked' cocrystal	Reference
	hemihydrate					
1	MAHKEN	phenol	acridine	✓	X	[187]
	monohydrate					
2	AJEZAR	aniline	phenazine	✓	X	[188]
3	CUWKAG	phenol	phosphine oxide	✓	✓	[189]
4	EVAFIR	carboxylic acid	diketone	✓	X	[190]
5	FEZQOR	phenol	phosphine oxide	✓	X	[191]
6	HOMXUC	phenol	carboxylate	✓	✓	[192]
7	IBUXUZ	amide	pyridine	✓	X	[193]
8	IBUYEK	amide	pyridine	✓	X	[193]
9	NUDMII	carboxylic acid	phosphine oxide	✓	X	[194]
10	UFENAY	carboxylic acid	phosphine oxide	✓	X	[195]
11	WUVKII	amine/amide	triazine/pyridine	✓	X	[196]
	sesquihydrate					
12	TIKPAF	aniline	sulfoxide	✓	X	[197]
	dihydrate					
13	**APAP2**	phenol/amide	pyridine	✓	✓	
14	AKAVIR	amide	bipyridine	✓	X	[198]
15	HOPJUS	thioamide	amine oxide	✓	X	[199]
16	IPEWAC	carboxylic acid	amine	✓	X	[200]
17	ITOCAV	silanol	pyridine	✓	✓	[201]
18	KIZXEW	carboxylic acid	carboxylic acid/ether	✓	X	[202]
19	NEWXOC	ethyne	phosphine oxide	✓	X	[203]
20	NUDMUU	carboxylic acid	phosphine oxide	✓	X	[195]
21	OGAHIN	carboxylic acid	sulfoxide	✓	X	[204]
22	QANMEY	amide/carboxylic acid	amide/carboxylic acid	✓	X	[205]
23	UHAHUG	phenol	ether	✓	✓	[206]
24	UHAJAO	phenol	ether	✓	X	[206]
25	YAXCEF01	phenol	ether	✓	X	[207]
	trihydrate					
26	ODEBUV	carboxylic acid/alcohol	phenanthroline	✓	X	[190]
27	SETQUE	phenol	pyridone	✓	✓	[208]
	trihemihydrate					
28	VEVLIS	ammonium	amine/amide/ether	X	X	[209]
	tetrahydrate					
29	**APAP1**	phenol/amide	pyridine	✓	✓	
30	BUJWIN	carboxylic acid	phenanthroline/diketone	✓	X	[210]
31	EBAWEK	anilic acid	pyrimidine	X	X	[211]
32	EBAWAG	anilic acid	pyrimidine	✓	X	[211]

In **APAP1**-**APAP3**, the masking of synthons occurs *via* bridging water molecules. In particular, the O-H(phenol)···N(pyridyl) and N-H(amide)···N(pyridyl) forces were adapted to incorporate one or two water molecules as a bridge between the functionalities. Analysis shows under the required arrangement of D-H···H_2O···A, 28 of the 30 cocrystal hydrates contain a single water bridge between the donor and acceptor

functionalities of a synthon. Of the remaining two structures, entry 31 has two bridging water molecules, akin to **APAP3**, whereas entry 28 has three water molecules injected between the donor and acceptor groups of the potential heterosynthon. We also note bridging water molecules can retain the designed hydrogen-bond-donor and –acceptor behavior of cocrystal components within a graph set notation.[197]

A second search was performed to identify structures, wherein, the solid components within the individual entries of Table 1 crystallize to yield a solid with a full synthon interaction, in essence identify structures comparable to **APAP4**. Five of the 30 combinations were identified as having corresponding anhydrous cocrystals with synthons containing uninterrupted hydrogen-bonding interactions (Table 2). Similar to our cocrystals with **APAP** and **BPE**, 4 of the 5 entries contain a phenol acting as the hydrogen-bond donor functionality of the supramolecular synthon.

Table 2 Cocrystals that exhibit a full synthon success contrary to corresponding cocrystal hydrates

Entry	CSD Reference Code	Cocrystal hydrate within Table 2	Donor	Acceptor	Full synthon success	Reference
1	CUWJUZ	3	phenol	phosphine oxide	✓	[189]
2	HOMXOW	6	phenol	carboxylate	✓	[192]
3	MACCID	17	silanol	pyridine	✓	[212]
4	ZOKYON	23	phenol	ether	✓	[207]
5	SETQOY	27	phenol	pyridone	✓	[208]

Whereas the entries in Table 2 demonstrate the ability of cocrystal components to have either masked or unmasked synthons, the molecule 3,5-dinitrobenzamide shows a propensity for masked synthons upon cocrystallization with bypyridines. Specifically cocrystallization with 4,4’-bipyridine, 1,2-bis(4-pyridyl)ethane, and **BPE** incorporated water molecules to give a channeled structure wherein the bipyridines are arranged within the channel to hydrogen bond to the water molecules and participate in weak secondary interactions with 3,5-dinitrobenzamide. Interestingly, the same masked synthon behavior is maintained in methanol solvates of 3,5-dinitrobenzamide and the series of bipyridines.

An additional study investigating the ability to form **APAP** cocrystals based on either the O-H(phenol)···N(pyridyl) or N-H(amide)···N(pyridyl) heterosynthons was completed with the CCF **PDA**. The diacid contains two carboxylic acid groups capable of acting as either hydrogen-bond donors or acceptors and a pyridine group that can act as a hydrogen-bond acceptor. Based on reported cocrystals, **APAP** has shown the ability to form a N-H(amide)···O(carboxy) heterosynthon in addition to the previously noted pyridine based heterosynthons.[169] Given **PDA** possesses pyridyl and acid functionalities we sought to determine whether cocrystallization would afford a solid wherein **APAP** hydrogen bonds with the pyridyl group in the wake of synthon competition and if solvent molecules would bridge hydrogen-bonding interactions as in the case of **APAP1**-**APAP3**. The CCF **PDA** has, to the best of our knowledge, only been crystallized in one multi-components solid.[213] Specifically, cocrystallization of **PDA** with *L*-serine afforded (**PDA**)·(*L*-serine) wherein the N-atom of the pyridyl group accepts a hydrogen bond from the ammonium group of *L*-serine (Fig. 24).

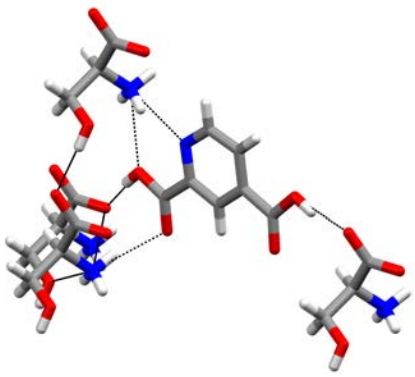

Figure 24 X-ray structure of (PDA)·(*L*-serine) wherein PDA donates and accepts two hydrogen bonds with *L*-serine.

The planar nature of **PDA** in the (**PDA**)·(*L*-serine) cocrystal suggested **PDA** may be used to promote a layered structure in an **APAP** cocrystal. Herein, we report a cocrystal of composition (**APAP5**) wherein **PDA** surprisingly undergoes intramolecular proton transfer to a zwitterionic form. The pyridine ring is protonated by the *ortho*-carboxylic acid groups, which changes the supramolecular landscape of **PDA** to enable the molecule to act as a hydrogen-bond donor through the pyridinium functionality. The resulting self-assembly process enables the amide group of **APAP** to participate in a N-H(amide)···O(carboxy) hydrogen bond to a carbonyl group of **PDA**. The cocrystal **APAP5**, to our surprise, is red in color despite each of the cocrystals components being white. The origins of the red color were investigated using DFT calculations. Additionally, a crystallographic analysis of **PDA** as a pure form, in the form of, **PDA2**, reveals **PDA** exists in the zwitterionic form akin to **APAP5**.

To screen for cocrystallization between **APAP** and **PDA** we employed the SMPT technique.[98] A 1:1 molar ratio of **APAP** and **PDA** was allowed to equilibrate at ambient conditions for one week before analysis *via* PXRD (Fig. 25).

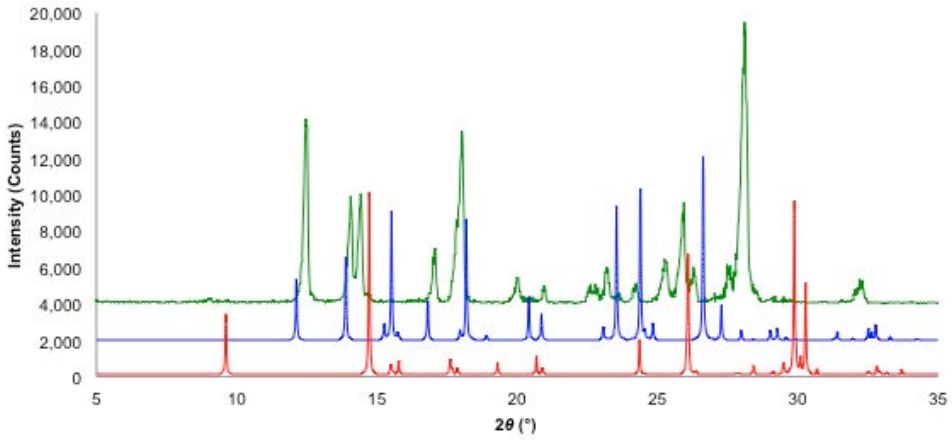

Figure 25 PXRD patterns from top to bottom: SMPT solid, calculated powder pattern for **APAP** Form I, and calculated powder pattern for **PDA**.

Analysis of powder patterns suggested a new solid form between **APAP** and **BPE**. In addition, a visual examination of the SMPT solid revealed a remarkable color change. The new phase exhibited a red color despite the lack of color exhibited by the individual cocrystal components (Fig. 26).

Figure 26 Photograph of powdered **APAP** Form I, **PDA**, and SMPT solid arranged from left to right respectively.

To determine the composition of the new phase identified by SMPT we employed slow-solvent evaporation to produce crystals suitable for single crystal X-ray diffraction studies.

APAP5 cocrystallizes in the monoclinic space group $P2_1/c$ with a molecule of **APAP** and **PDA** in the asymmetric unit. The N-atom of **PDA** is protonated by an intramolecular proton transfer from the *ortho*-carboxylic acid group. The crystal structure is based on centrosymmetric four-component hydrogen-bonded assemblies composed of two **APAP** molecules and two **PDA** zwitterions. The four component assemblies are sustained by the carboxy groups of each **PDA** participating in N-H(amide)···O(carboxy) (N···O: 2.916(2) Å) hydrogen bonds and charge-assisted N-H(pyridinium)···O(carboxylate) (N···O: 2.706(2) Å) hydrogen bonds (Fig. 27a).

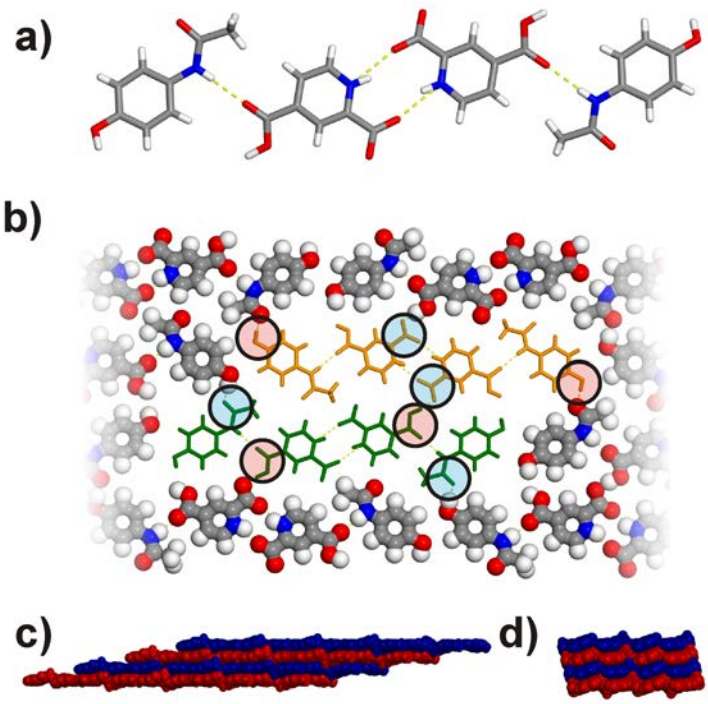

Figure 27 X-ray structure of **APAP5**: (a) four-component assembly of **APAP** and **PDA**, (b) pronounced 2D sheet within the 3D framework (donor and acceptor groups in red and blue circles, respectively), (c) layered structure viewed along the (2-11) and (010) crystallographic planes, and (d) assemblies viewed along (2-11) and (001) crystallographic planes.

The four-component assemblies interact with nearest-neighbor assemblies *via* O-H(hydroxy)···O(amide) (O···O: 2.651(2) Å) and O-H(carboxy)···O^-(carboxy) (O···O: 2.464(2) Å, 3.116(2) Å) hydrogen bonds. The interactions between the assemblies give rise to an infinite 3D hydrogen-bonded network with a pronounced 2D structure within the crystallographic (2 -1 1) plane. The assemblies within the plane are connected from above and below by the phenolic group of **APAP** and the acid group of **PDA**, which act as hydrogen-bond donors (Fig. 27b). The assemblies within planes are related through *c*-glide planes perpendicular to the *b*-axis. The molecules within the planes are stacked in an offset manner being sustained by O-H(phenol)···O(amide), O-H(carboxy)···O^- (carboxylate), and charge-assisted π···π interactions to give the 3D structure (Fig. 27c,d).

Intermolecular contacts between molecules of neighboring layers range from *ca.* 3.0 to 3.3 Å.

An analysis of the X-ray structure revealed the formation of the N-H(amide)···O(carboxy) heterosynthon between **APAP** and **PDA**. In this arrangement, **PDA**, in the form of a zwitterion, self-assembles *via* a supramolecular homosynthon that involves the *ortho*-carboxylate and pyridinium groups sustained by charge assisted N^+-H(pyridinium)···O^-(carboxylate) hydrogen bonds. The zwitterionic behavior of **PDA** contrasts the (**PDA**)·(*L*-serine) structure wherein **PDA** acted as a CCF in a non-zwitterionic form with zwitterionic *L*-serine. An examination of the structure and pK_a (pK_a = 3.00 ± 0.10 for *ortho*-carboxy–acid group; pK_a = 5.14 ± 0.10 for pyridyl group) values for the most acidic and basic functional groups of **PDA** suggest that the molecule may exist as either a non-zwitterionic or zwitterionic form.[214] Specifically, the ΔpK_a value lies in the range of -1 to 4 where proton transfer is considered to be less predictable and reliant on the crystalline environment. A recent report quantifies the likelihood of proton transfer within the unpredictable range of ΔpK_a equal to -1 through 4. In the case of **PDA**, the probability of proton transfer is estimated to be ~64%.[215]

During the course of our studies on **APAP5**, we also determined the structure of pure **PDA**. **PDA** and water crystallize in the monoclinic space group $P2_1/c$. The asymmetric unit consists of one molecule of **PDA** and one molecule of water. The **PDA** molecules are built into the crystal structure as zwitterions that form through proton transfer from the *ortho*-carboxyylic acid group to the pyridyl moiety. The zwitterion and water molecules self-assemble to form a 2D sheet sustained by N^+–H(pyridinium)···O(water) (N···O: 2.725(3) Å), O-H(carboxy)···O^-(carboxylate) (O···O: 2,458(2) Å), O-H(water)···O^-(carboxy) (O···O: 2.994(3) Å), O-H(water)···O^-(carboxy) (O···O: 2.806(3) Å) hydrogen bonds (Fig. 28a).

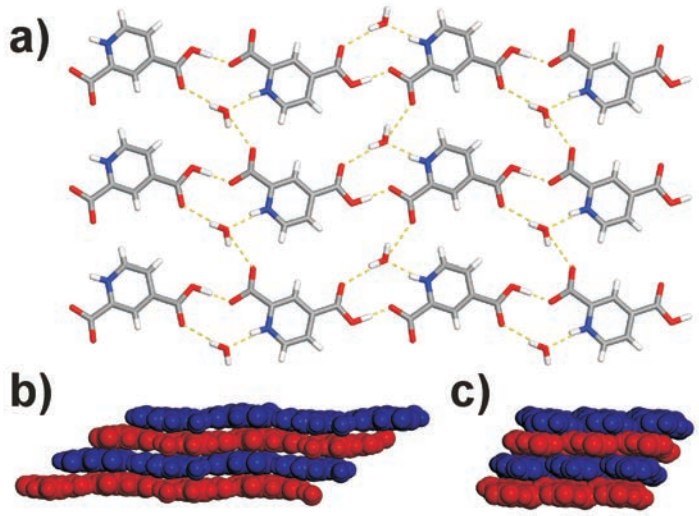

Figure 28 X-ray structure of **PDA1**: (a) 2D sheet of hydrogen-bonded **PDA** and water molecules, and (b,c) stacked 2D sheets sustained by face-to-face π-π interactions viewed along the *a* and *b* axes respectively.

The **PDA** and water molecules are related through 2-fold rotoinversion axes and glide planes. The sheets are stacked in an offset manner and held together by face-to-face π···π interactions (layer-to-layer separation distance: ~3.1 Å) (Fig. 28b,c). Akin to **APAP5**, the **PDA** molecules in **PDA1** were determined to crystallize in the zwitterionic form. The crystallization of the zwitterionic form of **PDA** as a monohydrate is consistent with a CSD analysis that suggests molecular crystals with charged functional groups are more prone to hydration.[165]

The single crystals of **APAP5** used for X-ray crystallography were grown *via* slow-solvent evaporation over the period of approximately one week. After one week, the resulting single crystals were imaged using a light microscope at 40x magnification (Fig. 29). A visual examination of the cocrystal using optical microscopy revealed the solid to be red in color. To rationalize the red color of the cocrystal, we performed TDOS calculations to determine the band gap of the solid.

By employing Density Functional Theory calculations we were able to calculate band structures and TDOS for **PDA**, **APAP**, and **APAP5** are shown in Fig. 30.

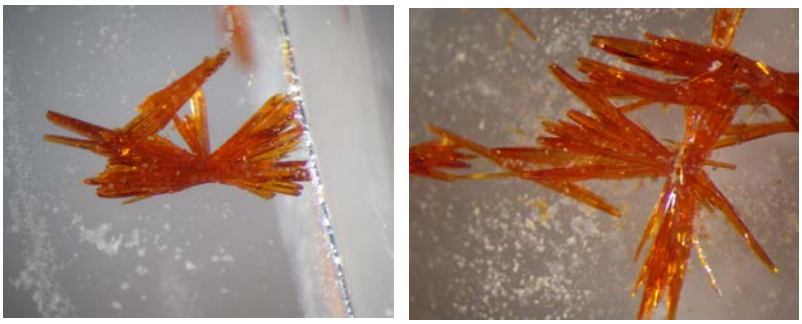

Figure 29 Single crystals of **APAP5** grown from an ethanol solution over the course of one week.

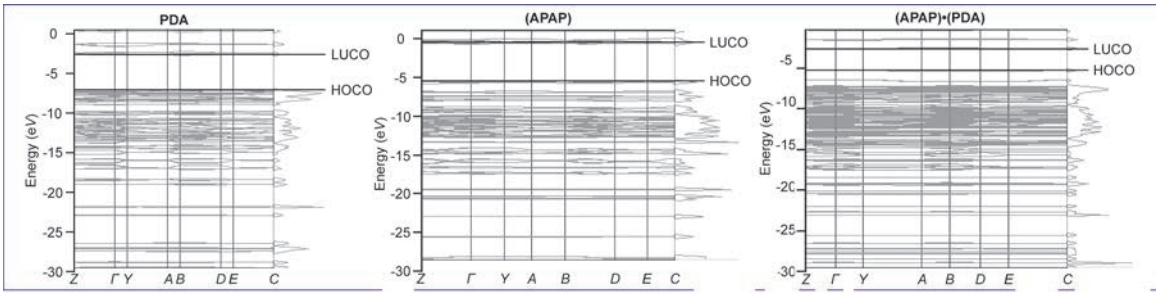

Figure 30 Density of states distributions for **PDA1**, **APAP**, and **APAP5**.

Both **PDA** and **APAP** as pure compounds were determined to be insulators with B3LYP calculated bandgap values of 4.37 and 4.56 eV, respectively. The highest occupied crystal orbital (HOCO) and lowest unoccupied crystal orbital (LUCO) of **PDA** are located at -7.05 and -2.69 eV whereas those for **APAP** are at -5.31 and -0.75 eV, respectively. Band structure and TDOS of **APAP5** showed the HOCO and LUCO are located at -5.15 and -2.65 eV respectively with a decrease in the bandgap from those of

the initial components to a calculated value of 2.49 eV. Detailed calculated cocrystal band structure analysis shows the major contribution to HOCO to come from **APAP** while LUCO comes from **PDA**. This observation suggests that intermolecular charge transfer occurs from **APAP** to **PDA** molecule with energies in the visible light range.

Although the components of **APAP5** self-assemble to form an infinite 3D hydrogen-bonded network, the intramolecular proton transfer of PDA enabled the components to form a pronounced 2D structure. The formation of the 2D structure can be attributed to donor and acceptor charge-transfer interactions that originate from the pyridinium ring of **PDA**, which sits directly above the phenol group of **APAP** (interatomic distances: N^{+}(pyridinium)···O(phenol) 3.38 Å). An evaluation of the cocrystal band structure and TDOS revealed the cocrystal to exhibit a smaller band gap (*i.e.* 2.49 eV) than the individual molecules in the pure solids **APAP** and **PDA** (*i.e.* 4.56 eV and 4.37 eV, respectively). The decrease in π-π^{*} separation can be viewed as an optimization of donor-acceptor interactions known to stabilize cocrystals involving aromatic carboxylic acids of different acidities.[216, 217] These observations are in agreement with the mechanism proposed for the intrastack phenyl-phenyl charge transfer proposed by Aakeroy *et al*.[218]

2.4. Summary and outlook

In our studies with **APAP** we successfully cocrystallized the molecule with CCFs that contain aromatic N-atoms. We described a series of cocrystal hydrates based on **APAP** and **BPE** that illustrate various forms of synthon behavior. In the case of **APAP1** and **APAP2** the cocrystal components unexpectedly align wherein all intermolecular interactions occur *via* bridging water molecules. An analysis of the CSD revealed 30 cocrystal hydrates that exhibit masked synthons akin to **APAP1** and **APAP2**. Moderate to "full" synthon successes were also achieved which highlights the unpredictable behavior between the cocrystal components. Here, water can be viewed as a flexible

element and alternative to facilitate efficient crystal packing.[49, 57] The occurrence of unexpected synthons was further realized upon cocrystallization of **APAP** and **PDA**. **PDA** exists as an unexpected zwitterion that alters the supramolecular landscape and negates the retrosynthetic approach employed to select the cocrystal components. That **PDA** can function as two forms suggests that **PDA** can serve as a flexible element, similar to water, to facilitate favorable solid-state interactions. Finally, in **APAP1-APAP5** we successfully obtained cocrystals with pronounced layered topologies. As part of our future efforts, we plan to study the compaction properties of these solids and compare the performance of the solids with **APAP** Form I and reported **APAP** cocrystals.

CHAPTER 3. PREPARATION OF ORGANIC NANOCRYSTALS BASED ON SUPRAMOLECULAR MATERIALS

Chapter 3 will encapsulate the research performed on organic nanocrystals, namely pharmaceutical nano-cocrystals and host-guest nanocrystals. The chapter will meld the efforts of two publications on organic nanocrystals with additional unpublished work. The first communication is adapted with permission from *Angewandte Chemie International Edition* [Sander, Bučar, Henry, Zhang, and MacGillivray (2010) Pharmaceutical nano-cocrystals: sonochemical synthesis by solvent selection and use of a surfactant, *49,* pp. 7284-7288]. Copyright 2010, John Wiley and Sons. An ensuing communication is adapted with permission from the *Journal of the American Chemical Society* [Sander, Bučar, Baltrusaitis, and MacGillivray (2012) Organic nanocrystals of the resorcinarene hexamer via sonochemistry: evidence of reversed crystal growth involving hollow morphologies, *134*, pp. 6900-6903]. Copyright 2012, American Chemical Society.

3.1. Introduction

Materials of nanometer scale dimensions have been the focus of an immense amount of research in the past three decades. Nanoscience largely comprises the study of the synthesis and size-dependent properties exhibited by inorganic-based nanocrystals (*e.g.* metals, metal oxides).[103, 219] The unique properties imparted to inorganic nanocrystals have found utility in a vast array of fields such as synthetic chemistry, materials science, and medicine (*e.g.* catalysts, semiconductors, medical diagnostic devices).[220-222] Alternatively, nanocrystals composed of purely organic components remain largely unexplored. The lack of development can be ascribed to two contributing factors. First, whereas inorganic nanocrystals are prepared by a variety of synthetic methods (*e.g.* decomposition of volatile organometallics, molten metal evaporation, chemical reduction), the general instability of organics precludes applying these

established techniques to the fabrication of organic nanocrystals.[223-225] Second, organic nanocrystals were originally hypothesized to lack size-dependent optical and electronic properties routinely observed in inorganic based nanocrystals.[219]

Prior to 1992, the preparation of organic nanocrystals was limited to crush and vapor growth techniques.[104] However, molecular crystals exposed to the crush technique underwent phase transformation and a limited number of organic systems (*e.g.* phthalocyanine) attain the thermal requirements of the vapor growth technique.[107] Consequently, Nakanishi and coworkers reported a reprecipitation method for the fabrication of organic nanocrystals in the absence of harsh conditions (*e.g.* high temperature).[104] The solvent displacement technique involves the dissolution of a hydrophobic molecule in a water miscible solvent and subsequent injection of the solution into rapidly stirred water. Led by the reprecipitation method, additional techniques have been developed that employ methodologies such as laser ablation, microwave-irradiation, microemulsions, and membrane reactors all of which have contributed to an increase in the number of reported organic nanocrystals.[107, 219] The library of organic nanocrystals largely consists of π-conjugated molecules, non-linear optical dyes, fluorescent dyes, and fullerene.[107]

Coupled to the increase in organic nanocrystals was the discovery that indeed organic nanocrystals exhibit a diverse set of size-dependent properties. For example, theoretical and experimental studies demonstrated the melting point of naphthalene was dependent on crystal size.[226] In 1996, Nakanishi *et al.* observed the first example of size dependent optical properties in organic nanocrystals.[105] The investigation utilized the reprecipitation method to prepare perylene nanocrystals with crystal sizes ranging from 50 nm to over 1 μm. The analysis of perylene nanocrystals showed the excitonic absorption peak narrowed and shifted to shorter wavelengths while strong emission from the free-exciton energy level was observed upon a reduction in the crystal size to nanometer-scale dimensions. Subsequent research on π-conjugated molecules has

reinforced organic nanocrystals exhibit interesting optical, electronic, and thermotropic properties.[106]

The reprecipitation method also afforded nanocrystals of diolefin derivatives which were used to study the size-dependent properties of solid-state polymerizations.[227] UV irradiation of the bulk crystals of the diolefins accumulate strain as the photopolymerization progresses and to alleviate stress the macro-crystals crack. Alternatively, monomer nanocrystals successfully release accumulated strain *via* deformation of the crystal shape to enable successful single-crystal-to-single-crystal polymerizations. The ability to generate single-crystal polymers from monomers (*e.g.* polydiacetylene derivatives) has potential materials applications owing to the conductivity and non-linear optical properties of such materials.[228]

Comprehensive reviews by Horn *et al.*,[229] Yao *et al.*,[219] and Park *et al.*[230] highlight an extension of the size-tunable properties of organic molecules, albeit, largely in amorphous nanoparticles. A notable example by Park was the observation of aggregation induced enhanced emission in 1-cyano-*trans*-1,2-bis(4'-methylbiphenyl)ethylene (**CNMBE**).[231] Generally, the confined and concentrated environment of the solid-state results in the fluorescence quenching of organic chromophores. Alternatively, the fabrication of **CNMBE** nanoparticles results in strong fluorescence whereas a solution of **CNMBE** has only weak fluorescence. The 700-fold increase in fluorescence intensity is attributed to the planarization and *J*-aggregate formation of the molecules in the solid-state. It is worth noting, the aggregation induced enhanced emission was absent in macro-sized crystals of **CNMBE** and is specific to nanoparticles. The solid-state behavior of cyano-substituted olefins (*e.g.* **CNMBE**) will be discussed in greater detail in Chapter 4. The ability of **CNMBE** to form *J*-aggregates in the solid-state was attributed to the functionality of the molecule (*i.e.* cyano groups) which prevented face-to-face stacking of the molecules. The results reported in this chapter represent the author's work on projects aimed towards further exploiting intermolecular interactions to fabricate

multi-component supramolecular nanocrystals. The consequences of assembling intermolecular interaction (*i.e.* supramolecular synthons) on the formation of organic nanocrystals will also be discussed.

3.2. Sonochemical synthesis of pharmaceutical nano-cocrystals by solvent selection and use of a surfactant

3.2.1. Introduction

Despite the unique physicochemical properties (*e.g.* molecular recognition) that emerge from the breadth of functional groups within organic solids translation of these properties into organic nanocrystals remains underdeveloped. In the pharmaceutical industry, approximately 60% of all pharmaceutical agents (PAs) currently in development are poorly water soluble and thus have poor bioavailability.[91] Methods of combating poor solubility and bioavailability are therefore of immense interest. Ideally, the methodology would employ a means of increasing aqueous solubility while retaining the molecular composition of the PA that provides the mechanism of action. Frequently pharmaceutical scientists improve the properties of a PA *via* salt formation or the development of an amorphous form of the PA.[92] Alternatively, nanosizing PAs has emerged as a means to improve physicochemical properties *via* non-covalent means. According to the Noyes-Whitney equation the increased surface area imparted to nanocrystals results in an increased dissolution rate.[91, 232] A slight increase in saturation solubility owing to the curvature and, hence, the high-energy surfaces of nanosized particles will also contribute to faster dissolution.[233]

Since Ambisome® was first approved in 1990 as a nanoparticle formulation less than 30 marketed products, based on single-component nanocrystalline solids, have been developed.[232, 234] The majority of these nanocrystals have been prepared *via* "top-down" processes.[235, 236] The approach relies on mechanical attrition in the presence of stabilizers to reduce macro-sized crystals to nanometer-scale dimensions. Examples of top-down

processes include media-milling and high-pressure homogenization. However, concerns exist regarding top-down processes, which include the lengthy processing time, high-energy input/consumption, contamination, generation of amorphous impurities, and inadequate particle size control. In addition, top-down processes may have an intrinsic inability to produce organic nanocrystals smaller than 100 nm owing to the ductile nature of molecular crystals and the ease in which these solids loose crystallinity.[229, 235-238] Thus, it has been recognized that the development of bottom-up approaches are necessary to facilitate the generation of crystalline particles with sizes on the order of tens to hundreds nanometers.[236]

That functionality can be readily incorporated and exploited in organic solids has become more apparent in recent years with cocrystals. The field of pharmaceutics has been a major beneficiary of cocrystal development wherein the properties of PAs have been improved using complementary molecules in the form of cocrystal formers (CCFs).[84, 86, 87, 93] Akin to nanosizing, pharmaceutical cocrystals are a viable alternative to polymorphs, amorphous dispersions, and salts as solid forms for active pharmaceutical ingredients (APIs). Since the introduction of pharmaceutical cocrystals by Almarsson and Zaworotko, cocrystals have become clearly distinguished from other API formulations.[93] As a comparison, the formation of a pharmaceutical salt wholly relies on the chemical composition of a PA to consist of ionizable functionalities whereas a cocrystal can exploit any functional group capable of assembling into a supramolecular synthon.[84] In addition, the coulombic interactions in salts largely negate the directionality of intermolecular interactions which, as in the case of acetaminophen cocrystals, can facilitate improved physical properties.[84] Lastly, pharmaceutical cocrystals are a design driven solid that employs a retrosynthetic approach to identify molecular components capable of assembling *via* supramolecular synthons.[93] Alternatively, the development of polymorphs or hydrates/solvates as a means to improve physicochemical properties can be dependent on a serendipitous event with no design in

the arrangement of molecules in the solid-state. Cocrystals containing a PA can improve physicochemical properties such as physical stability, solubility/dissolution rate, bioavailability, and mechanical properties and have been thoroughly reviewed by Zaworotko *et al.*,[86] Jones *et al.*,[84, 87] and Schultheiss *et al.*.[85] Importantly, in coupling the well-established benefits of pharmaceutical cocrystals with a decrease in particle size to the nanometer scale, one can expect to further improve properties of a PA (*e.g.* dissolution rate).

A lack of development of pharmaceutical cocrystals of nanodimensions can be ascribed to a diverse tapestry of functional groups that comprise PAs. Although a wealth of functional groups provides multiple design routes to assemble supramolecular synthons, the groups tend to amplify solubility differences between a CCF and PA.[81] Previously, we reported a method to synthesize nanosized cocrystals of (resorcinol)·(*trans*-1,2-bis(4-pyridyl)ethylene) based on a rapid precipitation method that utilizes ultrasonic irradiation and a single high-solubility solvent.[108] The method demonstrated the utility of sonochemistry by forming nano-cocrystals of a cocrystal with simple constituents based on two functional groups. Importantly, the sonochemical approach succeeded when rapid reprecipitation alone failed to yield nano-cocrystals.[108]

Despite the achievement of nano-cocrystals, the complexity of a PA can reduce the likelihood of finding a common solvent to cosolubilize the components of a pharmaceutical cocrystal so as to afford a product of nanometer-sized dimensions with a narrow size distribution appropriate for a dosage. The size distribution has consequences in terms of long-term stability in that the absence of particles with large size differences will reduce Ostwald ripening.[233] We expect the unique environment created by cavitation events during ultrasonic irradiation will aid in the rapid nucleation of a pharmaceutical cocrystal in spite of solubility differences between the components.[239] In fact, in the pharmaceutical industry, sonocrystallizations are routinely employed owing to an ability

to effect nucleation and provide crystals of an improved habit and size distribution, albeit of micron-sized crystals.[240-242]

In this section, we describe an approach to synthesizing pharmaceutical cocrystals of nanometer-scale dimensions. A dosage form comprising nano-cocrystals offers promise of enhanced dissolution rates and, thus, improved bioavailability and efficacy of medication by coupling the benefits of pharmaceutical cocrystals and nanocrystals. Although the general instability of organic solids largely precludes the application of inorganic-based fabrication methods sonochemistry has emerged as a harsh, yet transient, means to prepare cocrystals of nanometer scale dimensions.[108, 243] We demonstrate the use of ultrasonic irradiation to prepare nanometer-scale pharmaceutical cocrystals by utilizing multiple-solvents and a surfactant to account for the inherent solubility disparity between a PA and CCF.

The cocrystal of focus here is caffeine 2,4-dihydroxybenzoic acid monohydrate (**CAFF**)·(**DHBA**)·(H_2O) (**CAFF1**).[99] **CAFF** is one of the most frequently used model compounds in pharmaceutical cocrystal studies[96, 101, 102, 244, 245] while **DHBA** is enlisted in the Everything Added to Food in the United States (EAFUS) list. Improvements to the properties of **CAFF** *via* cocrystallization have been realized in the form of improved hygroscopicity and compaction.[96, 244] The components of **CAFF1** possess four functional groups [*i.e.* -OH, -CO_2H, C=O, N(lone pair)] that occupy six different chemical environments. The components form a two-dimensional (2D) graphite-like structure sustained by a combination of an intramolecular O-H(hydroxy)···O(carboxy) and an intermolecular O H(carboxy)···N(imidazole) hydrogen bond (Fig. 31). In **CAFF1**, the water molecule links two cocrystal components *via* O-H(water)···O(urea), O-H-(water)···O(amide) and O-H(hydroxy)···O(water) hydrogen bonds. The number and complementary nature of functional groups of a cocrystal will impact differences in solubilities of the components.[109] The prevalence, and impact, of solubility differences in cocrystal formation is reflected in the variety of techniques used to generate cocrystals.[98,

[109] In the case of **CAFF1**, the CCF and PA exhibit solubility differences of one to two orders of magnitude in common organic solvents, which is expected to preclude rapid assembly of the components to afford the formation of well-defined crystals of nanometer-scale dimensions.

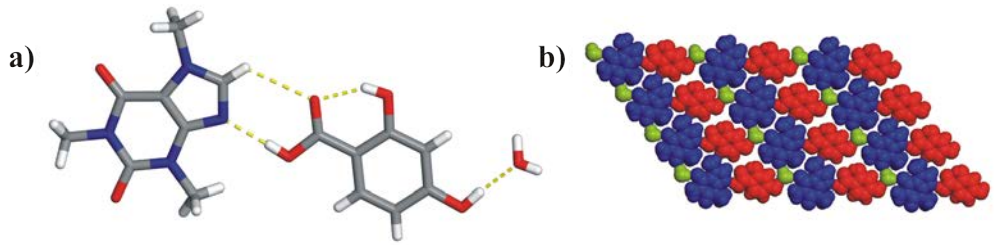

Figure 31 X-ray structure of **CAFF1**: (a) hydrogen-bonding interactions between cocrystals components and (b) the extension of those interactions into a 2D network.

Based on the knowledge gained from the **CAFF1** system we will examine the robust nature of our sonochemical approach on additional pharmaceutical cocrystals, namely (acetaminophen)·(theophylline) (**APAP6**)[95], (carbamazepine)·(saccharin) (**CBZ1**)[93], and (itraconazole)·(*L*-malic acid) (**ITZ1**)[94] (Fig. 32).

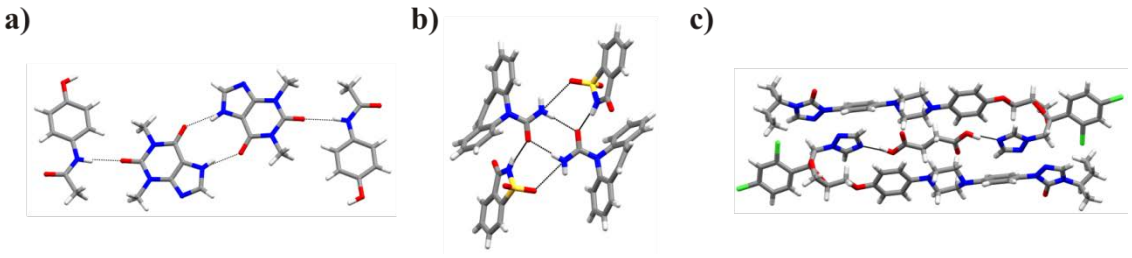

Figure 32 X-ray structure of (a) **APAP6**, (b) **CBZ1**, and (c) 2(**ITZ**)·(succinic acid) which is a structural analogue to **ITZ1** which has yet to be characterized *via* single crystal X-ray diffraction.

As previously noted, cocrystals based on **APAP** are of interest owing to an ability to improve the poor mechanical properties of **APAP** Form I. In addition, **APAP6** provides an opportunity to explore our sonochemical approach with a pharmaceutical cocrystal that comprises two PAs. Theophylline (**THEO**) is used clinically to treat various ailments such as asthma but the water solubility of **THEO** has presented problems in drug delivery.[246] The cocrystal **CBZ1**, is composed of the antiepileptic drug carbamazepine (**CBZ**) which is known to have issues regarding aqueous solubility and polymorphism.[93] **CBZ1** has been a targeted product of several cocrystallization strategies (*e.g.* mechanical milling) and is considered the most thoroughly studied pharmaceutical cocrystal.[86, 97, 109, 168, 247, 248] For example, a comparison of the performance of **CBZ1** to a marketed **CBZ** product demonstrated the cocrystal has a comparable oral absorption profile in dogs.[97] The vast literature based on **CBZ** and **CBZ1** solubility studies afford an opportunity to readily compare the performance of nano-**CBZ1**. Our rationale for selecting the third system, **ITZ1**, relates to the diverse functionality, high molecular weight, and conformational flexibility of itraconazole (**ITZ**). **ITZ** is an antifungal compound that has poor aqueous solubility but through cocrystallization with a series of dicarboxylic acids has achieved an aqueous solubility that compares with a commercial formulation of **ITZ**.[94] A study of pharmaceutical nano-cocrystals based on **ITZ1** will broaden the applicability of our sonochemical approach towards compounds currently in development in the pharmaceutical industry.

3.2.2. Materials and methods

3.2.2.1. Materials

Caffeine (*ReagentPlus*™), theophylline (minimum 98%), *L*-malic acid (97%), Span™-85 (Oleic acid (≥ 60%); linoleic acid (3-12%); linolenic acid (≤ 3%); palmitoleic acid (2-6%); balance primarily palmitic acid), and acetone (≥99.5%) were purchased from Sigma-Aldrich. Caffeine was recrystallized from acetonitrile (99.9% Fisher

Scientific). Acetaminophen (98%), saccharin (>98%), and 2,4-dihydroxybenzoic acid (97%) were purchased from Acros Organics. Carbamazepine (98%) and itraconazole (>95%) were purchased from Spectrum Chemicals. Lecithin (vegetable laboratory grade), chloroform (ACS Reagent, ≥99.8%), and hexanes (ACS Reagent, ≥98.5%) were purchased from Fisher Scientific. Ethanol (100%) was purchased from Decon Labs. Unless previously noted, all chemicals were used as received.

3.2.2.2. Powder X-ray diffraction

Powder X-ray diffraction (PXRD) data for the experiments involving the **CAFF1** were collected using an Inel G3000 diffractometer equipped with a curved position sensitive detector and parallel beam optics. The samples were loaded into aluminum sample holders and flattened using a glass slide. The diffractometer was operated with a copper anode tube (1.5 kW fine focus) at 40 kV and 30 mA. An incident beam germanium monochromator provided monochromatic $CuK_{\alpha 1}$ radiation. The diffractometer was calibrated using the attenuated direct beam at one-degree intervals. Calibration was checked using a silicon powder line position reference standard (NIST 640c). The program Symphonix[249] controlled the diffractometer and the data was analyzed using Jade[250] (version 6.5). PXRD data for **APAP6**, **CBZ1**, and **ITZ1** based experiments were collected on a Siemens D5000 X-ray diffractometer using $CuK_{\alpha 1}$ radiation. The samples were mounted on glass slides and leveled with a second glass slide. The diffractometer was equipped with a Bruker Sol-X energy-sensitive detector (scan type: locked coupled; scan mode: continuous; step size: 0.02^{o}; scan time: 2s/step).

3.2.2.3. Scanning electron microscopy

An aliquot of the resulting suspensions was directly placed on silicon wafers (Ted Pella, Inc.) for analysis. The silicon wafers were attached to aluminum sample stubs with colloidal silver (PELCO® Conductive Silver 187). The **CAFF1** samples were then

coated *in vacuo* with gold (Emitech K550 sputter coater, 35 mA, *ca*. 3 min). To enable omnidirectional coating, the vacuum was purged with Ar gas. Surfactant trials involving **APAP6** and **CBZ1** employed a spin coater (Laurell Technologies Corp., Model no.-WS-650SZ-6NPP/LITE) to remove excess surfactant. The SEM sample stub was rotated at 10000 rpm while an aliquot (1 mL) of the suspension was dropped on the rotating surface. Next the sample was rinsed with hexanes (1 mL) at 1000 rpm and dried before coating with gold. Studies involving **APAP6**, **CBZ1**, and **ITZ1** consisted of samples coated *in vacuo* with gold (Emitech K575X turbo sputter coater, 25 mA, 45s). To achieve omnidirectional coating the vacuum was purged with Ar gas and the samples were rotated during the coating process. The verify the crystal size and morphology the solids were imaged using a Hitachi S-4800 scanning electron microscopy (SEM) microscope employing accelerating voltages of 1.0-5.0 kV.

3.2.2.4. Dynamic light scattering

The average particle size for the **CAFF1** samples were determined by a Zetasizer Nano ZS (Malvern) operated at 25^{o}C with a 173^{o} scattering angle. In the case of **CAFF1**, particle size measurements performed of the solid prepared by the two-solvent approach required dilution of 250 μL of the original suspension into 3 mL of the 5% (w/v) Span-85 hexanes solution. The solid prepared by the single-solvent approach was analyzed directly. The average particle size and PDI were averaged over a set of three measurements.

3.2.2.5. Single-solvent sonochemical approach

3.2.2.5.1. **CAFF1** Trials

Cocrystals prepared *via* the single-solvent approach were obtained by separately dissolving 60 mg of **CAFF** and 48 mg of **DHBA** in 7 mL and 242 μL of acetone, respectively. The solutions were rapidly injected into 200 mL of hexanes placed inside

an ultrasonic cleaning bath (Branson 2510R-DTM; frequency: 42kHz ± 6% at 100W). The suspension was held at *ca*. 0°C during the 15 s of ultrasonic irradiation.

3.2.2.5.2. **APAP6** Trials

Cocrystals prepared *via* the single-solvent approach were originally investigated by separately dissolving **APAP** (151 mg, 0.827 mmol) and **THEO** (149 mg, 0.827 mmol) in 1 mL (827 mM) and 7 mL (118 mM) of ethanol respectively. **THEO** requires slight heating to dissolve in 7 mL of ethanol. The solutions were rapidly injected into 100 mL of hexanes placed inside an ultrasonic cleaning bath (Branson 2510R-DTM; frequency: 42kHz ± 6% at 100W). The suspension was held at *ca*. 0°C during the 30 s of ultrasonic irradiation. Additional studies employed injection solutions diluted to 10 mM. The 10 mM trial injected a 2 mL solution of **APAP** and a 2 mL solution of **THEO**. The dilution trials employed 100 mL of hexanes, held at *ca*. 0°C, as the anti-solvent was sonicated for 30 s.

3.2.2.6. Two-solvent sonochemical approach

3.2.2.6.1. **CAFF1** Trials

The two-solvent approach consisted of separately dissolving 125 mg of **CAFF** and 99 mg of **DHBA** in 1 mL of chloroform and 600 μL of acetone. The solutions were rapidly injected into 100 mL of hexanes placed located within an ultrasonic cleaning bath (Branson 2510R-DTM; frequency: 42kHz ± 6% at 100W). The suspension was held at *ca*. 0°C during the 15 s of sonication.

3.2.2.6.2. **CBZ1** Trials

The two-solvent approach that utilized concentrated injection solutions consisted of separately dissolving 84 mg of **CBZ** and 64 mg of **SAC** in 1 mL of chloroform and 1.5 mL of acetone. The solutions were rapidly injected into 100 mL of hexanes placed located within an ultrasonic cleaning bath (Branson 2510R-DTM; frequency: 42kHz ±

6% at 100W). The suspension was held at *ca*. 0°C during the 15 s of sonication. Additional studies employed injection solutions diluted to 10 mM. The 10 mM trial injected a 1 mL solution of **CBZ** and a 1 mL solution of **SAC**. The dilution trials employed 100 mL of hexanes, held at *ca*. 0°C, as the anti-solvent was exposed to ultrasonic irradiation for 30 s.

3.2.2.6.3. **ITZ1** Trials

The two-solvent approach consisted of separately dissolving 50 mg of **ITZ** and 9.5 mg of *L*-malic acid (**LMA**) in 1 mL of dichloromethane and 1 mL of acetone. The solutions were rapidly injected into 100 mL of hexanes placed located within an ultrasonic cleaning bath (Branson 2510R-DTM; frequency: 42kHz ± 6% at 100W). The suspension was held at *ca*. 0°C during the one min of sonication.

3.2.2.7. Sonocrystallizations with surfactant containing anti-solvent

3.2.2.7.1. **CAFF1** Trials

The single-solvent and two-solvent procedures were repeated using the same solvents, concentrations, volume of anti-solvent, but the composition of anti-solvent was changed to a 5% (w/v) Span-85 hexanes solution. An additional two-solvent procedure utilized a 1% (w/v) lecithin hexanes solution.

3.2.2.7.2. **APAP6** Trials

A solution of **APAP** dissolved in ethanol (2 mL, 10 mM) and a solution of **THEO** dissolved in ethanol (2 mL, 10 mM) was injected into an anti-solvent (100 mL) of 5% (w/v) Span-85 hexanes. The suspension was held at *ca*. 0°C and exposed to ultrasonic irradiation for 30 s.

3.2.2.7.3. **CBZ1** Trials

A solution of **CBZ** dissolved in chloroform (1 mL, 10 mM) and a solution of **SAC** dissolved in acetone (1 mL, 10 mM) was injected into an anti-solvent (100 mL) of 3% (w/v) Span-85 hexanes. The suspension was held at *ca*. 0°C during exposure to ultrasonic irradiation for 5 s.

3.2.3. Results and discussion

Our first experiments to generate nano-cocrystals of **CAFF1** involved a single-solvent sonochemical approach using acetone. Acetone was selected owing to an ability to dissolve both components while maintaining miscibility with the anti-solvent hexanes. **CAFF** and **DHBA** were separately dissolved in acetone then rapidly injected into a hexanes solution at *ca*. 0 °C under ultrasonic irradiation (Scheme 3). After 15 s of insonation the suspension was filtered and analyzed using PXRD, SEM, and DLS.

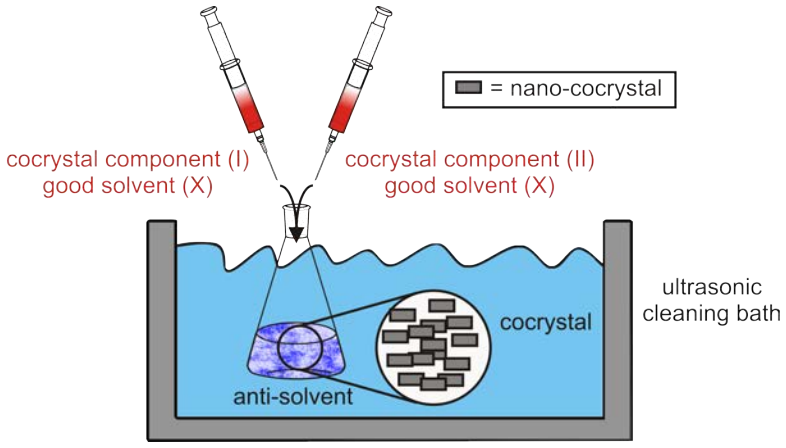

Scheme 3 Schematic of the single-solvent sonocrystallization approach.

An inspection of the PXRD pattern of the single-solvent precipitate showed an absence of the most intense peak for **CAFF** at 2θ = 12.0° and **DHBA** at 2θ = 13.7° (Fig. 33). A comparison of the diffractogram to the calculated powder pattern from single-

crystal data revealed peaks at 2θ = 10.7°, 12.9°, 17.4°, 21.5°, and 22.9°, which are consistent with cocrystal formation.

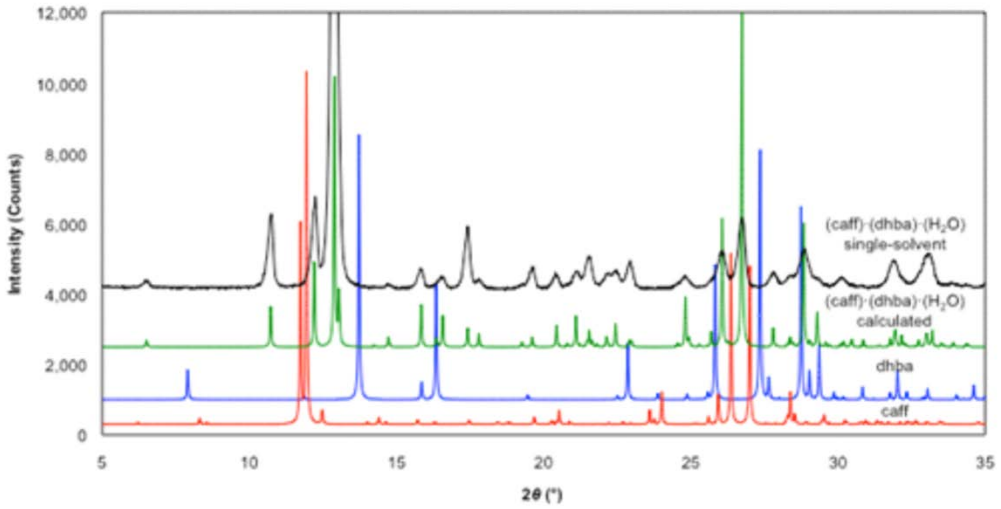

Figure 33 An overlay of PXRD patterns from the single-solvent approach, the single crystal data for **CAFF1**, and powder patterns from the individual cocrystal components.

SEM micrographs of the precipitate confirmed the presence of nanometer-sized crystals of plate morphologies. The smallest crystals exhibited widths of ca. 200 nm and lengths of ca. 200 nm. However, the individual crystal sizes varied from nano- to micrometer-scale dimensions (*i.e.* up to 5 microns) (Fig. 34). The micrographs also displayed agglomeration in the form of stacked, non-fused cocrystals, which is consistent with the formation of a nanosuspension.[235] Attempts to quantify the average particle size and size distribution *via* DLS were inconclusive owing to drifting intensity of scattered light caused by instability of the auto-correlation function.[251] The DLS results were determined to lie outside acceptable values, which suggested a broad particle size distribution and/or the presence of large particles caused by an association of nano-cocrystals within the dispersion.

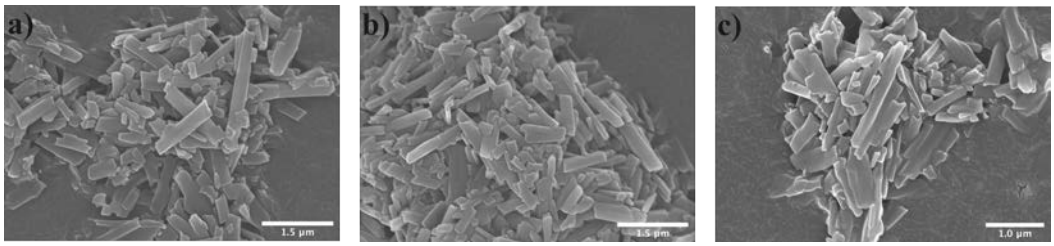

Figure 34 SEM micrographs (a-c) presenting the size distribution of agglomerated **CAFF1** obtained from the single-solvent approach.

To reduce or eliminate the micro-sized crystals, we devised a two-solvent sonochemical approach. We were inspired by studies on the solution-mediated phase transformation of metastable pharmaceutical crystals, wherein; high solubility solvents hastened the crystallization of stable polymorphs.[252, 253] The hypothesis that high solubility aids in nucleation can be supported by an examination of the nucleation rate, *J*, which can be described by the Arrhenius equation:

$$J = A\exp(-\frac{16\pi\gamma^3\nu^2}{3(kT)^3(\ln S)^2})$$

where *A* is the number of intermolecular collisions in solution, γ is the interfacial tension, ν is the molecular volume of the solute, *k* is the Boltzmann constant, *T* is the absolute temperature, and *S* is the degree of supersaturation.[254, 255] A high solubility solvent reduces interfacial tension, increases the degree of supersaturation, and increases the probability of intermolecular collisions, which culminates in an increase in the nucleation rate. We hypothesized that by cosolubilizing both **CAFF** and **DHBA** through the selection of a high-solubility solvent for each component the cocrystal would be more prone to rapidly nucleate and, thus, afford particles of nanometer-scale dimensions. Specifically, we modified the injection solvents according to solubility and dielectric constant. In such an experiment, the two solvents in the sonocrystallization would be

selected based on an ability to provide high solubility (*i.e.* >10 mg mL^{-1}) and miscibility with the anti-solvent.

To test our hypothesis, **CAFF** and **DHBA** were separately dissolved in chloroform and acetone, respectively, then rapidly injected into hexanes under ultrasonic irradiation at ca. 0 °C. After 15 s of irradiation the suspension was filtered, dried, and analyzed *via* PXRD to confirm in fact **CAFF1** was formed. To determine the particle size and morphology, the precipitate was analyzed using SEM. Unlike the single-solvent approach, the individual crystals that formed using the two-solvent method were exclusively of nanometer dimensions. The smallest particles displayed a width of *ca*. 190 nm and length of *ca*. 200 nm, while the largest crystals displayed a width of *ca*. 200 nm and length of *ca*. 800 nm (Fig. 35).

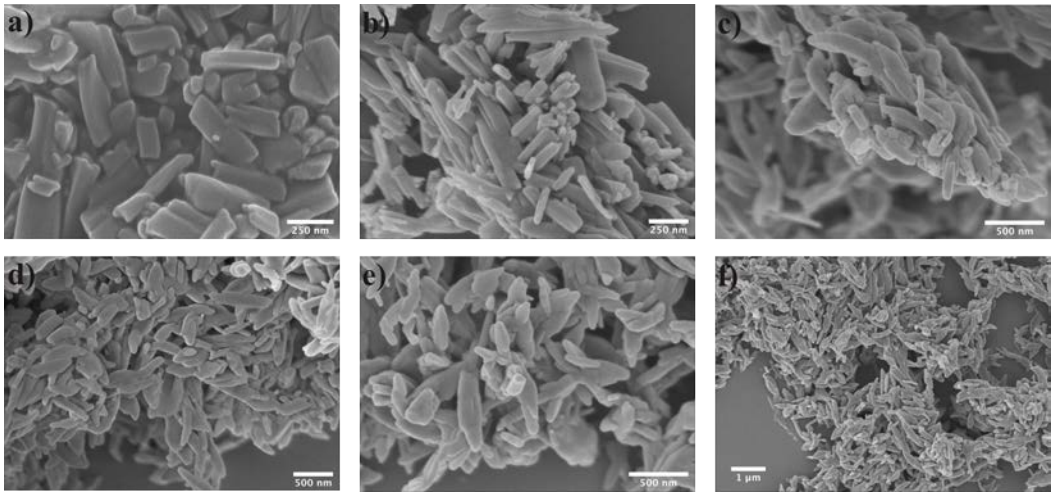

Figure 35 SEM micrographs (a-f) of agglomerated **CAFF1** prepared by the two-solvent sonochemical approach.

The decrease in crystal size when employing a two-solvent approach prompted an investigation into the necessity of coupling a two-solvent approach and ultrasonic irradiation. Indeed, when the two-solvent approach was repeated substituting ultrasound

for rapid stirring the resulting crystals exhibited rod and needle morphologies with lengths on the micrometer scale (Fig. 36). The results support the continued coupling of a two-solvent approach with rapid precipitation and simultaneous ultrasonic irradiation.

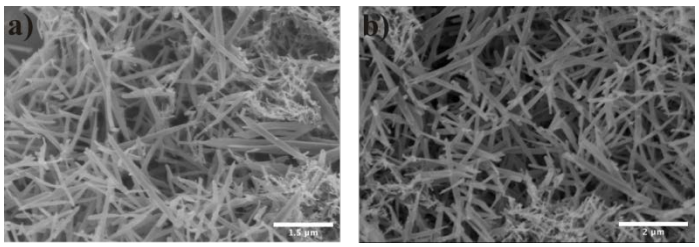

Figure 36 SEM micrographs (a,b) of agglomerated **CAFF1** prepared by the two-solvent in the absence of ultrasonic irradiation.

However, similar to the single-solvent method, micrographs revealed extensive agglomeration in form of stacked crystals when employing the two-solvent approach. Agglomeration can be expected owing to the supersaturated nature of the solution used to achieve the nanometer-sized crystals.[256] The agglomeration in the SEM micrographs was again manifested in the DLS experiment that suggested the presence of very large particles. The application of two solvents, however, resulted in a significant improvement in both particle size and distribution.

Although the two-solvent sonochemical method was successful in affording pharmaceutical cocrystals of nanometer-scale dimensions, we sought to reduce or eliminate the agglomeration. Agglomeration can influence solid dosage forms, with negative impacts on quality attributes such as dissolution rate and content uniformity.[237] Therefore, we turned to an investigation of the effects of surfactants on the agglomeration, as well as particle size and morphology, on our sonochemical preparation.[257] We expected a surfactant to coat the nano-cocrystals and, thus, provide a steric barrier to agglomeration.[235] The surfactant may also further reduce the size of the

nano-cocrystals, with a decrease in surface tension and an increase in nucleation rate. In addition, the adsorption of surfactants at a growing solid interface reduces the interfacial surface energy and inhibits particle growth.[254, 258, 259]

A pharmaceutically-acceptable surfactant, Sorbitan oleate (Span-85), was selected as the surfactant to be mixed with the anti-solvent hexanes.[260] A single-solvent crystallization was performed by preparing a solution of **CAFF** and **DHBA** in acetone followed by rapidly injecting the solutions into hexanes in the presence of 5% (w/v) Span-85 at ca. 0 °C under ultrasonic radiation. PXRD analysis confirmed cocrystal formation (Fig. 37).

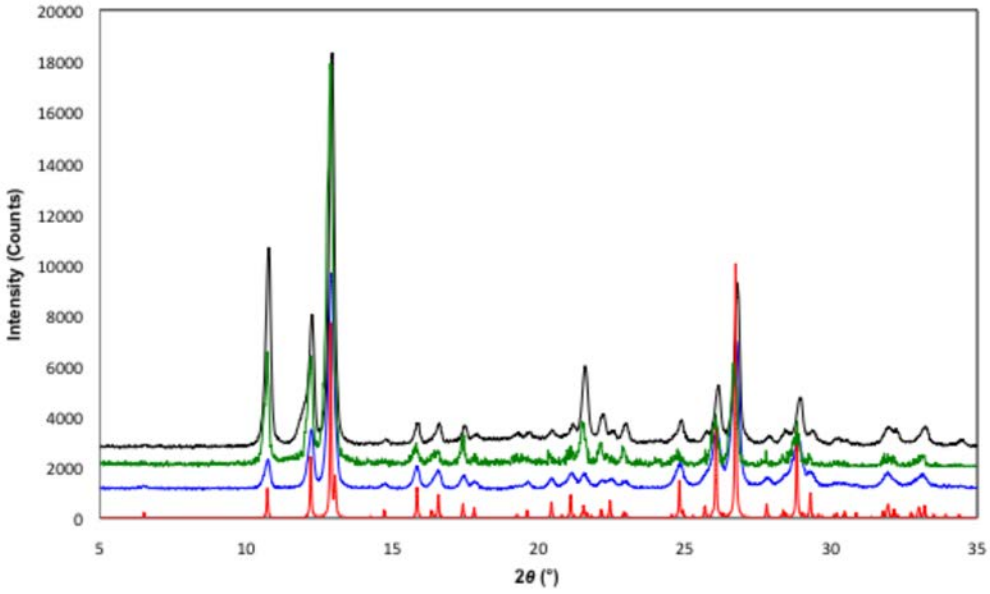

Figure 37 PXRD patters are arranged from top to bottom: two-solvent surfactant, single-solvent surfactant, two-solvent sonochemical, and calculated powder pattern for **CAFF1**.

An aliquot of the suspension was also analyzed using DLS. In contrast to the experiments without surfactant, DLS measurements of the single-solvent approach

resulted in average particle sizes of 280.1 nm ± 102.2 and polydispersity index (PDI) of 0.222 (Fig. 38). For the case of two solvents, the DLS revealed an average particle size of 136.4 nm ± 65.05 and PDI of 0.239. The application of the surfactant, thus, provided a means to affect both the agglomeration and crystal size using both the single- and two-solvent sonochemical methods.

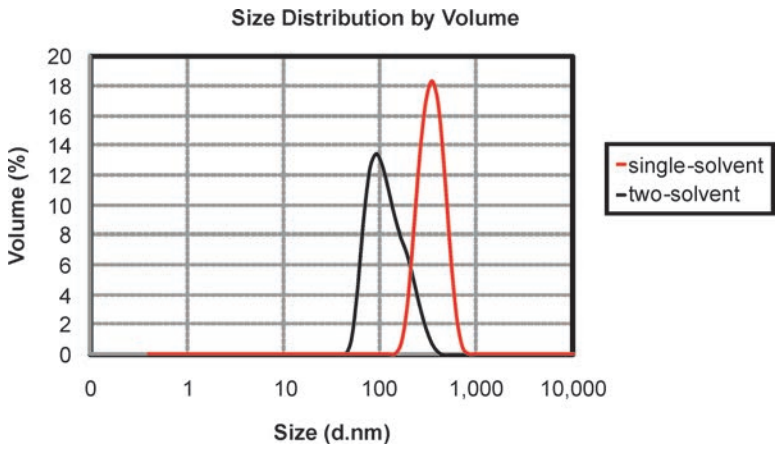

Figure 38 Particle size distribution for **CAFF1** from the single- and two-solvent approaches with Span-85 mixed in the anti-solvent.

SEM micrographs of the cocrystals obtained using the single-solvent sonochemical approach and Span-85 (Fig. 39) revealed morphologies based on spheres and plates. The spherical morphology can be attributed to modified crystal growth due to adhered surfactant on the crystal surface.[251] The crystals appeared dispersed with less stacking compared to those without surfactant. The micrographs using the single solvent also revealed micron-sized crystals of widths *ca*. 200 nm and lengths *ca*. 5 microns, which were not suggested by the DLS measurements.

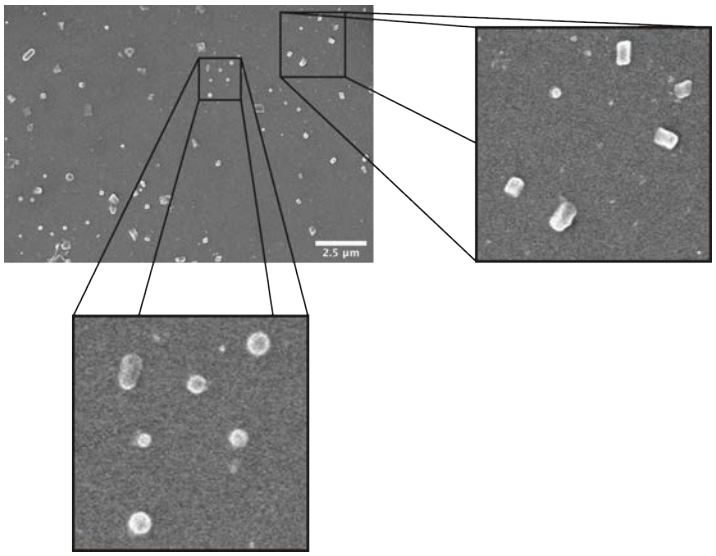

Figure 39 SEM micrograph **CAFF1** prepared by the single-solvent approach using a Span-85 hexanes anti-solvent.

Sphere and plate morphologies were also present when two different injection solvents were employed. The average particle sizes of the cocrystals, however, were more comparable to the DLS results with a lack of micron-sized crystals (Fig. 40).

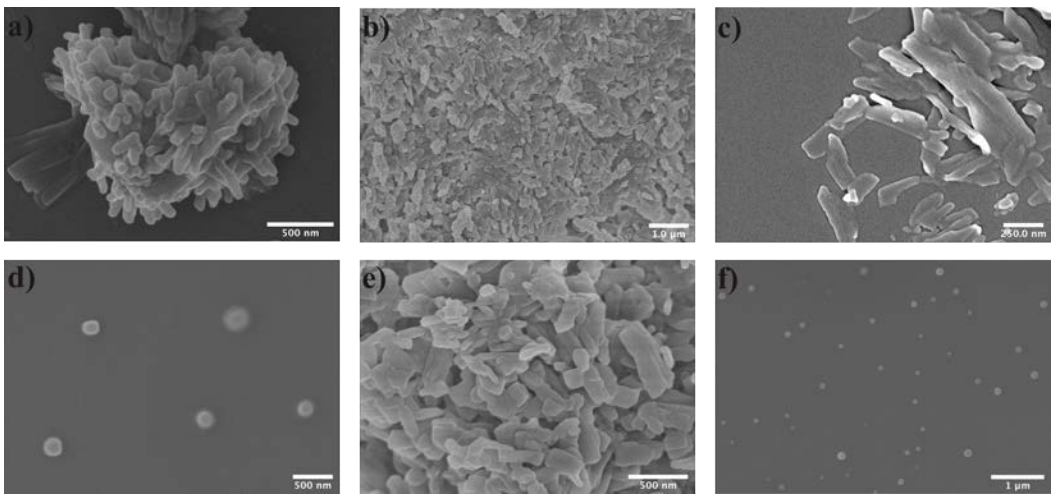

Figure 40 SEM micrographs (a-f) of **CAFF1** prepared by the two-solvent approach using a Span-85 hexanes anti-solvent.

The use of the surfactant, thus, promoted a general decrease in overall particle size, with a narrowed difference in particle size for the two-solvent approach. Collectively, the results demonstrate the utility of cosolubilizing the cocrystal components using two solvents and incorporating a surfactant to prepare pharmaceutical cocrystals of nanometer-sized dimensions.

To further investigate the role of surfactant in the synthesis of pharmaceutical nano-cocrystals we repeated the two-solvent sonochemical procedure with a 1% (w/v) lecithin hexanes anti-solvent. Analysis of the precipitate *via* SEM revealed crystals of rod and plate morphologies with crystals ranging in lengths from *ca*. 100 nm to *ca.* 1 μm (Fig. 41). The SEM micrographs suggest the lecithin hexanes anti-solvent produced a broad size distribution with larger particles when compared to the Span-85 trials. The difference in surfactant performance may be caused by a varied affinity for the crystal surfaces or the reduced concentration of lecithin in the surfactant owing to a limited miscibility with hexanes.

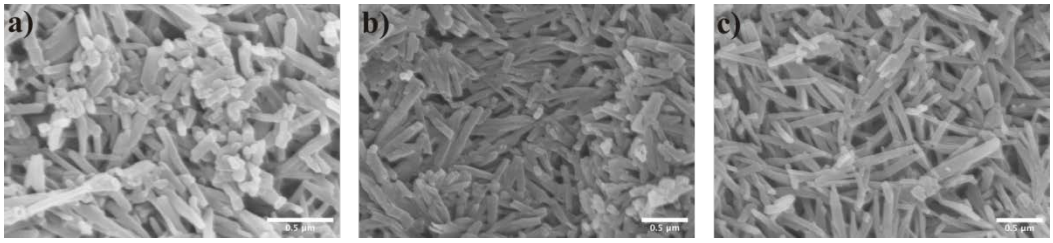

Figure 41 SEM micrographs (a-c) of **CAFF1** prepared by the two-solvent approach using a lecithin hexanes anti-solvent.

That **CAFF1** was synthesized in nanometer-scale dimensions encouraged us to study the effects of solvent, concentration, and the presence of surfactant on the formation of additional pharmaceutical nano-cocrystals, namely **APAP6**, **CBZ1**, and **ITZ1**. The first set of experiments on **APAP6** employed a single-solvent approach with

ethanol owing to an ability to readily solubilize both **APAP** and **THEO**. The cocrystal components were separately dissolved in a minimum amount of ethanol to achieve solutions near the saturation concentration. After rapid injection into hexanes with simultaneous exposure to ultrasonic irradiation the precipitate was analyzed *via* SEM (Fig. 42).

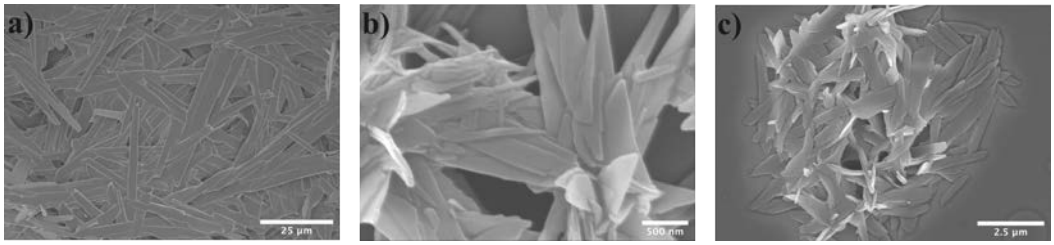

Figure 42 SEM micrographs (a-c) of the solid obtained by rapidly injecting concentrated ethanol solutions of **APAP** and **THEO**.

SEM micrographs revealed the resulting solid consisted of a rod-shaped precipitate with the length of the rods extending anywhere from tens to hundreds of microns. To reduce the crystal size we turned to dilute injection solvents.[104, 251] We expected the dilution would limit the amount of material available for crystal growth at the nucleation sites dispersed throughout the anti-solvent. In fact, when the single-solvent sonochemical procedure was repeated with the cocrystal components separately dissolved to give 10 mM solutions the result was a dramatic decrease in the crystal size observed in SEM micrographs (Fig 43). The resulting precipitate exhibited a plate morphology of nanometer-scale dimensions with agglomeration observed in the form of stacked plates.

The synthesis of nanometer-scale crystals by employing injection solvents of a 10 mM concentration was further investigated with the 5% (w/v) Span-85 hexanes anti-solvent. Analysis of the precipitate *via* SEM again revealed crystals of plate

morphologies with nanometer-scale dimensions as small as *ca*. 154 nm for the side of a plate (Fig. 44).

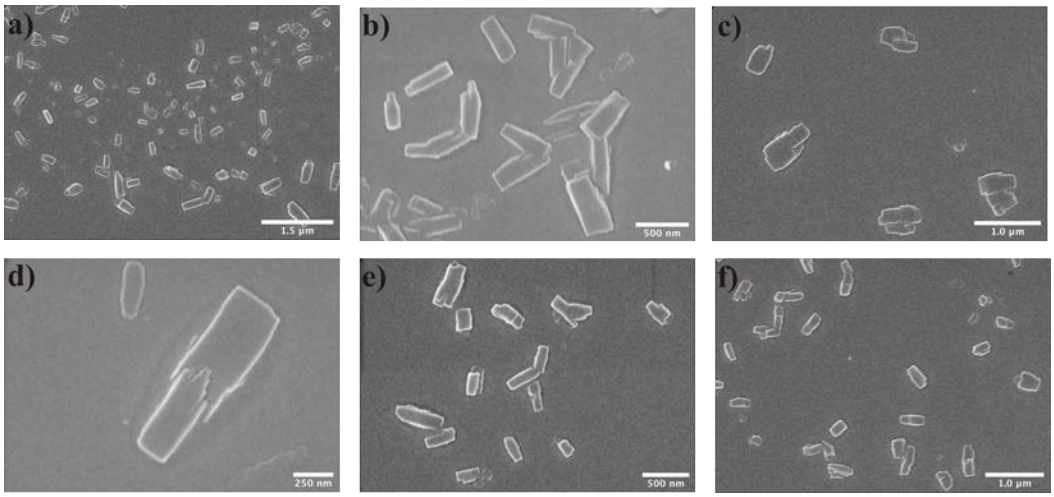

Figure 43 SEM micrographs (a-f) of the solid obtained by rapidly injecting 10 mM solutions of **APAP** and **THEO**.

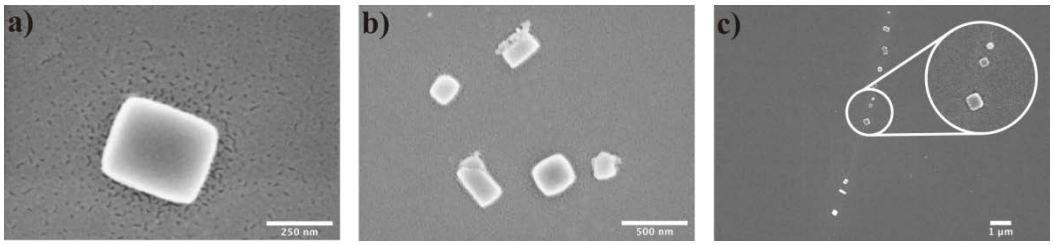

Figure 44 SEM micrographs (a-c) of the solid obtained by rapidly injecting 10 mM solutions of **APAP** and **THEO** into a 5% (w/v) Span-85 hexanes anti-solvent.

Akin to the study of **APAP6**, we investigated the conditions necessary to achieve nano-cocrystals of **CBZ1** by varying the injection solvent concentration and the presence of surfactant in the anti-solvent. To cosolubilize the cocrystal components **CBZ** and **SAC** we employed the two-solvent approach, wherein, **CBZ** was dissolved in chloroform

and **SAC** was dissolved in acetone to achieve solutions near the point of saturation. Analysis of the solid obtained from the two-solvent approach *via* PXRD and SEM confirmed we had achieved the cocrystal **CBZ1** however the solid consisted of micron sized crystals with morphologies that were either spherical, plate, or rod shaped (Fig. 45a). Motivated by the study of **APAP6**, we pursued a reduction in crystal size by employing injection solvents with a 10 mM concentration. In this case, when the two-solvent sonochemical procedure was repeated with diluted injection solvents we obtained a precipitate with a distorted rod-shaped morphology with the length of the rods extending into micrometer dimensions (Fig. 45b). The third iteration of the two-solvent approach involved incorporating the anti-solvent 3% (w/v) Span-85 hexanes in combination with the dilute injection solvents (*i.e.* 10 mM). SEM analysis of the solid generated by this procedure showed a dramatic decrease in size to nanometer-scale dimensions when compared to the procedure that used hexanes as the anti-solvent (Fig. 45c).

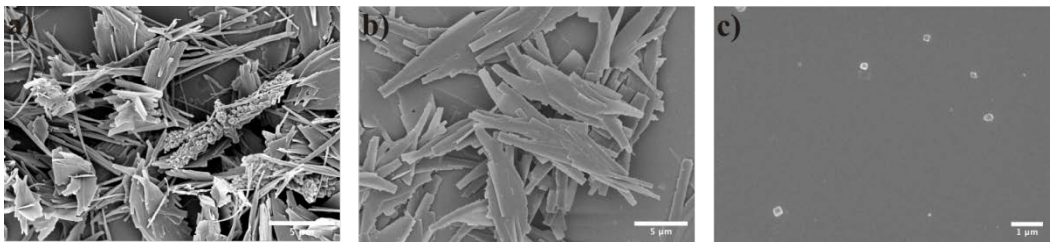

Figure 45 SEM micrographs of the solids obtain by employing (a) concentrated injection solutions, (b) dilute injection solutions, and (c) dilute injection solutions of **CBZ** and **SAC** coupled with a 3% (w/v) Span-85 hexanes anti-solvent.

As part of our ongoing studies and future work we will investigate pharmaceutical cocrystals similar to **ITZ1** that have a diverse tapestry of functional group and

conformational freedom. To date, efforts to obtain nano-cocrystals of **ITZ1** have resulted in the isolation of spherical particles of nanometer-scale dimensions (Fig. 46).

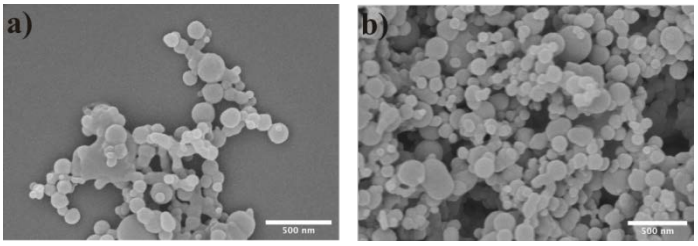

Figure 46 SEM micrographs (a,b) that represent the spherical nanoparticles obtain in our efforts to achieve nano-cocrystals of **ITZ1**.

Although the solid obtained from the two-solvent sonochemical approach yields nanoparticles, PXRD analysis supports the spherical particles correspond to an amorphous precipitate. Upon exposure to ultrasonic irradiation for extended periods of time (*i.e.* 3 hrs), PXRD confirms the solid remains amorphous. As part of our future studies, we will continue to explore challenging systems such as **ITZ1** to determine the conditions that can fabricate nano-cocrysals of compositions similar to **ITZ1**. The studies will include extensive solvent screening, seeding, crystallizations at a range of temperatures, and the use of alternative sources of heat (*e.g.* microwave irradiation).[261]

3.2.4. Summary

To conclude, we have introduced a method to fabricate pharmaceutical nano-cocrystals based on a sonochemical approach that utilizes solvent selection and use of a surfactant. The method accommodates the inherent solubility difference between the cocrystal components of a pharmaceutical cocrystal. We will continue to work on PAs with poor dissolution rates and bioavailability whose properties could be greatly

enhanced by coupling the solubility advantages imparted to pharmaceutical cocrystals and nanocrystals.

3.3. Host-guest nanocrystals via sonochemistry: evidence of reversed crystal growth involving hollow morphologies

3.3.1. Introduction

An appreciable number of nanocrystals exhibit cubic symmetries and shapes at the molecular and bulk scales, respectively. However, in purely organic systems a cubic lattice is rare.[262] A search of the Cambridge Structural Database reveals that less than 0.1% of all reported purely organic crystals are cubic.[263, 264] The lack of organic systems can be attributed to the anisotropy of molecules that largely prohibits packing from meeting cubic symmetry requirements.[265] *C*-methylcalix[4]resorcinarene (**CMCR**) is an example of an organic system that crystallizes in the rare cubic space group *I*432.[266] Six resorcinarene molecules and eight water molecules self-assemble to form a chiral sphere in the solid-state sustained by 60 hydrogen bonds (Fig. 47).

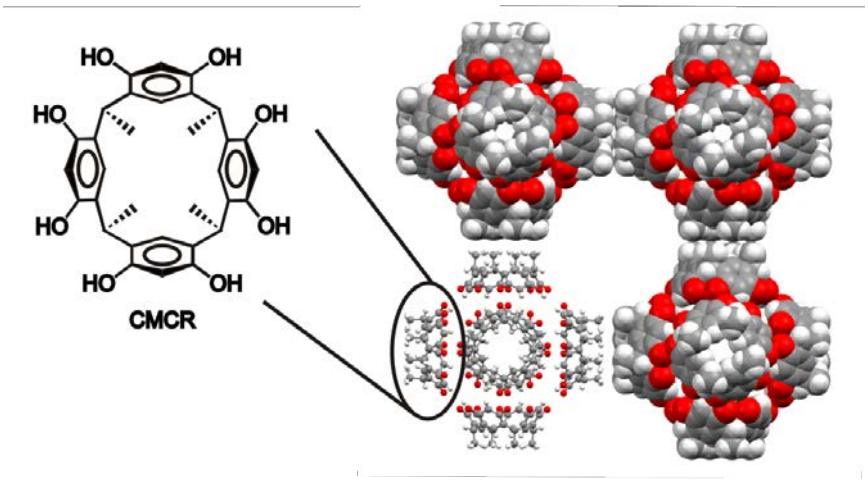

Figure 47 Molecular structure of **CMCR** and cubic solid-state packing of **CMCR** hexamer (solvent molecules omitted for clarity).

The resorcinarene hexamer is an important entry in the field of supramolecular cages that was pioneered by Rebek *et al.* in their report of a molecular tennis ball that self-assembles *via* hydrogen bonding of glycoluril subunits.[267] Subsequent research in the field of supramolecular chemistry has shown immense interest in hexameric assemblies of resorcin[4]arenes, calix[4]pyrroles, and pyrogallol[4]arenes owing to an ability to encapsulate guests with potential applications in fields such as drug delivery and catalysis.[268-273] For example, the encapsulation of a Au(I) catalyst within the resorcinarene hexamer was shown to alter the catalytic products.[274] Resorcinarenes have also been identified as excellent surfactants for the dispersion, and self-assembly, of metal nanoparticles into well-defined structures.[275] However, the development of resorcinarenes, and more generally, host-guest systems as nanocrystals remains largely unexplored.[276-278]

With this in mind, we report the fabrication of nanocrystals comprised of the **CMCR** hexamer. The nanocrystals are achieved *via* a sonochemical approach with crystals as small as 157 nm. The application of ultrasound offers a versatile approach to form nanostructured materials inaccessible by conventional methodologies.[108, 279-281] Here, we show that not only is sonochemistry critical to the formation of **CMCR** nanocrystals but ultrasonic irradiation affords hollow crystals. Crystals with hollow interiors of interest include dendrimers, graphite, silica, metals, and inorganic materials that have potential applications in a variety of fields (*e.g.* drug delivery).[279, 282-285] The **CMCR** crystals described here are the first reported hollow, polyhedral nanocrystals composed of purely organic components.[286] Formation of the hollow crystals can be attributed to a reversed crystal growth mechanism recently elucidated by Zhou *et al.* to account for the formation of hollow zeolite crystals.[287-290] The stages of reversed crystal growth include oriented aggregation of nanoparticles, surface recrystallization, and growth from the surface-to-core.

3.3.2. Materials and methods

3.3.2.1. Materials

C-methylcalix[4]resorcinarene (**CMCR**) (≥90%) was purchased from Sigma-Aldrich whilst nitrobenzene (>99%) was purchased from Acros Organics.

3.3.2.2. Crystallizations

Macro-sized crystals of the **CMCR** hexamer were grown *via* slow-solvent evaporation of a nitrobenzene (NO_2Ph) solution. Following the original report, we dissolved **CMCR** (15 mg, 27.5 mmol) in boiling NO_2Ph (5 mL). PXRD confirmed the corresponding precipitate was the **CMCR** hexamer. A typical preparation of nano- and micrometer-sized crystals of **CMCR** involved dissolving **CMCR** (3.0 mg, 5.5 mmol) in boiling nitrobenzene (NO_2Ph, 1 mL) and rapidly injecting the solution into water (10 mL). During injection, the water was simultaneously stirred and exposed to ultrasonic irradiation. After 2 min, an aliquot was removed for analysis. When then nanocrystallization procedure was repeated in the absence of ultrasonic irradiation, the same solvents and concentrations were employed but the mixture was stirred for 30 min. Experiments performed with the goal of decreasing the rate of nanocrystallization utilized a NO_2Ph at 20-fold dilution.

3.3.2.3. Powder X-ray diffraction

PXRD data for **CMCR** crystallizations were collected on a Siemens D5000 X-ray diffractometer using $CuK_{\alpha 1}$ radiation. The samples were mounted on glass slides and leveled with a second glass slide. The diffractometer was equipped with a Bruker Sol-X energy-sensitive detector (scan type: locked coupled; scan mode: continuous; step size: 0.02^{o}; scan time: 2s/step).

3.3.2.4. Scanning electron microscopy and particle size determination

An aliquot of the resulting suspensions was placed on silicon wafers (Ted Pella, Inc.) fastened to aluminum sample stubs with colloidal silver (PELCO® Conductive Silver 187). The samples were coated with gold *in vacuo* (Emitech K575X turbo sputter coater, 25 mA, 45s). To enable omnidirectional coating, the vacuum was purged with Ar gas and the samples were rotated during the coating process. The verify crystal sizes and morphologies the solids were imaged using a Hitachi S-4800 SEM microscope employing accelerating voltages of 3.0-5.0 kV. To calculate the average crystal size from SEM micrographs, ImageJ software was employed. The diameters of over 1500 crystals were fit to a Gaussian distribution to provide a size distribution.

3.3.2.5. Transmission electron microscopy

Samples were placed on carbon-coated copper grids (Ted Pella, Inc. Carbon-Type B 300 mesh). Analysis was performed using a JEOL 2100F field emission transmission electron microscope (TEM) at 200 kV accelerating voltage.

3.3.2.6. Solution-mediated phase transformation studies

Hexamer and hydrate formation was studied using competitive slurries. The **CMCR** hydrate was isolated *via* solution-mediated phase transformation of a **CMCR**-water suspension after equilibration for 3 days at ambient conditions. The pure hexamer was prepared by recrystallization of **CMCR** from nitrobenzene. Competitive slurries employed equimolar amounts of pure resorcinarene hexamer and **CMCR** hydrate suspended in nitrobenzene, water, and a 1:1 (v/v) nitrobenzene/water mixture. The nitrobenzene and water suspensions were equilibrated at ambient conditions for 9 days before isolation and analysis *via* PXRD. Suspension in a 1:1 (v/v) nitrobenzene/water mixture was allowed to equilibrate for 12 days at ambient conditions before analysis *via* PXRD.

3.3.3. Results and discussion

In the original report, the **CMCR** hexamer was prepared by crystallization from boiling NO_2Ph over the course of two weeks.[266] The result was light yellow crystals of cubic morphology suitable for single crystal X-ray diffraction. When the procedure was repeated, we obtained a yellow precipitate that PXRD confirmed as the **CMCR** hexamer. A close examination of SEM micrographs revealed a mixture of crystalline morphologies consisting of large flakes and rhombic dodecahedra. The rhombic-dodecahedral crystals ranged in size from 4 μm to 40 μm in diameter while the size of the flakes was not uniform and varied on the order of hundreds of micrometers (Fig. 48).

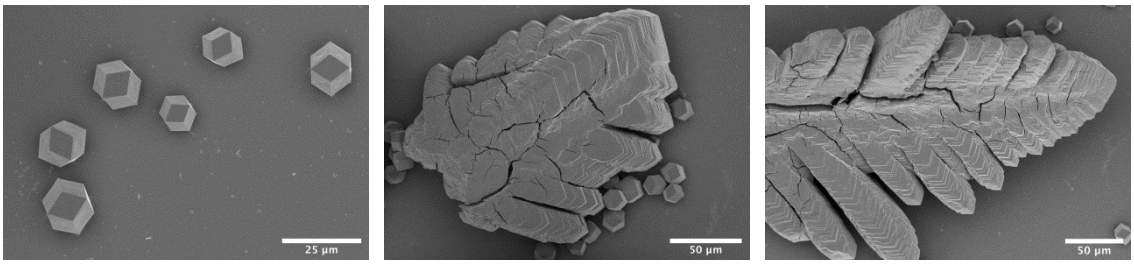

Figure 48 SEM micrographs of the **CMCR** hexamer prepared *via* slow-solvent evaporation revealing crystals of flake and rhombic-dodecahedral morphology.

To synthesize **CMCR** hexamer crystals reduced to nanometer dimensions we turned to sonochemistry.[279] The coupling of rapid precipitation and sonochemistry has been shown to afford multi-component nanocrystals, or cocrystals, of purely organic components.[108, 281] A typical preparation consisted of dissolving **CMCR** in boiling NO_2Ph and rapidly injecting the solution into water. During the injection, the water was simultaneously stirred and exposed to ultrasonic irradiation. After two min, an aliquot was removed for analysis by PXRD, SEM, and TEM.

Close examination of SEM and TEM micrographs revealed crystals of rhombic dodecahedron morphology (Fig. 49a,b). The crystal sizes were in fact reduced and fit to a Gaussian distribution characterized by an average diameter of 630 nm (s.d. 315 nm) with well-defined morphologies as small as 157 nm (Fig. 49c).

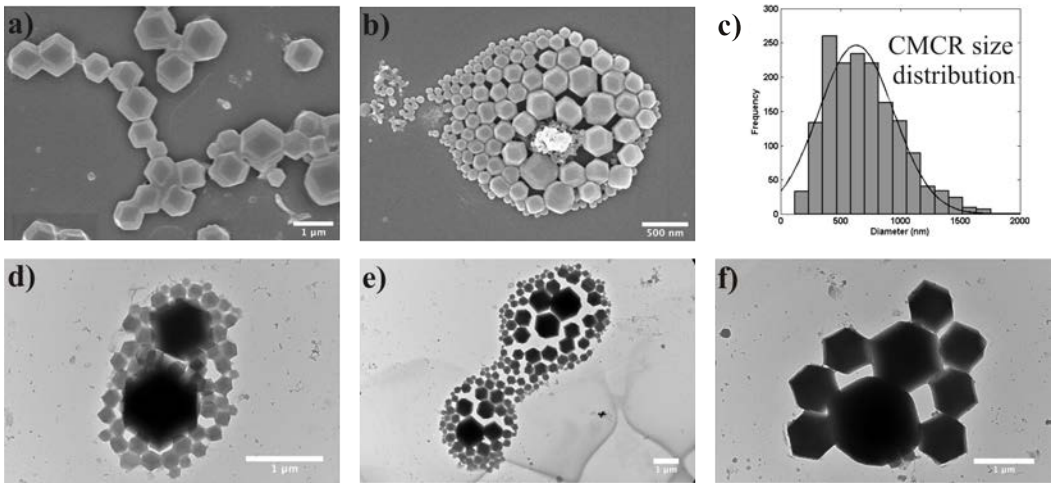

Figure 49 (a,b) SEM micrographs of **CMCR** crystals formed *via* sonocrystallization. (c) Particle size distribution of the solid prepared *via* sonochemistry and (d-f) corresponding TEM micrographs of **CMCR** crystals.

PXRD analysis confirmed the solid from the sonochemical approach to be the **CMCR** hexamer with additional peaks assigned to an uncharacterized hydrate of the resorcinarene (Fig. 50). Indeed, a solid with a PXRD pattern that matched these additional peaks was obtained directly from a **CMCR**-water suspension after equilibration for 3 days. A propensity of **CMCR** to form hydrates, and solvates in general, is well documented.[291] SEM analysis of the **CMCR**-water suspension solid revealed a solid of a micron-sized rods (Fig. 51). The relationship between the **CMCR**-hydrate and resorcinarene hexamer was studied using competitive slurries containing an equimolar amount of each crystalline phase in NO_2Ph, water, and a 1:1 (v/v) NO_2Ph water mixture. When NO_2Ph was employed as the SMPT solvent the solid mixture

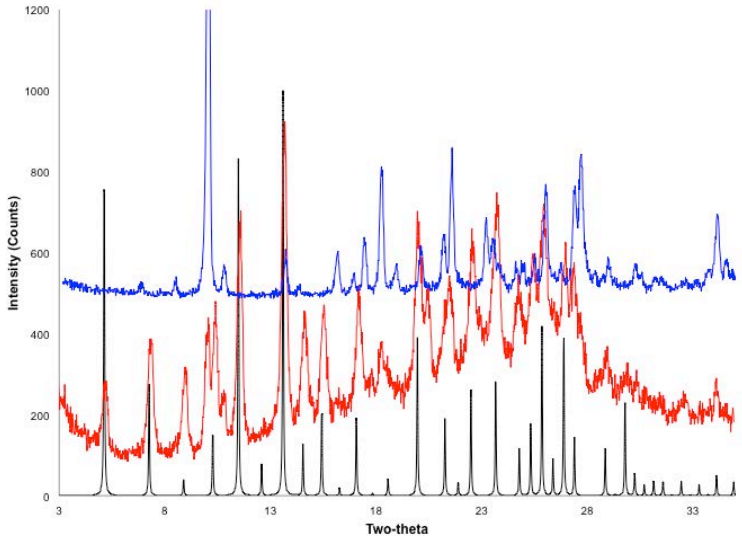

Figure 50 Comparison of PXRD data for **CMCR** nanocrystals to the calculated powder pattern of **CMCR** from single crystal data. The patterns arranged from top to bottom are: **CMCR**-hydrate, nano-**CMCR**, and calculated **CMCR**.

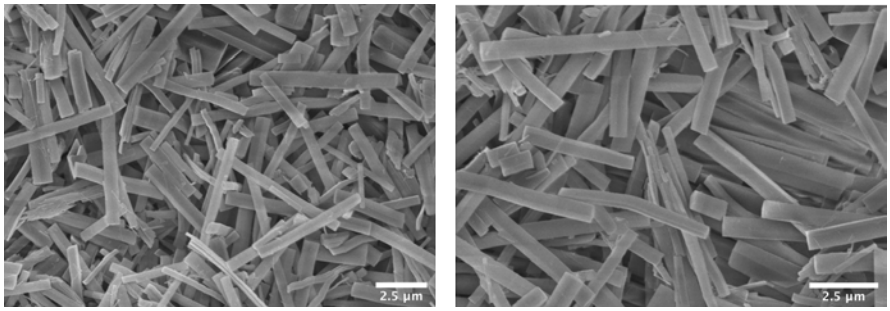

Figure 51 SEM micrograph of the **CMCR** hydrate obtained *via* a water suspension.

converted to the pure hexamer. In contrast, when water was used as the SMPT solvent, the solid mixture underwent phase transformation to the pure **CMCR** hydrate. Interestingly, resuspension of solid **CMCR** hydrate in pure NO_2Ph showed partial conversion to the resorcinarene hexamer after equilibration for 3 days at ambient conditions. Raising the temperature of the partially converted suspension to 50^{o}C caused complete phase transformation to the hexamer after 12 hrs. The suspension of both

CMCR phases in the 1:1 (v/v) NO_2Ph water mixture showed no change in the crystalline phase after 12 days of equilibration.

When the nanocrystallization of the **CMCR** hexamer was repeated with vigorous stirring alone the resulting solid was composed of smooth spherical particles that ranged in size from 40-900 nm in diameter (Fig. 52a). When the suspension was allowed to age for 2 months, no change in size or morphology was observed (Fig. 52b). The smooth spheres could be converted, however, to the rhombic dodecahedron crystals upon exposure to ultrasound. SEM analysis clearly demonstrated the presence of well-defined crystals, albeit, of micron dimensions (Fig. 52c). From these observations, we concluded that the rapid precipitation coupled to ultrasound was also necessary to obtain the nano-sized crystals of **CMCR**.

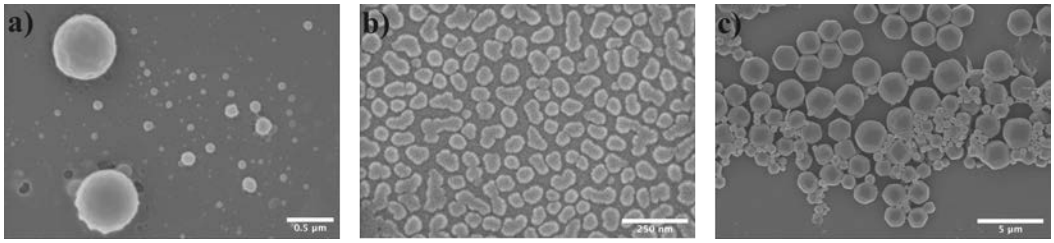

Figure 52 SEM micrographs of **CMCR** solid (a) prepared in the absence of ultrasonic irradiation, (b) after allowing the sample to age for two months, and (c) smooth spheres converted to a rhombic-dodecahedral morphology after exposure to ultrasonic irradiation.

During the sonochemical preparation of **CMCR** nanocrystals, we observed rhombic dodecahedron nanocrystals that exhibit a hollow morphology (Fig. 53). SEM micrographs displayed rhombic dodecahedron crystals that were likely fragmented (Fig. 53a-c) into two pieces or, remarkably, formed with a hole to reveal a hollow interior (Fig. 53d). The fragmented polyhedra exhibit a spherical interior and provide approximate shell thicknesses ranging from 70 nm to 230 nm. The occurrence of the hollow crystals

was not size dependent, as crystals from 500 nm to 4 μm in diameter exhibited hollow morphologies. Crystals with hollow polyhedral topologies have only been observed for inorganic-based materials, with zeolite analcime and zeolite A being the only examples based on a porous structure.[287-290, 292] The zeolites formed according to a reversed crystal growth mechanism that initiated with oriented aggregation of nanoparticles, was followed by surface recrystallization, and concluded with growth from surface-to-core *via* Ostwald ripening.[287]

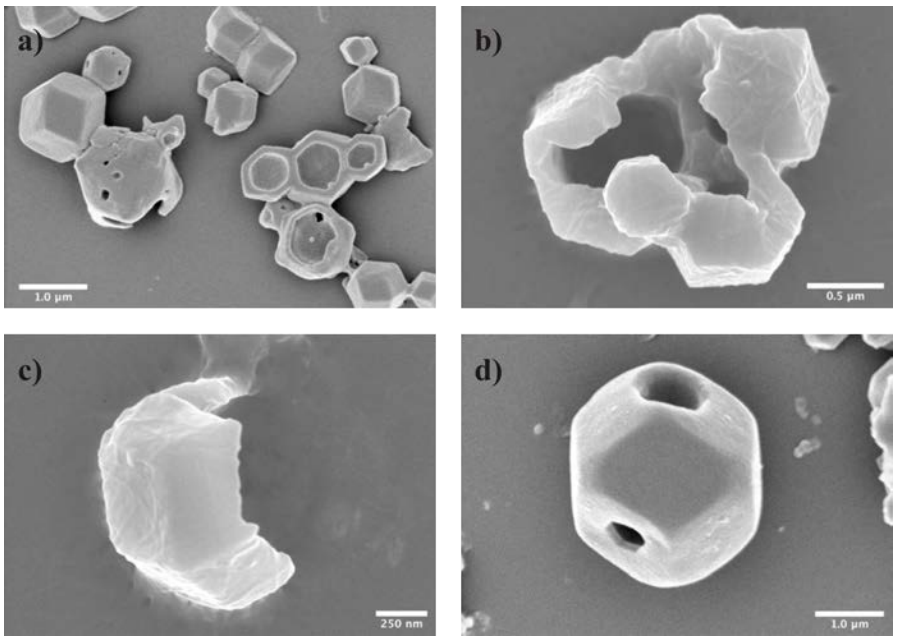

Figure 53 SEM micrographs of (a-c) fragmented crystals and (d) a rhombic dodecahedron from with a hole.

To gain insight into the formation of the hollow **CMCR** crystals, crystallization studies were performed in NO_2Ph at 20-fold dilution. A dilution was employed to slow the rate of nanocrystallization and observe stages of crystallization, however, crystal growth remained rapid compared to zeolites.[293, 294] An SEM analysis of the dilution

study revealed plate-like crystals upon only 45 s of sonication, which included sizes as small as 70 nm (Fig. 54a,b).

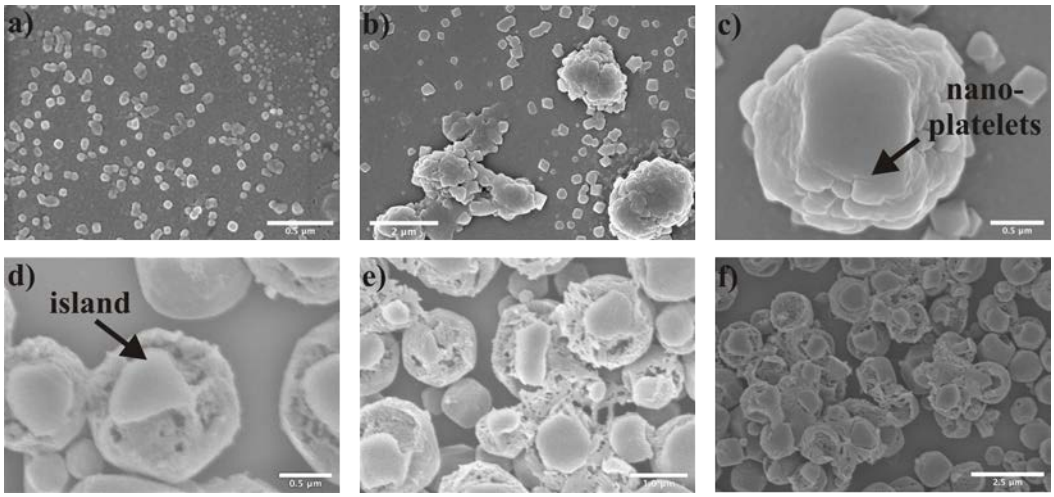

Figure 54 (a, b) Comparison of SEM micrographs of organic nanocrystals of **CMCR** after sonication for (a, b) 45 s and (c) 2 min at 20-fold dilution in NO_2Ph. (c-f) SEM micrographs showing partial surface crystallization of islands having a triangular shape.

Exposure to ultrasonic irradiation for 2 min converted the plates to a rhombic dodecahedron morphology. Building units, in the form of nanoplatelets, remained visible with clear boundaries on the surface of the polyhedra (Fig. 54c).[287] The presence of platelets was consistent with an oriented aggregation process in which nanocrystallites organize to share identical crystallographic orientation, whereupon, fusion occurs at the interface to form a single crystal.[128, 295-297] Indeed, SEM micrographs taken in our original attempts to form nanocrystals of **CMCR**, *without dilution* and as in the case of preparing zeolites,[289] revealed disordered aggregates with triangular crystalline "*islands*" (Fig. 54d). The triangular islands coincide with partial surface crystallization which continues grow over the surface, and remarkably self-adjust, until the entire surface corresponds to the faces of a rhombic dodecahedron (Fig. 54e,f). To our knowledge,

CMCR is the first observation of a purely organic solid to exhibit crystal formation through a reversed growth mechanism. These observations are particularly important given that surface-adsorbed organics enhance the interparticle interactions that support such a mechanism.[287]

3.4. Summary

In this chapter, we have presented the sonochemical preparation of purely organic, multi-component, nanocrystals. In the case of the **CMCR** hexamer, we demonstrated the sonochemical approach induces rapid nucleation of the **CMCR** host-guest nanocrystals, which undergo oriented aggregation to yield rhombic dodecahedral nanocrystals and hollow rhombic dodecahedral crystals. The mechanism is attributed to a reversed crystal growth process heretofore only observed in inorganic materials. It is worth noting that although the sonochemical approach involves rapid nucleation the **CMCR** hexamer successfully self-assembles to form a capsule sustained by 60 hydrogen bonds. The ability to synthesize supramolecular nanocrystals with diverse intermolecular interactions, such as in the host-guest nanocrystal and pharmaceutical nano-cocrystals, will be crucial as supramolecular chemistry continues to evolve into a field of complex matter.[298]

CHAPTER 4. INTEGRATING FUNTIONAL GROUP DIVERSITY INTO TEMPLATED [2+2] PHOTOREACTIONS

4.1. Introduction

A common misconception is that the rigid and confined environment of the solid-state imparts inertness. Contrary to popular belief the solid-state has exhibited a surprising amount of flexibility which is exemplified in the ability of solids to undergo guest uptake/removal,[299] catalytic reactions,[300] chain reactions,[301] and single-crystal-to-single-crystal reactions.[302] The field of design-driven solid-state reactions was pioneered by Schmidt *et al.* in the 1960's while investigating the [2+2] photodimerization of olefins in the solid-state.[80, 111, 112] The study defined a topochemical postulate for the [2+2] photodimerization of olefins in the solid-state. Specifically, olefins can be expected to undergo a cycloaddition reaction when aligned parallel and within 4.2 Å. However, the sensitivity of the solid-state to functional group substitutions and crystal packing forces make aligning olefins an arduous task. To impart some degree of control over the arrangement of molecules in the solid-state MacGillivray *et al.* introduced a template approach to enforce topochemical alignment of olefins in the solid-state.[113] In particular, the linear template, resorcinol, juxtaposes two *trans*-1,2-bis(4-pyridyl)ethylene (**BPE**) molecules such that olefins undergo a [2+2] photodimerization upon exposure to UV light. The template-controlled approach has proven to be modular in that the alignment of olefins is tolerant to template switching (*i.e.* substituted resorcinol), an expansion of the pyridyl moieties to include molecules such as di- and triolefins, and a reversal of the code wherein linear templates in the form of a bipyridines direct the photodimerization of dicarboxylic acids.[88] Template-controlled photoreactions have also been realized in metal complexes.[51, 116, 303, 304] For example, the tendency of Ag(I) ions to adopt a linear coordination geometry and participate in argentophilic interactions at distances up to 3.8 Å makes Ag(I) ions an ideal candidate for arranging olefins composed of silver-

coordinating functional groups.[117-119] In fact, Ag···Ag forces have successfully oriented molecules such as 4-pyridylstyrenes and 4-vinylpyridines to undergo cycloaddition reactions in the solid-state.[51, 303]

Despite the success of the template approach, reactive olefins generally lack functional group diversity as many olefins are based on symmetric bipyridines and dicarboxylic acids.[305] A persistent challenge in crystal engineering is the design of templated [2+2] photoreactions based on unsymmetrical olefins wherein both ends of the molecule are capable participating in hydrogen bonds. Previously, the utility of unsymmetrical photoproducts was realized in our group in the hydrogen-bond-directed solid-state synthesis of *rctt*-1,2-bis(2-pyridyl)-3,4-bis(4-pyridyl)cyclobutane and *rctt*-1,2-bis(2-pyridyl)-3,4-bis(3-pyridyl).[306-308] The tetrapyridine photoproducts assembly with Cu(II) ions to from polyhedra with tunable sizes based on the cyclobutane isomer employed. Resorcinol-based templates have also successfully aligned olefins with pyridine and ester substituents.[309] In this case, the ester group was used to mask the carboxylic group of acrylic acids which, through synthon competition, prevented aligning olefins for cycloaddition reactions. The strategy afforded cyclobutane products based on pyridine and ester functional groups and, after a postsynthetic step, generated carboxylic acid groups in place of the esters. Additional investigations have pursued the alignment of unsymmetric olefins for [2+2] photodimerization by utilizing salt formation or metal ions (*e.g.* Ag(I)).[310, 311] Notably, Birada *et al.* successfully photoreacted a series of unsymmetric olefins *via* Ag···Ag directing forces.[305] The approach yielded cyclobutane products that feature pyridines paired with amides, carboxylic acids, or esters. Encouraged by these results, we believe there remain immense opportunities to further diversify [2+2] photodimerizations and realize the potential materials science applications of these products. To achieve this goal we investigated cyano-substituted olefins.

The introduction of a new functional group into a template-directed solid-state reaction requires a comprehensive understanding of the solid-state behavior of the moiety so as to provide a reasonable prediction of the impact the functionality will have on the self-assembly process. With respect to crystal engineering studies, investigations on the cyano group have focused on their participation in weak intermolecular interactions such as C≡N···X (X = H, Cl, Br) or dipolar interactions between cyano groups.[18, 19, 312-314] Recently, Jones *et al.* investigated the impact cocrystallization has on solid-state luminesce.[315] The study utilized the chromophore 1,4-bis-*p*-cyanostyrylbenzene and explored the ability of the cyano groups to participate in supramolecular synthons based on halogen- or hydrogen bonds. The results demonstrated the ability to modify the solid-state optical properties of a chromophore *via* non-covalent means and revealed the active role cyano groups play in the intermolecular interactions between cocrystal components. With respect to our resorcinol-based template approach, Zaworotko *et al*. provide the most applicable study on the supramolecular synthon behavior of cyano groups.[316] The study aimed to establish a hierarchy of supramolecular synthons based on the intermolecular interactions within a series of cocrystals. The cocrystal components were composed of molecules that contain an alcohol, pyridine, or cyano group. In total, 17 cocrystals were fully characterized and structural analysis revealed all the cocrystals were sustained by a O-H(alcohol)···N(pyridine) heterosynthon. The persistence of the O-H(alcohol)···N(pyridine) heterosynthon in the presence of the cyano functionality suggests olefinic precursors that comprise pyridine and cyano substituents are amenable to topochemical alignment by resorcinol templates *via* phenol···pyridine hydrogen bonds.

Extending these same expectations to the library of silver salts is tempered by the ability of cyano groups to form coordination bonds with metals.[317] A notable example of cyano coordination bonds by Robson *et al.* demonstrated the ability to construct a three-dimensional (3D) coordination polymer with a diamondoid topology sustained by Cu···N≡C coordination bonds (Fig. 55).[53] Furthermore, Ag(I)···N≡C coordination bonds

have yielded intriguing supramolecular solids such as ethylenediaminetetrapropionitrile silver complexes which are capable of performing anion exchange.[317]

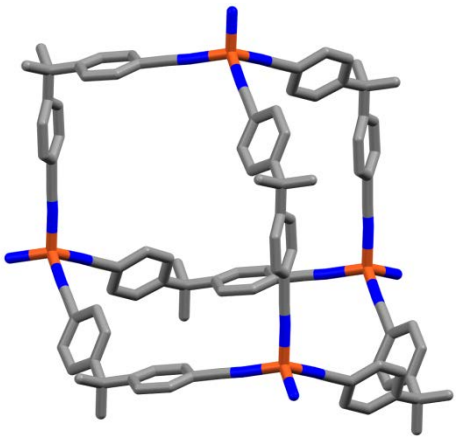

Figure 55 X-ray crystal structure of a diamondoid structure based on CuI[4,4′,4″,4‴-tetracyanotetraphenylmethane]BF_4 (solvent and counterions omitted for clarity). Reprinted with permission of John Wiley and Sons, copyright 2011.

Although the assembly of cyano-substituted molecules may be challenging, the functional group possesses physical properties that are transferable to materials science applications. For example, Park *et al.* recently reported fluorescence switching in acrylonitrile derivatives.[318] The fluorescence modulation was attributed to a reversible [2+2] cycloaddition reaction involving the acrylonitrile moiety. When the cyclobutane product is synthesized residual unreacted molecules are forced into a conformation that 'turns on' fluorescence emission. The shear induced fluorescence could be 'turned-off' by thermally annealing the powder at a temperature that causes thermal dissociation of the cyclobutane ring to regenerate the starting olefin. The ability of cyano-substituted olefins to undergo reversible [2+2] photodimerizations has potential applications in optical memory devices. Although reversible [2+2] photodimerizations have been reported the use of a template-driven approach has yet to be investigated.[318, 319] As

previously noted, the use of a supramolecular approach to align cyano-substituted chromophores may enable tuning of the optical properties through template switching and by directing the cycloaddition reaction towards the desired state (*e.g.* cyclobutane ring).

Herein, we report the topochemical alignment of a series of unsymmetrical cyano-substituted olefins *via* resorcinol- and silver-based templates (Fig. 56).

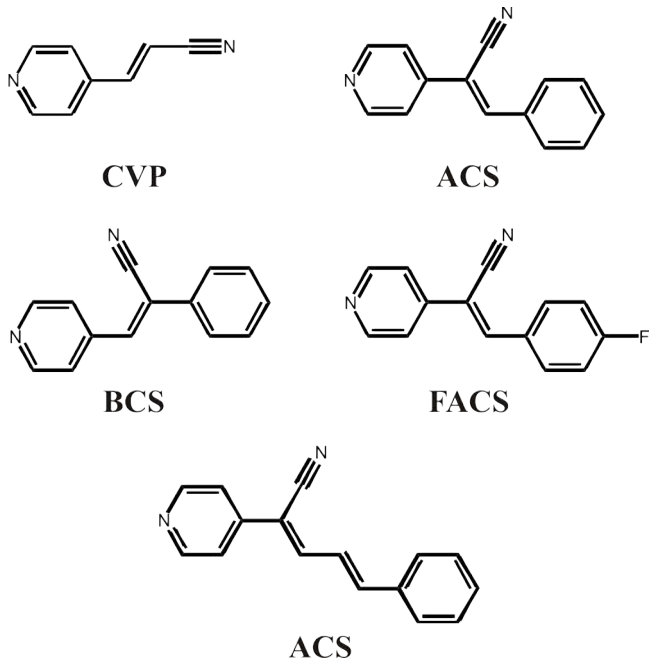

Figure 56 Chemical structures of cyano-substituted olefins employed in our study.

In particular, the results demonstrated that resorcinol self-assembles with *trans*-4-pyridineacrylonitrile (**CVP**) to form a cocrystal wherein the olefins are aligned to undergo a [2+2] photodimerization. Surprisingly, the cocrystals synthesized to date are photostable after exposure to UV light. Therefore, we turned to our library of silver salts based on non-chelating polyatomic oxoanions. Crystallization of **CVP** with Ag(I) ions resulted in stereospecific and quantitative yields upon UV irradiation. The utility of

Ag(I) ions to assembly acrylonitrile derivatives for cycloaddition reactions was further studied in a series of stilbenes and a cyano-substituted diene. The results represent the first evidence of reliably aligning, and reacting, cyano-substituted olefins with a template approach so that the physical properties of such materials may be exploited.

4.2. Materials and methods

4.2.1. Materials

4-Pyridinecarboxaldehyde (97%), 4-Pyridylacetonitrile monohydrate (98%), benzylcyanide (98%), 4-fluorobenzaldehyde (98%), *trans*-cinnamaldehyde (99%), silver(I) chlorate (≥99.9%), silver(I) perchlorate hydrate (99%), silver(I) trifluoromethanesulfonate (≥99%), silver(I) pentafluoropropionate (98%), silver(I) heptafluorobutyrate (97%), palladium(II) acetate (98%), dichloromethane (≥99.8%), and methanol (ACS Reagent, ≥99.8%) were purchased from Sigma-Aldrich. tetrabutylammonium chloride (95%) was purchased from Acros Organics. Silver(I) nitrate (≥99.7%), acetonitrile (99.9%), N,N-dimethylformamide (≥99.8%), magnesium sulfate (powder certified), sodium carbonate (99.7%), sodium methoxide (powder laboratory), Celite 545®, ethyl acetate (≥99.5%), and hexanes (≥98.5%) were purchased from Fisher Scientific. Ethanol (100%) was purchased from Decon Labs. Zinc oxide nanopowder (Zinc content ≥99%, crystal size ≤ 10 nm) was purchased from Strem Chemicals. 4-Iodopyridine was previously prepared based on a literature procedure.[320] Templates used in cocrystallization studies were made available from commercial sources or synthesized using standard literature procedures. All purchased chemicals were used as received.

4.2.2. Synthesis of *trans*-4-pyridineacrylonitrile

CVP was synthesized based on a literature procedure. Briefly, a round-bottom flask was charged with 4-iodopyridine (0.84 g, 4.1 mmol), acrylonitrile (0.9 mL, 14

mmol), palladium(II) acetate (18.0 mg, 0.08 mmol), tetrabutylammonium chloride (1.03 g, 3.7 mmol), sodium bicarbonate (1.2 g, 14.3 mmol), and N,N-dimethylformamide (10 mL). The mixture was heated to 110^{o}C with stirring for 14 hours. The resulting mixture was left to cool to room temperature then the solvent was removed using a rotary evaporator. Dichloromethane (30 mL) was added then filtered to remove solid impurities. The organic layer was washed with water (3x10 mL), dried over anhydrous magnesium sulfate, and evaporated with a rotary evaporator to obtain a dark oil. The oil was subsequently refluxed in hexanes (2x20 mL) ,which was decanted from the oil. The resulting hexanes solution was allowed to cool to room temperature and allow the precipitation of white needles. The solid was dissolved in boiling hexanes, decanted from an oil impurity, and allowed to cool to room temperature to precipitate white needles. ^{1}H NMR data for **CVP**: (DMSO-d_6, 300 MHz) δ 8.65-8.67 (2H's, dd, pyridine), δ 7.71-7.65 (1H, d, ethylene), δ 7.60-7.58 (2H's, dd, pyridine), δ 6.79-6.73 (1H, d, ethylene). ^{1}H NMR spectroscopy confirmed the isolated solid matched the previously reported spectrum for **CVP**. Yield: 0.181 g (34%).

4.2.3. Synthesis of (*Z*)-α-(4-Pyridyl)-(β-phenylacrylonitrile)

ACS was synthesized based on a modified literature procedure. Briefly, 4-pyridylacetonitrile hydrochloride (0.72 g, 4.7 mmol) was combined with a saturated sodium carbonate solution until the acid was neutralized. The product was subsequently extracted with dichloromethane (3x5 mL). The dichloromethane fractions were combined, dried with anhydrous magnesium sulfate, filtered, and evaporated to dryness using a rotary evaporator. The resulting solid was immediately combined with benzaldehyde (0.50 g, 4.7 mmol) and nanocrystalline zinc oxide (84.0 mg, 1.0 mmol). The reaction vessel was placed in an ultrasonic cleaning bath (Branson 2510R-DTM; frequency: 42kHz ± 6% at 100W) and exposed to ultrasonic irradiation for 80 min at

ambient conditions. After 80 min, hexanes (2 mL) was added to the reaction mixture and the solid was thoroughly mixed by hand before an additional 20 minutes of sonication. Ethanol (25 mL) was added to the reaction mixture followed by filtration through Celite to remove solid impurities. A solid was precipitated *via* addition of water (25 mL) and subsequently redissolved by boiling the ethanol water mixture. Cooling to ambient conditions resulted in precipitation of colorless crystals. ^{1}H NMR data for **ACS**: (DMSO-d_6, 300 MHz) δ 8.70-8.68 (2H's, dd, pyridine), δ 8.34 (1H, s, ethylene), δ 8.01-7.98 (2H's, dd, pyridine), δ 7.76-7.74 (2H's, dd, phenyl), δ 7.60-7.55 (3H's, m, phenyl). Yield: 613 mg (64%).

4.2.4. Synthesis of (*Z*)-α-Phenyl-β-(4-pyridyl)acrylonitrile

BCS was synthesized according to the following procedure. A round bottom flask was charged with 4-pyridinecarboxaldehyde (0.5 g, 4.7 mmol), benzylcyanide (0.57 g, 4.9 mmol), sodium methoxide (0.10 g, 1.9 mmol), and methanol (15 mL) then heated to reflux for 24 hours. The solvent was evaporated with a rotary evaporator to yield an oil. The oil was combined with boiling hexanes (50 mL) that upon cooling to ambient conditions precipitated a colorless solid. The solid was recrystallized using an ethanol water solution to yield colorless crystals. ^{1}H NMR data for **BCS**: (DMSO-d_6, 300 MHz) δ 8.77-8.75 (2H's, m, pyridine), δ 8.11 (1H, s, ethylene), δ 7.83-7.80 (4H's, m, pyridine, phenyl), δ 7.58-7.49 (3H's, m, phenyl). ^{1}H NMR spectroscopy confirmed the isolated solid matched the previously reported spectrum for **BCS**. Yield: 75 mg (8%).

4.2.5. Synthesis of (*Z*)-α-(4-Pyridyl)-β-(4-fluorophenyl)acrylonitrile)

FACS was synthesized according to the following procedure. The compound 4-pyridylacetonitrile hydrochloride (0.36g, 2.4 mmol) was combined with a saturated sodium carbonate solution until the acid was neutralized. The product was subsequently extracted with dichloromethane (3x5 mL). The dichloromethane fractions were

combined, dried with anhydrous magnesium sulfate, filtered, and evaporated to dryness using a rotary evaporator. The resulting solid was immediately combined with 4-fluorobenzaldehyde (0.29 g, 2.4 mmol) and nanocrystalline zinc oxide (84.0 mg, 1.0 mmol). The reaction vessel was placed in an ultrasonic cleaning bath (Branson 2510R-DTM; frequency: 42kHz ± 6% at 100W) and exposed to ultrasonic irradiation for 80 min at ambient conditions. After 80 min, hexanes (2 mL) was added to the reaction mixture and the solid was thoroughly mixed by hand and sonicated an additional 20 minutes. Ethanol (25 mL) was added to the reaction mixture followed by filtration through Celite to remove solid impurities. A solid was precipitated *via* addition of water (25 mL) and subsequently redissolved by boiling the ethanol water mixture. Cooling to ambient conditions resulted in precipitation of colorless crystals. ^{1}H NMR data for **FACS**: (DMSO-d_6, 300 MHz) δ 8.72-8.70 (2H's, dd, pyridine), δ 8.35 (1H, d, ethylene), δ 8.10-8.05 (2H's, dd, phenyl), δ 7.75-7.73 (2H's, dd, pyridine), δ 7.49-7.42 (2H's, dd, phenyl). Yield: 230 mg (44%).

4.2.6. Synthesis of (*Z,E*)-α-(3-Phenyl-2-propen-1-ylidene)-4-pyridineacetonitrile

ACD was synthesized based on a modified literature procedure. Briefly, 4-pyridylacetonitrile hydrochloride (0.50 g, 3.3 mmol) was combined with a saturated sodium carbonate solution until the acid was neutralized. The product was subsequently extracted with dichloromethane (3x5 mL). The dichloromethane fractions were combined, dried with anhydrous magnesium sulfate, filtered, and evaporated to dryness using a rotary evaporator. The resulting solid was immediately combined with *trans*-cinnamaldehyde (0.43 g, 3.3 mmol) and nanocrystalline zinc oxide (84.0 mg, 1.0 mmol). The reaction vessel was placed in an ultrasonic cleaning bath (Branson 2510R-DTM; frequency: 42kHz ± 6% at 100W) and exposed to ultrasonic irradiation for 80 min at ambient conditions. After 80 min, hexanes (2 mL) was added to the reaction mixture and

the solid was thoroughly mixed by hand before an additional 20 minutes of sonication. Ethanol (25 mL) was added to the reaction mixture followed by filtration through Celite to remove solid impurities. A solid was precipitated *via* addition of water (25 mL) and subsequently redissolved by boiling the ethanol water mixture. Cooling to ambient conditions resulted in precipitation of yellow crystals. ^{1}H NMR data for **ACD**: (DMSO-d_6, 300 MHz) δ 8.70-8.65 (2H's, dd, pyridine), δ 8.24-8.20 (1H, d, ethylene), δ 7.69-7.66 (2H's, dd, phenyl), δ 7.65-7.63 (2H's, dd, pyridine), δ 7.47-7.42 (4H's, m, ethylene, phenyl), δ 7.39-7.28 (1H's, dd, ethylene). Yield: 462 mg (64%).

4.2.7. Single crystal preparation

Single crystals of composition (**CVP**)·(4,6-dichlororesorcinol) (**CVP1**), (**CVP**)·(4,6-diiodoresorcinol) (**CVP2**), (**CVP**)·(4,6-di-tert-butylresorcinol) (**CVP3**), 2(**CVP**)· (4,6-dibromoresorcinol) (**CVP4**), 2(**CVP**)·(4-hexylresorcinol) (**CVP5**), and 2(**CVP**)·(4-dodecylresorcinol) (**CVP6**) were grown by slow-solvent evaporation. Single crystals were grown from a solution containing a 1:1molar ratio of cocrystal components except in the case of **CVP4** which employed a 2:1 ratio of **CVP** to 4,6-ditertbutylresorcinol. Single crystals of **CVP1**-**CVP4** were prepared by dissolving the solid mixtures in a 1:1 water acetonitrile mixture while **CVP5** and **CVP6** employed a 9:1 (v/v) hexanes ethanol solvent mixture to dissolve the corresponding solid mixtures. The solutions were left to slowly evaporate at ambient conditions until suitable single crystals were observed.

Single crystals of composition [Ag(**CVP**)$_2$(CH_3CN)][NO_3] (**CVP7**), [Ag_3(**CVP**)$_5$][ClO_4]$_3$ (**CVP8**), [Ag_2(**CVP**)$_4$][$C_4F_7O_2$]$_2$ (**CVP9**), [Ag_2(**ACS**)$_4$][ClO_3]$_2$ (**ACS1**), [Ag_2(**ACS**)$_4$][ClO_4]$_2$ (**ACS2**), [Ag(**ACS**)$_2$][$C_3F_5O_2$] (**ACS3**), [Ag(**ACS**)$_2$][$C_4F_7O_2$] (**ACS4**), [Ag(**BCS**)$_2$][NO_3] (**BCS1**), [Ag(**BCS**)$_2$][ClO_4] (**BCS2**), [Ag_2(**FACS**)$_4$][ClO_3] (**FACS1**), [Ag(**ACD**)$_2$][ClO_3] (**ACD1**), [Ag(**ACD**)$_2$][ClO_4] (**ACD2**), [Ag(**ACD**)$_2$][CF_3SO_3] (**ACD3**), and [Ag(**ACD**)$_2$][$C_3F_5O_2$] (**ACD4**) were grown

by slow-solvent evaporation of an acetonitrile solution containing a 2:1 molar ratio of organic ligand to silver salt. Upon dissolution, the vial was allowed to equilibrate to ambient conditions and solvent was slowly evaporated until suitable single crystals were observed.

Single crystals of compositions $[Ag(\mathbf{dCbPCB})(H_2O)NO_3]_\infty$ (**dCbPCB1**, where **dCbPCB** = *rctt*-1,2-dicyano-3,4-bis(4-pyridyl)cyclobutane) *via* recrystallization of the solid obtained after UV-irradiation of **CVP7**. The solid was dissolved in a 1:1 (v/v) water ethanol solvent mixture, filtered through a cotton plug, and allowed to equilibrate to ambient conditions before slow-solvent evaporation. The solvent was slowly evaporated until single crystals were observed.

4.2.8. Single crystal X-ray diffraction measurements

Crystal data was collected on a Nonius Kappa CCD single-crystal X-ray diffractometer using graphite-monochromated MoK_α radiation (λ = 0.71073 Å) at ambient conditions for all structures except **ACD1-ACD4** and **dCbPCB1** which were collected at liquid nitrogen temperatures. Structure solution and refinement was accomplished using SHELXL-97.[173] All non-hydrogen atoms were refined anisotropically. Hydrogen atoms associated with carbon atoms were refined in geometrically constrained riding positions. The resorcinol hydrogen atoms were calculated in an optimal hydrogen bonding geometry.

4.2.9. NMR spectrocopy

In all cases the ^1H NMR spectra were collected in DMSO-d_6 solutions on a Bruker DPX 300 NMR spectrometer.

4.2.10. Photoreactivity studies

In a typical photoreaction experiment solid was gently ground between two Pyrex glass plates. The plates were placed in a photoreactor cabinet equipped with a broad

band 450 W medium-pressure Hg-lamp. The plates were flipped after 10 hours of irradiation and after every 20 hours the solid between the plates was thoroughly mixed.

4.3. Results and discussion

4.3.1. Cocrystallization and photoreactivity of **CVP** with resorcinol templates

A total of six cocrystals composed of **CVP** and resorcinol templates were obtained. Three cocrystals contained a 2:1 ratio of **CVP** to the resorcinol template. The cocrystals comprise three-component assemblies that orient **CVP** molecules to enable the formation of weak dimers *via* C-H···N interactions between **CVP** molecules. The remaining three cocrystals were based on a 1:1 ratio of the cocrystal components and formed discrete four-component assemblies. Within the assemblies **CVP** molecules were arranged in a head-to-tail fashion.

Specifically, solid **CVP1** crystallizes in the monoclinic space group $P2_1/c$ with an asymmetric unit that contains a molecule of **CVP** and a 4,6-dichlororesorcinol (**4,6-dicl-res**) molecule. The resorcinol-based template organizes the **CVP** molecules into discrete four-component assemblies. The **CVP** molecules are arranged in a head-to-tail fashion within the assembly sustained by two O-H(phenol)···N(pyridyl) (O···N: 2.743(3) Å) and two O-H(phenol)···N(cyano) (O···N: 2.834(3) Å) hydrogen bonds (Fig. 57).

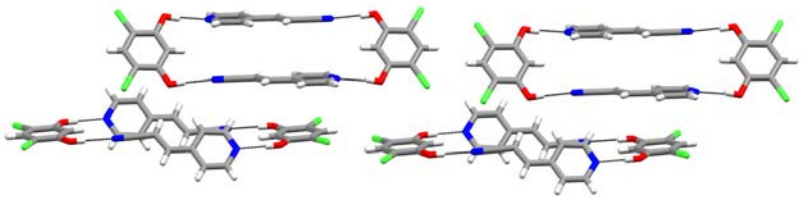

Figure 57 Perspective view of the X-ray crystal structure **CVP1** wherein the four-component assemblies form a series of 1D chains that pack in an offset manner.

The olefins are stacked parallel but the distance between the calculated centroids of the assembled olefins (4.51 Å) lies outside the distance stated in the topochemical postulate. Neighboring assemblies interact *via* weak C-H···Cl interactions to form a 1D chain of assemblies. The chains pack in an offset, edge-to-face, arrangement that enables π···π interactions between **4,6-dicl-res** molecules and a pyridyl group of **CVP** molecules from neighboring assemblies.

Akin to **CVP1**, solid **CVP2** crystallizes in the triclinic space group $P\bar{1}$ with an asymmetric unit that contains a **CVP** molecule that is unequally disordered over two positions and a 4,6-diiodoresorcinol (**4,6-dii-res**) molecule. The **4,6-dii-res** arranges the **CVP** molecules into discrete four-component assemblies with the **CVP** molecules arranged in a head-to-tail fashion. The four-component assembly is held together by O-H(phenol)···N(pyridyl) (O···N: 2.690(3) Å) and O-H(phenol)···N(cyano) (O···N: 2.906(2) Å) hydrogen bonds. An olefin within each assembly is disordered which results in both parallel and anti-parallel alignment of the olefins. The distance between the calculated centroids of the assembled olefins (5.03 Å) lies outside the distance requirement stated by the topochemical postulate. The four-component assemblies propagate into a supramolecular ladder along the *b*-axis sustained by I···O (3.29 Å) interactions between **4,6-dii-res** molecules and weak π···π interactions between **CVP** molecules (Fig. 58). The supramolecular ladder aligns **CVP** molecules of neighboring assemblies in either a parallel or an anti-parallel arrangement based on the disorder of the **CVP** molecules. The olefins of neighboring assemblies (4.28 Å) also lie outside the distance requirements for a cycloaddition reaction. The supramolecular ladders pack *via* weak I···I interactions into a 2D sheet that alternates **CVP** and **4,6-dii-res** molecules. The sheets stack in an offset manner sustained by weak C-H···O between **CVP** and **4,6-dii-res** molecules.

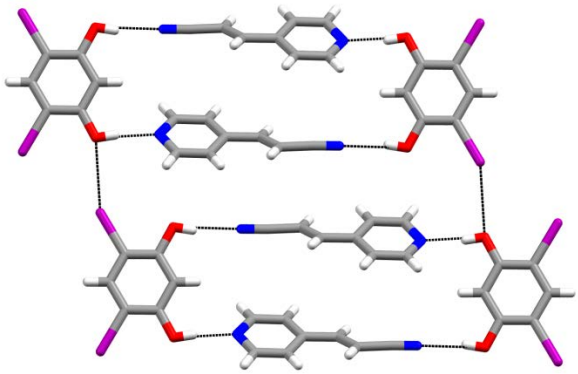

Figure 58 Perspective of the X-ray crystal structure **CVP2** wherein the four-component assemblies extend into a supramolecular ladder along the b-axis.

The third example of a 1:1 ratio of cocrystal components is **CVP3**. The structure crystallizes in the triclinic space group $P\bar{1}$ with an asymmetric unit that consists of a **CVP** molecule unequally disordered over two positions and a 4,6-di-tert-butylresorcinol (**4,6-ditert-res**) molecule. As was the case in **CVP1-2**, the **4,6-ditert-res** template organizes **CVP** molecules into discrete four-component assemblies with **CVP** molecules arranged in a head-to-tail fashion. The four-component assembly is held together by O-H(phenol)···N(pyridyl) (O···N: 2.798(1) Å) and O-H(phenol)···N(cyano) (O···N: 2.989(1) Å) hydrogen bonds. The disordered olefins within the assembly result in both parallel and anti-parallel alignment of the olefins. The distance between the calculated centroid for each olefin (4.94 Å) lies outside the distance requirement for a [2+2] photodimerization (Fig. 59). Neighboring assemblies stack in an edge-to-face arrangement to enable by C-H···N and C-H···π interactions. The packing of assemblies extends into a 1D column of along the *b*-axis. Adjoining 1D columns are arranged to enable hydrophobic packing of the tert-butyl groups of **4,6-ditert-res** molecules. The column packing results in alternating columns of **CVP** and **4,6-ditert-res** molecules.

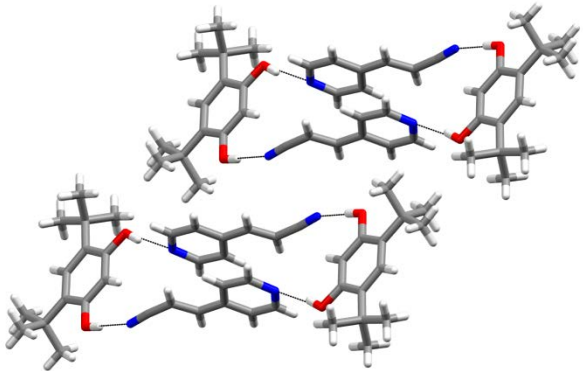

Figure 59 X-ray crystal structure **CVP3** viewed along the *c*-axis to reveal the packing of neighboring assemblies.

In surprising contrast to the other 4,6-substituted resorcinols, 4,6-dibromoresorcinol (**4,6-dibr-res**) does not organize **CVP** into four-component assembly. Alternatively, **CVP4** crystallizes in the triclinic space group $P\bar{1}$ with an asymmetric unit that contains a molecule of **CVP**, a **CVP** molecule that is unequally disordered over two positions, and a **4,6-dibr-res** molecule. The **4,6-dibr-res** molecules exclusively participate in O-H(phenol)···N(pyridyl) hydrogen bonds that organizes the **CVP** molecules into three-component assemblies. Specifically, the **CVP** molecules are arranged in a head-to-head fashion within the assembly sustained by O-H(phenol)···N(pyridyl) (O···N: 2.713(5) Å, 2.774(4) Å) hydrogen bonds. The olefins are stacked parallel and the distance between the calculated centroids of the assembled olefins (3.84 Å) meets the distance requirement for a photodimerization. Neighboring assemblies arrange **CVP** molecules to form **CVP** dimers sustained by weak C-H···N interactions between the cyano and olefin functionalities (Fig. 60a). The packing of assemblies extends into a 1D column along the *b*-axis sustained by Br···O (3.34 Å) interactions between **4,6-dibr-res** molecules and weak π···π interactions between **CVP** molecules (Fig. 60b). Adjacent 1D columns pack to enable weak C-H···π and π···π

interactions between the columns to form alternating columns of **4,6-dibr-res** molecules and **CVP** dimers.

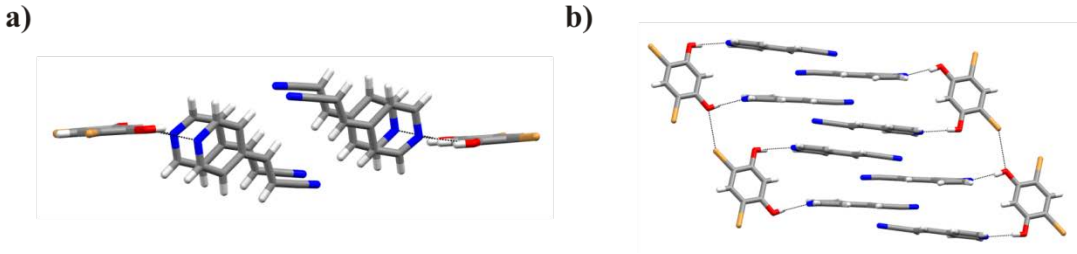

Figure 60 X-ray structure of **CVP4** (a) along the *b*-axis to reveal the packing of neighboring assemblies sustained by **CVP** dimers. (b) **CVP4** viewed along the *c*-axis to reveal the assembly of 1D columns.

Unlike the previous resorcinol based templates, **CVP5** is the result of a cocrystallization between **CVP** and a mono-substituted resorcinol, 4-hexylresorcinol (**4-hex-res**). The structure crystallizes in the triclinic space group $P\bar{1}$ with an asymmetric unit that consists of two **CVP** molecules that are unequally disordered over two positions and a **4-hex-res** molecule. Similar to **CVP4**, the **4-hex-res** template organizes the **CVP** molecules into discrete three-component assemblies with **CVP** molecules arranged in a head-to-head fashion. The three-component assembly is sustained by O-H(phenol)···N(pyridyl) (O···N: 2.751(6) Å, 2.840(2) Å) hydrogen bonds. The disordered olefins within each assembly align in either parallel or criss-cross conformations. The distance between the calculated centroid for each olefin (4.05 Å) lies at a distance favorable a cycloaddition reaction. Adjacent assemblies orient **CVP** molecules to form dimers that participate in weak C-H···N interactions between the cyano and ethylene moieties (Fig. 61a). Neighboring assemblies are arranged in a manner to enable hydrophobic packing of the alkyl chains of **4-hex-res**. The interdigitated alkyl chains result in a 2D layer of alternating **CVP** and **4-hex-res** molecules (Fig. 61b). The

stacking of 2D layers forms weak O···C interactions between the phenol and cyano functionalities.

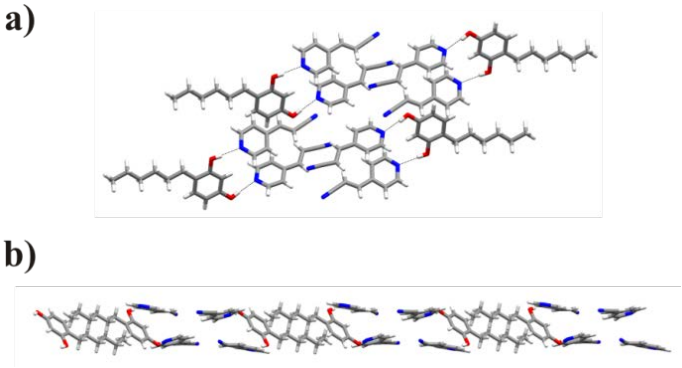

Figure 61 Solid **CVP5** wherein (a) neighboring three-component assemblies participate in weak C-H···N interactions between **CVP** molecules and (b) a perspective view of the interdigitated alkyl chains that results in 2D sheets.

The sixth cocrystal with **CVP**, solid **CVP6** crystallizes in the triclinic space group $P\bar{1}$ with an asymmetric unit that consists of two **CVP** molecules and a 4-dodecylresorcinol (**4-dod-res**) molecule. Akin to **CVP4-5**, **4-dod-res** aligns the **CVP** molecules in a head-to-head fashion within a three-component assembly. **CVP6** is the third cocrystal that exclusively participates in O-H(phenol)···N(pyridyl) (O···N: 2.796(2) Å, 2.798(2) Å) hydrogen bonds. The olefins within the assembly are in a parallel conformation and at a distance (olefin centroid-centroid distance 3.88 Å) suitable for a [2+2] photodimerization. The **CVP** molecules within the assemblies pack in manner that enables **CVP** molecules to form dimers sustained by weak C-H···N interactions between the cyano and ethylene functionalities. The alkyl chains of **4-dod-res** molecules pack in an interdigitated manner, akin to **CVP5**, which results in a 2D layer of alternating **4-dod-res** and **CVP** molecules (Fig. 62). The layers of **CVP6** overlap to enable hydrophobic

packing of the alkyl chains of **4-dod-res** and weak π···π interactions between **CVP** molecules.

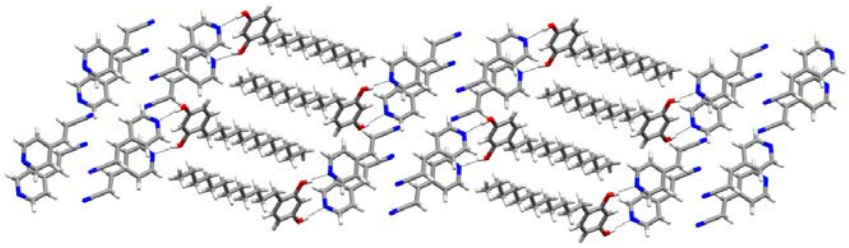

Figure 62 Solid **CVP6** viewed along the *a*-axis which reveals a 2D sheet of alternating **CVP** molecules and **4-dod-res** molecules that possess interdigitated alkyl chains.

Structural analyses of solids **CVP1-6** revealed the persistence of three- and four-component cocrystals. In the case of four-component cocrystals, the cyano groups participate in a surprising phenol···cyano heterosynthon but align olefins at distances > 4.2 Å (Table 3).

Table 3 Interatomic distances and synthon behavior involving **CVP** and resorcinol-based templates

Cocrystal	Ratio of **CVP**:res	O···N distance (Å)	C=C distances within assemblies (Å)	O-H···N≡C heterosynthon
CVP1	1:1	2.743(3), 2.834(3)	4.51	✓
CVP2	1:1	2.690(3), 2.906(2)	5.03	✓
CVP3	1:1	2.798(1), 2.989(1)	4.93	✓
CVP4	2:1	2.713(5), 2.774(4)	3.84	X
CVP5	2:1	2.751(6), 2.840(2)	4.05	X
CVP6	2:1	2.796(2), 2.798(2)	3.88	X

Alternatively, **CVP4-6** assemble to form three-component assemblies that topochemically align **CVP** molecules. Based on this analysis, **CVP4-6** are the cocrystals expected to undergo a cycloaddition reaction.

To test whether the olefins of **CVP1-6** are photoreactive, powdered samples were exposed to UV irradiation. Analysis *via* ^{1}H NMR spectroscopy reveals the olefins, even in solids **CVP4-6**, are photostable. Examples of crystals that satisfy the topochemical criterion, yet, are photostable have been reported. Previously, the photostability of compounds such as 4-hydroxy-3-nitrocinnamate has been ascribed to extensive hydrogen bonding within the layered structure. Similar to 4-hydroxy-3-nitrocinnamate, **CVP4-6** consists of **CVP** molecules that participate in C-H···N interactions within the sheets of the layered structures. The lack of photoreactivity in **CVP4-6** may be attributed to the energy cost of breaking these extended networks.

4.3.2. Crystallization and photoreactivity of **CVP** with silver templates

To achieve solids wherein **CVP** molecules undergo a [2+2] photodimerization we turned to our library of silver salts. A total of three structures involving **CVP** and Ag(I) ions were obtained. Specifically, **CVP** and $AgNO_3$ crystallize in the orthorhombic space group $Pna2_1$ with an asymmetric unit that consists of two **CVP** molecules, a $AgNO_3$, and a molecule of the crystallization solvent acetonitrile. The Ag(I) ions of solid **CVP7** coordinate two pyridine groups and two cyano groups from **CVP** molecules in a tetrahedral geometry. The tetrahedral centers are directly stacked to form a 1D column of Ag(I) ions along the *c*–axis wherein the column is sustained by Ag···Ag forces (Ag···Ag distance 3.68 Å) (Fig. 63a). The NO_3^- anions lie in close proximity to the Ag(I) ions yet are non-coordinating and, along with acetonitrile molecules, fill the void space *via* C-H···X (X=O, N) interactions (Fig. 63b). The assembly of Ag(I) ions results in infinite stacks of **CVP** molecules that are arranged in a face-to-face conformation wherein the olefins lie parallel and at distances (olefin centroid-to-centroid distances 3.60 Å, 3.77 Å) suitable for a [2+2] photodimerization. The tetrahedral centers extend three-dimensionally to from a four-fold interpenetrated diamondoid network (Fig. 63c). The

even number of interpenetrating nets provides an environment wherein [2+2] photodimerizations can occur between diamondoid networks without residual unreacted networks (Fig. 63d).

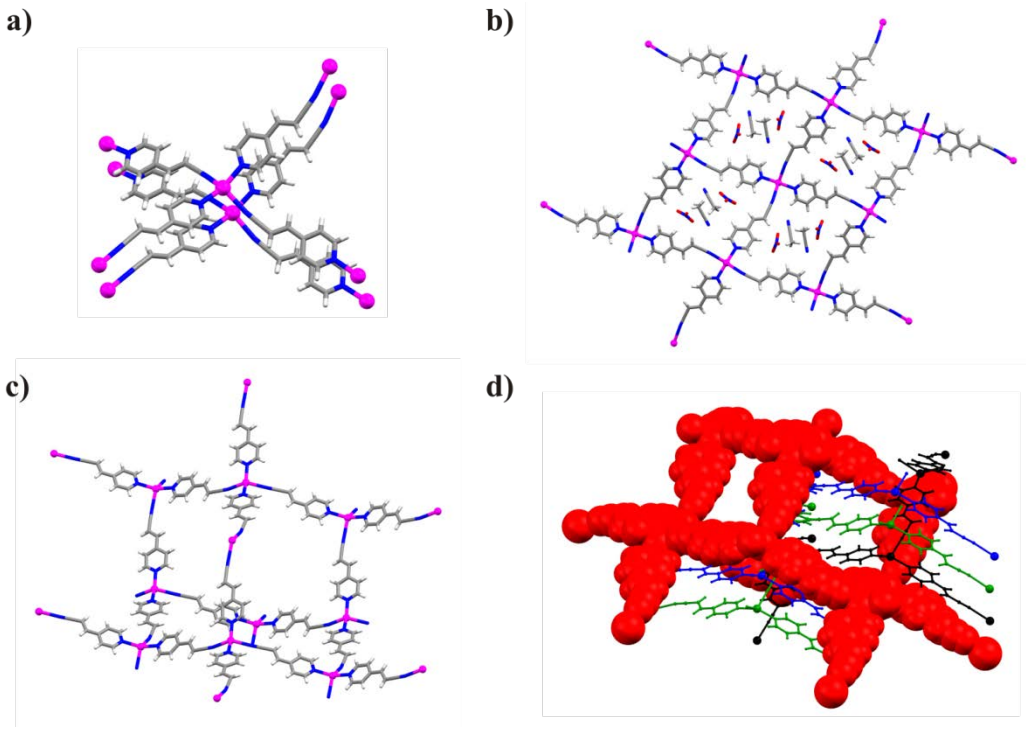

Figure 63 X-ray structure of **CVP7**: (a) stacking of tetrahedral Ag(I) ions which arranges **CVP** molecules at a favorable distance and orientation for [2+2] photodimerization, (b) view along the *c*–axis to reveal the space filling role of NO_3^- and acetonitrile, (c) a single diamondoid network, and (c) a perspective view of the four-fold interpenetrated diamondoid networks.

CVP and $AgClO_4$ crystallize as **CVP8** in the monoclinic space group $P2_1/c$ with an asymmetric unit that consists of five **CVP** molecules and three $AgClO_4$. The Ag(I) ions and **CVP** molecules self-assemble to form a dinuclear complex sustained by Ag···Ag forces (Ag···Ag distance 3.39 Å). The primary coordination sphere of the Ag(I) ions within the complex are based on a linear geometry that involves two transoid nitrogen atoms from the pyridyl groups of **CVP** molecules. In addition, the ClO_4^- anions of the

complex weakly coordinate the Ag(I) ions *via* Ag···O interactions. The olefins within the complex are approximately parallel and lie at distances (3.78 Å, 4.02 Å), which meet the distance requirement stated in the topochemical postulate. To arrange the dinuclear complexes, an additional 'sacrificial' complex between Ag(I) and **CVP** is formed which involves a Ag(I) ion coordinating two transoid **CVP** molecules *via* pyridyl nitrogen atoms. The Ag(I) ion of the sacrificial complex participates in four Ag···N≡C interactions with the cyano groups of two neighboring dinuclear complexes to form a pseudo octahedral geometry. In addition, the **CVP** molecules of the sacrificial complex oriented in the axial position align two additional dinuclear complexes *via* bifurcated Ag···N≡C interactions (Fig. 64). In total, the sacrificial complex produces complex 2D layers that stack *via* weak C-H···X (X= N, O) interactions.

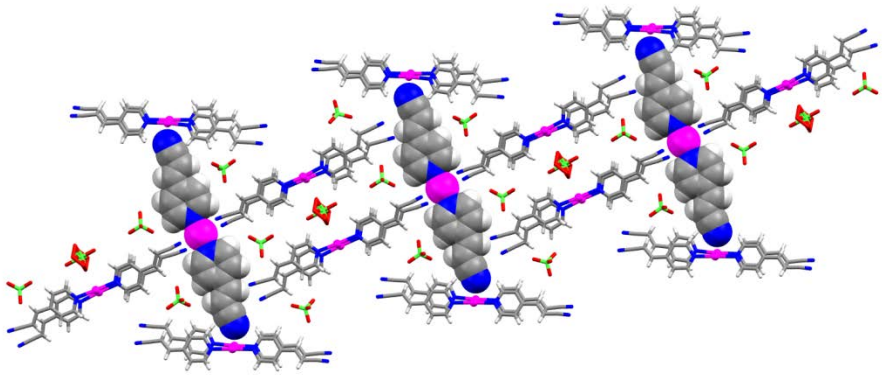

Figure 64 Perspective of the X-ray structure **CVP8** which forms a 2D layer of dinuclear complexes aligned *via* sacrificial mononuclear Ag(I) complexes.

Crystallization of **CVP** and $AgC_4F_7O_2$ results in solid **CVP9**. The structure crystallizes in the monoclinic space group $P2_1$ with an asymmetric unit composed of four **CVP** molecules that are unequally disordered over two positions and two $AgC_4F_7O_2$. The Ag(I) ions and **CVP** molecules self-assemble to form a dinuclear complex sustained by Ag···Ag forces (Ag···Ag distance 3.30 Å). The primary coordination sphere of the

Ag(I) ions is based on a T-shaped geometry that involves two transoid N-atoms from pyridyl functionalities and an oxygen atom of the carboxylate anion coordinating each Ag(I) ion of the dinuclear complex (Fig. 65a). The second $C_4F_7O_2^-$ anion lies in close proximity to Ag(I) cations yet participate in only C-H···O interactions. The olefins within the complex are arranged in either parallel or criss-cross conformations depending on the disorder of the **CVP** molecules but the separation distance (olefin centroid-to-centroid distances 3.82 Å, 4.19 Å) between the olefins satisfies the criteria for a cycloaddition reaction in the solid-state. The dinuclear complexes self-assembles into a "zipper"-like structure sustained by bifurcated Ag···N≡C interactions between neighboring complexes (Fig. 65b). The zipper layers of **CVP9** are stacked in an offset manner that enables weak Ag···π interactions between the layers.

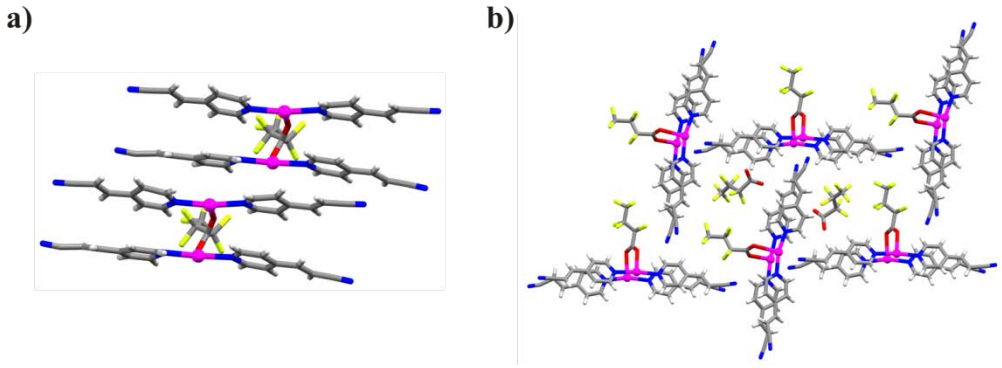

Figure 65 X-ray structure of **CVP9**: (a) stacking of dinuclear assemblies sustained by Ag···π interactions and (b) "zipper"-like structure that forms between neighboring complexes to yield 2D layers.

The photoreactivity of the three different assemblies involving **CVP** and Ag(I) ions were investigated. Based on structural analyses of **CVP7-9** the olefins within the assemblies conform to the criterion of the topochemical postulate thus a [2+2] photoreaction can be expected to occur upon exposure to UV irradiation. In the case of

CVP8, the sacrificial complexes that align neighboring assemblies will preclude a 100% yield. To monitor the extent of photoreactivity, we employed ^{1}H NMR spectroscopy. The photoreaction was characterized by the upfield shift of the H-atoms assigned to the pyridyl moiety and the concurrent loss of olefinic protons with the appearance of peaks at 4.63 and 4.70 ppm indicating cyclobutane formation. Notably, UV irradiation **CVP7-9** yielded a single cyclobutane photoproduct with the corresponding ^{1}H NMR spectrum: (DMSO-d_6, 300 MHz) δ 8.36-8.34 (4H's, d, pyridine), δ 7.11-7.09 (4H's, d, pyridine), δ 4.70-4.63 (4H's, m, cyclobutane). A summary of the interatomic distances as well as percent yields based on the ratio of the area of the pyridyl H-atoms before and after photoreaction are contained in Table 4.

Table 4 Interatomic distances and photoreaction yields for **CVP7-9**

Structure	Ag···Ag distance (Å)	C=C distances within assemblies (Å)	Percent yield
CVP7	3.68	3.60, 3.77	100%
CVP8	3.39	3.78, 4.02	84%
CVP9	3.30	3.82, 4.19	98%

To assign the stereochemistry of resulting product, the solid obtained after UV irradiation of **CVP7** was recrystallized (Fig. 66).

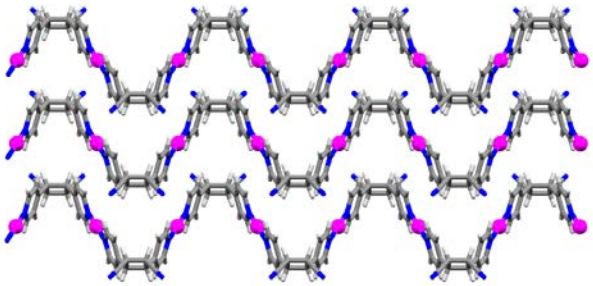

Figure 66 Perspective of the X-ray crystal structure **dCbPCB1** wherein neighboring 1D coordination polymers connect v*ia* Ag···N≡C interactions.

The resulting solid, **dCbPCB1** confirmed the photoproduct was indeed the head-to-head product *rctt*-1,2-dicyano-3,4-bis(4-pyridyl)cyclobutane. The phtotoproduct and Ag(I) ions assemble to form a 1D coordination polymer sustained by Ag···N bonds with the pyridyl moieties. The 1D polymers are connected *via* Ag···N≡C to stack in a stepwise manner.

4.3.3. Crystallization and photoreactivity of **ACS** with silver templates

Based on the success of using Ag(I) ions to align and react **CVP** molecules, we decided to again utilize silver salts for the alignment and photodimerization of **ACS** molecules. We wondered not only if Ag(I) ions could successfully template the photodimerization of **ACS** molecules but what intermolecular interactions the cyano group would participate in. Unlike **CVP**, the cyano group of **ACS** is located in a sterically confined environment, which may preclude intermolecular interaction such as silver coordination bonds. In our investigation a total of four complexes composed of **ACS** and Ag(I) ions were obtained.

ACS and $AgClO_3$ crystallize as solid **ACS1** in the triclinic space group $P\bar{1}$ with an asymmetric unit that consists of four **ACS** molecules and two $AgClO_3$. Structural analysis provides strong evidence the Ag(I) ions and **ACS** molecules self-assemble to form a dinuclear complex sustained by Ag···Ag forces (Ag···Ag distance 3.50 Å). The Ag(I) ions adopt a T-shaped geometry characterized by the coordination of two transoid **ACS** molecules *via* pyridyl moieties and a single oxygen atom from the ClO_3^- anions. The olefins within the complex are topochemically aligned at distances (olefin centroid-to-centroid distances 3.56 Å, 3.88 Å) that suitable for a cycloaddition reaction. In fact, the crystals are very light sensitive and highly reactive, which is reflected in the partial single-crystal-to-single-crystal (SCSC) reaction the crystals undergo during data

collection until reaching a composition that causes the crystals cracks (Fig. 67). The occupational parameters for the olefin and cyclobutane carbons are 0.75 and 0.25 respectively. Current efforts have not yielded a sufficient model despite the use of restraints and constraints and may require recollection of single crystal data in the dark. Neighboring complexes stack in an offset arrangement to enable Ag···π and π···π interactions between that extend into a 2D sheet. As a consequence of the π···π stacking, **ACS** molecules between the complexes participate are arranged in a head-to-tail fashion, which positions olefins at a distance (centroid-to-centroid distance 3.74 Å) suitable for a [2+2] photodimerization.

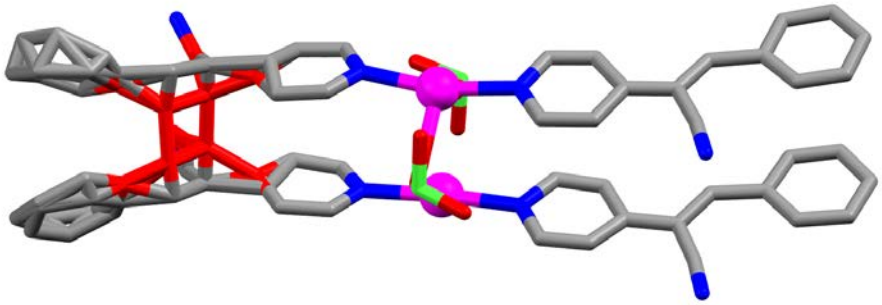

Figure 67 Perspective of the X-ray crystal structure **ACS1** that shows a dinuclear assembly wherein a set of olefins has partially reacted during data collection. The cyclobutane ring and atoms directly bonded to the ring are colored red.

ACS and $AgClO_4$ crystallize as solid **ACS2** in the triclinic space group $P\bar{1}$ with an asymmetric unit that consists of six **ACS** molecules and three $AgClO_4$. Structural analysis provides strong evidence the Ag(I) ions and **ACS** molecules self-assemble to form dinuclear complexes sustained by Ag···Ag forces (Ag···Ag distances 3.50 Å, 3.84 Å). A Ag(I) ion adopts a T-shaped geometry characterized by the coordination of two transoid **ACS** molecules *via* pyridyl moieties and the coordination of a single oxygen atom from the ClO_4^- anion. The other two Ag(I) ions adopts a linear geometry that

coordinates two transoid **ACS** molecules *via* pyridyl moieties. In this instance, the ClO_4^- anions lie in close proximity and participate in Ag···O interactions. The olefins within the complexes are topochemically aligned (olefin centroid-to-centroid distances 3.71 Å, 3.82 Å) and expected to undergo a [2+2] photodimerization. Akin to **ACS1**, two sets of olefins undergo a partial SCSC cycloaddition reaction during data collection until reaching a composition that causes the crystals to crack (Fig. 68). The occupational parameters for the olefin and cyclobutane carbons are 0.55 and 0.45 respectively for one set and 0.49 and 0.51 for the second set of olefin and cyclobutane carbons. Current efforts have not yielded a sufficient model despite the use of restraints and constraints and may require recollection of single crystal data in the dark. Similar to **ACS1**, neighboring complexes stack in an offset arrangement that enables Ag···π and π···π interactions. The formation of 2D sheets arranges the **ACS** molecules of neighboring complexes in a head-to-tail manner wherein the olefins are at a distance (centroid-to-centroid distance 4.04 Å) suitable for photodimerization.

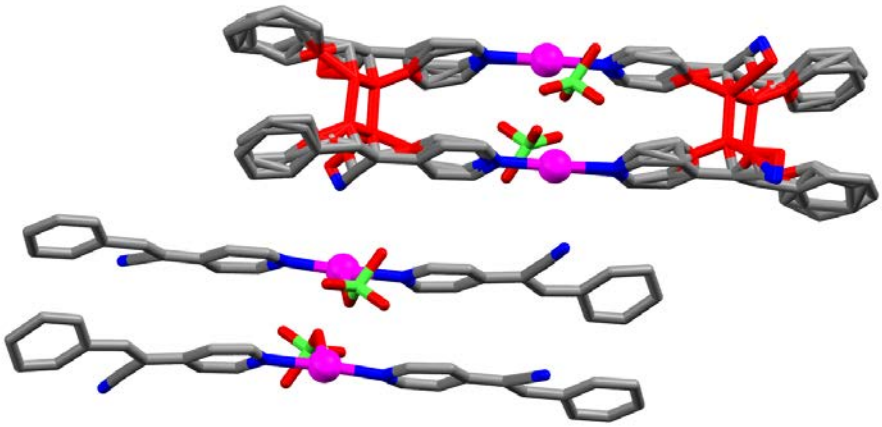

Figure 68 Perspective view of **ACS2** that reveals two distinct dinuclear assemblies that align olefins for a photodimerization. In one complex, the olefins partially react during data collection. The cyclobutane carbons and atoms directly bonded to the ring are colored red.

ACS and $AgC_3F_5O_2$ crystallize as solid **ACS3** in the triclinic space group $P\bar{1}$ with an asymmetric unit that consists of two **ACS** molecules and a $AgC_3F_5O_2$. The Ag(I) ions and **ACS** molecules self-assemble to form a dinuclear complex sustained by Ag···Ag forces (Ag···Ag distance 3.28 Å). Each Ag(I) ion is coordinated by two transoid **ACS** molecules in a linear geometry *via* pyridyl moieties. The olefins within the complex are arranged in a parallel conformation and lie at a distance (olefin centroid-to-centroid distances 4.01 Å) that suitable for a cycloaddition reaction. The $C_3F_5O_2^-$ anions lie orthogonal to the dinuclear complexes, which enables bridging Ag···O interactions between complexes (Fig. 69). The bridging carboxylates couple with C-H···N interactions between neighboring cyano and ethylene functionalities to form a 2D sheet. The sheets stack in an ABAB manner. As a consequence of stacking, **ACS** molecules between the layers are arranged in a head-to-tail fashion which positions the olefins at a distance (centroid-to-centroid distance 4.01 Å), which also meets the distance criterion for a [2+2] photodimerization.

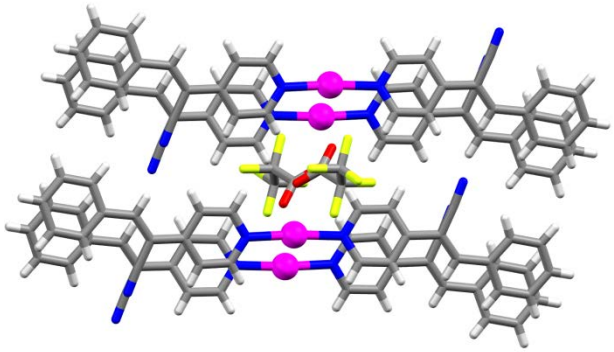

Figure 69 Perspective of the X-ray crystal structure **ACS4** which reveals the bridging dinuclear assemblies *via* carboxylate anions to form a 2D sheet.

ACS and $AgC_4F_7O_2$ crystallize as solid **ACS4** in the triclinic space group $P\bar{1}$ with an asymmetric unit that consists of two **ACS** molecules and a $AgC_4F_7O_2$. The Ag(I)

ions and **ACS** molecules self-assemble to form a dinuclear complex sustained by Ag···Ag forces (Ag···Ag distance 3.27 Å). Each Ag(I) ion is coordinated by two transoid **ACS** molecules in a linear geometry *via* pyridyl moieties. The olefins within the complex are arranged in a parallel conformation at a distance (olefin centroid-to-centroid distances 4.10 Å) that satisfies the topochemical postulate (Fig. 70). Akin to **ACS3**, The $C_4F_7O_2^-$ anions lie orthogonal to the dinuclear complexes and participate in bridging Ag···O interactions between complexes. The bridging carboxylates couple with C-H···N interactions between neighboring cyano and ethylene functionalities to form a 2D sheet. The sheets stack in an ABAB manner. As a consequence of stacking, **ACS** molecules between the layers participate in π···π interactions and are arranged in a head-to-tail fashion, which positions the olefins at a distance (centroid-to-centroid distance 4.03 Å) suitable for a [2+2] photodimerization.

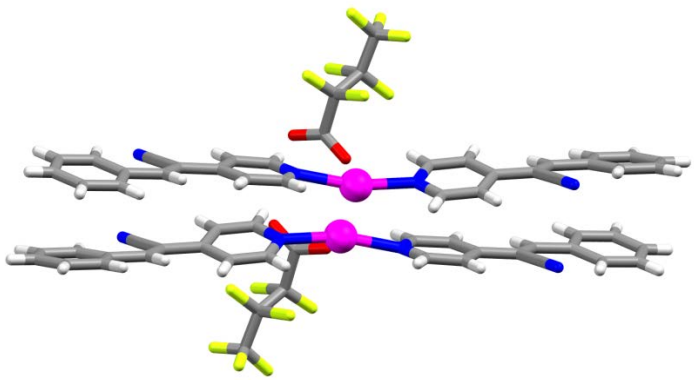

Figure 70 X-ray structure of **ACS4** wherein Ag(I) ions assemble **ACS** molecules in a dinuclear complex suitable for a [2+2] photodimerization.

Structural analyses of **ACS1-4** indicate the olefins of **ACS** are topochemically aligned and can be expected to undergo a [2+2] photodimerization. However, solids **ACS1**, **ACS2**, and **ACS4** have the potential to undergo head-to-head photoreactions

within the complex or head-to-tail photoreactions with **ACS** molecules in neighboring assemblies. After UV irradiation, ^{1}H NMR spectroscopy is used to follow the reactivity. Photodimerization of the olefins is concluded based on the upfield shift of pyridyl and phenyl H-atoms and the concurrent disappearance of the olefinic proton with the growth of peaks in the region of 5.51-5.92 ppm indicating cyclobutane formation. The major product after UV irradiation of **ACS1-2** has the corresponding ^{1}H NMR spectrum: (DMSO-d_6, 300 MHz) δ 8.51-8.49 (4H's, dd, pyridine), δ 7.52-7.49 (4H's, dd, pyridine), δ 7.33-7.31 (6H's, m, phenyl), δ 7.19-7.16 (4H's, m, phenyl), δ 5.50 (2H's, s, cyclobutane). The photoproduct formed after UV irradiation of **ACS4** has the corresponding ^{1}H NMR spectrum: (DMSO-d_6, 300 MHz) δ 8.57-8.55 (4H's, dd, pyridine), δ 7.53-7.50 (4H's, m, phenyl), δ 7.41-7.39 (4H's, dd, pyridine), δ 7.34-7.31 (6H's, m, phenyl), δ 5.90 (2H's, s, cyclobutane). A summary of interatomic distances and the percent yields calculated from the ratio of the area of the pyridyl H-atoms before and after photoreaction are contained in Table 5.

Table 5 Interatomic distances and photoreaction yields for **ACS1-4**

Structure	Ag···Ag distance (Å)	C=C distances within assemblies (Å)	Percent yield
ACS1	3.50	3.56, 3.88	92%, 85% HH
ACS2	3.50, 3.84	3.71, 3.82	95%, 95% HH
ACS3	3.28	4.01	< 5%, HT
ACS4	3.37	4.10	43%, HT

To date, attempts to obtain suitable single crystals of the photoproducts have been unsuccessful. However, based on ^{1}H NMR spectroscopy we are able to determine if the photoproducts are in a head-to-head or head-to-tail arrangement. An analysis of ^{1}H NMR data reveals two peaks consistent with cyclobutane formation in our photoreactivity studies with **ACS**, a singlet at 5.50 pm and a singlet 5.90 ppm. Based on the substitution patterns, the head-to-tail photoproducts can be assigned to the singlet at 5.90 ppm owing

to the protons of the cyclobutane ring containing cyano substituents at both alpha positions. In comparison, the head-to-head photoproducts arrange the cyclobutane protons in an environment wherein the protons experience deshielding from a single cyano substituted α-carbon. The difference in substitution patterns accounts for the 0.40 ppm shift in cyclobutane peaks and enables assignment of the singlet at 5.50 ppm to a head-to-head photoproduct. In total, there are 10 possible photoproducts resulting from the head-to-head photodimerization of **ACS** (Fig. 71). Within these possibilities, only compounds **1** and **2** in Figure 71 have a symmetry element (*i.e.* mirror plan) that accounts for the singlet observed *via* ^{1}H NMR spectroscopy. Compound **1** corresponds to the expected product based on the arrangement of **ACS** molecules within **ACS1-2** whereas compound **2** would require isomerization of the **ACS** molecules followed by the cycloaddition reaction. The high degree of symmetry in the head-to-tail products precludes assigning the product to a limited number of possibilities.

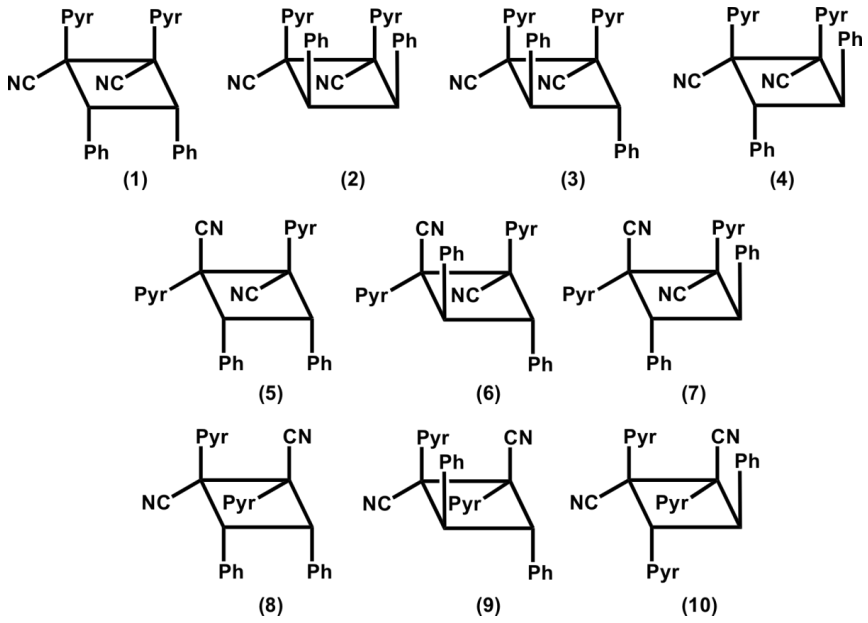

Figure 71 Possible head-to-head photoproducts of **ACS**.

4.3.4. Crystallization of **BCS** with silver templates

Solid **BCS1** crystallizes in the triclinic space group $P\bar{1}$ with an asymmetric unit composed of two **BCS** molecules and a $AgNO_3$. The primary coordination sphere of the Ag(I) ions consists of a T-shaped geometry involving two transoid N-atoms from the pyridyl moieties of **BCS** and a single oxygen atom from a NO_3^- anion. The complexes self-assemble into a 2D sheet sustained by Ag···N≡C interactions between adjacent complexes (Fig. 72). To accommodate the steric requirements of such an arrangement a pyridyl moiety of each complex rotates to a 37.3° angle with respect to the acrylonitrile functionality. In this arrangement, the Ag(I) ions orient **BCS** molecules transoid yet lack the designed Ag···Ag interactions which guides olefins into a topochemical arrangement. The 2D sheets pack in an offset arrangement that enables weak π···π interactions between neighboring **BCS** molecules. As a consequence, one **BCS** molecule within each T-shaped assembly is arranged in a head-to-tail fashion and at a distance (olefin centroid-to-centroid distance 3.98 Å) suitable for a cycloaddition reaction.

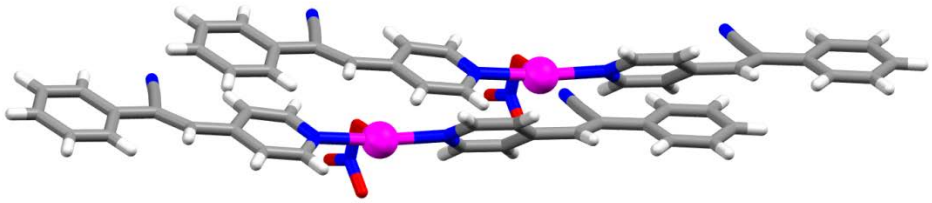

Figure 72 Perspective view of **BCS1** which shows the packing of neighboring complexes into a 2D sheet *via* Ag···N≡C interactions.

Solid **BCS2** crystallizes in the triclinic space group $P\bar{1}$ with an asymmetric unit composed of two **BCS** molecules and a $AgClO_4$. The primary coordination sphere of the Ag(I) ions consists of a linear geometry involving two transoid N-atoms from the pyridyl moieties of **BCS** molecules. The ClO_4^- anions lie in close proximity to the Ag(I) ions

participating in weak Ag···O interactions. The complexes self-assemble into a 2D sheet *via* Ag···N≡C interactions between adjacent complexes (Fig. 73). As a consequence of sheet formation, a pyridyl moiety of each complex rotates to a 38.68^{o} angle with respect to the acrylonitrile functionality. In this arrangement, the Ag(I) ions orient **BCS** molecules transoid yet lack the designed Ag···Ag forces utilized to stack olefins. The packing of 2D sheets in an offset arrangement enables weak π···π and Ag···π interactions between the layers and arranges **BCS** molecules at distances (> 4.20 Å) unfavorable for [2+2] photodimerizations.

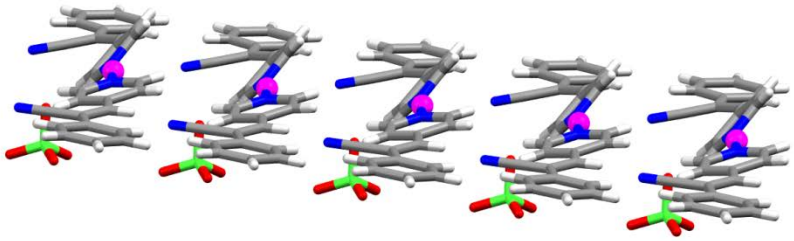

Figure 73 Perspective of the X-ray crystal structure **BCS2** wherein Ag(I) complexes extend into a 2D sheet unsuitable for [2+2] photodimerization.

Solids **BCS1-2** provide insight into the solid-state behavior of structural isomers based on cyano-substituted stilbazoles. In structures **ACS1-4** crystallization with Ag(I) ions resulted in dinuclear assemblies sustained by Ag···Ag forces. Within the assemblies, the olefins of **ACS** molecules were topochemically aligned and, in the case of **ACS1-2**, resulted in quantitative yields of a head-to-head photoproduct. Although the cyano groups within **ACS1-4** participate in C-H···N≡C or Ag···N≡C interactions the forces did not preclude the formation of a dinuclear assembly. Alternatively, **BCS1-2** are composed of cyano groups that also participate in C-H···N≡C or Ag···N≡C interactions yet the forces result in 1D tapes. The assembly of 1D tapes results in structures void of Ag···Ag

forces and **BCS** molecules aligned in a head-to-head arrangement suitable for a [2+2] photodimerization.

Although an analysis of **BCS1-2** suggests the solids are not suitable for the quantitative production of photoproducts the photoreactivity was explored. Following UV irradiation ^{1}H NMR spectroscopy was used characterize the reactivity. Photodimerization of the olefins was concluded based on an upfield shift of pyridyl- and phenyl H-atoms coupled with the disappearance of the olefinic proton to go along with the growth of a cyclobutane peak in region of 5.55-5.95 ppm. A summary of interatomic distances in addition to the percent yields calculated from the ratio of the area of the pyridyl H-atoms before and after photoreaction are contained in Table 6.

Table 6 Interatomic distances and photoreaction yields for **BCS1-2**

Structure	Ag···Ag distance (Å)	Nearest C=C distances (Å)	Percent yield
BCS1	N/A	3.98	48%, HT
BCS2	N/A	4.44	35%, HT

The photoproduct after UV irradiation of **BCS1-2** has the corresponding ^{1}H NMR spectrum: (DMSO-d_6, 300 MHz) δ 8.52-8.50 (4H's, dd, pyridine), δ 7.49-7.47 (4H's, dd, pyridine), δ 7.41-7.35 (10H's, m, phenyl), δ 5.95 (2H's, s, cyclobutane). To date, attempts to obtain suitable single crystals of the photoproduct have been unsuccessful. However, the assignment of potential **BCS** photoproducts can be performed using the same analysis of ^{1}H NMR spectra as was done in the assignment of **ACS** photoproducts. Specifically, the downfield shift of the cyclobutane singlet (5.95 ppm) is consistent the protons of the cyclobutane ring containing cyano substituents at both alpha positions. In comparison, the singlet assigned to the **ACS** head-to-tail photoproduct is observed at 5.90 ppm. Akin to **ACS**, the high symmetry of the potential **BCS** head-to-tail photoproducts precludes assigning the stereochemistry of the photoproducts to a limited number of

possibilities. In addition, UV irradiation of **BCS2** resulted in the formation of a photoproduct despite the arrangement of the olefins in a non-topochemical alignment. A suggested mechanism for this reaction is the migration of molecules guided by the glide planes granted the neighboring planes do not interlock.

4.3.4. Crystallization and photoreactivity of **FACS** with silver templates

As part of our continuing investigation into the assembly of cyano-substituted olefins we wanted to determine the solid-state assembly of these molecules in the wake of simple chemical substitutions. Incorporating functional group diversity would enable the tuning of optical properties and, potentially, the ability to induce reversible [2+2] cycloadditions. To date we have obtained a single crystal structure with **FACS**. Solid **FACS1** crystallizes in the triclinic space group $P\bar{1}$ with an asymmetric unit that comprises two **FACS** molecules and a $AgClO_3$. The primary coordination sphere of the Ag(I) ions consists of a T-shaped geometry involving two transoid N-atoms from the pyridyl moieties of **FACS** molecules and a single oxygen atom from ClO_3^- anions. The metal and organic components assemble to form a dinuclear assembly sustained by Ag···Ag (Ag···Ag distance 3.45 Å) and an additional Ag···O interaction from ClO_3^- anions. The dinuclear assembly organizes the olefins of **FACS** in a parallel conformation at a distance (centroid-to-centroid distance 3.96 Å), which meets the requirement stated in the topochemical postulate (Fig. 74a). The dinuclear assembly propagates into 2D sheets *via* C-H···N interactions along the *a*-axis and C-H···F interactions (Fig. 74b). The 2D sheets are organized in an offset manner that enables Ag···π and π···π interactions between the layers. As a result, the olefins between neighboring complexes are separated at a distance unsuitable for a [2+2] photodimerizations between complexes.

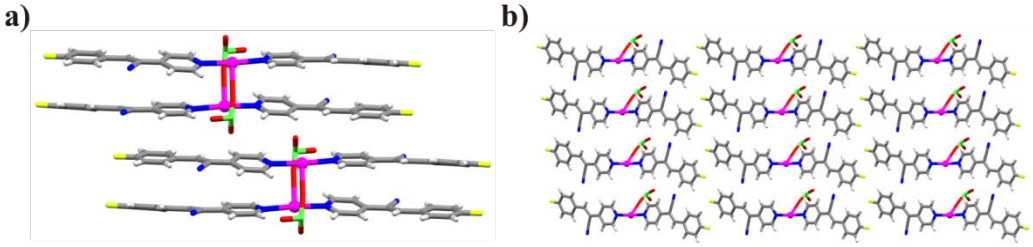

Figure 74 X-ray structure of **FACS1**: (a) Perspective view of neighboring complexes stacked in an offset manner sufficiently spaced to prevent reaction between assemblies and (b) a perspective view of the 2D sheets sustained by C-H···N and C-H···F interactions.

UV irradiation of powdered **FACS1**, followed by ^{1}H NMR spectroscopy, resulted in quantitative formation (*ca.* 98% yield) of a cyclobutane photoproduct. Similar to **ACS** and **BCS**, photodimerization of the olefins is concluded based on the upfield shift of pyridyl and phenyl H-atoms and the concurrent disappearance of the olefinic proton with the growth of a peak at 5.51 ppm indicating cyclobutane formation. The major product after UV irradiation of **FACS1**, (*i.e.* 94% of the photoproduct) has the corresponding ^{1}H NMR spectrum: (DMSO-d_6, 300 MHz) δ 8.51-8.49 (4H's, d, pyridine), δ 7.50-7.48 (4H's, d, pyridine), δ 7.22-7.20 (8H's, m, phenyl), δ 5.51 (2H's, s, cyclobutane). To date, attempts to obtain suitable single crystals of the photoproduct have been unsuccessful. However, the similarities between **ACS** and **FACS** enable us to reduce the number of potential photoproducts. Specifically, the observation of a cyclobutane singlet at 5.51 ppm is consistent with a head-to-head photoproduct wherein the protons of the cyclobutane ring contain a single cyano substituent at the alpha positions. In comparison, the singlet assigned to the **ACS** head-to-head photoproduct is observed at 5.50 ppm. Following the same analysis employed on the **ACS** photoproducts reduces the number of potential **FACS1** photoproducts to two compounds.

Owing to the ability of cyano-substituted olefins to undergo reverse [2+2] cycloadditions during thermal annealing we were interested in the thermal behavior of the

FACS1 photoproduct. Specifically, the solid obtained after UV irradiation of **FACS1** was placed inside an oven at 100°C. After 41 hours the resulting solid was analyzed *via* ^{1}H NMR spectroscopy. Based on the ^{1}H NMR spectrum, the solid contained an 86:14 ratio of **FACS** to cyclobutane photoproduct. With possible switching mechanisms in mind, the solid was again exposed to UV irradiation and, after 28 hours of exposure, the solid consisted of a 74:26 ratio of photoproduct to **FACS**. In comparison, when the solid obtained after UV irradiation of **ACS1** (*i.e.* 92% cyclobutane photoproduct, 85% HH) was placed in an oven at 100°C, a 77:23 ratio of **ACS** to photoproduct was obtained but after 17 days in the oven. Although the switching process requires further investigation, results to date suggest the template approach can be extended to cyano-substituted stilbazoles with simple functional group substitutions.

4.3.4. Crystallization of **ACD** with silver templates

To further determine the reliability of Ag(I) ions to assemble cyano-substituted olefins for [2+2] cycloadditions we turned to dienes. Specifically, **ACD** and $AgClO_3$ crystallizes as solid **ACD1** in the triclinic space group $P\bar{1}$ with an asymmetric unit that comprises two **ACD** molecules, a $AgClO_3$, and a water molecule. The primary coordination sphere of the Ag(I) ions consists of a linear geometry involving two transoid pyridine moieties of **ACD** molecules. The ClO_3^- anions lie in close proximity to the Ag(I) ions with a single oxygen atom participating in a bifurcated Ag···O interaction. The resulting assembly of metal and organic components is a dinuclear assembly wherein the Ag(I) ions are organized to participate in Ag···Ag (Ag···Ag distance 3.45 Å) interactions (Fig. 75). Within the dinuclear assembly, the **ACD** molecules are in a head-to-head arrangement with olefins aligned in a parallel conformation and at distances (olefin centroid-to-centroid distances 3.84 Å, 3.90 Å). The nearest-neighbor complexes are aligned in a parallel, offset, fashion that results in Ag···π and π···π interactions between the layers yet the sole olefins organized to undergo photoreactions are within the

complex. The stacking of complexes results in 1D column that pack with adjacent columns *via* C-H···N interactions involving cyano groups and C-H···O interactions with the ClO_3^- anions.

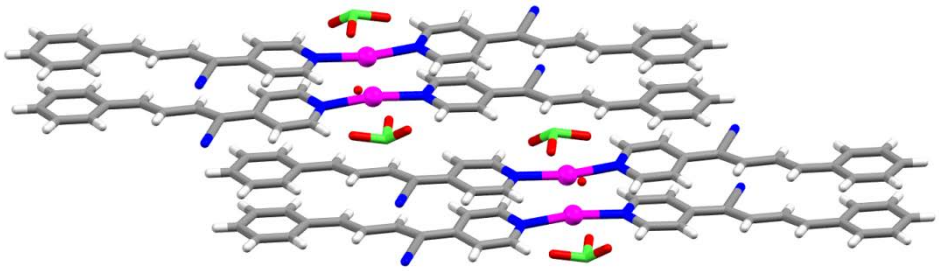

Figure 75 X-ray structure of **ACD1** which consists of dinuclear complexes that stack in an offset manner to align only the olefins within the complex for a photoreaction.

ACD2 crystallizes in the triclinic space group $P\bar{1}$ with an asymmetric unit composed of two **ACD** molecules and a $AgClO_4$. The Ag(I) ions crystallize with a primary coordination sphere consisting of a T-shaped geometry that organizes two pyridine moieties of **ACD** molecules transoid and coordinates a cyano group from an adjacent **ACD** molecule which results in an **ACD** tetramer complex (Fig. 76a).

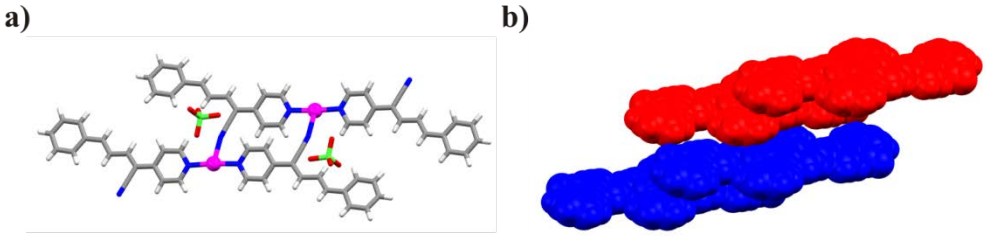

Figure 76 X-ray structure of **ACD2**: (a) **ACD** tetramer complex and (b) neighboring stepwise chains which orient the olefins of adjacent chains sufficiently close for a head-to-tail photodimerization.

The ClO_4^- anions lie in close proximity to Ag(I) ions with a single oxygen atom participating in a bifurcated Ag···O interaction. Each Ag(I) ion of the **ACD** tetramer complex is organized to participate in Ag···Ag (Ag···Ag distance 3.42 Å) interactions that propagates the tetramers in a stepwise chain. The Ag···Ag interactions within the chain orient the olefins of **ACD** molecules in an approximately parallel arrangement and distance (olefin centroid-to-centroid distances 3.78 Å, 3.88 Å) that meets the requirements stated in the topochemical postulate for [2+2] photodimerizations in the solid-state. However, neighboring chains pack in an offset manner that enables π···π interactions between **ACD** molecules and places the **ACD** molecules of neighboring chains in a head-to-tail arrangement wherein the olefins are approximately parallel and at a distance (olefin centroid-to-centroid distances 3.91 Å) favorable for [2+2] photodimerizations (Fig. 76b).

ACD and $AgCF_3SO_3$ self-assemble to yield solid **ACD3**. The metal and organic components crystallize in the triclinic space group $P\bar{1}$ with an asymmetric unit that consists of two **ACD** molecules and a $AgCF_3SO_3$. The primary coordination sphere of Ag(I) ions consists of a linear geometry that organizes the N-atoms of two pyridyl moieties transoid. The $CF_3SO_3^-$ anions lie in close proximity to Ag(I) ions with a single oxygen atom participating in a Ag···O interaction. The Ag(I) ions are organized to participate in Ag···Ag (Ag···Ag distance 3.75 Å) interactions that also assemble the olefins of **ACD** molecules in an approximately parallel arrangement and distances (olefin centroid-to-centroid distances 3.90 Å, 4.07 Å) suitable for [2+2] photodimerizations in the solid-state. In fact, the data suggest the crystal may undergo a partial SCSC reaction that could require the further use of constraints and restraints Nearest-neighbor complexes extend into a stepwise chain *via* Ag···N≡C interactions (Fig. 77). The chains pack *via* Ag···π and π···π interactions so that the **ACD** molecules of neighboring chains are arranged in a head-to-tail arrangement with topochemically aligned olefins (olefin centroid-to-centroid distances 3.80 Å, 3.82 Å).

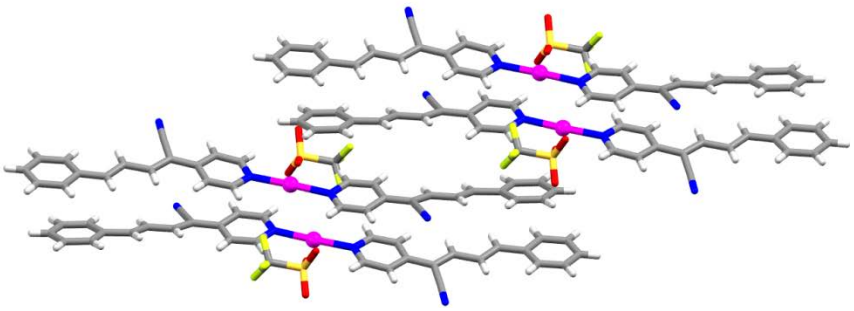

Figure 77 Perspective view of **ACD3** that reveals the offset packing of neighboring complexes *via* Ag···π and π···π interactions.

Solid **ACD4** crystallizes in the triclinic space group $P\bar{1}$ with an asymmetric unit that consists of two **ACD** molecules and a $AgC_3F_5O_2$. The Ag(I) primary coordination sphere comprises a linear geometry that coordinates the pyridyl moieties of **ACD** in a transoid conformation. The Ag(I) ions within **ACD4** are stacked to participate in Ag···Ag (Ag···Ag distance 3.22 Å) interactions that assembles the olefins of **ACD** into dinuclear complexes with olefins that are parallel arrangement and at separation distances (olefin centroid-to-centroid distances 4.01 Å, 4.03 Å) that satisfies the conditions outlined in the topochemical postulate. The $C_3F_5O_2^-$ anions lie perpendicular to the dinuclear assemblies and bridge neighboring complexes *via* Ag···O interactions into a 1D tape (Fig. 78a). In addition, the $C_3F_5O_2^-$ anions participate in C-F···H interactions which results in a 2D sheet of alternating Ag(I) complexes and carboxylate anions. The 2D sheets stack with in an ABAB manner sustained π···π interactions between **ACD** molecules while the anions crosslink the layers *via* Ag···O and C-F···H interactions. The resulting 2D layers orient **ACD** molecules of neighboring complexes in a head-to-tail arrangement with olefins that are approximately parallel and at a distance (olefin centroid-to-centroid distances 3.76 Å), which allows a [2+2] photodimerization between dinuclear complexes (Fig. 78b).

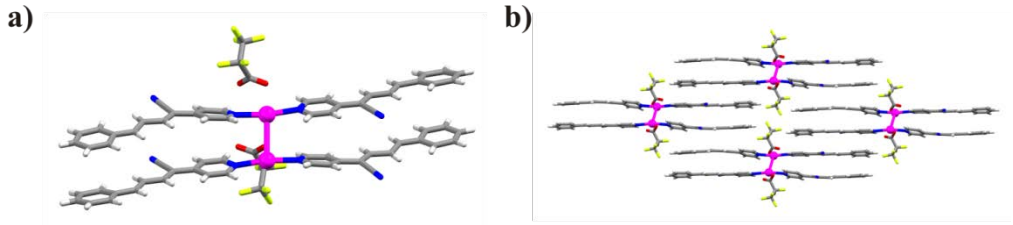

Figure 78 X-ray structure of **ACD4**: (a) perspective view of a dinuclear complex and (b) ABAB packing of 2D layers viewed along the *a*-axis.

In total we have successfully achieved four crystal structures based on **ACD** and Ag(I) ions. In solids **ACD1-4** we observed the formation of dinuclear assemblies of varying Ag···Ag distances yet the olefins within the assemblies were topochemically aligned (Table 7).

Table 7 Interatomic distances and photoreaction yields for **ACS1-4**

Structure	Ag···Ag distance (Å)	C=C distances within assemblies (Å)
ACD1	3.30	3.84, 3.90
ACD2	3.42	3.78, 3.88
ACD3	3.75	4.07, 3.90
ACD4	3.22	4.02, 4.03

However, in solids **ACD 2-4** the olefins of neighboring complexes are aligned in a head-to-tail arrangement at distances and geometries suitable for a photodimerization. During the course of photoreactivity studies, the accessibility of multiple olefins may preclude quantitative and stereospecific yields. To counteract undesirable photoproducts we can continue to crystallize **ACD** with silver salts in an attempt to limit the potential of photodimerization between assemblies. Although unexpected photoproducts may not follow the design principals the result may still be a molecules of great interest.

4.4. Summary

In conclusion, a template approach has been employed to align cyano-substituted olefins in the solid-state. In the case of resorcinol-based templates, cocrystallizations with **CVP** resulted in topochemically aligned olefins, however, upon UV irradiation the solids remained photostable. A change in the template approach to our library of silver salts resulted in successful alignment of **CVP** molecules and, in the case of **CVP1**, a quantitative and stereospecific photoproduct. The ability to align cyano-substituted olefins with Ag(I) ions was further investigated with a series of stilbazoles. Interestingly, crystallization of the structural isomers **ACS** and **BCS** with Ag(I) resulted in dramatically different solid-state assemblies. The solids based on **ACS** crystallized as dinuclear assemblies suitable for [2+2] photodimerizations whereas the **BCS** solids crystallized as 1D tapes void of argentophilic interactions. The third stilbazole investigated, **FACS**, provided insight into the robust assembly process in the wake of simple chemical modifications. Importantly, **FACS1** was successfully photodimerized in the solid-state and, after thermal annealing, regenerated the starting **FACS** molecules. An additional study on the assembly of **ACD** molecules further enforced the ability Ag(I) ions to align cyano-substituted olefins in the solid-state. We expect the findings in this chapter will aid in the development of highly tailorable cyano-substituted chromophores for optical memory applications.

CHAPTER 5. COCRYSTALS OF IODINATED CONTRAST AGENTS

5.1. Introduction

Computed tomography (CT) imaging is one of the most commonly used diagnostic tools in medicine.[321] The technique is based on X-ray attenuation and is capable of providing 3D images with spatial resolutions of < 1 mm in clinical settings.[322] Contrast agents that contain elements of a high atomic (Z) number are employed to provide contrast between the region of interest and the surrounding tissue. The efficient X-ray attenuation imparted to contrast agents is ascribed to the increased photoelectron effect from high Z number elements.[323] However, the delivery of high Z number elements as part of a non-toxic material presents a formulation challenge in that the material must also retain high specificity, loading, and clearance from the body. Indeed, for gastrointestinal tract imaging the only CT contrast agents currently approved for clinical use are based on iodinated molecules or barium sulfate.[324]

The origins of iodinated contrast agents can be traced back to the original work on X-rays. As early as 1896 iodine was identified as a high Z number element that absorbs X-ray radiation.[325] However, free iodide ions have adverse effects on the human body (*e.g.* thyroid).[326] In 1953 diatrizoic acid (**DTA**) was introduced as the first contrast agent with covalently bound iodine atoms to improve biocompatibility.[327] To achieve acceptable water solubility the molecule was formulated as either a sodium or meglumine salt.[328] Despite the aqueous solubility and low toxicity of **DTA** formulations the pain associated with intravenous injections was severely limiting. Almén determined the chemotoxicity of these formulations was due to an overloading of the homeostasis of the body by the rapid injection of large volumes of high-osmolality solutions.[329] The

discovery spurned the development of many modern day contrast agents that are based on non-ionic, water-soluble, iodinated molecules formulated to meet osmolality, viscosity, toxicity, and hydrophilicity requirements (*e.g.* iodixanol) (Fig. 79).[328]

a)

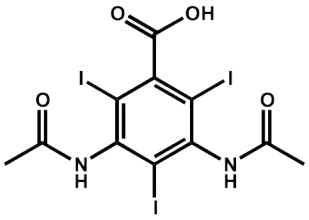

b)

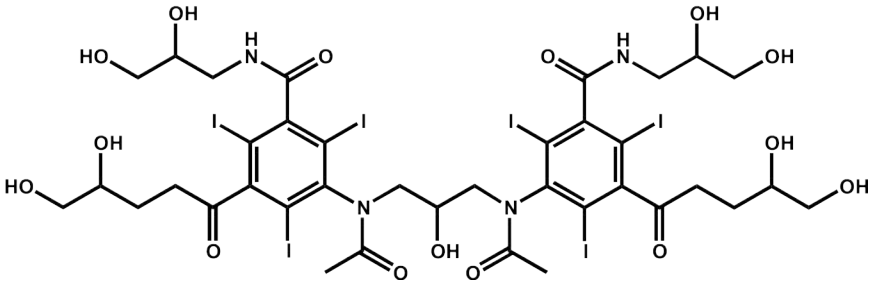

Figure 79 Chemical structures of the clinically administered contrast agents (a) **DTA** and (b) iodixanol.

Common issues that plague small-molecule contrast agents are difficulties in delivering high concentrations of iodine, an inability to perform targeted imaging, the necessity of large doses to achieve contrast, and insufficient circulation time in the blood.[323, 326] However, contrast agents of nanometer-scale dimensions can be synthesized to overcome issues that plague conventional small-molecule contrast agent formulations. The first example of X-ray imaging with nanoparticulates traces back to the use of Thorotrast (*i.e.* thorium dioxide) in the 1930s.[330] Thorium affords high X-ray opacity, however, the human body retains the radioactive element at a sufficiently high rate to

cause cancer formation. Not until the last 15 years was research into nanoparticulate contrast agents fully revived. Ideally, a formulation that consists of a nanometer-scale contrast agent would meet the following criteria: high selectivity, high signal-to-noise ratio, easily dispersed in solvents, exhibit physical stability towards a variety of environments, limit non-specific binding, resist uptake into the mononuclear phagocyte system, long circulation times, and amenable to clearance mechanisms.[321] In addition, the formulation of contrast agent nanoparticles may require sizes greater than 50 nm to avoid extensive extravascular distribution.[331] To achieve these goals, the focus has been on the development of nanometer-scale contrast agents based on iodinated molecules. The preference toward iodinated molecules can be attributed to the preexisting clinical use of iodinated contrast agents.[321] To date, the strategies to fabricate iodinated nanoparticles have focused on using polymers,[332, 333] emulsions,[334, 335] liposomes,[336] lipoproteins,[337] and solid nanoparticles.[324, 338-341]

Covalent modifications to 2,3,5-triiodobenzoic acid have yielded products amenable to both the polymer- and emulsion-based nanoparticle strategies. Research into the use of polymers as nanometer-sized contrast agents has largely focused on incorporating iodinated functional groups into polymer backbones. In the case of 2,3,5-triiodobenzoic acid, the molecule was reacted with 2-hydroxyethyl methacrylate to give the starting monomer 2-methacryloyloxyethyl(2,3,5-triiodobenzoate) that, upon emulsion polymerization in the presence of sodium dodecyl sulfate, yields polymeric nanoparticles.[332] *In vivo* studies have demonstrated the iodinated nanoparticles afford significant enhancement of the spleen, liver, kidneys, and lymph nodes. An alternative strategy reacted 2,3,5-triiodobenzoic acid with long chain alcohols (*e.g.* 2-octanol) to

yield a series of iodinated oils.[334] The oils could be emulsified with surfactants (*e.g.* Pluronic F68) to yield nanoparticles with an iodinated core. The surfactant-stabilized emulsions showed, *in vivo*, an ability to provide signal enhancement and longer circulation times when compared with other liquid contrast agents.

The use of covalent modifications to achieve iodinated nanoparticles has also been reported for solid nanoparticles. Specifically, **DTA** was esterified to provide a compound, N1177, with poor aqueous solubility (*ca.* 2 μg/mL).[339] Macrosized crystals of N1177 were reduced to nanometer-scale dimensions *via* media milling. The top-down process consists of mechanically shearing macro-sized crystals in the presence of a surfactant. An intravenous injection of N1177 nanoparticles, with a biocompatible surfactant, provided a means to specifically accumulate a contrast agent at the site of atherosclerotic plaques, which resulted in a safe and effective means to image the region of interest. Alternatively, inhalation of N1177 nanoparticles, specifically nanoparticle aggregates, provided a means to effectively target lungs.[340] Whereas iodinated contrast agents administered intravenously exhibit insufficient circulation times to localize in the lungs, inhalation of nanoparticle aggregates effectively reach, disperse, and coat the lungs.[340]

Herein, we report our research progress on the development of nanometer-sized contrast agents based on cocrystals. The cocrystallization approach will utilize components based on iodinated contrast agents previously approved by the FDA and a complementary cocrystal former (CCF). The iodinated contrast agents and CCFs were selected on the basis of an ability to interact *via* non-covalent means (*i.e.* supramolecular synthons).[81] Previously, the efficacy of delivering iodine payloads *via* multi-component

nanocrystals was shown with metal-organic frameworks. The technique utilized coordination bonds between iodinated bridging ligands (*i.e.* 2,3,5,6-tetraiodo-1,4-benzenedicarboxylic acid) and metal cations (*i.e.* Cu(II) and Zn(II)) to effectively delivery of iodine payloads, albeit, of a formulation which may pose biocompatibility issues.[129] The cocrystallization approach affords an opportunity to modulate the properties of nanometer-sized contrast agents based on the selected CCF. Recently, examination of 25 pharmaceutical cocrystals revealed the solubility of the cocrystal was proportional to the solubility of the CCF.[248] Therefore, one can envision achieving a poorly soluble contrast agent based cocrystal by targeting CCFs with poor aqueous solubility, or vice versa to achieve greater water solubility. In contrast, the previously described methods used to achieve nanoparticles employed a covalent approach to achieve nanoparticles with desired physicochemical properties. The covalent approach can be time consuming, provide potentially low-yielding reactions, and the formation of new covalent bonds may create difficulties when submitting the material for government approval.[342]

The development of iodinated nano-cocrystals first required the compilation of a series of cocrystals composed of iodinated contrast agents. The research included tailoring the CCFs to enable the assembly of supramolecular synthons between the CCFs and the selected contrast agents. Therefore, we performed extensive cocrystal screening to identify complementary functional groups that could assemble synthons in the absence of proton transfer, which would result in salt formation. The resulting library of iodinated cocrystals not only provides a series of candidates for the fabrication of contrast agent based nano-cocrystals, but an understanding of intermolecular interactions that can

be exploited to synthesize additional iodinated cocrystals. Moreover, the knowledge gained in the sonochemical preparation of multi-component nanocrystals will be applied to the synthesis of contrast agent based nano-cocrystals. Herein, we describe a series of multicomponent solids based on the contrast agents **DTA**, acetrizoic acid (**ATA**), and iopanoic acid (**IPA**) (Fig. 80).

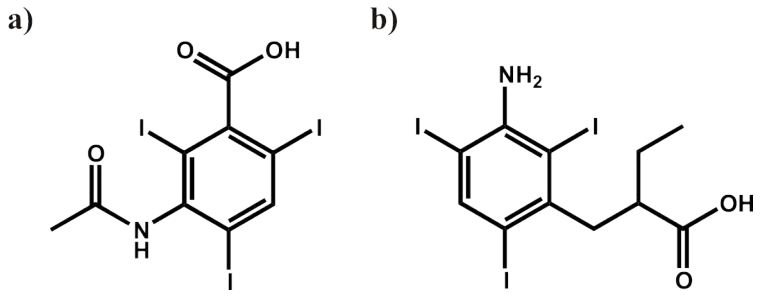

Figure 80 Chemical structures of (a) **ATA** and (b) **IPA**.

DTA remains a commonly used contrast agent (trade names: Hypaque and Gastrografin) for the imaging of the gastrointestinal tract. Although **DTA** is typically administered as a sodium salt recent reports have demonstrated agglomerated nanoparticles of **DTA**, similar to N1177, can be delivered to the lungs and provide sufficient X-ray attenuation.[324] **ATA** is a structural analog of **DTA**, which was administered as sodium acetrizoate. The compound was used as an aortagraphic contrast medium but administration of the sodium salt formulation was discontinued owing to toxicity concerns.[343] The third contrast agent, **IPA**, has been used clinically to image the gallbladder and treat certain thyroid conditions (*e.g.* hyperthyroidism).[344] The selected contrast agents all contain hydrogen-bond-donor and –acceptor groups to be exploited in cocrystallization studies. Specifically, we expect the carboxylic acid functionality of the

contrast agents to interact with CCFs that contain hydrogen-bond-acceptor groups (*e.g.* acid···pyridine heterosynthon). In fact, crystallizations performed with *trans*-1,2-bis(4-pyridyl)ethylene (**BPE**), phenazine (**PHE**), acridine (**ACR**), *trans,trans,trans*- 1,6-bis(4-pyridyl)-1,3,5-hexatriene (**BPH**), and 3,6-Diamono-4,5-diiodoacridine (**DDA**) provided multicomponent solids with the iodinated contrast agents (Fig. 81).

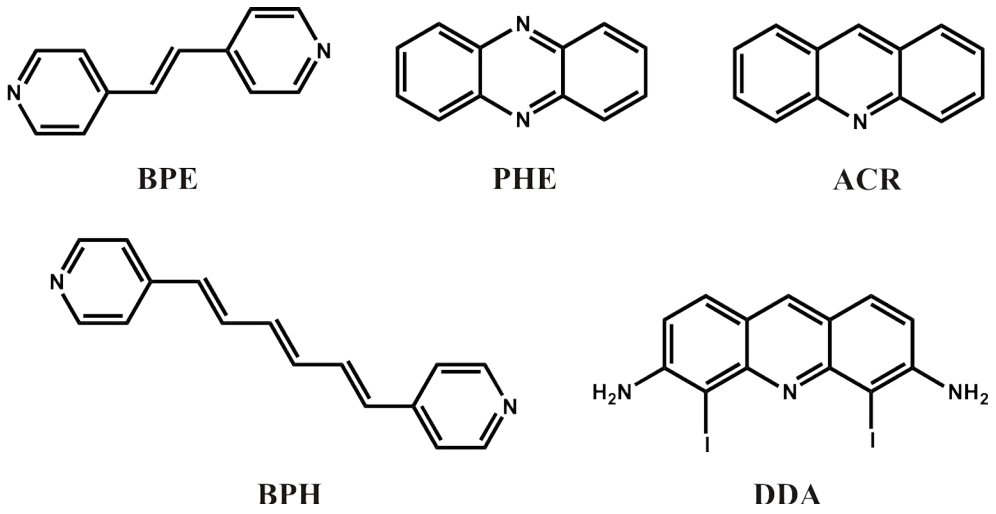

Figure 81 Chemical structures of cocrystal formers.

5.2. Materials and methods

5.2.1. Materials

Diatrizoic acid dihydrate (meets USP testing specifications), p-toluenesulfonic acid monohydrate (≥98%), dichloromethane (≥99.8%), and methanol (ACS Reagent, ≥99.8%) were purchased from Sigma-Aldrich. Acridine (98%), phenazine (98%), chloramine-T trihydrate (≥97%), and potassium iodide (>99%) were purchased from Acros Organics. Iopanoic acid (>98%) was purchased from TCI America. Acetrizoic acid (>98%) and Proflavine HCl (>97%) were purchased from MP Biomedicals.

Acetonitrile (99.9%), dimethylsulfoxide (≥99.9%), N,N-dimethylformamide (≥99.8%), magnesium sulfate (powder certified), sodium thiosulfate (≥98%), sodium bicarbonate (99.7%), and ethyl acetate (≥99.5%) were purchased from Fisher Scientific. Ethanol (100%) was purchased from Decon Labs. The compound *trans,trans,trans*- 1,6-bis(4-pyridyl)-1,3,5-hexatriene was previously prepared based on a literature procedure.[345] All purchased chemicals were used as received.

5.2.2. Synthesis of 3,6-Diamino-4,5-diiodoacridine

DDA was synthesized based on a literature procedure.[346] A round-bottom flask was charged with Proflavine HCl (1.4 g, 5.70 mmol) in water (150 mL). The solution was heated to 40°C then solid $NaHCO_3$ was added until a pH of 10 was achieved. The suspension was filtered and a yellow solid was isolated. A round-bottom flask was charged with the yellow solid (1.0 g, 4.79 mmol), potassium iodide (1.982 g, 11.946 mmol), Chloramine-T (3.366 g, 11.946 mmol), and dimethylformamide (20 mL) then reacted at ambient conditions for 1 hour. The resulting suspension was poured into water and the product was extracted with 3x50 mL of ethyl acetate. The ethyl acetate fractions were combined, reacted with sodium thiosulfate (25 mg), dried over anhydrous $MgSO_4$, and evaporated using a rotary evaporator. To remove the *p*-toluenesulfonamide impurity, the resulting solid was dissolved in 250 mL of dichloromethane and excess *p*-toluenesulfonic acid monohydrate (1.26 g, 7.34 mmol) was added. After one hour of equilibration a dark red solid was isolated (608 mg 28% yield). ^{1}H NMR spectroscopy verified the spectrum of the isolated solid matched the previously reported spectrum for **DDA**.

5.2.3. Single crystal preparation

Single crystals of composition (**DTA**)·2(H_2O) (**DTA1**) were grown by slow-solvent evaporation. **DTA** (20 mg) was dissolved in a 1:1 (v/v) water ethanol solution and allowed to equilibrate to ambient conditions until single crystals were obtained.

Single crystals of composition 2(**DTA**)$^{-}$·(2H-**BPE**)$^{2+}$·8(H_2O) (**DTA2**) and (**DTA**)·(**PHE**) (**DTA3**) were prepared *via* slow solvent evaporation. **DTA2** and **DTA3** were prepared from a 2:1 molar ratio (70 mg total) of **DTA** to CCF. Single crystals of **DTA2** and **DTA3** were obtained by dissolving the solid mixtures in a 1:1 (v/v) water ethanol or 1:1 (v/v) methanol acetonitrile solution, respectively. The solutions were left to slowly evaporate at ambient conditions until suitable single crystals were observed. Single crystals of composition (**DTA**)$^{-}$·(H-**DDA**)$^{+}$·4(H_2O) (**DTA4**) were grown from the dissolution of a 1:1 molar ratio (27 mg total) of the cocrystal components in a 1:1:1 (v/v) ethanol water N,N-dimethylformamide solvent mixture. The solution was left to slowly evaporate at ambient condition until suitable crystals were observed.

Single crystals of composition 2(**ATA**)$^{-}$·(2H-**BPE**)$^{2+}$·1.2(H_2O) (**ATA1**) and (**ATA**)·(**PHE**) (**ATA2**) were achieved *via* slow-solvent evaporation of a 1:2 molar ratio (129 mg total) of **ATA** to CCF. **ATA1** and **ATA2** were obtained by dissolving the polycrystalline solids using a 1:1 (v/v) methanol acetonitrile solvent mixture. The solutions were allowed to equilibrate to ambient conditions and left undisturbed to slowly evaporate until single crystals were observed. Single crystals of (**ATA**)$^{-}$·(H-**ACR**)$^{+}$ (**ATA3**) and (**ATA**)$^{-}$·(H-**DDA**)$^{+}$·2(H_2O) (**ATA4**) were achieved *via* slow-solvent evaporation. A physical mixture of the cocrystal components in a 1:1 molar ratio (37 mg and 25 mg total) was dissolved in 1:1 (v/v) methanol acetonitrile or 1:1 (v/v) water ethanol respectively. The solutions were equilibrated to ambient conditions then solvent was allowed to slowly evaporate until single crystals were obtained.

Single crystals of compositions (**IPA**)·0.5(**BPE**) (**IPA1**), (**IPA**)·0.5(**PHE**) (**IPA2**), and (**IPA**)·0.5(**BPH**) (**IPA3**) were prepared by dissolving a physical mixture of the cocrystal components present in a 2:1 ratio of **IPA** to CCF (132 mg, 132 mg, and 25 mg total respectively) in acetonitrile. After equilibration to ambient conditions the solvent was allowed to slowly evaporate until single crystals were observed.

5.2.4. Single crystal X-ray diffraction measurements

Crystal data was collected on a Nonius Kappa CCD single-crystal X-ray diffractometer at liquid nitrogen temperatures using graphite-monochromated MoKα radiation (λ = 0.71073 Å). Structure solution and refinement was accomplished using SHELXL-97.[173] All non-hydrogen atoms were refined anisotropically. Hydrogen atoms associated with carbon atoms were refined in geometrically constrained riding positions. If possible, hydrogen atoms associated with oxygen and nitrogen atoms were located in the Fourier-difference electron density maps.

ATA1 contains highly disordered solvent molecules. The Fourier-difference map revealed electron densities that could be ascribed to water molecules. Despite extensive use of restraints, an acceptable solvent model was not achieved. The crystal structure was treated with the SQUEEZE routine of PLATON.[347] The solvent molecules were determined to occupy 45.0 $Å^3$. An electron count of 12 electrons per unit cell corresponds to approximately 1.2 molecules of water per asymmetric unit.

5.3. Results and discussion

Herein, we report a series of structures based iodinated contrast agents and CCFs that contain sp^2-hybridized N-atoms. The ΔpK_a values between the carboxylic acid group of the contrast agents and the conjugate acid of the CCFs contributed to whether we obtained a cocrystal or a salt. In total we obtained ten multi-component structures that contain iodinated contrast agents, five cocrystals and five salts.

Our investigation into cocrystals based on iodinated contrast agents began with efforts to characterize **DTA**, **ATA**, and **IPA** *via* single crystal X-ray diffraction to understand behavior of these molecules in the solid-state. To date, efforts to grow suitable single crystals of **ATA** and **IPA** from a variety of solvents (*i.e.* polar to non-polar solvents that may or may not possess hydrogen bonding functionalities) have resulted in needle-like crystals unsuitable for single-crystal X-ray diffraction. Alternatively, we

successfully grew single crystals of **DTA** from a 1:1 (v/v) methanol water solvent mixture. Previous reports have characterized an anhydrous and a dihydrate form of **DTA** by infrared spectroscopy and X-ray powder diffraction yet, to the best of our knowledge, a full structural characterization of the molecule has not been reported. Solid **DTA1** crystallizes in the triclinic space group $P\bar{1}$ with an asymmetric unit that comprises one **DTA** molecule and two water molecules. The **DTA** molecules assemble to give dimers that are arranged to form N-H(amide)···O(carboxy) (N···O: 2.829(4) Å) hydrogen bonds and weak I···π (3.86 Å) interactions. The remaining amide functionalities connect neighboring **DTA** dimers *via* N-H(amide)···O(carbonyl) (N···O: 2.831(5) Å) hydrogen bonds to extend the arrangement into a 1D column along the *a*-axis (Fig. 82).

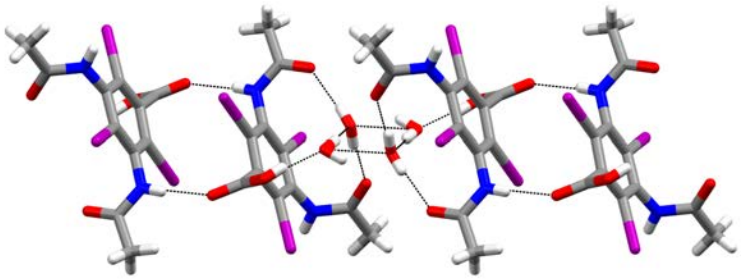

Figure 82 Perspective view of **DTA1** wherein **DTA** molecules assemble into dimers. The dimers propagate along the *a*-axis to yield 1D columns bridged by water tetramers.

The 1D columns stack along the *c*-axis *via* hydrogen bonding water molecules that assemble to form a cyclic tetramer. Specifically, **DTA** molecules donate a hydrogen bond to the water tetramer in the form of a O-H(carboxy)···O(water) (O···O: 2.507(5) Å) hydrogen bond and accept hydrogen bonds from water molecules *via* O-H(water)···O(carbonyl) (O···O: 2.697(5) Å, 2.788(4) Å) interactions. The water tetramer is completed by O-H(water)···O(water) (O···O: 2.716(5) Å, 2.731(5) Å) interactions. The

water rings effectively bridge neighboring **DTA** molecules into 2D sheets that stack with adjacent layers in an overlapping fashion sustained by weak I···I (3.95 Å) interactions.

Cocrystallization studies were undertaken by employing CCFs that contain an aromatic N-atom capable of forming a O-H(carboxy)···N(pyridyl) heterosynthon. Specifically, we selected the symmetric bipyridine **BPE**, which is a simple bifunctional acceptor that forms cocrystals with a variety of hydrogen bond donors. Solid **DTA2** crystallizes in the triclinic space group $P\bar{1}$ with an asymmetric unit that contains two **DTA**, one half **BPE** that lies on a center of inversion, one half **BPE** that lies on a center of inversion and is unequally disordered over two orientations, and eight water molecules. The N-atoms of the **BPE** molecules are protonated by the carboxylic acid group of **DTA**. The **DTA** molecules of the salt are arranged to form charge assisted N^+-H(pyridinium)···O^-(carboxylate) (N···O: 2.505(5) Å, 2.558(6) Å)hydrogen bonds to the pyridinium rings of **BPE** (Fig. 83).

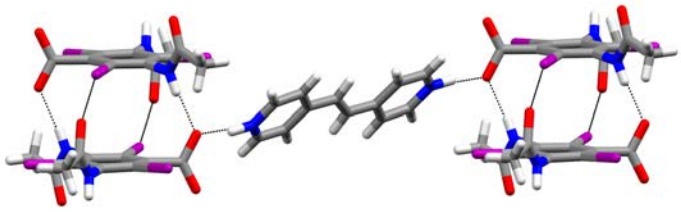

Figure 83 Perspective of the X-ray crystal structure **DTA2** wherein **BPE** molecules are oriented between **DTA** dimers (water molecules omitted for clarity).

Akin to **DTA1**, the **DTA** molecules form dimers sustained by N-H(amide)···O(carbonyl) (N···O: 2.792(7) Å, 2.803(6) Å) hydrogen bonds and weak I···π (3.70 Å) interactions which hydrogen bond to **BPE** molecules to propagate a stepwise chain in the solid-state. The inclusion of water molecules results in two distinct acyclic chains that each comprises four water molecules. The water hydrogen bonding interactions result in a

complex 3D network wherein the amide and carboxylate functionalities of **DTA** act as hydrogen-bond-donors and -acceptors to the water tetramers.

Owing to the salt formation and water affinity of **DTA2** we investigated cocrystal formation between **ATA** and **BPE**. **ATA** offers a similar chemical composition to **DTA** but the benzoic acid derivative has a hydrogen atom at the 5 position instead of an amide group that may alter the water affinity. **ATA** and **BPE** crystallize in the triclinic space group $P\bar{1}$ with an asymmetric unit that contains two **ATA** molecules and one **BPE** molecule. The N-atoms of **BPE** are protonated by the carboxylic acid group of **ATA**. Akin to **DTA2**, the protonated **BPE** molecules are arranged to form charge assisted N^+-H(pyridinium)···O^-(carboxylate) (N···O: 2.564(5) Å, 2.640(5) Å) hydrogen bonds with stacked **ATA** molecules (Fig. 84).

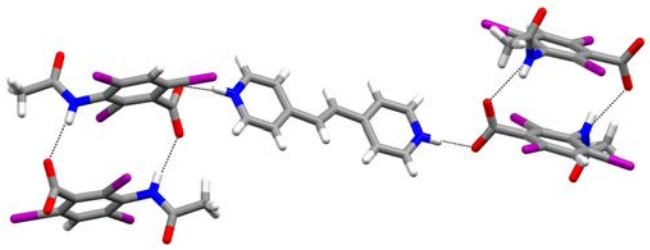

Figure 84 X-ray structure of **ATA1** viewed along the *b*-axis (water molecules omitted for clarity).

The stacked **ATA** molecules are sustained by N-H(amide)···O(carboxy) (N···O: 2.840(6) Å, 2.923(6) Å) hydrogen bonds and weak I···π (3.98 Å) interactions. Akin to **DTA2**, the **ATA** and **BPE** molecular assembly extends in the solid-state to produce a stepwise chain. The 1D chains pack in an offset manner sustained by weak C-H···O forces and diffuse water molecules that fill the space between the voids to yield a 3D network. The water molecules present in the solid occupy approximately 2% of the unit cell contents.

The predominance of salt formation in **DTA2** and **ATA1** inspired cocrystallization studies with the contrast agent **IPA**. **IPA** retains a triiodobenzene core but, unlike the benzoic acid derivatives **DTA** and **ATA**, the carboxylic acid group of **IPA** is covalently bound to an aliphatic group. In this arrangement, **IPA** exhibits a reduced acidity (*i.e.* calculated pK_a values are ~4.50 for **IPA**, ~0.92 for **DTA**, and ~1.13 for **ATA**) [348] that is expected to promote cocrystal formation with **BPE**. In fact, the components **IPA** and **BPE** crystallize in the absence of proton transfer in the space group $P\bar{1}$ with one **IPA** molecule and one half **BPE** molecule that lies on a center of inversion. **IPA** and **BPE** assemble to form a carboxylic acid···pyridine heterosynthon (O···N: 2.712(5) Å) in an S-shaped arrangement. The assembly propagates in *via* N-H(amine)···O(carboxy) (N···O: 2.980(7) Å) hydrogen bonds along the *a*-axis to yield a supramolecular ladder (Fig. 85).

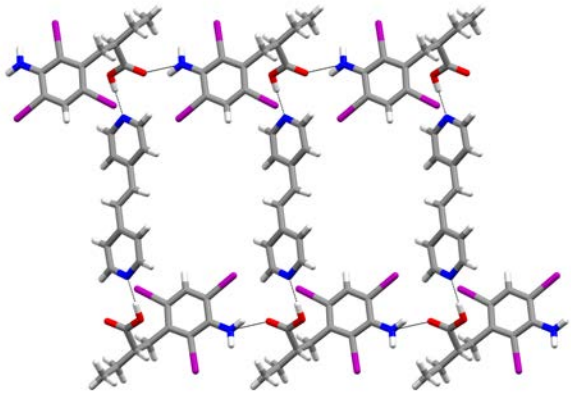

Figure 85 X-ray structure of **IPA1** viewed along the *c*-axis to reveal a supramolecular ladder.

The **BPE** molecules represent the rungs of the ladder with a separation distance of 9.57 Å. Adjacent supramolecular ladders pack in an interdigitated manner to fill the void

between the rungs of the ladder that results in pronounced 2D layers. Neighboring layers pack in an overlapping fashion sustained by weak I···π (3.98 Å) interactions.

Based on our crystallization study with **BPE** we determined a CCF that contains an aromatic N-atom with a reduced basicity would promote cocrystallization with **DTA**, **ATA**, and **IPA**. Therefore, we turned to **PHE** owing to the availability of two aromatic N-atoms for the formation of supramolecular synthons and a lower pK_a value than **BPE** (~1.60 versus ~5.50).[348] The cocrystallization strategy was first examined by crystallizing **DTA** and **PHE**. The components of **DTA3** crystallize in the triclinic space group $P\bar{1}$ with an asymmetric unit that contains a **DTA** and a **PHE** molecule. The components are arranged to form O-H(carboxy)···N(pyridyl) (O···N: 2.647(5) Å) hydrogen bonds and weak I···N (3.12 Å) interactions between the **DTA** and **PHE** molecules (Fig. 86).

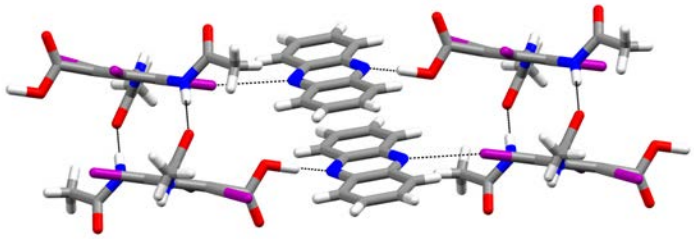

Figure 86 Perspective view of **DTA3** wherein **PHE** molecules hydrogen bond to a 1D column of **DTA** molecules.

Akin to **DTA1-DTA2**, the **DTA** molecules stack *via* N-H(amide)···O(carboxy) (N···O: 2.819(5) Å, 2.849(5) Å) to form a 1D chain along the *a*-axis. The **PHE** molecules stack along the *a*-axis being separated by 3.85 Å and 5.73 Å. The pillared arrangement results in alternating columns of **DTA** and **PHE** to produce a 3D network. The neighboring layers of **DTA3** stack in an ABAB manner than enables I···I (4.01 Å) interactions.

The ability of **PHE** to form cocrystals with iodinated contrast agents was further realized with **ATA**. The cocrystal components of **ATA2** crystallize in the orthorhombic space group *Pbca* with a molecule of **ATA** and **PHE** in the asymmetric unit. The crystal structure is based on centrosymmetric four-component assemblies composed of two molecules of **ATA** and two molecules of **PHE**. The assembly is sustained by a dimer formation between **ATA** molecules, akin to **ATA1**, that contains N-H(amide)···O(carboxy) (N···O: 2.974(5) Å) hydrogen bonds and O-H(carboxy)···N(pyridyl) (O···N: 2.624(5) Å) interactions between **ATA** and **PHE** to complete the assembly (Fig. 87a). The **ATA** dimers interact with adjacent dimers that have rotated to enable I···O (2.95 Å) interactions. The arrangement propagates into a layered structure along the *b*-axis. The **PHE** molecules stack in an offset manner to allow π···π interactions with a separation of 4.52 Å between the molecules. The extended 1D columns of **PHE** molecules pack in an interdigitated manner to enable C-H···π between the **PHE** molecules of neighboring columns. The resulting **PHE** columns are coupled with the **ATA** dimers to yield alternating layers of **PHE** and **ATA** (Fig. 87b).

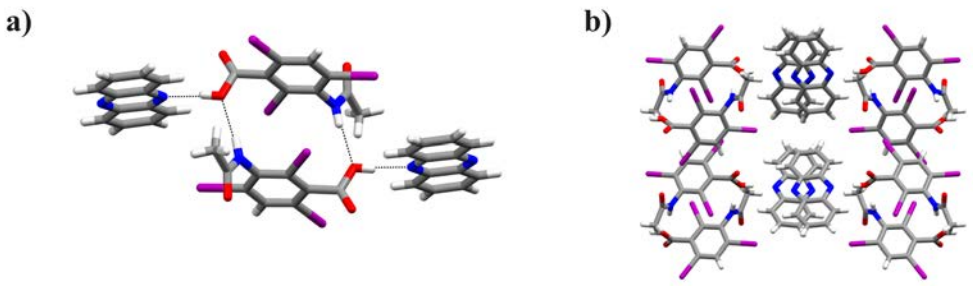

Figure 87 (a) Perspective view of the four-component assembly that comprises **ATA2** and (b) the layers of **ATA** and **PHE** viewed along the *a*-axis.

The third cocrystal with **PHE** involves **IPA** and **PHE** crystallizing in the monoclinic space group $P2_1/c$ with an asymmetric unit that comprises one **IPA** molecule

and a half **PHE** molecule that lies on a center of inversion. The solid **IPA2** consists of a discrete three component assemblies involving two **IPA** molecules and one **PHE** that hydrogen bond *via* O-H(carboxy)···N(pyridyl) (O···N: 2.786(6) Å) interactions (Fig. 88a). Unlike **IPA1**, the aniline functionality of **IPA** does not participate in a hydrogen bond to extend the assembly into a supramolecular ladder. Consequently, the three-component assemblies form zig-zag chains *via* hydrophobic packing of the **IPA** alkyl chains. The chains interact in an offset manner *via* π···π interactions between **IPA** and **PHE** (Fig. 88b).

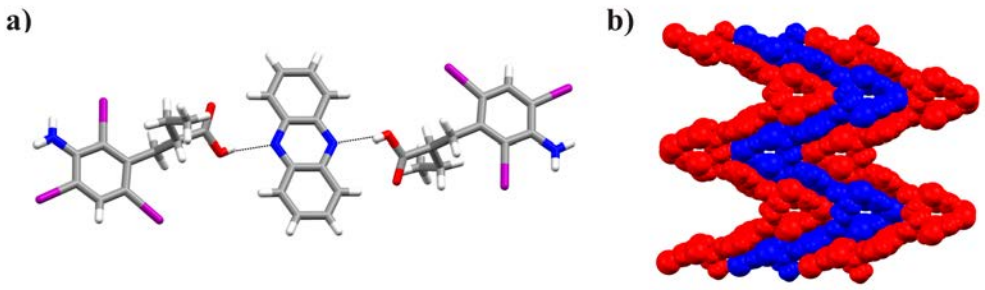

Figure 88 X-ray structure of **IPA2** showing (a) the three-component assemblies viewed along the *b*-axis and (b) packing of zig-zag chains viewed along the *c*-axis.

The role of the ΔpK_a between cocrystal components on cocrystallization was further investigated with the CCFs **ACR**, **BHT**, and **DDA**. Based on the calculated ΔpK_a values, crystallization of the CCFs with **IPA** would favor a cocrystal ($\Delta pK_a < 1.2$) while crystallizations with **DTA** or **ATA** are expected to yield salts ($\Delta pK_a > 4.5$).

ACR contains a single aromatic N-atom of similar basicity to **BPE**. Thus cocrystal screening with **ACR** and the iodinated contrast agents is expected yield solids similar to the **BPE** trials with respect to salt or cocrystal formation. Cocrystallization trials with the contrast agents **DTA**, **ATA**, and **IPA** were pursued, and to date, we have obtained single crystals of a multi-component solid composed of **ATA** and **ACR**

(**ATA3**). Solid **ATA3** crystallizes in the triclinic space group $P\bar{1}$ with a molecule of **ATA** and **ACR** in the asymmetric unit. The **ATA** molecules are arranged in a dimer motif similar to **ATA1** and **ATA2** wherein the amide functionalities participate in N-H(amide)···O(carboxy) (N···O: 2.815(3) Å) hydrogen bonds. The dimers arrange in a manner that enable I···O (2.83 Å) interactions between adjacent assemblies that propagates into a 1D chain. The packing of **ATA** chains is sustained by I···I (3.84 Å) interactions that extend the chains into a corrugated layer. The N-atom of **ACR** molecules is protonated by the carboxylic acid group of **ATA** molecules to form charge assisted N^+-H(pyridinium)···O^-(carboxylate) (N···O: 2.643(4) Å) hydrogen bonds (Fig. 89a). The **ACR** molecules stack in an offset, head-to-tail, arrangement that consists of separation distances of 5.31 Å and 4.59 Å. The compilation of **ATA** and **ACR** columns results in a 3D arrangement based on alternating **ATA** and **ACR** layers (Fig. 89b).

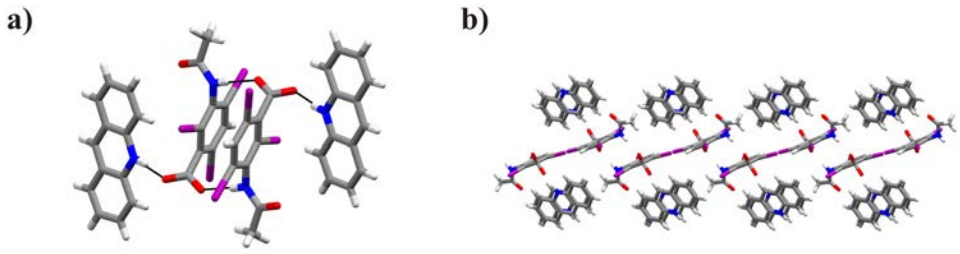

Figure 89 X-ray structure of **ATA3** showing (a) the four-component assemblies viewed along the *c*-axis and (b) layered arrangement of **ATA** and **ACR** molecules viewed along the *a*-axis.

Efforts are underway to continue our investigation of **ACR** *via* single crystals of a solid that comprises **DTA** and **ACR**. Moreover, cocrystallization trials between **IPA** and **ACR** are under investigation. To date, attempts to cocrystallize **IPA** and **ACR** *via* solution and mechanochemistry techniques have resulted in oils.

The survey of CCFs was continued with the ditopic receptor **BHT**. As expected crystallization of **IPA** and **BHT** results in cocrystal formation. Solid **IPA3** crystallizes in the triclinic space group $P\bar{1}$ with an asymmetric unit that contains a molecule of **IPA** and a half molecule of **BHT**. **IPA** molecules are arranged to participate in O-H(carboxy)···N(pyridine) (O···N: 2.709(7) Å) hydrogen bonds with each pyridyl ring of the **BHT** molecules. The **IPA** molecules extend this arrangement into a supramolecular ladder, similar to **IPA1**, through N-H(amine)···O(carboxy) (N···O: 2.923(7) Å) hydrogen bonds between neighboring **IPA** molecules. The **BHT** molecules serve as the rungs of the supramolecular ladder with separation distances of 10.46 Å (Fig. 90). The supramolecular ladders pack *via* I···I (3.70 Å) interactions between neighboring ladders to yield a 2D sheet. The layers of **IPA3** stack in an offset manner sustained by weak C-H···N interactions between **IPA** and **BHT** molecules of adjacent layers and the hydrophobic packing of the alkyl chains of **IPA** within the void space between the rungs of the supramolecular ladders. Crystallizations between **DTA** and **ATA** and the CCF **BHT** are under continued exploration with the expectation of salt formation in both instances.

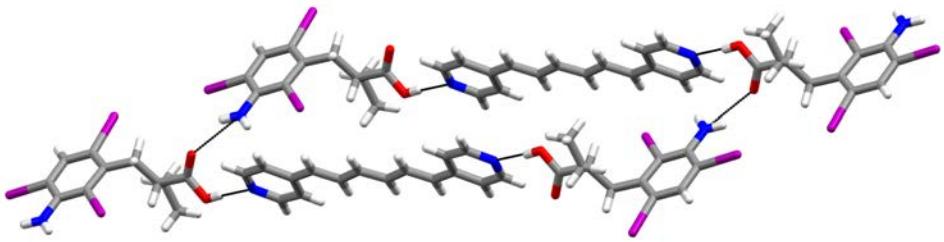

Figure 90 X-ray structure of **IPA3** viewed along the *a*-axis to reveal a supramolecular ladder with **BHT** molecules serving as the rungs of the ladder.

The final CCF in our survey, **DDA**, affords another example of the effect the ΔpK_a value plays on cocrystal formation. In addition, **DDA** is the first example in our

continued efforts to identify iodinated CCFs with complementary functional groups for the assembly of supramolecular synthons with **DTA**, **ATA**, and **IPA**. **DDA** possesses an aromatic N-atom and two iodine atoms that may sterically limit the accessibility of the N-atom. In addition, the calculated pK_a of **DDA** (~5.74) suggests a high probability of salt formation with **DTA** and **ATA**. In fact, **DTA4** crystallizes in the triclinic space group $P\bar{1}$ with a **DTA** molecule, a **DDA** molecule, and four water molecules in the asymmetric unit. The aromatic N-atom of **DDA** molecules is protonated by the carboxylic acid group of **DTA**, which classifies this solid as a salt, not a cocrystal. Each **DTA** molecule of the salt is arranged to participate in N-H(amine)···O(carbonyl) (N···O: 2.800(8) Å) and N-H(amine)···O$^-$(carboxylate) (N···O: 2.761(8) Å) hydrogen bonds with three neighboring **DTA** molecules which continues in a manner to which yields 1D columns based **DTA** molecules along the *a*-axis. The packing of **DTA** columns is sustained by I···O (3.30 Å) interactions and hydrogen bonding interaction with included water molecules. The water molecules assemble into a series of acyclic chains based on six water molecules that cross-link *via* hydrogen bonds to an additional two water molecules (Fig. 91).

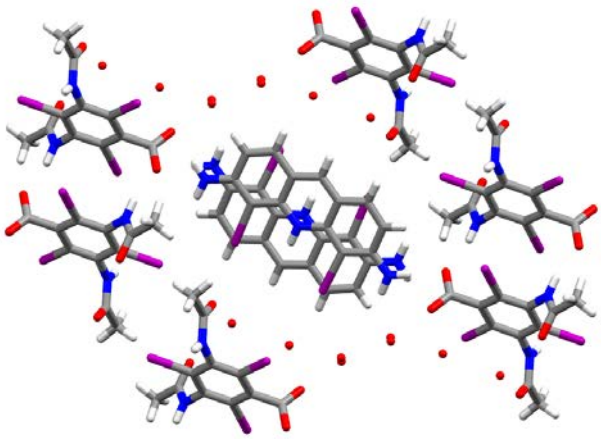

Figure 91 X-ray structure of **DTA4** viewed along the *a*-axis, wherein, **DTA** and water molecules assemble into a channeled network that encapsulates stacked **DDA** molecules.

The arrangement is similar to that of the classical description of a hairy polymer. The resulting hydrogen bonding interactions between **DTA** and water form a channeled structure wherein **DDA** molecules fill the void. The **DDA** molecules within the columns stack in a head-to-tail arrangement separated by 3.49 Å and 4.72 Å. The carboxylate functionality of **DTA** molecules are anchor the **DDA** *via* N-H(amine)···O(carboxylate) (N···O: 3.093(10) Å)hydrogen bonds.

Similar to **DTA4**, crystallization of **ATA** and **DDA** results in protonation of the aromatic N-atom of **DDA** molecules by the carboxylic acid group of **ATA** molecules. **ATA4** crystallizes in the triclinic space group $P\bar{1}$ with an **ATA** molecule, a **DDA** molecule, and two water molecules in the asymmetric unit. As is the case in **ATA1-ATA3**, the **ATA** molecules arrange in a dimer motif sustained by N-H(amide)···O(carbonyl) (N···O: 2809(5) Å). The carboxylate functionalities of the **ATA** dimers accept hydrogen bonds in the form of N-H(amine)···O(carboxylate) (N···O: 2.881(5) Å, 2.873(5) Å) interactions from **DDA** molecules. Between **ATA** dimers a pair of **DDA** molecules stacks in a head-to-tail fashion separated by 3.59 Å. The carboxylate···amine interactions extend to give 1D chains of alternating **ATA** and **DDA** dimers (Fig. 92a).

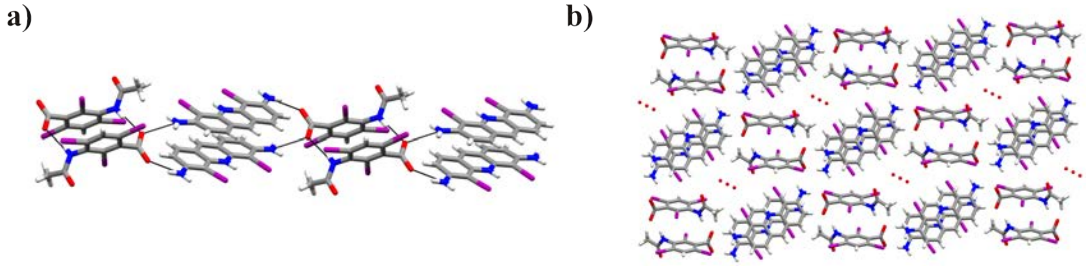

Figure 92 (a) Perspective view of the 1D chains that comprise **ATA4** (water molecules omitted for clarity) and (b) a packing view along *a*-axis.

Owing to an additional carboxylate···amine interaction, adjacent chains pack in an ABAB manner within a 2D sheet. The layers of **ATA4** participate in weak π···π and I···I interactions with crystallized water molecules completing the 3D packing. The water molecules are arranged as an infinite 1D chain that propagates along the *a*-axis (Fig. 92b).

5.4. Summary and outlook

The results presented in this chapter provide the first examples of cocrystals based on iodinated contrast agents. In total, we successfully characterized, *via* single crystal X-ray diffraction, five cocrystals and five salts that contain iodinated contrast agents. The results establish a library of cocrystals composed of contrast agents and a knowledge base of intermolecular interactions to be exploited in the design of additional cocrystals with tailored properties, akin to pharmaceutical cocrystals. Specifically, the results demonstrate that CCFs that contain aromatic N-atoms are capable of reliably forming cocrystals when the ΔpK_a value is less than one. Therefore, future cocrystallization studies with **DTA** and **ATA** will require CCFs with a sufficiently low basicity (*e.g.* phenazine). The results our cocrystallization studies suggest **IPA** is more amenable to cocrystallization owing to a reduced acidity, however, cocrystals composed of **IPA** have been limited to ditopic CCFs.

Although the pK_a values and hydrogen-bond-acceptor capabilities of the CCFs are the major contributors to the outcome of cocrystallization trials, the presence of additional functionalities plays a major role in the 3D arrangement of the cocrystal components. Specifically, **DTA** and **ATA** have amide functionalities that have yet to participate in a supramolecular synthon between the cocrystal components. Instead, the excess of hydrogen bonding moieties results in consistent dimer formation between **DTA** or **ATA** molecules regardless of cocrystal or salt formation. In addition, the triiodobenzene core of the contrast agents contributes to the 3D arrangement of the

cocrystal components *via* I···X (X = I, O, or π) but has yet to cause a masked synthon, or a case of a moderate synthon success, between the cocrystal components. A structural analysis of our 10 multi-component solids suggest the designed supramolecular synthon between the cocrystal components can readily assemble in spite of potential synthon competition from amide and iodine moieties. The results obtained in our initial study on iodinated cocrystals will aid in the discovery of additional iodinated cocrystals and provide a library of precursors to be used in the synthesis of contrast agent based nano-cocrystals. The achievement of iodinated nano-cocrystals will require applying the lessons learned in the synthesis of multi-component nano-cocrystals. Specifically we will explore tailoring the solvent, concentration, insonation time, anti-solvent, and presence of surfactant to meet the specific requirements of each iodinated cocrystal system.

CHAPTER 6. CONCLUSIONS AND FUTURE WORK

In our cocrystallization studies with **APAP** we encountered a surprising amount of synthon variability between the cocrystal components. In solids **APAP1-2** the cocrystal substituents lack direct hydrogen bonding interactions. Instead, the cocrystals components only participate in intermolecular interactions *via* bridging water molecules. The lack of intermolecular interactions between the designed cocrystal components was described as masked synthons. In addition, we obtained moderate to complete synthon successes between the cocrystal components in **APAP3** and **APAP4**, respectively. The variability in synthons between **APAP** and **BPE** suggests an imperfect match between the cocrystal components. Future endeavors would determine if a more suitable crystalline environment involving the components could be identified in the form of an anhydrous cocrystal, additional hydrated/solvated cocrystals, or a three component cocrystal composed of **APAP** and **BPE**. The occurrence of unexpected synthons was further realized upon cocrystallization of **APAP** and the zwitterionic form **PDA**. That **PDA** can function as two forms suggests that **PDA** could serve as a flexible cocrystal component in future cocrystallization experiments. Finally, in **APAP1-APAP5** we successfully obtained cocrystals with pronounced layered topologies. As part of our future efforts, we plan to study the compaction properties of these solids.

In chapter 3 we introduced a sonochemical method that effectively fabricates pharmaceutical nano-cocrystals and nanocrystals based on a host-guest system. The method accommodates the inherent solubility difference between the cocrystal components of pharmaceutical cocrystals. We believe the sonochemical approach has the potential to synthesize a diverse range of organic nanocrystals and as part of our future efforts we will strive to synthesize pharmaceutical nano-cocrystals based on PAs with poor dissolution rates and bioavailability. In addition, we plan to quantify the solubility and dissolution rate advantages imparted to pharmaceutical nano-cocrystals. Outside of

our pharmaceutical interests, we are also exploring organic and metal-organic crystals that exhibit the same nonclassical crystal growth observed with **CMCR** and the potential role sonochemistry plays in the assembly of these materials.

In chapter four we demonstrated the successful alignment of cyano-substituted olefins in the solid-state by utilizing the template approach. Specifically, we were able to align and photoreact **CVP** molecules in a manner that generated a quantitative and stereospecific photoproduct. Additionally, we showed Ag(I) ions could successfully align cyano-substituted olefins based on stilbazoles and a diene. As part of our future efforts we will focus on the structural characterization of our photoproducts and the photoreactivity of metal complexes with our diene molecule **ACD**. In addition, we plan to fully explore the ability to regenerate the starting cyano-substituted olefins through a thermal annealing process, akin to **FACS1**. Specifically, the preliminary results with **FACS1** suggest the assembly process of these molecules is resistant to simple chemical modifications that would enhance the ability to tailor the properties of our solid. Our efforts will strive towards the synthesis of a solid that allows for the generation of a cyano-substituted photoproduct that can be formed and disassembled multiple times without a loss in fidelity.

The work composed in chapter 5 represents our efforts in the field of cocrystals based on iodinated contrast agents. To date we have characterized five cocrystals and five salts that comprise iodinated contrast agents. The results establish a knowledge base of intermolecular interactions to be exploited in the design of future cocrystals with tailored properties. Based on our results we will continue to investigate cocrystals based on CCFs with sufficiently low basicities to prevent salt formation. In addition, the next phase of our efforts will utilize our isolated cocrystals as model systems for the fabrication of nano-cocrystals composed of iodinated contrast agents. To achieve of iodinated nano-cocrystals will require tailoring the solvent, concentration, insonation time, anti-solvent, and presence of surfactant to meet the specific requirements of each

system. After the successful synthesis of contrast agent based nano-cocrystals we will investigate their effectiveness with contrast variation measurements.

REFERENCES

1. Lehn, J.-M., Cryptates - inclusion complexes of macropolycyclic receptor molecules. *Pure Appl. Chem.* **1978**, *50* (9-10), 871-892.

2. Lehn, J.-M., Supramolecular chemistry - scope and perspectives molecules - supermolecules - molecular devices. In *Nobel lectures, chemistry 1981-1990*, Frängsmyr, T.; Malmström, B. G., Eds. World Scientific: Singapore, 1992; p 708.

3. Pedersen, C. J., Cyclic polyethers and their complexes with metal salts. *J. Am. Chem. Soc.* **1967**, *89* (10), 2495-2496.

4. Lehn, J. M., Supramolecular chemistry - scope and perspectives molecules, supermolecules, and molecular devices. *Angew. Chem. Int. Ed.* **1988**, *27* (1), 89-112.

5. Cram, D. J., The design of molecular hosts, guests, and their complexes (nobel lecture). *Angew. Chem. Int. Ed.* **1988**, *27* (8), 1009-1020.

6. Steed, J. W.; Atwood, J. L., *Supramolecular chemistry*. 2nd ed.; John Wiley & Sons, Ltd: Chichester, 2009.

7. Dunitz, J. D., Phase transitions in molecular crystals from a chemical viewpoint. *Pure Appl. Chem.* **1991**, *63* (2), 177-185.

8. Desiraju, G. R., *Crystal engineering the design of organic solids*. Elsevier: New York, 1989.

9. Goshe, A. J.; Steele, I. M.; Ceccarelli, C.; Rheingold, A. L.; Bosnich, B., Supramolecular recognition: On the kinetic lability of thermodynamically stable host-guest association complexes. *Proc. Natl. Acad. Sci. USA* **2002**, *99* (8), 4823-4829.

10. Novoa, J. J.; D'Oria, E.; Carvajal, M. A., *Understanding the nature of the intermolecular interactions in molecular crystals. A theoretical perspective*. Wiley-VCH Verlag GmbH & Co. KGaA: 2007; p 25-57.

11. Parsegian, V. A., *Van der waals forces : A handbook for biologists, chemists, engineers, and physicists*. Cambridge University Press: New York, 2006; p 380.

12. Garratt, P. J.; Ng, Y. F.; Steed, J. W., Molecular design using electrostatic interactions. Part 2: Synthesis and properties of flexible dipodand di- and tetra-cations with restricted conformations. Charge, shape and size in molecular complexation. *Tetrahedron* **2000**, *56* (26), 4501-4509.

13. Ilioudis, C. A.; Tocher, D. A.; Steed, J. W., A highly efficient, preorganized macrobicyclic receptor for halides based on ch center dot center dot center dot and nh center dot center dot center dot anion interactions. *J. Am. Chem. Soc.* **2004**, *126* (39), 12395-12402.

14. Steed, J. W., A modular approach to anion binding podands: Adaptability in design and synthesis leads to adaptability in properties. *Chem. Commun.* **2006**, (25), 2637-2649.

15. Lee, J. W.; Samal, S.; Selvapalam, N.; Kim, H.-J.; Kim, K., Cucurbituril homologues and derivatives: New opportunities in supramolecular chemistry. *Acc. Chem. Res.* **2003**, *36* (8), 621-630.

16. Lagona, J.; Mukhopadhyay, P.; Chakrabarti, S.; Isaacs, L., The cucurbit[n]uril family. *Angew. Chem. Int. Ed.* **2005**, *44* (31), 4844-4870.

17. Wood, P. A.; Borwick, S. J.; Watkin, D. J.; Motherwell, W. D. S.; Allen, F. H., Dipolar c n center dot center dot center dot c n interactions in organic crystal structures: Database analysis and calculation of interaction energies. *Acta Crystallogr. Sect. B* **2008**, *64*, 393-396.

18. Gavezzotti, A., Packing analysis of organic crystals containing carbonyl or cyano groups. *J. Phys. Chem.* **1990**, *94* (10), 4319-4325.

19. Lee, S.; Mallik, A. B.; Fredrickson, D. C., Dipolar−dipolar interactions and the crystal packing of nitriles, ketones, aldehdyes, and c(sp2)−f groups. *Cryst. Growth Des.* **2003**, *4* (2), 279-290.

20. Saenger, W., *Principles of nucleic acid structure*. Springer-Verlag: New York, 1984; p 556.

21. Churchill, C. D. M.; Rutledge, L. R.; Wetmore, S. D., Effects of the biological backbone on stacking interactions at DNA-protein interfaces: The interplay between the backbone center dot center dot center dot pi and pi center dot center dot center dot pi components. *Phys. Chem. Chem. Phys.* **2010**, *12* (43), 14515-14526.

22. Hunter, C. A.; Sanders, J. K. M., The nature of pi-pi interactions. *J. Am. Chem. Soc.* **1990**, *112* (14), 5525-5534.

23. Jennings, W. B.; Farrell, B. M.; Malone, J. F., Attractive intramolecular edge-to-face aromatic interactions in flexible organic molecules. *Acc. Chem. Res.* **2001**, *34* (11), 885-894.

24. Sherrill, C. D., *Computations of noncovalent π interactions*. John Wiley & Sons, Inc.: 2009; p 1-38.

25. Hunter, C. A., Meldola lecture - the role of aromatic interactions in molecular recognition. *Chem. Soc. Rev.* **1994**, *23* (2), 101-109.

26. Burley, S. K.; Petsko, G. A., Aromatic-aromatic interaction - a mechanism of protein-structure stabilization. *Science* **1985**, *229* (4708), 23-28.

27. Fyfe, M. C. T.; Stoddart, J. F., Synthetic supramolecular chemistry. *Acc. Chem. Res.* **1997**, *30* (10), 393-401.

28. Desiraju, G. R.; Gavezzotti, A., Crystal-structures of polynuclear aromatic-hydrocarbons - classification, rationalization and prediction from molecular-structure. *Acta Crystallogr. Sect. B* **1989**, *45*, 473-482.

29. Sunner, J.; Nishizawa, K.; Kebarle, P., Ion-solvent molecule interactions in the gas-phase - the potassium-ion and benzene. *J. Phys. Chem.* **1981**, *85* (13), 1814-1820.

30. Deakyne, C. A.; Meotner, M., Unconventional ionic hydrogen-bonds .2. Nh+...Pi - complexes of onium ions with olefins and benzene-derivatives. *J. Am. Chem. Soc.* **1985**, *107* (2), 474-479.

31. Ma, J. C.; Dougherty, D. A., The cation-pi interaction. *Chem. Rev.* **1997**, *97* (5), 1303-1324.

32. Stauffer, D. A.; Dougherty, D. A., Ion-dipole effect as a force for molecular recognition in organic media. *Tetrahedron Lett.* **1988**, *29* (47), 6039-6042.

33. Petti, M. A.; Shepodd, T. J.; Barrans, R. E.; Dougherty, D. A., Hydrophobic binding of water-soluble guests by high-symmetry, chiral hosts - an electron-rich receptor-site with a general affinity for quaternary ammonium-compounds and electron-deficient pi-systems. *J. Am. Chem. Soc.* **1988**, *110* (20), 6825-6840.

34. Shepodd, T. J.; Petti, M. A.; Dougherty, D. A., Tight, oriented binding of an aliphatic guest by a new class of water-soluble molecules with hydrophobic binding-sites. *J. Am. Chem. Soc.* **1986**, *108* (19), 6085-6087.

35. Shepodd, T. J.; Petti, M. A.; Dougherty, D. A., Molecular recognition in aqueous-media - donor-acceptor and ion dipole interactions produce tight-binding for highly soluble guests. *J. Am. Chem. Soc.* **1988**, *110* (6), 1983-1985.

36. Stauffer, D. A.; Barrans, R. E.; Dougherty, D. A., Concerning the thermodynamics of molecular recognition in aqueous and organic media - evidence for significant heat-capacity effects. *J. Org. Chem.* **1990**, *55* (9), 2762-2767.

37. De Wall, S. L.; Meadows, E. S.; Barbour, L. J.; Gokel, G. W., Synthetic receptors as models for alkali metal cation-pi binding sites in proteins. *Proc. Natl. Acad. Sci. USA* **2000**, *97* (12), 6271-6276.

38. Gokel, G. W.; Barbour, L. J.; Ferdani, R.; Hu, J. X., Lariat ether receptor systems show experimental evidence for alkali metal cation-pi interactions. *Acc. Chem. Res.* **2002**, *35* (10), 878-886.

39. Hu, J. X.; Barbour, L. J.; Gokel, G. W., Probing alkali metal-pi interactions with the side chain residue of tryptophan. *Proc. Natl. Acad. Sci. USA* **2002**, *99* (8), 5121-5126.

40. Schottel, B. L.; Chifotides, H. T.; Dunbar, K. R., Anion-pi interactions. *Chem. Soc. Rev.* **2008**, *37* (1), 68-83.

41. Beer, P. D.; Gale, P. A., Anion recognition and sensing: The state of the art and future perspectives. *Angew. Chem. Int. Ed.* **2001**, *40* (3), 486-516.

42. Quiñonero, D.; Garau, C.; Rotger, C.; Frontera, A.; Ballester, P.; Costa, A.; Deyá, P. M., Anion-pi interactions: Do they exist? *Angew. Chem. Int. Ed.* **2002**, *41* (18), 3389-3392.

43. Alkorta, I.; Rozas, I.; Elguero, J., An attractive interaction between the pi-cloud of c6f6 and electron-donor atoms. *J. Org. Chem.* **1997**, *62* (14), 4687-4691.

44. Gallivan, J. P.; Dougherty, D. A., Can lone pairs bind to a pi system? The water center dot center dot center dot hexafluorobenzene interaction. *Org. Lett.* **1999**, *1* (1), 103-105.

45. Danten, Y.; Tassaing, T.; Besnard, M., On the nature of the water-hexafluorobenzene interaction. *J. Phys. Chem. A* **1999**, *103* (18), 3530-3534.

46. Mascal, M.; Armstrong, A.; Bartberger, M. D., Anion-aromatic bonding: A case for anion recognition by pi-acidic rings. *J. Am. Chem. Soc.* **2002**, *124* (22), 6274-6276.

47. Rosokha, Y. S.; Lindeman, S. V.; Rosokha, S. V.; Kochi, J. K., Halide recognition through diagnostic "anion-pi" interactions: Molecular complexes of cl-, br-, and i- with olefinic and aromatic pi receptors. *Angew. Chem. Int. Ed.* **2004**, *43* (35), 4650-4652.

48. Campos-Fernandez, C. S.; Schottel, B. L.; Chifotides, H. T.; Bera, J. K.; Bacsa, J.; Koomen, J. M.; Russell, D. H.; Dunbar, K. R., Anion template effect on the self-assembly and interconversion of metallacyclophanes. *J. Am. Chem. Soc.* **2005**, *127* (37), 12909-12923.

49. Hay, B. P.; Custelcean, R., Anion−π interactions in crystal structures: Commonplace or extraordinary? *Cryst. Growth Des.* **2009**, *9* (6), 2539-2545.

50. Pyykko, P., Strong closed-shell interactions in inorganic chemistry. *Chem. Rev.* **1997**, *97* (3), 597-636.

51. Chu, Q. L.; Swenson, D. C.; MacGillivray, L. R., A single-crystal-to-single-crystal transformation mediated by argentophilic forces converts a finite metal complex into an infinite coordination network. *Angew. Chem. Int. Ed.* **2005**, *44* (23), 3569-3572.

52. Horvath, U. E. I.; McKenzie, J. M.; Cronje, S.; Raubenheimer, H. G.; Barbour, L. J., Intermolecular aurophilic interactions facilitate assembly of a complex rotaxane in solution. *Chem. Commun.* **2009**, (43), 6598-6600.

53. Hoskins, B. F.; Robson, R., Design and construction of a new class of scaffolding-like materials comprising infinite polymeric frameworks of 3-d-linked molecular rods - a reappraisal of the zn(cn)2 and cd(cn)2 structures and the synthesis and structure of the diamond-related frameworks [n(ch3)4][cuiznii(cn)4] and cui[4,4',4",4"'-tetracyanotetraphenylmethane]bf4.Xc6h5no2. *J. Am. Chem. Soc.* **1990**, *112* (4), 1546-1554.

54. Holliday, B. J.; Mirkin, C. A., Strategies for the construction of supramolecular compounds through coordination chemistry. *Angew. Chem. Int. Ed.* **2001**, *40* (11), 2022-2043.

55. Johnson, D. W.; Xu, J. D.; Saalfrank, R. W.; Raymond, K. N., Self-assembly of a three-dimensional [ga-6(l-2)(6)] metal-ligand "cylinder". *Angew. Chem. Int. Ed.* **1999**, *38* (19), 2882-2885.

56. Sato, S.; Ishido, Y.; Fujita, M., Remarkable stabilization of m12l24 spherical frameworks through the cooperation of 48 pd(ii) pyridine interactions. *J. Am. Chem. Soc.* **2009**, *131* (17), 6064-6065.

57. Nam, J. M.; Thaxton, C. S.; Mirkin, C. A., Nanoparticle-based bio-bar codes for the ultrasensitive detection of proteins. *Science* **2003**, *301* (5641), 1884-1886.

58. Kitaura, R.; Kitagawa, S.; Kubota, Y.; Kobayashi, T. C.; Kindo, K.; Mita, Y.; Matsuo, A.; Kobayashi, M.; Chang, H.-C.; Ozawa, T. C.; Suzuki, M.; Sakata, M.; Takata, M., Formation of a one-dimensional array of oxygen in a microporous metal-organic solid. *Science* **2002**, *298* (5602), 2358-2361.

59. Maspoch, D.; Ruiz-Molina, D.; Wurst, K.; Domingo, N.; Cavallini, M.; Biscarini, F.; Tejada, J.; Rovira, C.; Veciana, J., A nanoporous molecular magnet with reversible solvent-induced mechanical and magnetic properties. *Nat. Mater.* **2003**, *2* (3), 190-195.

60. Coronado, E.; Galan-Mascaros, J. R.; Gomez-Garcia, C. J.; Laukhin, V., Coexistence of ferromagnetism and metallic conductivity in a molecule-based layered compound. *Nature* **2000**, *408* (6811), 447-449.

61. Millward, A. R.; Yaghi, O. M., Metal−organic frameworks with exceptionally high capacity for storage of carbon dioxide at room temperature. *J. Am. Chem. Soc.* **2005**, *127* (51), 17998-17999.

62. Leininger, S.; Olenyuk, B.; Stang, P. J., Self-assembly of discrete cyclic nanostructures mediated by transition metals. *Chem. Rev.* **2000**, *100* (3), 853-907.

63. Metrangolo, P.; Neukirch, H.; Pilati, T.; Resnati, G., Halogen bonding based recognition processes: A world parallel to hydrogen bonding. *Acc. Chem. Res.* **2005**, *38* (5), 386-395.

64. Metrangolo, P.; Meyer, F.; Pilati, T.; Resnati, G.; Terraneo, G., Halogen bonding in supramolecular chemistry. *Angew. Chem. Int. Ed.* **2008**, *47* (33), 6114-6127.

65. Metrangolo, P.; Carcenac, Y.; Lahtinen, M.; Pilati, T.; Rissanen, K.; Vij, A.; Resnati, G., Nonporous organic solids capable of dynamically resolving mixtures of diiodoperfluoroalkanes. *Science* **2009**, *323* (5920), 1461-1464.

66. Metrangolo, P.; Resnati, G., Chemistry - halogen versus hydrogen. *Science* **2008**, *321* (5891), 918-919.

67. Legon, A., The interaction of dihalogens and hydrogen halides with lewis bases in the gas phase: An experimental comparison of the halogen bond and the hydrogen bond. In *Halogen bonding*, Metrangolo, P.; Resnati, G., Eds. Springer Berlin / Heidelberg: 2008; Vol. 126, pp 17-64.

68. Walsh, R. B.; Padgett, C. W.; Metrangolo, P.; Resnati, G.; Hanks, T. W.; Pennington, W. T., Crystal engineering through halogen bonding: Complexes of

nitrogen heterocycles with organic iodides. *Cryst. Growth Des.* **2001**, *1* (2), 165-175.

69. Metrangolo, P.; Meyer, F.; Pilati, T.; Resnati, G.; Terraneo, G., Mutual induced coordination in halogen-bonded anionic assemblies with (6,3) cation-templated topologies. *Chem. Commun.* **2008**, (14), 1635-1637.

70. Lehn, J. M., *Supramolecular chemistry: Concepts and perspectives*. VCH: Weinheim, 1995.

71. Jeffrey, G. A., *An introduction to hydrogen bonding*. Oxford University Press: New York, 1997; p vii, p 303.

72. Pauling, L., The nature of the chemical bond. Application of results obtained from the quantum mechanics and from a theory of paramagnetic susceptibility to the structure of molecules. *J. Am. Chem. Soc.* **1931**, *53*, 1367-1400.

73. Pauling, L., *The nature of the chemical bond and the structure of molecules and crystals; an introduction to modern structural chemistry*. Cornell University Press;H. Milford, Oxford University Press: Ithaca, N.Y., London, 1939; p 429.

74. Desiraju, G. R., Chemistry beyond the molecule. *Nature* **2001**, *412* (6845), 397-400.

75. Desiraju, G. R., Hydrogen bridges in crystal engineering: Interactions without borders. *Acc. Chem. Res.* **2002**, *35* (7), 565-573.

76. Anfinsen, C. B., Principles that govern folding of protein chains. *Science* **1973**, *181* (4096), 223-230.

77. Whitesides, G. M.; Mathias, J. P.; Seto, C. T., Molecular self-assembly and nanochemistry - a chemical strategy for the synthesis of nanostructures. *Science* **1991**, *254* (5036), 1312-1319.

78. Philp, D.; Stoddart, J. F., Self-assembly in natural and unnatural systems. *Angew. Chem. Int. Ed.* **1996**, *35* (11), 1154-1196.

79. Pepinsky, R., New concept in crystallography. *Phys. Rev.* **1955**, *100*, 971.

80. Schmidt, G. M. J., Photodimerization in the solid state. *Pure Appl. Chem.* **1971**, *27*, 647-678.

81. Desiraju, G. R., Supramolecular synthons in crystal engineering—a new organic synthesis. *Angew. Chem. Int. Ed.* **1995**, *34* (21), 2311-2327.

82. Corey, E. J., General methods for the construction of complex molecules. *Pure Appl. Chem.* **1967**, *14* (1), 19-38.

83. Wang, X.; Simard, M.; Wuest, J. D., Molecular tectonics - 3-dimensional organic networks with zeolitic properties. *J. Am. Chem. Soc.* **1994**, *116* (26), 12119-12120.

84. Friščić, T.; Jones, W., Benefits of cocrystallisation in pharmaceutical materials science: An update. *J. Pharm. Pharmacol.* **2010**, *62* (11), 1547-1559.

85. Schultheiss, N.; Newman, A., Pharmaceutical cocrystals and their physicochemical properties. *Cryst. Growth Des.* **2009**, *9* (6), 2950-2967.

86. Shan, N.; Zaworotko, M. J., The role of cocrystals in pharmaceutical science. *Drug Discov. Today* **2008**, *13* (9-10), 440-446.

87. Jones, W.; Motherwell, S.; Trask, A. V., Pharmaceutical cocrystals: An emerging approach to physical property enhancement. *MRS Bull.* **2006**, *31* (11), 875-879.

88. Macgillivray, L. R.; Papaefstathiou, G. S.; Friščić, T.; Hamilton, T. D.; Bučar, D.-K.; Chu, Q.; Varshney, D. B.; Georgiev, I. G., Supramolecular control of reactivity in the solid state: From templates to ladderanes to metal-organic frameworks. *Acc. Chem. Res.* **2008**, *41* (2), 280-291.

89. Sokolov, A. N.; Friscic, T.; MacGillivray, L. R., Enforced face-to-face stacking of organic semiconductor building blocks within hydrogen-bonded molecular cocrystals. *J. Am. Chem. Soc.* **2006**, *128* (9), 2806-2807.

90. Kapadia, P. P.; Ditzler, L. R.; Baltrusaitis, J.; Swenson, D. C.; Tivanski, A. V.; Pigge, F. C., Semiconducting organic assemblies prepared from tetraphenylethylene tetracarboxylic acid and bis(pyridine)s via charge-assisted hydrogen bonding. *J. Am. Chem. Soc.* **2011**, *133* (22), 8490-8493.

91. Junghanns, J. U.; Müller, R. H., Nanocrystal technology, drug delivery and clinical applications. *Int. J. Nanomedicine* **2008**, *3* (3), 295-309.

92. Zhang, G. G. Z.; Zhou, D., Chapter 2 - crystalline and amorphous solids. In *Developing solid oral dosage forms*, Yihong, Q.; Yisheng, C.; Geoff, G. Z. Z.; Lirong, L.; William R. PorterA2 - Yihong Qiu, Y. C. G. G. Z. Z. L. L.; William, R. P., Eds. Academic Press: San Diego, 2009; pp 25-60.

93. Almarsson, O.; Zaworotko, M. J., Crystal engineering of the composition of pharmaceutical phases. Do pharmaceutical co-crystals represent a new path to improved medicines? *Chem. Commun.* **2004**, (17), 1889-1896.

94. Remenar, J. F.; Morissette, S. L.; Peterson, M. L.; Moulton, B.; MacPhee, J. M.; Guzman, H. R.; Almarsson, O., Crystal engineering of novel cocrystals of a triazole drug with 1,4-dicarboxylic acids. *J. Am. Chem. Soc.* **2003**, *125* (28), 8456-8457.

95. Karki, S.; Friscic, T.; Fábián, L.; Laity, P. R.; Day, G. M.; Jones, W., Improving mechanical properties of crystalline solids by cocrystal formation: New compressible forms of paracetamol. *Adv. Mater.* **2009**, *21* (38-39), 3905-3909.

96. Sun, C. C.; Hou, H., Improving mechanical properties of caffeine and methyl gallate crystals by cocrystallization. *Cryst. Growth Des.* **2008**, *8* (5), 1575-1579.

97. Hickey, M. B.; Peterson, M. L.; Scoppettuolo, L. A.; Morrisette, S. L.; Vetter, A.; Guzman, H.; Remenar, J. F.; Zhang, Z.; Tawa, M. D.; Haley, S.; Zaworotko, M. J.; Almarsson, O., Performance comparison of a co-crystal of carbamazepine with marketed product. *Eur. J. Pharm. Biopharm.* **2007**, *67* (1), 112-119.

98. Zhang, G. G. Z.; Henry, R. F.; Borchardt, T. B.; Lou, X. C., Efficient co-crystal screening using solution-mediated phase transformation. *J. Pharm. Sci.* **2007**, *96* (5), 990-995.

99. Bučar, D.-K.; Henry, R. F.; Lou, X. C.; Duerst, R. W.; MacGillivray, L. R.; Zhang, G. G. Z., Cocrystals of caffeine and hydroxybenzoic acids composed of multiple supramolecular heterosynthons: Screening via solution-mediated phase transformation and structural characterization. *Cryst. Growth Des.* **2009**, *9* (4), 1932-1943.

100. Bučar, D.-K.; Henry, R. F.; Duerst, R. W.; Lou, X. C.; MacGillivray, L. R.; Zhang, G. G. Z., A 1:1 cocrystal of caffeine and 2-hydroxy-1-naphthoic acid obtained via a slurry screening method. *J. Chem. Crystallogr.* **2010**, *40* (11), 933-939.

101. Bučar, D. K.; Henry, R. F.; Lou, X. C.; Duerst, R. W.; Borchardt, T. B.; MacGillivray, L. R.; Zhang, G. G. Z., Co-crystals of caffeine and hydroxy-2-naphthoic acids: Unusual formation of the carboxylic acid dimer in the presence of a heterosynthon. *Mol. Pharmaceutics* **2007**, *4* (3), 339-346.

102. Bučar, D.-K.; Henry, R. F.; Lou, X.; Borchardt, T. B.; Zhang, G. G. Z., A "hidden" co-crystal of caffeine and adipic acid. *Chem. Commun.* **2007**, (5), 525-527.

103. Mansoori, G. A., *Principles of nanotechnology : Molecular-based study of condensed matter in small systems*. World Scientific: Hackensack, N.J., 2005; p 341.

104. Kasai, H.; Nalwa, H. S.; Oikawa, H.; Okada, S.; Matsuda, H.; Minami, N.; Kakuta, A.; Ono, K.; Mukoh, A.; Nakanishi, H., A novel preparation method of organic microcrystals. *Jpn. J. Appl. Phys.* **1992**, *31*, L1132.

105. Kasai, H.; Kamatani, H.; Okada, S.; Oikawa, H.; Matsuda, H.; Nakanishi, H., Size-dependent colors and luminescences of organic microcrystals. *Jpn. J. Appl. Phys.* **1996**, *35*, L221.

106. Masuhara, H.; Nakanishi, H.; Sasaki, K., *Single organic nanoparticles*. 1 ed.; Springer: Berlin, Heidelberg, New York, 2003; p 402.

107. Baba, K.; Kasai, H.; Nishida, K.; Nakanishi, H., *Functional organic nanocrystals*. 2011.

108. Bučar , D. K.; MacGillivray, L. R., Preparation and reactivity of nanocrystalline cocrystals formed via sonocrystallization. *J. Am. Chem. Soc.* **2007**, *129* (1), 32-33.

109. Childs, S. L.; Rodriguez-Hornedo, N.; Reddy, L. S.; Jayasankar, A.; Maheshwari, C.; McCausland, L.; Shipplett, R.; Stahly, B. C., Screening strategies based on solubility and solution composition generate pharmaceutically acceptable cocrystals of carbamazepine. *CrystEngComm* **2008**, *10* (7), 856-864.

110. Karunatilaka, C.; Bučar, D.-K.; Ditzler, L. R.; Friščić, T.; Swenson, D. C.; MacGillivray, L. R.; Tivanski, A. V., Softening and hardening of macro- and nano-sized organic cocrystals in a single-crystal transformation. *Angew. Chem. Int. Ed.* **2011**, *50* (37), 8642-8646.

111. Cohen, M. D.; Schmidt, G. M. J.; Sonntag, F. I., 384. Topochemistry. Part ii. The photochemistry of trans-cinnamic acids. *J. Chem. Soc.* **1964**, 2000-2013.

112. Schmidt, G. M. J., 385. Topochemistry. Part iii. The crystal chemistry of some trans-cinnamic acids. *J. Chem. Soc.* **1964**, 2014-2021.

113. MacGillivray, L. R.; Reid, J. L.; Ripmeester, J. A., Supramolecular control of reactivity in the solid state using linear molecular templates. *J. Am. Chem. Soc.* **2000**, *122* (32), 7817-7818.

114. Friščić, T.; Macgillivray, L. R., 'Template-switching': A supramolecular strategy for the quantitative, gram-scale construction of a molecular target in the solid state. *Chem. Commun.* **2003**, (11), 1306-1307.

115. Friscic, T.; MacGillivray, L. R., Reversing the code of a template-directed solid-state synthesis: A bipyridine template that directs a single-crystal-to-single-crystal [2+2] photodimerisation of a dicarboxylic acid. *Chem. Commun.* **2005**, (46), 5748-5750.

116. Papaefstathiou, G. S.; Zhong, Z. M.; Geng, L.; MacGillivray, L. R., Coordination-driven self-assembly directs a single-crystal-to-single-crystal transformation that exhibits photocontrolled fluorescence. *J. Am. Chem. Soc.* **2004**, *126* (30), 9158-9159.

117. Jung, O.-S.; Kim, Y. J.; Lee, Y.-A.; Kang, S. W.; Choi, S. N., Tunable transannular silver−silver interaction in molecular rectangles. *Cryst. Growth Des.* **2003**, *4* (1), 23-24.

118. Brandys, M.-C.; Puddephatt, R. J., Ring, polymer and network structures in silver() complexes with dipyridyl and diphosphine ligands. *Chem. Commun.* **2001**, (16), 1508-1509.

119. Munakata, M.; Ning, G. L.; Suenaga, Y.; Kuroda-Sowa, T.; Maekawa, M.; Ohta, T., A one-dimensional metallocyclophane with columnar aromatic stacking: The silver(i) η2-coordination complex of 1,2-benztriphenylene. *Angew. Chem. Int. Ed.* **2000**, *112* (24), 4729-4731.

120. Ohba, S.; Hosomi, H.; Ito, Y., In situ x-ray observation of pedal-like conformational change and dimerization of trans-cinnamamide in cocrystals with phthalic acid. *J. Am. Chem. Soc.* **2001**, *123* (26), 6349-6352.

121. Eddaoudi, M.; Kim, J.; Rosi, N.; Vodak, D.; Wachter, J.; O'Keeffe, M.; Yaghi, O. M., Systematic design of pore size and functionality in isoreticular mofs and their application in methane storage. *Science* **2002**, *295* (5554), 469-472.

122. Li, H.; Eddaoudi, M.; O'Keeffe, M.; Yaghi, O. M., Design and synthesis of an exceptionally stable and highly porous metal-organic framework. *Nature* **1999**, *402* (6759), 276-279.

123. Mulfort, K. L.; Hupp, J. T., Chemical reduction of metal−organic framework materials as a method to enhance gas uptake and binding. *J. Am. Chem. Soc.* **2007**, *129* (31), 9604-9605.

124. Matsuda, R.; Kitaura, R.; Kitagawa, S.; Kubota, Y.; Belosludov, R. V.; Kobayashi, T. C.; Sakamoto, H.; Chiba, T.; Takata, M.; Kawazoe, Y.; Mita, Y., Highly controlled acetylene accommodation in a metal–organic microporous material. *Nature* **2005**, *436* (7048), 238-241.

125. Zhang, J.-P.; Kitagawa, S., Supramolecular isomerism, framework flexibility, unsaturated metal center, and porous property of ag(i)/cu(i) 3,3‘,5,5‘-tetrametyl-4,4‘-bipyrazolate. *J. Am. Chem. Soc.* **2008**, *130* (3), 907-917.

126. Tanabe, K. K.; Wang, Z.; Cohen, S. M., Systematic functionalization of a metal−organic framework via a postsynthetic modification approach. *J. Am. Chem. Soc.* **2008**, *130* (26), 8508-8517.

127. Li, Q.; Zhang, W.; Miljanić, O. Š.; Sue, C.-H.; Zhao, Y.-L.; Liu, L.; Knobler, C. B.; Stoddart, J. F.; Yaghi, O. M., Docking in metal-organic frameworks. *Science* **2009**, *325* (5942), 855-859.

128. Kitagawa, S.; Kitaura, R.; Noro, S.-i., Functional porous coordination polymers. *Angew. Chem. Int. Ed.* **2004**, *43* (18), 2334-2375.

129. deKrafft, K. E.; Xie, Z.; Cao, G.; Tran, S.; Ma, L.; Zhou, O. Z.; Lin, W., Iodinated nanoscale coordination polymers as potential contrast agents for computed tomography. *Angew. Chem. Int. Ed.* **2009**, *48* (52), 9901-9904.

130. Férey, G., Hybrid porous solids: Past, present, future. *Chem. Soc. Rev.* **2008**, *37* (1), 191-214.

131. Boldyreva, E. V.; Shakhtshneider, T. P.; Vasilchenko, M. A.; Ahsbahs, H.; Uchtmann, H., Anisotropic crystal structure distortion of the monoclinic polymorph of acetaminophen at high hydrostatic pressures. *Acta Crystallog. B* **2000**, *56* (2), 299-309.

132. Haisa, M.; Kashino, S.; Maeda, H., The orthorhombic form of p-hydroxyacetanilide. *Acta Crystallog. B* **1974**, *B30*, 2510-2512.

133. Haisa, M.; Kashino, S.; Kawai, R.; Maeda, H., The monoclinic form of p-hydroxyacetanilide. *Acta Crystallog. B* **1976**, *B32*, 1283-1285.

134. Fachaux, J. M.; Guyot-Hermann, A. M.; Guyot, J. C.; Conflant, P.; Drache, M.; Veesler, S.; Boistelle, R., Pure paracetamol for direct compression part i. Development of sintered-like crystals of paracetamol. *Powder Technol.* **1995**, *82* (2), 123-128.

135. Roberts, R. J.; Rowe, R. C., The young's modulus of pharmaceutical materials. *Int. J. Pharm.* **1987**, *37* (1–2), 15-18.

136. Duncanhewitt, W. C.; Weatherly, G. C., Modeling the uniaxial compaction of pharmaceutical powders using the mechanical-properties of single-crystals .1. Ductile materials. *J. Pharm. Sci.* **1990**, *79* (2), 147-152.

137. Danielson, D. W.; Morehead, W. T.; Rippie, E. G., Unloading and postcompression viscoelastic stress versus strain behavior of pharmaceutical solids. *J. Pharm. Sci.* **1983**, *72* (4), 342-345.

138. Desai, R.; Neau, S.; Pather, S.; Johnston, T., Fine-particle ethylcellulose as a tablet binder in direct compression, immediate-release tablets. *Dru Dev. Ind. Pharm.* **2001**, *27* (7), 633.

139. Fachaux, J. M.; Guyot Hermann, A. M.; Guyot, J. C.; Conflant, P.; Drache, M.; Huvenne, J. P.; Bouche, R., Compression ability improvement by solvation/desolvation process: Application to paracetamol for direct compression. *Int. J. Pharm.* **1993**, *99* (2–3), 99-107.

140. Beyer, T.; Day, G. M.; Price, S. L., The prediction, morphology, and mechanical properties of the polymorphs of paracetamol. *J. Am. Chem. Soc.* **2001**, *123* (21), 5086-5094.

141. DiMartino, P.; GuyotHermann, A. M.; Conflant, P.; Drache, M.; Guyot, J. C., A new pure paracetamol for direct compression: The orthorhombic form. *Int. J. Pharm.* **1996**, *128* (1-2), 1-8.

142. Rasenack, N.; Müller, B. W., Crystal habit and tableting behavior. *Int. J. Pharm.* **2002**, *244* (1–2), 45-57.

143. Hendriksen, B. A.; Grant, D. J. W.; Meenan, P.; Green, D. A., Crystallisation of paracetamol (acetaminophen) in the presence of structurally related substances. *J. Cryst. Growth* **1998**, *183* (4), 629-640.

144. Chow, A. H. L.; Grant, D. J. W., Modification of acetaminophen crystals. Ii. Influence of stirring rate during solution-phase growth on crystal properties in the presence and absence of p-acetoxyacetanilide. *Int. J. Pharm.* **1988**, *41* (1–2), 29-39.

145. Chow, A. H. L.; Grant, D. J. W., Modification of acetaminophen crystals. Iii. Influence of initial supersaturation during solution-phase growth on crystal properties in the presence and absence of p-acetoxyacetanilide. *Int. J. Pharm.* **1988**, *42* (1–3), 123-133.

146. Akande, O. F.; Rubinstein, M. H.; Ford, J. L., Examination of the compaction properties of a 1:1 acetaminophen:Microcrystalline cellulose mixture using precompression and main compression. *J. Pharm. Sci.* **1997**, *86* (8), 900-907.

147. Mikhailenko, M. A., Growth of large single crystals of the orthorhombic paracetamol. *J. Cryst. Growth* **2004**, *265* (3-4), 616-618.

148. Lang, M.; Grzesiak, A. L.; Matzger, A. J., The use of polymer heteronuclei for crystalline polymorph selection. *J. Am. Chem. Soc.* **2002**, *124* (50), 14834-14835.

149. Nichols, G.; Frampton, C. S., Physicochemical characterization of the orthorhombic polymorph of paracetamol crystallized from solution. *J. Pharm. Sci.* **1998**, *87* (6), 684-693.

150. Fabbiani, F. P. A.; Allan, D. R.; Marshall, W. G.; Parsons, S.; Pulham, C. R.; Smith, R. I., High-pressure recrystallisation - a route to new polymorphs and solvates of acetamide and parabanic acid. *J. Cryst. Growth* **2005**, *275* (1-2), 185-192.

151. Boldyreva, E.; Drebushchak, V.; Paukov, I.; Kovalevskaya, Y.; Drebushchak, T., Dsc and adiabatic calorimetry study of the polymorphs of paracetamol. *J. Therm. Anal. Calorim.* **2004**, *77* (2), 607-623.

152. Al-Zoubi, N.; Kachrimanis, K.; Malamataris, S., Effects of harvesting and cooling on crystallization and transformation of orthorhombic paracetamol in ethanolic solution. *Eur. J. Pharm. Sci.* **2002**, *17* (1-2), 13-21.

153. Al-Zoubi, N.; Malamataris, S., Effects of initial concentration and seeding procedure on crystallisation of orthorhombic paracetamol from ethanolic solution. *Int. J. Pharm.* **2003**, *260* (1), 123-135.

154. Al-Zoubi, N.; Nikolakakis, I.; Malamataris, S., Crystallization conditions and formation of orthorhombic paracetamol from ethanolic solution. *J. Pharm. Pharmacol.* **2002**, *54* (3), 325-333.

155. Kachrimanis, K.; Fucke, K.; Noisternig, M.; Siebenhaar, B.; Griesser, U., Effects of moisture and residual solvent on the phase stability of orthorhombic paracetamol. *Pharm. Res.* **2008**, *25* (6), 1440-1449.

156. Zimmermann, B.; Baranović, G., Thermal analysis of paracetamol polymorphs by ft-ir spectroscopies. *J. Pharm. Biomed. Anal.* **2011**, *54* (2), 295-302.

157. Hollingsworth, M. D., Crystal engineering: From structure to function. *Science* **2002**, *295* (5564), 2410-2413.

158. Fábián, L., Cambridge structural database analysis of molecular complementarity in cocrystals. *Cryst. Growth Des.* **2009**, *9* (3), 1436-1443.

159. Desiraju, G. R., Crystal engineering: A brief overview. *J. Chem. Sci.* **2010**, *122* (5), 667-675.

160. Desiraju, G. R., Crystal engineering: A holistic view. *Angew. Chem. Int. Ed.* **2007**, *46* (44), 8342-8356.

161. Bhatt, P. M.; Azim, Y.; Thakur, T. S.; Desiraju, G. R., Co-crystals of the anti-hiv drugs lamivudine and zidovudine. *Cryst. Growth Des.* **2009**, *9* (2), 951-957.

162. Otwinowski, Z.; Schevitz, R. W.; Zhang, R.-G.; Lawson, C. L.; Joachimiak, A.; Marmorstein, R. Q.; Luisi, B. F.; Sigler, P. B., Crystal structure of *trp* repressor/operator complex at atomic resolution. *Nature* **1988**, *335* (22), 321-329.

163. Clarke, H. D.; Arora, K. K.; Bass, H.; Kavuru, P.; Ong, T. T.; Pujari, T.; Wojtas, L.; Zaworotko, M. J., Structure-stability relationships in cocrystal hydrates: Does the promiscuity of water make crystalline hydrates the nemesis of crystal engineering? *Cryst. Growth Des.* **2010**, *10* (5), 2152-2167.

164. Infantes, L.; Chisholm, J.; Motherwell, S., Extended motifs from water and chemical functional groups in organic molecular crystals. *CrystEngComm* **2003**, *5*, 480-486.

165. Infantes, L.; Fabian, L.; Motherwell, W. D. S., Organic crystal hydrates: What are the important factors for formation. *CrystEngComm* **2007**, *9* (1), 65-71.

166. Infantes, L.; Motherwell, S., Water clusters in organic molecular crystals. *CrystEngComm* **2002**, *4* (75), 454-461.

167. Gillon, A. L.; Feeder, N.; Davey, R. J.; Storey, R., Hydration in molecular crystals - a cambridge structural database analysis. *Cryst. Growth Des.* **2003**, *3* (5), 663-673.

168. Aitipamula, S.; Chow, P. S.; Tan, R. B. H., Polymorphs and solvates of a cocrystal involving an analgesic drug, ethenzamide, and 3,5-dinitrobenzoic acid. *Cryst. Growth Des.* **2010**, *10* (5), 2229-2238.

169. Oswald, I. D. H.; Allan, D. R.; McGregor, P. A.; Motherwell, W. D. S.; Parsons, S.; Pulham, C. R., The formation of paracetamol (acetaminophen) adducts with hydrogen-bond acceptors. *Acta Crystallogr. Sect. B* **2002**, *58*, 1057-1066.

170. Symponix; Inel Corp.: Artenay, France.

171. Jade 6.5; Materials Data, Inc.: Livermore, CA, 2002.

172. SaintPlus, (1997-2003) Bruker AXS Inc., Madison, WI, USA.

173. Sheldrick, G. M., A short history of shelx. *Acta Cryst.* **2008**, *A64*, 112-122.

174. SaintPlus, (1997-2003) Bruker AXS Inc., Madison, WI, USA.

175. R. Dovesi, V. R. Saunders, C. Roetti, R. Orlando, C. M. Zicovich-Wilson, F. Pascale, B. Civalleri, K. Doll, N. M. Harrison, I. J. Bush, P. D'Arco, M. Llunell. 2006. OT CRYSTAL'06. User's Manual; University of Torino: Torino.

176. 2004. XSHELL. v6.3.1ed., Madison, WI USA: Bruker AXS Inc.

177. Becke, A. D., Density-functional thermochemistry. Iii. The role of exact exchange. *J. Chem. Phys.* **1993**, *98*, 5648-5652.

178. Lee, C.; Yang, W.; Parr, R. G., Development of the colle-salvetti correlation-energy formula into a functional of the electron density. *Phys. Rev. B* **1988**, *37*.

179. Searle, B. G., Dl visualize. *Comput. Phys. Commun.* **2001**, *137*, 25-32.

180. Khan, M.; Enkelmann, V.; Brunklaus, G., O-h center dot center dot center dot n heterosynthon: A robust supramolecular unit for crystal engineering. *Cryst. Growth Des.* **2009**, *9* (5), 2354-2362.

181. Desiraju, G. R., Hydration in organic-crystals - prediction from molecular-structure. *J. Chem. Soc., Chem. Commun.* **1991**, (6), 426-428.

182. Etter, M. C., Encoding and decoding hydrogen-bond patterns of organic-compounds. *Acc. Chem. Res.* **1990**, *23* (4), 120-126.

183. Toda, F.; Tanaka, K.; Sekikawa, A., Host-guest complex formation by a solid-solid reaction. *J. Chem. Soc., Chem. Commun* **1987**, (4), 279-280.

184. Lien Nguyen, K.; Friscic, T.; Day, G. M.; Gladden, L. F.; Jones, W., Terahertz time-domain spectroscopy and the quantitative monitoring of mechanochemical cocrystal formation. *Nat. Mater.* **2007**, *6* (3), 206-209.

185. Shan, N.; Toda, F.; Jones, W., Mechanochemistry and co-crystal formation: Effect of solvent on reaction kinetics. *Chem. Commun.* **2002**, (20), 2372-2373.

186. Friščić, T.; Jones, W., Recent advances in understanding the mechanism of cocrystal formation via grinding. *Cryst. Growth Des.* **2009**, *9* (3), 1621-1637.

187. Braga, D.; Grepioni, F.; Maini, L.; Mazzeo, P. P.; Rubini, K., Solvent-free preparation of co-crystals of phenazine and acridine with vanillin. *Thermochim. Acta* **2010**, *507-08*, 1-8.

188. Czapik, A.; Gdaniec, M., Phenazine-naphthalene-1,5-diamine-water (1/1/2). *Acta Crystallogr. E* **2009**, *65*, O3177-U1333.

189. Antipin, M. Y.; Akhmedov, A. I.; Struchkov, Y. T.; Matrosov, E. I.; Kabachnik, M. I., Structure of organo-phosphorus compounds .23. An x-ray crystallographic study of the molecular-complex of triphenylphosphine oxide with tetrachloropyrocatechol, ph3po-c6cl4(oh)2, and its hydrate, ph3po-c6cl4(oh)2-h2o. *J. Struct. Chem.* **1983**, *24* (6), 888-893.

190. Wang, M. F., 1,4-dihydroquinoxaline-2,3-dione-5-nitroisophthalic acid-water (1/1/1). *Acta Crystallogr. E* **2011**, *67*, O1581-U1949.

191. Ueda, M.; Mochida, T.; Furukawa, S.; Suzuki, H.; Moriyama, H.; Mori, H., Crystal structures and magnetic properties of hydrogen-bonded nitronyl nitroxide radicals and their metal complexes. *Mol. Cryst. Liq. Cryst.* **2002**, *379*, 153-158.

192. Buczak, G.; Dega-Szafran, Z.; Katrusiak, A.; Szafran, M., Crystal structure and vibrational spectra of the 1 : 1 and 1 : 2 complexes of pyridine betaine with pentachlorophenol. *J. Mol. Struct.* **1997**, *437*, 143-151.

193. PrakashaReddy, J.; Pedireddi, V. R., Synthesis and analysis of some adducts of 3,5-dinitrobenzamide. *Tetrahedron* **2004**, *60* (40), 8817-8827.

194. Smith, G.; Lynch, D. E.; Byriel, K. A.; Kennard, C. H. L., Molecular cocrystals of carboxylic acids .24. Cocrystals involving triphenylphosphine oxide: Structures of the unique adduct hydrates of triphenylphosphine oxide with adamantane carboxylic acid and terephthalic acid, and the anhydrous adduct with o-phthalic acid. *Z. Kristallogr.* **1997**, *212* (2), 130-134.

195. Al-Farhan, K. A., *J. Saudi Chem. Soc.* **2000**, *4*, 169.

196. Cheney, M. L.; Shan, N.; Healey, E. R.; Hanna, M.; Wojtas, L.; Zaworotko, M. J.; Sava, V.; Song, S. J.; Sanchez-Ramos, J. R., Effects of crystal form on solubility and pharmacokinetics: A crystal engineering case study of lamotrigine. *Cryst. Growth Des.* **2010**, *10* (1), 394-405.

197. Rafilovich, M.; Bernstein, J.; Hickey, M. B.; Tauber, M., Benzidine: A co-crystallization agent for proton acceptors. *Cryst. Growth Des.* **2007**, *7* (9), 1777-1782.

198. Pedireddi, V. R.; PrakashaReddy, J., Supramolecular pseudopolymorphs: Double helix and planar structures with channels. *Tetrahedron Lett.* **2003**, *44* (35), 6679-6681.

199. Arora, K. K.; Talwelkar, M. S.; Pedireddi, V. R., Supramolecular synthesis of some molecular adducts of 4,4 '-bipyridine n,n '-dioxide. *New J. Chem.* **2009**, *33* (1), 57-63.

200. Lemmerer, A., Seven hexamethylenetetramine (hmta) complexes with mono- and dicarboxylic acids: Analysis of packing modes of hmta complexes in the literature. *Acta Crystallogr. Sect. B* **2011**, *67*, 177-192.

201. Turkington, D. E.; Lough, A. J.; Ferguson, G.; Glidewell, C., Hydrogen-bonded adducts of triphenylsilanol with diamines: A finite ten-molecule aggregate, and chain, sheet and framework structures built from o-h center dot center dot center dot o, o-h center dot center dot center dot n and c-h center dot center dot center dot pi(arene) hydrogen bonds. *Acta Crystallogr. Sect. B* **2004**, *60*, 238-248.

202. Lynch, D. E.; Smith, G.; Byriel, K. A.; Kennard, C. H. L., Molecular cocrystals of carboxylic-acids .2. The crystal-structure of the 1-2 adduct of phenoxyacetic acid with 3,5-dinitrobenzoic acid. *Aust. J. Chem.* **1991**, *44* (7), 1017-1022.

203. Kariuki, B. M.; Harris, K. D. M.; Philp, D.; Robinson, J. M. A., A triphenylphoshine oxide-water aggregate facilitates an exceptionally short c-h center dot center dot center dot o hydrogen bond. *J. Am. Chem. Soc.* **1997**, *119* (51), 12679-12680.

204. Senthil Kumar, V. S.; Nangia, A.; Katz, A. K.; Carrell, H. L., Molecular complexes of some mono- and dicarboxylic acids with trans-1,4-dithiane-1,4-dioxide. *Cryst. Growth Des.* **2002**, *2* (4), 313-318.

205. Sarangarajan, T. R.; Panchanatheswaran, K.; Low, J. N.; Glidewell, C., Piperazine-2,5-dione-oxalic acid-water (1/1/2) and a redetermination of piperazine-2,5-dione, both at 120 k: Hydrogen-bonded sheets containing multiple ring types. *Acta Crystallogr. Sect. C* **2005**, *61*, O118-O121.

206. Britton, D.; Chantooni, M. K., Crystal structures of complexes of tri-, tetra-, or nonaethyleneglycol dimethyl ether with dichloropicric acid and water. *J. Chem. Crystallogr.* **2001**, *31* (1), 5-16.

207. Chantooni, M. K.; Britton, D.; Kolthoff, I. M., X-ray crystal-structure of the 1/2/2 pentaethyleneglycol dimethyl ether(pentaglyme) - dichloropicric acid - water complex - infrared studies of the 1/2/2 complexes with triglyme, tetraglyme, and pentaglyme. *J. Cryst. Spectrosc.* **1993**, *23* (6), 497-503.

208. Lavy, T.; Meirovich, N.; Sparkes, H. A.; Howard, J. A. K.; Kaftory, M., Cocrystals composed of 4,4 '-(fluorene-9,9-diyl) diphenol and 6-methyl-2h-pyridone. *Acta Crystallogr. Sect. C* **2007**, *63*, O89-O92.

209. Smith, G.; Wermuth, U. D.; Healy, P. C.; Young, D. J., Strychnine-8-ammonio-2-naphthalenesulfonate-water (1/1/3.5): The first structure of a strychnine or brucine compound with a zwitterionic species. *J. Chem. Crystallogr.* **2006**, *36* (12), 805-811.

210. Hadadzadeh, H.; Rezvani, A. R.; Abdolmaleki, M. K.; Ghasemi, K.; Esfandiari, H.; Daryanavard, M., Pyridine-2,6-dicarboxylic acid (dipic): Crystal structure from co-crystal to a mixed ligand nickel(ii) complex. *J. Chem. Crystallogr.* **2010**, *40* (1), 48-57.

211. Zaman, B.; Udachin, K. A.; Ripmeester, J. A., Supramolecular grid and layer architectures. Hydrogen bonds and halogen-halogen interactions influenced by bromo-, chloro-, and cyano-substituted anilic acids. *Cryst. Growth Des.* **2004**, *4* (3), 585-589.

212. Bowes, K. F.; Ferguson, G.; Lough, A. J.; Glidewell, C., The 1 : 1 adduct of triphenylsilanol and 4,4 '-bipyridyl, and three pairwise-concomitant triclinic polymorphs of the 4 : 1 adduct having z ' = 0.5, 1 and 4. *Acta Crystallogr. Sect. B* **2003**, *59*, 277-286.

213. Linag, P., A cocrystal of pyridine-2,4-dicarboxylic acid and serine. *Acta Crystallogr. E* **2008**, *E64*, o43.

214. Calculated values were obtained from the Sci-Finder Scholar database (version 2007) calculated using Advanced Chemistry Development (ACD/Labs) Software (version 8.14) for Solaris (copyright 1994-2010 ACD/Labs).

215. Cruz-Cabeza, A. J., Acid-base crystalline complexes and the pka rule. *CrystEngComm* **2012**, *14*, 6362-6365.

216. Sharma, C. V. K.; Panneerselvam, K.; Pilati, T.; Desiraju, G. R., Molecular recognition involving an interplay of o-h · · · o, c-h · · · o, and π · · · π-interactions. The anomalous crystal-structure of the 1:1 complex 3,5-dinitrobenzoic acid-4-(n,n-dimethylamino)benzoic acid. *J. Chem. Soc., Perkin Trans.* **1993**, *2*, 2209-2216.

217. Aakeröy, C. B.; Beatty, A. M.; Helfrich, B. A., Total synthesis supramolecular style: Design and hydrogen-bond-directed assembly of ternary supermolecules. *Angew. Chem. Int. Ed.* **2001**, *40*, 3240-3242.

218. Aakeröy, C. B.; Bahra, G. S.; Brown, C. R.; Hitchcock, P. B.; Patell, Y.; Seddon, K. R., L-proline 2,5-dihydroxybenzoic acid (1/1): A zwitterion co-crystal. *Acta Chem. Scand.* **1995**, *49*, 762-767.

219. Zhao, Y. S.; Fu, H.; Peng, A.; Ma, Y.; Xiao, D.; Yao, J., Low-dimensional nanomaterials based on small organic molecules: Preparation and optoelectronic properties. *Adv. Mater.* **2008**, *20* (15), 2859-2876.

220. Somorjai, G. A., Modern surface science and surface technologies: An introduction. *Chem. Rev.* **1996**, *96* (4), 1223-1235.

221. Burda, C.; Chen, X. B.; Narayanan, R.; El-Sayed, M. A., Chemistry and properties of nanocrystals of different shapes. *Chem. Rev.* **2005**, *105* (4), 1025-1102.

222. Rosi, N. L.; Mirkin, C. A., Nanostructures in biodiagnostics. *Chem. Rev.* **2005**, *105* (4), 1547-1562.

223. Kwon, E.; Oikawa, H.; Kasai, H.; Nakanishi, H., A fabrication method of organic nanocrystals using stabilizer-free emulsion. *Cryst. Growth Des.* **2007**, *7* (4), 600-602.

224. Köhler, J. M.; Fritzsche, W., *Nanotechnology : An introduction to nanostructuring techniques*. Wiley-VCH: Weinheim, 2004; p 272.

225. Kang, P.; Chen, C. N.; Hao, L. Y.; Zhu, C. L.; Hu, Y.; Chen, Z. Y., A novel sonication route to prepare anthracene nanoparticles. *Mater. Res. Bull.* **2004**, *39* (4-5), 545-551.

226. Jiang, Q.; Shi, H. X.; Zhao, M., Melting thermodynamics of organic nanocrystals. *J. Chem. Phys.* **1999**, *111* (5), 2176-2180.

227. Takahashi, S.; Miura, H.; Kasai, H.; Okada, S.; Oikawa, H.; Nakanishi, H., Single-crystal-to-single-crystal transformation of diolefin derivatives in nanocrystals. *J. Am. Chem. Soc.* **2002**, *124* (37), 10944-10945.

228. Baba, K.; Kasai, H.; Okada, S.; Nakanishi, H.; Oikawa, H., Fabrication of diacetylene nanofibers and their dynamic behavior in the course of solid-state polymerization. *Mol. Cryst. Liq. Cryst.* **2006**, *445* (1), 161/[451]-166/[456].

229. Horn, D.; Rieger, J., Organic nanoparticles in the aqueous phase - theory, experiment, and use. *Angew. Chem. Int. Ed.* **2001**, *40* (23), 4331-4361.

230. An, B.-K.; Gierschner, J.; Park, S. Y., Π-conjugated cyanostilbene derivatives: A unique self-assembly motif for molecular nanostructures with enhanced emission and transport. *Acc. Chem. Res.* **2011**, *45* (4), 544-554.

231. An, B.-K.; Kwon, S.-K.; Jung, S.-D.; Park, S. Y., Enhanced emission and its switching in fluorescent organic nanoparticles. *J. Am. Chem. Soc.* **2002**, *124* (48), 14410-14415.

232. Müller, R. H.; Jacobs, C.; Kayser, O., Nanosuspensions as particulate drug formulations in therapy: Rationale for development and what we can expect for the future. *Adv. Drug. Deliver. Rev.* **2001**, *47* (1), 3-19.

233. Patravale, V. B.; Date, A. A.; Kulkarni, R. M., Nanosuspensions: A promising drug delivery strategy. *J. Pharm. Pharmacol.* **2004**, *56* (7), 827-840.

234. Wang, G. D.; Mallet, F. P.; Ricard, F.; Heng, J. Y. Y., Pharmaceutical nanocrystals. *Curr. Opin. Chem. Eng.* **2012**, *1* (2), 102-107.

235. Van Eerdenbrugh, B.; Van den Mooter, G.; Augustijns, P., Top-down production of drug nanocrystals: Nanosuspension stabilization, miniaturization and transformation into solid products. *Int. J. Pharm.* **2008**, *364* (1), 64-75.

236. Kesisoglou, F.; Panmai, S.; Wu, Y. H., Nanosizing - oral formulation development and biopharmaceutical evaluation. *Adv. Drug. Deliver. Rev.* **2007**, *59* (7), 631-644.

237. Keck, C. M.; Muller, R. H., Drug nanocrystals of poorly soluble drugs produced by high pressure homogenisation. *Eur. J. Pharm. Biopharm.* **2006**, *62* (1), 3-16.

238. Dhumal, R. S.; Biradar, S. V.; Yamamura, S.; Paradkar, A. R.; York, P., Preparation of amorphous cefuroxime axetil nanoparticles by sonoprecipitation for enhancement of bioavailability. *Eur. J. Pharm. Biopharm.* **2008**, *70* (1), 109-115.

239. Suslick, K. S., Sonochemistry. *Science* **1990**, *247* (4949), 1439-1445.

240. Ruecroft, G.; Hipkiss, D.; Ly, T.; Maxted, N.; Cains, P. W., Sonocrystallization: The use of ultrasound for improved industrial crystallization. *Org. Process Res. Dev.* **2005**, *9* (6), 923-932.

241. Kelly, D. R.; Harrison, S. J.; Jones, S.; Masood, M. A.; Morgan, J. J. G., Rapid crystallization using ultrasonic irradiation-sonocrystallisation. *Tetrahedron Lett.* **1993**, *34* (16), 2689-2690.

242. Manish, M.; Harshal, J.; Anant, P., Melt sonocrystallization of ibuprofen: Effect on crystal properties. *Eur. J. Pharm. Sci.* **2005**, *25* (1), 41-48.

243. Bang, J. H.; Suslick, K. S., Sonochemical synthesis of nanosized hollow hematite. *J. Am. Chem. Soc.* **2007**, *129* (8), 2242-+.

244. Trask, A. V.; Motherwell, W. D. S.; Jones, W., Pharmaceutical cocrystallization: Engineering a remedy for caffeine hydration. *Cryst. Growth Des.* **2005**, *5* (3), 1013-1021.

245. Friščić, T.; Childs, S. L.; Rizvi, S. A. A.; Jones, W., The role of solvent in mechanochemical and sonochemical cocrystal formation: A solubility-based approach for predicting cocrystallisation outcome. *CrystEngComm* **2009**, *11* (3), 418-426.

246. The Merck Index. 14th ed.; Merck & Co., Inc.: Whitehouse Station, NJ, USA, 2001.

247. Bak, A.; Gore, A.; Yanez, E.; Stanton, M.; Tufekcic, S.; Syed, R.; Akrami, A.; Rose, M.; Surapaneni, S.; Bostick, T.; King, A.; Neervannan, S.; Ostovic, D.; Koparkar, A., The co-crystal approach to improve the exposure of a water-insoluble compound: Amg 517 sorbic acid co-crystal characterization and pharmacokinetics. *J. Pharm. Sci.* **2008**, *97* (9), 3942-3956.

248. Good, D. J.; Rodriguez-Hornedo, N., Solubility advantage of pharmaceutical cocrystals. *Cryst. Growth Des.* **2009**, *9* (5), 2252-2264.

249. Symphonix; Inel Corp.: Artenay, France

250. Jade 6.5; Materials Data, Inc.: Livermore, CA, 2002.

251. Chung, H. R.; Kwon, E.; Kawa, H.; Kasai, H.; Nakanishi, H., Effect of solvent on organic nanocrystal growth using the reprecipitation method. *J. Cryst. Growth* **2006**, *294* (2), 459-463.

252. Gu, C.-H.; Young, V.; Grant, D. J. W., Polymorph screening: Influence of solvents on the rate of solvent-mediated polymorphic transformation. *J. Pharm. Sci.* **2001**, *90* (11), 1878-1890.

253. Gong, Y.; Collman, B. M.; Mehrens, S. M.; Lu, E.; Miller, J. M.; Blackburn, A.; Grant, D. J. W., Stable-form screening: Overcoming trace impurities that inhibit solution-mediated phase transformation to the stable polymorph of sulfamerazine. *J. Pharm. Sci.* **2008**, *97* (6), 2130-2144.

254. Mullin, J. W., *Crystallization*. 4th ed.; Butterworth-Heinemann: Oxford ; Boston, 2001; p 594.

255. Mori, J.; Miyashita, Y.; Oliveira, D.; Kasai, H.; Oikawa, H.; Nakanishi, H., Stopped-flow analysis on the mechanism of perylene nanoparticle formation by the reprecipitation method. *J. Cryst. Growth* **2009**, *311* (3), 553-555.

256. Lindenberg, C.; Schöll, J.; Vicum, L.; Mazzotti, M.; Brozio, J., L-glutamic acid precipitation: Agglomeration effects. *Cryst. Growth Des.* **2007**, *8* (1), 224-237.

257. Rabinow, B. E., Nanosuspensions in drug delivery. *Nat. Rev. Drug Discov.* **2004**, *3* (9), 785-796.

258. Matteucci, M. E.; Hotze, M. A.; Johnston, K. P.; Williams, R. O., Drug nanoparticles by antisolvent precipitation: Mixing energy versus surfactant stabilization. *Langmuir* **2006**, *22* (21), 8951-8959.

259. Dalvi, S. V.; Dave, R. N., Controlling particle size of a poorly water-soluble drug using ultrasound and stabilizers in antisolvent precipitation. *Ind. Eng. Chem. Res.* **2009**, *48* (16), 7581-7593.

260. Liu, Y.; Dong, X. Y.; Sun, Y., Characterization of reversed micelles of cibacron blue f-3ga modified span 85 for protein solubilization. *J. Colloid. Interf. Sci.* **2005**, *290* (1), 259-266.

261. Baba, K.; Kasai, H.; Okada, S.; Oikawa, H.; Nakanishi, H., Novel fabrication process of organic microcrystals using microwave-irradiation. *Jpn. J. Appl. Phys.* **2000**, *39*, L1256.

262. Moorthy, J. N.; Natarajan, R.; Savitha, G.; Venugopalan, P., Influence of weaker interactions on the self-assembly of rigid molecular scaffolds based on tetraarylbimesityls. *Cryst. Growth Des.* **2006**, *6* (4), 919-924.

263. Allen, F. H., The cambridge structural database: A quarter of a million crystal structures and rising. *Acta Crystallogr. Sect. B* **2002**, *B58*, 380-388.

264. Field, J. E.; Combariza, M. Y.; Vachet, R. W.; Venkataraman, D., Spontaneous assembly of a hydrogen-bonded tetrahedron. *Chem. Commun.* **2002**, (19), 2260-2261.

265. Ward, M. D.; Horner, M. J., Structure and order in soft matter: Symmetry transcending length scale. *CrystEngComm* **2004**, *6*, 401-407.

266. MacGillivray, L. R.; Atwood, J. L., A chiral spherical molecular assembly held together by 60 hydrogen bonds. *Nature* **1997**, *389* (6650), 469-472.

267. Wyler, R.; de Mendoza, J.; Rebek, J., A synthetic cavity assembles through self-complementary hydrogen bonds. *Angew. Chem. Int. Ed.* **1993**, *32* (12), 1699-1701.

268. Shivanyuk, A.; Rebek, J., Reversible encapsulation by self-assembling resorcinarene subunits. *Proc. Natl. Acad. Sci. USA* **2001**, *98* (14), 7662-7665.

269. Atwood, J. L.; Barbour, L. J.; Jerga, A., Organization of the interior of molecular capsules by hydrogen bonding. *Proc. Natl. Acad. Sci. USA* **2002**, *99* (8), 4837-4841.

270. Avram, L.; Cohen, Y., Spontaneous formation of hexameric resorcinarene capsule in chloroform solution as detected by diffusion nmr. *J. Am. Chem. Soc.* **2002**, *124* (51), 15148-15149.

271. Shivanyuk, A.; Rebek, J., Reversible encapsulation of multiple, neutral guests in hexameric resorcinarene hosts. *Chem. Commun.* **2001**, (23), 2424-2425.

272. Gil-Ramirez, G.; Benet-Buchholz, J.; Escudero-Adan, E. C.; Ballester, P., Solid-state self-assembly of a calix[4]pyrrole-resorcinarene hybrid into a hexameric cage. *J. Am. Chem. Soc.* **2007**, *129* (13), 3820-+.

273. Avram, L.; Cohen, Y.; Rebek Jr, J., Recent advances in hydrogen-bonded hexameric encapsulation complexes. *Chem. Commun.* **2011**, *47* (19), 5368-5375.

274. Cavarzan, A.; Scarso, A.; Sgarbossa, P.; Strukul, G.; Reek, J. N. H., Supramolecular control on chemo- and regioselectivity via encapsulation of (nhc)-au catalyst within a hexameric self-assembled host. *J. Am. Chem. Soc.* **2011**, *133* (9), 2848-2851.

275. Wei, A., Calixarene-encapsulated nanoparticles: Self-assembly into functional nanomaterials. *Chem. Commun.* **2006**, (15), 1581-1591.

276. Clark, T. E.; Makha, M.; Sobolev, A. N.; Rohrs, H.; Atwood, J. L.; Raston, C. L., Engineering nanorafts of calixarene polyphosphonates. *Chem. Eur. J.* **2008**, *14* (13), 3931-3938.

277. Martin, A. D.; Boulos, R. A.; Stubbs, K. A.; Raston, C. L., Phosphonated calix[4]arene-based amphiphiles as scaffolds for fluorescent nano-fibres. *Chem. Commun.* **2011**, *47* (26), 7329-7331.

278. Heaven, M. W.; Cave, G. W. V.; McKinlay, R. M.; Antesberger, J.; Dalgarno, S. J.; Thallapally, P. K.; Atwood, J. L., Hydrogen-bonded hexamers self-assemble as spherical and tubular superstructures on the sub-micron scale. *Angew. Chem. Int. Ed.* **2006**, *45* (37), 6221-6224.

279. Bang, J. H.; Suslick, K. S., Applications of ultrasound to the synthesis of nanostructured materials. *Adv. Mater.* **2010**, *22* (10), 1039-1059.

280. Zeiger, B. W.; Suslick, K. S., Sonofragmentation of molecular crystals. *J. Am. Chem. Soc.* **2011**, *133* (37), 14530-14533.

281. Sander, J. R. G.; Bučar, D.-K.; Henry, R. F.; Zhang, G. G. Z.; MacGillivray, L. R., Pharmaceutical nano-cocrystals: Sonochemical synthesis by solvent selection and use of a surfactant. *Angew. Chem. Int. Ed.* **2010**, *49* (40), 7284-7288.

282. Percec, V.; Peterca, M.; Dulcey, A. E.; Imam, M. R.; Hudson, S. D.; Nummelin, S.; Adelman, P.; Heiney, P. A., Hollow spherical supramolecular dendrimers. *J. Am. Chem. Soc.* **2008**, *130* (39), 13079-13094.

283. Lu, A. H.; Li, W. C.; Hao, G. P.; Spliethoff, B.; Bongard, H. J.; Schaack, B. B.; Schuth, F., Easy synthesis of hollow polymer, carbon, and graphitized microspheres. *Angew. Chem. Int. Ed.* **2010**, *49* (9), 1615-1618.

284. Schacht, S.; Huo, Q.; Voigt-Martin, I. G.; Stucky, G. D.; Schüth, F., Oil-water interface templating of mesoporous macroscale structures. *Science* **1996**, *273* (5276), 768-771.

285. Hu, J.; Chen, M.; Fang, X.; Wu, L., Fabrication and application of inorganic hollow spheres. *Chem. Soc. Rev.* **2011**, *40* (11), 5472-5491.

286. Lee, S. J.; Malliakas, C. D.; Kanatzidis, M. G.; Hupp, J. T.; Nguyen, S. T., Amphiphilic porphyrin nanocrystals: Morphology tuning and hierarchical assembly. *Adv. Mater.* **2008**, *20* (18), 3543-+.

287. Zhou, W. Z., Reversed crystal growth: Implications for crystal engineering. *Adv. Mater.* **2010**, *22* (28), 3086-3092.

288. Zhan, H.; Yang, X.; Wang, C.; Chen, J.; Wen, Y.; Liang, C.; Greer, H. F.; Wu, M.; Zhou, W., Multiple nucleation and crystal growth of barium titanate. *Cryst. Growth Des.* **2012**.

289. Chen, X.; Qiao, M.; Xie, S.; Fan, K.; Zhou, W.; He, H., Self-construction of core,shell and hollow zeolite analcime icositetrahedra:, a reversed crystal growth process via oriented aggregation of nanocrystallites and recrystallization from surface to core. *J. Am. Chem. Soc.* **2007**, *129* (43), 13305-13312.

290. Yang, X.; Fu, J.; Jin, C.; Chen, J.; Liang, C.; Wu, M.; Zhou, W., Formation mechanism of catio3 hollow crystals with different microstructures. *J. Am. Chem. Soc.* **2010**, *132* (40), 14279-14287.

291. Kuzmicz, R.; Kowalska, V.; Domagala, S.; Stachowicz, M.; Wozniak, K.; Kolodziejski, W., X-ray diffraction, ft-ir, and c-13 cp/mas nmr structural studies of solvated and desolvated c-methylcalix[4]resorcinarene. *J. Phys. Chem. B* **2010**, *114* (32), 10311-10320.

292. Zhang, X. J.; Dong, C.; Zapien, J. A.; Ismathullakhan, S.; Kang, Z. H.; Jie, J. S.; Zhang, X. H.; Chang, J. C.; Lee, C. S.; Lee, S. T., Polyhedral organic microcrystals: From cubes to rhombic dodecahedra. *Angew. Chem. Int. Ed.* **2009**, *48* (48), 9121-9123.

293. Oliveira, D.; Baba, K.; Mori, J.; Miyashita, Y.; Kasai, H.; Oikawa, H.; Nakanishi, H., Nanocrystallization mechanism of organic compounds in the reprecipitation method by stopped-flow analysis. *Jpn. J. Appl. Phys.* **2009**, *48* (10), 105003.

294. Penn, R. L.; Banfield, J. F., Imperfect oriented attachment: Dislocation generation in defect-free nanocrystals. *Science* **1998**, *281* (5379), 969-971.

295. Penn, R. L., Kinetics of oriented aggregation. *J. Phys. Chem. B* **2004**, *108* (34), 12707-12712.

296. Cölfen, H.; Antonietti, M., Mesocrystals: Inorganic superstructures made by highly parallel crystallization and controlled alignment. *Angew. Chem. Int. Ed.* **2005**, *44* (35), 5576-5591.

297. Zhang, Q.; Liu, S.-J.; Yu, S.-H., Recent advances in oriented attachment growth and synthesis of functional materials: Concept, evidence, mechanism, and future. *J. Mater. Chem.* **2009**, *19* (2), 191-207.

298. Lehn, J.-M., Toward complex matter: Supramolecular chemistry and self-organization. *Proc. Natl. Acad. Sci. USA* **2002**, *99* (8), 4763-4768.

299. Atwood, J. L.; Barbour, L. J.; Jerga, A.; Schottel, B. L., Guest transport in a nonporous organic solid via dynamic van der waals cooperativity. *Science* **2002**, *298* (5595), 1000-1002.

300. Sokolov, A. N.; Bučar, D.-K.; Baltrusaitis, J.; Gu, S. X.; MacGillivray, L. R., Supramolecular catalysis in the organic solid state through dry grinding. *Angew. Chem. Int. Ed.* **2010**, *122* (25), 4369-4373.

301. Kuzmanich, G.; Vogelsberg, C. S.; Maverick, E. F.; Netto-Ferreira, J. C.; Scaiano, J. C.; Garcia-Garibay, M. A., Reaction mechanism in crystalline solids: Kinetics and conformational dynamics of the norrish type ii biradicals from α-adamantyl-p-methoxyacetophenone. *J. Am. Chem. Soc.* **2011**, *134* (2), 1115-1123.

302. Friščić, T.; MacGillivray, L. R., Single-crystal-to-single-crystal [2+2] photodimerizations: From discovery to design. *Z. Kristallogr.* **2005**, *220* (4), 351-363.

303. Georgiev, I. G.; Bucar, D.-K.; MacGillivray, L. R., Stereospecific and quantitative photodimerisation of terminal olefins in the solid state. *Chem. Commun.* **2010**, *46* (27), 4956-4958.

304. Kole, G. K.; Tan, G. K.; Vittal, J. J., Solid state photodimerization of trans-2-(4-pyridyl)-4-vinylbenzoic acid via salt formation and isomerisation of cyclobutane compounds in solution. *CrystEngComm* **2012**, *14* (21), 7438-7443.

305. Santra, R.; Biradha, K., Nitrate ion assisted argentophilic interactions as a template for solid state [2 + 2] photodimerization of pyridyl acrylic acid, its methyl ester, and acryl amide. *Cryst. Growth Des.* **2010**, *10* (8), 3315-3320.

306. Hamilton, T. D.; Bučar, D. K.; MacGillivray, L. R., Coding a coordination-driven self-assembly via a hydrogen bond-directed solid-state synthesis: An unexpected chiral tetrahedral capsule. *Chem. Commun.* **2007**, (16), 1603-1604.

307. Hamilton, T. D.; Papaefstathiou, G. S.; MacGillivray, L. R., A polyhedral host constructed using a linear template. *J. Am. Chem. Soc.* **2002**, *124* (39), 11606-11607.

308. Papaefstathiou, G. S.; Hamilton, T. D.; Friscic, T.; MacGillivray, L. R., Self-assembled metal-organic squares derived from linear templates as exemplified by a polydentate ligand that provides access to both a polygon and polyhedron. *Chem. Commun.* **2004**, (3), 270-271.

309. Elacqua, E.; Kaushik, P.; Groeneman, R. H.; Sumrak, J. C.; Bučar, D.-K.; MacGillivray, L. R., A supramolecular protecting group strategy introduced to the organic solid state: Enhanced reactivity through molecular pedal motion. *Angew. Chem. Int. Ed.* **2012**, *51* (4), 1037-1041.

310. Kole, G. K.; Tan, G. K.; Vittal, J. J., Photoreactivity of ag(i) complexes and coordination polymers of pyridyl acrylic acids. *Cryst. Growth Des.* **2011**, *12* (1), 326-332.

311. Kole, G. K.; Tan, G. K.; Vittal, J. J., Role of anions in the synthesis of cyclobutane derivatives via [2 + 2] cycloaddition reaction in the solid state and their isomerization in solution. *J. Org. Chem.* **2011**, *76* (19), 7860-7865.

312. Reddy, D. S.; Ovchinnikov, Y. E.; Shishkin, O. V.; Struchkov, Y. T.; Desiraju, G. R., Supramolecular synthons in crystal engineering. 3. Solid state architecture and synthon robustness in some 2,3-dicyano-5,6-dichloro-1,4-dialkoxybenzenes1. *J. Am. Chem. Soc.* **1996**, *118* (17), 4085-4089.

313. Suss, H. I.; Neels, A.; Hulliger, J., 2,4,6-tris(4-cyanophenoxy)-1,3,5-triazine (cnpot): Trigonal synthons in crystal engineering. *CrystEngComm* **2005**, *7* (61), 370-373.

314. Desiraju, G. R.; Harlow, R. L., Cyano-halogen interactions and their role in the crystal structures of the 4-halobenzonitriles. *J. Am. Chem. Soc.* **1989**, *111* (17), 6757-6764.

315. Yan, D.; Delori, A.; Lloyd, G. O.; Friščić, T.; Day, G. M.; Jones, W.; Lu, J.; Wei, M.; Evans, D. G.; Duan, X., A cocrystal strategy to tune the luminescent properties of stilbene-type organic solid-state materials. *Angew. Chem. Int. Ed.* **2011**, *50* (52), 12483-12486.

316. Bis, J. A.; Vishweshwar, P.; Weyna, D.; Zaworotko, M. J., Hierarchy of supramolecular synthons: Persistent hydroxyl···pyridine hydrogen bonds in cocrystals that contain a cyano acceptor. *Mol. Pharmaceutics* **2007**, *4* (3), 401-416.

317. Min, K. S.; Suh, M. P., Silver(i)−polynitrile network solids for anion exchange: Anion-induced transformation of supramolecular structure in the crystalline state. *J. Am. Chem. Soc.* **2000**, *122* (29), 6834-6840.

318. Chung, J. W.; You, Y.; Huh, H. S.; An, B.-K.; Yoon, S.-J.; Kim, S. H.; Lee, S. W.; Park, S. Y., Shear- and uv-induced fluorescence switching in stilbenic π-dimer crystals powered by reversible [2 + 2] cycloaddition. *J. Am. Chem. Soc.* **2009**, *131* (23), 8163-8172.

319. Novak, K.; Enkelmann, V.; Wegner, G.; Wagener, K. B., Crystallographic study of a single crystal to single crystal photodimerization and its thermal reverse reaction. *Angew. Chem. Int. Ed.* **1993**, *32* (11), 1614-1616.

320. Coudret, C., Efficient syntheses of 4-iodopyridine and of 4-pyridylboronic acid pinacol ester. *Synthetic Commun.* **1996**, *26* (19), 3543-3547.

321. Hahn, M.; Singh, A.; Sharma, P.; Brown, S.; Moudgil, B., Nanoparticles as contrast agents for in-vivo bioimaging: Current status and future perspectives. *Analytical and Bioanalytical Chemistry* **2011**, *399* (1), 3-27.

322. Worthy, S., High resolution computed tomography of the lungs. *BMJ* **1995**, *310* (6980), 616.

323. Yu, S.-B.; Watson, A. D., Metal-based x-ray contrast media. *Chem. Rev.* **1999**, *99* (9), 2353-2378.

324. El-Gendy, N.; Aillon, K. L.; Berkland, C., Dry powdered aerosols of diatrizoic acid nanoparticle agglomerates as a lung contrast agent. *Int. J. Pharm.* **2010**, *391* (1–2), 305-312.

325. Haschek, E.; Lindenthal, T. O., Ein bertrag zur ractischen verwerthung der photogrphie nach roentgen. *Wien. Klin. Wochenschr.* **1896**, *9* (63).

326. Krause, W.; Schneider, P., Chemistry of x-ray contrast agents. In *Contrast agents ii*, Krause, W., Ed. Springer Berlin / Heidelberg: 2002; Vol. 222, pp 107-150.

327. Sovak, M., Contrast media: A journey almost sentimental. *Invest. Radiol.* **1994**, *29 Suppl 1*, S4-14.

328. Idée, J.-M.; Nachman, I.; Port, M.; Petta, M.; Le Lem, G.; Le Greneur, S.; Dencausse, A.; Meyer, D.; Corot, C., Iodinated contrast media: From non-specific to blood-pool agents. In *Contrast agents ii*, Krause, W., Ed. Springer Berlin / Heidelberg: 2002; Vol. 222, pp 151-171.

329. Almén, T., The etiology of contrast medium reactions. *Invest. Radiol.* **1994**, *29*, S37-S45.

330. Becker, N.; Liebermann, D.; Wesch, H.; Van Kaick, G., Mortality among thorotrast-exposed patients and an unexposed comparison group in the german thorotrast study. *Eur. J. Cancer* **2008**, *44* (9), 1259-1268.

331. Pan, D.; Williams, T. A.; Senpan, A.; Allen, J. S.; Scott, M. J.; Gaffney, P. J.; Wickline, S. A.; Lanza, G. M., Detecting vascular biosignatures with a colloidal, radio-opaque polymeric nanoparticle. *J. Am. Chem. Soc.* **2009**, *131* (42), 15522-15527.

332. Galperin, A.; Margel, D.; Baniel, J.; Dank, G.; Biton, H.; Margel, S., Radiopaque iodinated polymeric nanoparticles for x-ray imaging applications. *Biomaterials* **2007**, *28* (30), 4461-4468.

333. Aviv, H.; Bartling, S.; Kieslling, F.; Margel, S., Radiopaque iodinated copolymeric nanoparticles for x-ray imaging applications. *Biomaterials* **2009**, *30* (29), 5610-5616.

334. de Vries, A.; Custers, E.; Lub, J.; van den Bosch, S.; Nicolay, K.; Grüll, H., Block-copolymer-stabilized iodinated emulsions for use as ct contrast agents. *Biomaterials* **2010**, *31* (25), 6537-6544.

335. Ho Kong, W.; Jae Lee, W.; Yun Cui, Z.; Hyun Bae, K.; Gwan Park, T.; Hoon Kim, J.; Park, K.; Won Seo, S., Nanoparticulate carrier containing water-insoluble

iodinated oil as a multifunctional contrast agent for computed tomography imaging. *Biomaterials* **2007**, *28* (36), 5555-5561.

336. Elrod, D. B.; Partha, R.; Danila, D.; Casscells, S. W.; Conyers, J. L., An iodinated liposomal computed tomographic contrast agent prepared from a diiodophosphatidylcholine lipid. *Nanomed. Nanotech. Biol. Med.* **2009**, *5* (1), 42-45.

337. Skajaa, T.; Cormode, D. P.; Falk, E.; Mulder, W. J. M.; Fisher, E. A.; Fayad, Z. A., High-density lipoprotein–based contrast agents for multimodal imaging of atherosclerosis. *Arteriosclerosis, Thrombosis, and Vascular Biology* **2010**, *30* (2), 169-176.

338. McIntire, G. L.; Bacon, E. R.; Toner, J. L.; Cornacoff, J. B.; Losco, P. E.; Illig, K. J.; Nikula, K. J.; Muggenburg, B. A.; Ketai, L., Pulmonary delivery of nanoparticles of insoluble, iodinated ct x-ray contrast agents to lung draining lymph nodes in dogs. *J. Pharm. Sci.* **1998**, *87* (11), 1466-1470.

339. Hyafil, F.; Cornily, J.-C.; Feig, J. E.; Gordon, R.; Vucic, E.; Amirbekian, V.; Fisher, E. A.; Fuster, V.; Feldman, L. J.; Fayad, Z. A., Noninvasive detection of macrophages using a nanoparticulate contrast agent for computed tomography. *Nat. Med.* **2007**, *13* (5), 636-641.

340. Aillon, K. L.; El-Gendy, N.; Dennis, C.; Norenberg, J. P.; McDonald, J.; Berkland, C., Iodinated nanoclusters as an inhaled computed tomography contrast agent for lung visualization. *Mol. Pharmaceutics* **2010**, *7* (4), 1274-1282.

341. Van Herck, J.; De Meyer, G.; Martinet, W.; Salgado, R.; Shivalkar, B.; De Mondt, R.; Van De Ven, H.; Ludwig, A.; Van Der Veken, P.; Van Vaeck, L.; Bult, H.; Herman, A.; Vrints, C., Multi-slice computed tomography with n1177 identifies ruptured atherosclerotic plaques in rabbits. *Basic Research in Cardiology* **2010**, *105* (1), 51-59.

342. Seto, C. T.; Whitesides, G. M., Self-assembly of a hydrogen-bonded 2 + 3 supramolecular complex. *J. Am. Chem. Soc.* **1991**, *113* (2), 712-713.

343. Lance, E. M.; Killen, D. A.; Scott, H. W. J., A plea for caution in the use of sodium acetrizoate (urokon) for aortography. *Ann. Surg.* **1959**, *150* (1), 172.

344. Dhillon, K. S.; Cohan, P.; Kelly, D. F.; Darwin, C. H.; Iyer, K. V.; Chopra, I. J., Treatment of hyperthyroidism associated with thyrotropin-secreting pituitary adenomas with iopanoic acid. *Journal of Clinical Endocrinology & Metabolism* **2004**, *89* (2), 708-711.

345. McWhinnie, S. L. W.; Thomas, J. A.; Hamor, T. A.; Jones, C. J.; McCleverty, J. A.; Collison, D.; Mabbs, F. E.; Harding, C. J.; Yellowlees, L. J.; Hutchings, M. G., Mono- and bimetallic bipyridyl polyene complexes containing 17-electron molybdenum mononitrosyl centers: Electrochemical, spectroscopic, and magnetic studies. *Inorg. Chem.* **1996**, *35* (3), 760-774.

346. Martin, R. F.; Kelly, D. P., Synthesis and n.M.R. Spectra of substituted aminoiodoacridines. *Aust. J. Chem.* **1979**, *32* (12), 2637-2646.

347. Spek, A. L., A multipurpose crystallographic tool. *Acta Crystallogr.* **1990**, *A46*, C34.

348. Calculated values were obtained from the Sci-Finder Scholar database (2012) calculated using Advanced Chemistry Development (ACD/Labs) Software V11.02 (copyright 1994-2012 ACD/Labs)

APPENDIX. CRYSTALLOGRAPHIC DATA RETRIEVED FROM SINGLE-CRYSTAL X-RAY DIFFRACTION STUDIES

Table A1 Crystallographic data for **APAP1**, **APAP2**, and **APAP3** (Chapter 2).

	APAP1	**APAP2**	**APAP3**
Chemical formula	$(C_8H_9O_2N)$• $1.5(C_{12}H_{10}N_2)$• $4(H_2O)$	$(C_8H_9O_2N)$• $1.5(C_{12}H_{10}N_2)$• $2(H_2O)$	$(C_8H_9O_2N)$• $(C_{12}H_{10}N_2)$• $2(H_2O)$
M_r	496.56	460.52	369.41
Crystal system	triclinic	triclinic	monoclinic
a/Å	8.4243(14)	9.2028(9)	6.5584(5)
b/Å	12.227(2)	11.5290(12)	40.426(3)
c/Å	13.193(2)	11.7206(12)	7.1631(5)
α/°	96.960(2)	93.3410(10)	90.00
β/°	93.427(2)	99.5260(10)	97.5890(10)
γ/°	101.280(2)	102.8040(10)	90.00
V/Å^3	1318.0(4)	1190.1(2)	1882.5(2)
T/K	100(2)	100(2)	100(2)
Space group	$P\bar{1}$	$P\bar{1}$	$P2_1/c$
Z	2	2	4
Radiation type	MoK_α	MoK_α	MoK_α
θ range	1.56 to 27.55	1.77 to 27.57	2.02 to 27.50
μ/mm^{-1}	0.090	0.088	0.092
D_c/gcm^{-3}	1.251	1.285	1.303
No. of refl. measured	15528	13902	21710
No. of indep. Refl.	5980	5375	4326
R_{int}	0.0388	0.0154	0.0208
R_1 ($I > 2\sigma(I)$)	0.0370	0.0358	0.0411
$wR(F^2)$ ($I > 2\sigma(I)$)	0.1150	0.1322	0.1265
R_1 (all data)	0.0443	0.0413	0.0470
$wR(F^2)$ (all data)	0.1250	0.1398	0.1330
GooF on F^2	0.878	1.181	0.878

Table A2 Crystallographic data for **APAP4**, **APAP5**, and **PDA1** (Chapter 2).

	APAP3	**APAP5**	**PDA1**
Chemical formula	$(C_{12}H_{10}N_2)$• $2(C_8H_9O_2N)$• (C_2H_6O)	$(C_8H_9NO_2)$• $(C_7H_5NO_4)$	$(C_7H_5NO_4)\cdot(H_2O)$
M_r	530.61	318.28	185.14
Crystal system	triclinic	monoclinic	monoclinic
a/Å	8.835(3)	$P2_1/c$	$P2_1/c$
b/Å	10.724(3)	7.162(1)	6.905(4)
c/Å	15.174(4)	14.245(3)	18.404(11)
α/°	91.638(4)	14.000(3)	6.822(4)
β/°	100.515(4)	90.00	90.00
γ/°	106.191(4)	104.180(2)	119.373(6)
V/Å^3	1352.6(7)	90.00	90.00
T/K	100(2)	100(2)	100(2)
Space group	$P\bar{1}$	$P2_1/c$	$P2_1/c$
Z	2	4	4
Radiation type	MoK_α	MoK_α	MoK_α
θ range	1.98 to 27.49	0.99 to 23.20	3.39 to 27.31
μ/mm^{-1}	0.090	0.120	0.092
D_c/gcm^{-3}	1.303	1.527	1.628
No. of refl. measured	15926	15833	8358
No. of indep. Refl.	6122	3175	1699
R_{int}	0.1800	0.052	0.085
R_1 ($I > 2\sigma(I)$)	0.0625	0.039	0.044
$wR(F^2)$ ($I > 2\sigma(I)$)	0.1653	0.053	0.049
R_1 (all data)	0.0715	0.068	0.098
$wR(F^2)$ (all data)	0.1757	0.056	0.107
GooF on F^2	1.053	1.065	1.136

Table A3 Crystallographic data for **CVP1**, **CVP2**, and **CVP3** (Chapter 4).

	CVP1	**CVP2**	**CVP3**
molecular formula	$(C_8H_6N_2)$• $(C_6H_4O_2Cl_2)$	$(C_8H_9O_2N)$• $(C_6H_4O_2I_2)$	$(C_8H_9O_2N)$• $(C_{14}H_{22}O_2)$
M_r	437.29	694.25	482.61
Crystal system	monoclinic	triclinic	triclinic
a/Å	13.0926(14)	8.4710(9)	9.1439(10)
b/Å	7.5193(9)	9.2826(10)	9.6497(11)
c/Å	14.7458(16)	11.6704(13)	13.6057(15)
α/°	90.00	102.326(5)	97.591(5)
β/°	107.197(5)	105.714(5)	90.874(5)
γ/°	90.00	110.876(5)	115.608(5)
V/Å^3	1386.8(3)	774.82(15)	1069.6(2)
T/K	298(2)	298(2)	298(2)
Space group	$P2_1/c$	$P\bar{1}$	$P\bar{1}$
Z	3	1	2
D_c/gcm^{-3}	1.251	1.488	1.499
F(000)	672	334	516
Radiation type	MoK_α	MoK_α	MoK_α
θ range	1.00 to 27.88	2.72 to 25.00	2.80 to 25.00
μ/mm^{-1}	0.381	2.057	0.095
crystal size	0.28 x 0.25 x 0.03	0.24 x 0.20 x 0.07	0.33 x 0.32 x 0.195
range of indices	-15 → 15 -8 → 8 -17 → 17	-10 → 10 -11 → 9 -13 → 13	-10 → 10 -10 → 11 -16 → 16
no. of refl. measured	9122	4692	6744
unique refl.	2424	2702	3741
no. parameters	171	212	286
refl. with ($I > 2\sigma(I)$)	2122	2493	2922
R_{int}	0.0197	0.0200	0.0149
R_1 ($I > 2\sigma(I)$)	0.0371	0.0226	0.0478
$wR(F^2)$ ($I > 2\sigma(I)$)	0.1098	0.0567	0.1334
R_1 (all data)	0.0430	0.0252	0.0617
$wR(F^2)$ (all data)	0.1140	0.0581	0.1439
GooF on F^2	1.096	1.086	1.068
Δ_r (max., min.) eÅ^{-3}	0.470, -0.372	0.347, -0.816	0.184, -0.156

Table A4 Crystallographic data for **CVP4**, **CVP5**, and **CVP6** (Chapter 4).

	CVP4	**CVP5**	**CVP6**
molecular formula	$2(C_8H_6N_2)\bullet(C_6H_4O_2Br_2)$	$2(C_8H_6N_2)\bullet(C_{12}H_{18}O_{22})$	$2(C_8H_6N_2)\bullet(C_{18}H_{30}O_2)$
M_r	600.27	448.51	538.72
Crystal system	triclinic	triclinic	triclinic
a/Å	8.5802(10)	7.7627(9)	7.3562(8)
b/Å	8.8420(10)	9.6272(11)	10.2292(11)
c/Å	15.5407(17)	18.3437(19)	22.852(3)
α/°	96.690(5)	82.307(5)	80.932(5)
β/°	102.636(5)	77.993(5)	90.209(5)
γ/°	106.651(5)	73.699(5)	69.040(5)
V/Å^3	1081.8(2)	1282.8(2)	1582.4(3)
T/K	298(2)	298(2)	298(2)
Space group	$P\bar{1}$	$P\bar{1}$	$P\bar{1}$
Z	2	2	2
D_c/gcm^{-3}	1.843	1.161	1.131
F(000)	597	472	580
Radiation type	MoK_α	MoK_α	MoK_α
θ range	2.57 to 25.00	2.78 to 25.00	2.57 to 25.00
μ/mm^{-1}	3.785	0.075	0.071
crystal size	0.26 x 0.14 x 0.12	0.20 x 0.15 x 0.02	0.26 x 0.12 x 0.08
range of indices	-10 → 10 -10 → 10 -16 → 16	-9 → 9 -11 → 11 -21 → 21	-8 → 8 -12 → 12 -27 → 27
no. of refl. measured	6576	8141	9118
unique refl.	3796	4498	5559
no. parameters	253	369	364
refl. with ($I > 2\sigma(I)$)	3412	2384	3322
R_{int}	0.0222	0.0399	0.0290
R_1 ($I > 2\sigma(I)$)	0.0388	0.0581	0.0503
$wR(F^2)$ ($I > 2\sigma(I)$)	0.0981	0.1358	0.1234
R_1 (all data)	0.0436	0.1270	0.0985
$wR(F^2)$ (all data)	0.1010	0.1604	0.1410
GooF on F^2	1.033	0.980	1.056
Δ_r (max., min.) eÅ^{-3}	0.666, -0.603	0.121, -0.210	0.145, -0.140

Table A5 Crystallographic data for **CVP7**, **CVP8**, and **CVP9** (Chapter 4).

	CVP7	**CVP8**	**CVP9**
molecular formula	$[C_{18}H_{15}AgN_6O_3]$	$[C_{40}H_{30}N_{10}Ag_3Cl_3O_{12}]$	$[C_{40}H_{24}Ag_2F_{14}N_8O_4]$
M_r	471.23	1272.76	1162.42
Crystal system	orthorhombic	monoclinic	monoclinic
a/Å	18.5811(19)	9.9716(11)	8.0016(9)
b/Å	14.1610(15)	31.140(4)	14.7447(16)
c/Å	7.3368(8)	14.5766(16)	19.2034(19)
α/°	90.00	90.00	90.00
β/°	90.00	91.796(5)	101.943(5)
γ/°	90.00	90.00	90.00
V/Å^3	1930.5(4)	4524.0(9)	2216.6(4)
T/K	190(2)	298(2)	298(2)
Space group	$Pna2_1$	$P2_1/c$	$P2_1$
Z	4	10	4
D_c/gcm^{-3}	1.621	1.716	1.742
F(000)	944	2320	1144
Radiation type	MoK_α	MoK_α	MoK_α
θ range	2.88 to 25.00	2.60 to 25.00	2.57 to 25.00
μ/mm^{-1}	1.076	1.290	0.993
crystal size	0.22 x 0.07 x 0.065	0.24 x 0.24 x 0.11	0.25 x 0.20 x 0.20
range of indices	-22 → 22 -16 → 16 -8 → 8	-11 → 11 -36 → 36 -17 → 17	-9 → 9 -17 → 17 -22 → 22
no. of refl. measured	12461	26648	14762
unique refl.	3372	7931	7733
no. parameters	254	602	737
refl. with ($I > 2\sigma(I)$)	2673	5699	6803
R_{int}	0.0374	0.0324	0.0192
R_1 ($I > 2\sigma(I)$)	0.0319	0.0530	0.0381
$wR(F^2)$ ($I > 2\sigma(I)$)	0.0755	0.1609	0.1065
R_1 (all data)	0.0480	0.0754	0.0442
$wR(F^2)$ (all data)	0.0827	0.1751	0.1113
GooF on F^2	1.067	1.044	1.037
Δ_r (max., min.) eÅ^{-3}	0.349, -0.793	0.829, -0.529	0.455, -0.334

Table A6 Crystallographic data for **ACS1**, **ACS2**, and **ACS3** (Chapter 4).

	ACS1	**ACS2**	**ACS3**
molecular formula	$[C_{56}H_{40}Ag_2Cl_2N_8O_6]$	$[C_{84}H_{60}Ag_3Cl_3N_{12}O_{12}]$	$[C_{31}H_{20}AgF_5N_4O_2]$
M_r	1209.84	1859.4	683.38
Crystal system	triclinic	triclinic	triclinic
a/Å	9.1839(8)	9.4992(10)	6.9653(8)
b/Å	15.6172(14)	14.4406(15)	13.5306(15)
c/Å	19.4092(18)	19.750(2)	16.4500(17)
α/°	68.046(3)	73.820(5)	112.299(5)
β/°	83.031(6)	88.563(5)	99.666(5)
γ/°	81.334(6)	89.953(5)	96.144(5)
V/Å^3	2546.03(4)	2601.0(5)	1389.0(3)
T/K	298(2)	293(2)	298(2)
Space group	$P\bar{1}$	$P\bar{1}$	$P\bar{1}$
Z	4	4	2
D_c/gcm^{-3}	1.131	1.531	1.634
F(000)	580	1168	684
Radiation type	MoK_α	MoK_α	MoK_α
θ range	1.00 to 25.35	1.47 to 25.00	3.02 to 25.00
μ/mm^{-1}	0.071	0.918	0.796
crystal size	0.26 x 0.10 x 0.02	0.25 x 0.11 x 0.06	0.26 x 0.03 x 0.03
range of indices	-10 → 8 -15 → 18 -22 → 22	-8 → 11 -17 → 17 -23 → 23	-8 → 7 -16 → 16 -19 → 19
no. of refl. measured	12314	13073	8808
unique refl.	8328	8762	4879
no. parameters	355	340	389
refl. with ($I > 2\sigma(I)$)	3996	4956	3732
R_{int}	0.0489	0.0403	0.0260
R_1 ($I > 2\sigma(I)$)	0.0809	0.229	0.0515
$wR(F^2)$ ($I > 2\sigma(I)$)	0.6180	0.5731	0.1254
R_1 (all data)	0.2635	0.2899	0.0727
$wR(F^2)$ (all data)	0.3508	0.6028	0.1324
GooF on F^2	2.0890	2.243	1.072
Δ_r (max., min.) eÅ^{-3}	5.470, -3.770	4.213, -3.817	0.481, -0.390

Table A7 Crystallographic data for **ACS4**, **BCS1**, and **BCS2** (Chapter 4).

	ACS4	**BCS1**	**BCS2**
molecular formula	$[C_{32}H_{20}AgF_7N_4O_2]$	$[C_{28}H_{20}AgN_5O_3]$	$[C_{28}H_{20}AgClN_2O_4]$
M_r	733.39	582.36	619.18
Crystal system	triclinic	triclinic	triclinic
a/Å	6.9761(8)	9.2245(10)	9.1125(10)
b/Å	13.8376(15)	11.5461(13)	9.3126(10)
c/Å	16.6025(18)	11.5808(13)	15.5414(17)
α/°	108.032(5)	102.053(5)	106.186(5)
β/°	99.829(5)	93.159(5)	96.120(5)
γ/°	94.454(5)	94.606(5)	94.201(5)
V/Å^3	1487.0(3)	1199.1(2)	1930.5(4)
T/K	298(2)	298(2)	298(2)
Space group	$P\bar{1}$	$P\bar{1}$	$P\bar{1}$
Z	2	2	3
D_c/gcm^{-3}	1.638	1.613	1.646
F(000)	732	588	612
Radiation type	MoK_α	MoK_α	MoK_α
θ range	2.97 to 25.00	2.76 to 25.00	2.29 to 25.00
μ/mm^{-1}	0.759	0.882	1.384
crystal size	0.22 x 0.10 x 0.06	0.34 x 0.18 x 0.10	0.30 x 0.15 x 0.07
range of indices	-7 → 8 -16 → 16 -19 → 19	-10 → 10 -13 → 13 -13 → 13	-10 → 10 -11 → 11 -18 → 18
no. of refl. measured	9440	7601	6249
unique refl.	5227	4207	4092
no. parameters	415	334	343
refl. with ($I > 2\sigma(I)$)	4463	3512	2894
R_{int}	0.0150	0.0176	0.0350
R_1 ($I > 2\sigma(I)$)	0.0446	0.0349	0.0485
$wR(F^2)$ ($I > 2\sigma(I)$)	0.1396	0.0922	0.1269
R_1 (all data)	0.0521	0.0449	0.0801
$wR(F^2)$ (all data)	0.1501	0.0966	0.1509
GooF on F^2	0.773	1.085	1.073
Δ_r (max., min.) eÅ^{-3}	0.745, -0.603	0.332, -0.684	0.445, -0.663

Table A8 Crystallographic data for **FACS1**, **ACD1**, and **ACD2** (Chapter 4).

	FACS1	**ACD1**	**ACD2**
molecular formula	$[C_{28}H_{18}Ag\,F_2ClN_4O_3]$	$[C_{32}H_{26}AgClN_4O_4]$	$[C_{32}H_{24}AgClN_4O_4]$
M_r	639.78	673.89	671.87
Crystal system	triclinic	triclinic	triclinic
a/Å	7.1717(8)	9.4493(10)	10.8341(12)
b/Å	8.8085(10)	10.6147(12)	11.1865(12)
c/Å	21.383(3)	15.9157(17)	12.5884(14)
α/°	84.435(5)	80.998(5)	72.547(5)
β/°	83.781(5)	82.360(5)	81.869(5)
γ/°	72.365(5)	65.024(5)	82.576(5)
V/Å^3	1276.8(3)	1425.3(3)	1434.7(3)
T/K	298(2)	190(2)	190(2)
Space group	$P\bar{1}$	$P\bar{1}$	$P\bar{1}$
Z	2	2	2
D_c/gcm^{-3}	1.664	1.528	1.555
F(000)	640	664	680
Radiation type	MoK_α	MoK_α	MoK_α
θ range	3.25 to 27.91	1.30 to 25.00	2.58 to 25.00
μ/mm^{-1}	0.948	0.842	0.841
crystal size	0.33 x 0.10 x 0.05	0.22 x 0.20 x 0.19	0.40 x 0.22 x 0.20
range of indices	-9 → 9 -11 → 11 -28 → 28	-11 → 11 -12 → 12 -18 → 18	-12 → 12 -12 → 13 -14 → 14
no. of refl. measured	11068	9559	8536
unique refl.	6079	4996	4977
no. parameters	352	379	379
refl. with ($I > 2\sigma(I)$)	4304	4694	4307
R_{int}	0.0210	0.0096	0.0251
R_1 ($I > 2\sigma(I)$)	0.0418	0.0486	0.0400
$wR(F^2)$ ($I > 2\sigma(I)$)	0.1113	0.1528	0.1030
R_1 (all data)	0.0649	0.0564	0.0486
$wR(F^2)$ (all data)	0.1267	0.1787	0.1079
GooF on F^2	1.010	1.194	1.087
Δ_r (max., min.) eÅ^{-3}	0.688, -0.535	1.272, -1.365	0.586, -0.661

Table A9 Crystallographic data for **ACD3**, **ACD4**, and **dCyPCB1** (Chapter 4).

	ACD3	**ACD4**	**dCbPCB1**
molecular formula	$[C_{33}H_{24}AgF_3N_4O_3S]$	$[C_{35}H_{24}AgF_5N_4O_2]$	$[C_{16}H_{14}AgN_5O_4]$
M_r	721.49	735.46	448.20
Crystal system	triclinic	triclinic	monoclinic
a/Å	9.8738(10)	6.9009(8)	8.3913(9)
b/Å	11.1690(12)	13.2949(14)	12.7850(14)
c/Å	14.8004(15)	18.2924(19)	8.4713(9)
α/°	80.108(5)	108.934(5)	90.00
β/°	72.736(5)	95.705(5)	111.077(5)
γ/°	84.930(5)	96.092(5)	90.00
V/Å^3	1534.3(2)	1562.4(3)	848.02(16)
T/K	190(2)	190(2)	298(2)
Space group	$P\bar{1}$	$P\bar{1}$	$P2_1/m$
Z	2	2	2
D_c/gcm^{-3}	1.562	1.593	1.685
F(000)	728	754	428
Radiation type	MoK_α	MoK_α	MoK_α
θ range	2.70 to 24.99	1.19 to 25.00	3.03 to 24.99
μ/mm^{-1}	0.784	0.717	1.214
crystal size	0.30 x 0.235 x 0.12	0.34 x 0.25 x 0.06	0.24 x 0.20 x 0.15
range of indices	-11 → 11 -13 → 13 -17 → 17	-7 → 8 -15 → 15 -21 → 21	-9 → 9 -15 → 13 -10 → 10
no. of refl. measured	8873	10037	5063
unique refl.	5208	5383	1547
no. parameters	406	424	124
refl. with ($I > 2\sigma(I)$)	3698	4296	1469
R_{int}	0.0394	0.0357	0.0207
R_1 ($I > 2\sigma(I)$)	0.0651	0.0815	0.0362
$wR(F^2)$ ($I > 2\sigma(I)$)	0.1788	0.2308	0.1004
R_1 (all data)	0.0964	0.1063	0.0379
$wR(F^2)$ (all data)	0.1986	0.2596	0.1016
GooF on F^2	1.054	1.086	1.101
Δ_r (max., min.) eÅ^{-3}	1.867, -0.824	1.892, -1.969	0.719, -0.496

Table A10 Crystallographic data for **DTA1**, **DTA2**, and **DTA3** (Chapter 5).

	DTA1	**DTA2**	**DTA3**
molecular formula	$(C_{11}H_9I_3N_2O_4)$• $2(H_2O)$	$2(C_{11}H_9I_3N_2O_4)$• $(C_{12}H_{10}N_2)$•$8(H_2O)$	$(C_{11}H_9I_3N_2O_4)$• $(C_{12}H_8N_2)$
M_r	649.93	1554.18	794.11
Crystal system	triclinic	triclinic	triclinic
a/Å	7.8482(8)	11.2939(12)	9.3094(10)
b/Å	9.4672(10)	12.9968(14)	11.8845(13)
c/Å	13.3327(14)	17.4122(18)	12.5047(13)
α/°	89.642(5)	85.179(5)	97.618(5)
β/°	75.457(5)	82.290(5)	96.007(5)
γ/°	71.142(5)	74.558(5)	110.948(5)
V/Å^3	904.38(16)	2438.2(4)	1263.2(2)
T/K	190(2)	190(2)	190(2)
Space group	$P\bar{1}$	$P\bar{1}$	$P\bar{1}$
Z	2	2	2
D_c/gcm^{-3}	2.387	1.921	2.088
F(000)	600	1312	748
Radiation type	MoK_α	MoK_α	MoK_α
θ range	2.67to 24.99	5.88 to 25.00	3.12 to 25.00
μ/mm^{-1}	5.210	3.869	3.748
crystal size	0.17 x 0.15 x 0.12	0.30 x 0.21 x 0.12	0.30 x 0.06 x 0.04
range of indices	-9 → 9 -11 → 11 -15 → 15	-13 → 13 -15 → 14 -20 → 20	-11 → 11 -14 → 14 -14 → 14
no. of refl. measured	6149	15975	8359
unique refl.	3186	8396	4432
no. parameters	217	535	317
refl. with ($I > 2\sigma(I)$)	2905	6876	3844
R_{int}	0.0130	0.0171	0.0276
R_1 ($I > 2\sigma(I)$)	0.0230	0.0451	0.0641
$wR(F^2)$ ($I > 2\sigma(I)$)	0.0555	0.1163	0.0348
R_1 (all data)	0.0263	0.0550	0.0671
$wR(F^2)$ (all data)	0.0569	0.1226	0.1016
GooF on F^2	1.166	1.103	1.101
Δ_r (max., min.) eÅ^{-3}	0.631, -0.797	3.002, -2.195	1.654, -0.830

Table A11 Crystallographic data for **DTA4**, **ATA1**, and **ATA2** (Chapter 5).

	DTA4	**ATA1**	**ATA2**
molecular formula	$(C_{11}H_9I_3N_2O_4)$• $(C_{13}H_9I_2N_3)$•4(H_2O)	2$(C_9H_6I_3NO_3)$• $(C_{12}H_{10}N_2)$•1.2(H_2O)	$(C_9H_6I_3NO_3)$• $(C_{12}H_8N_2)$
M_r	1147.01	131754	737.07
Crystal system	triclinic	triclinic	orthorhombic
a/Å	7.8000(9)	12.2041(13)	8.6090(9)
b/Å	13.3504(14)	12.9758(14)	17.1461(18)
c/Å	16.0520(17)	13.4396(14)	30.482(4)
α/°	84.855(5)	74.267(5)	90.00
β/°	82.368(5)	71.973(5)	90.00
γ/°	89.155(5)	69.907(5)	90.00
V/Å^3	1650.1(3)	1868.0(3)	4499.5(9
T/K	190(2)	190(2)	190(2)
Space group	$P\bar{1}$	$P\bar{1}$	*Pbca*
Z	2	2	4
D_c/gcm^{-3}	2.164	2.304	2.079
F(000)	988	1192	2640
Radiation type	MoK_α	MoK_α	MoK_α
θ range	1.53 to 25.00	2.83 to 25.00	1.34 to 24.99
μ/mm^{-1}	4.747	5.034	4.188
crystal size	0.095 x 0.065 x 0.01	0.26 x 0.205 x 0.12	0.30 x 0.28 x 0.11
range of indices	-9 → 9 -15 → 15 -19 → 19	-14 → 14 -15 → 15 -15 → 15	-9 → 10 -19 → 20 -36 → 36
no. of refl. measured	10934	12273	21917
unique refl.	5799	6508	3960
no. parameters	379	419	272
refl. with ($I > 2\sigma(I)$)	4480	5790	3597
R_{int}	0.0320	0.0165	0.0320
R_1 ($I > 2\sigma(I)$)	0.0405	0.0317	0.0247
$wR(F^2)$ ($I > 2\sigma(I)$)	0.0901	0.0767	0.0853
R_1 (all data)	0.0624	0.0374	0.0325
$wR(F^2)$ (all data)	0.0969	0.0793	0.1072
GooF on F^2	1.070	1.068	1.226
Δ_r (max., min.) eÅ^{-3}	1.339, -0.785	2.031, -1.817	1.295, -0.993

Table A12 Crystallographic data for **ATA3**, **ATA4**, and **IPA1** (Chapter 5).

	ATA3	**ATA4**	**IPA1**
molecular formula	$(C_9H_6I_3NO_3)$• $(C_{13}H_9N)$	$(C_9H_6I_3NO_3)$• $(C_{13}H_9I_2N_3)$	$(C_{11}H_{12}I_3NO_2)$• $0.5(C_{12}H_{10}N_2)$
M_r	736.06	1053.92	662.03
Crystal system	triclinic	triclinic	triclinic
a/Å	9.8557(10)	7.6651(9)	9.5729(11
b/Å	10.3617(11)	12.9363(14)	9.9475(11)
c/Å	11.8242(12)	14.0768(15)	11.9114(13)
α/°	83.405(5)	93.001(5)	94.183(5)
β/°	67.066(5)	92.666(5)	97.819(5)
γ/°	80.694(5)	102.307(5)	117.345(5)
V/Å^3	1095.6(2)	1359.5(3)	986.27(19)
T/K	190(2)	190(2)	190(2)
Space group	$P\bar{1}$	$P\bar{1}$	$P\bar{1}$
Z	2	2	2
D_c/gcm^{-3}	2.231	2.487	2.536
F(000)	688	928	712
Radiation type	MoK_α	MoK_α	MoK_α
θ range	1.87 to 25.00	2.24to 25.00	1.75 to 25.00
μ/mm^{-1}	4.306	5.750	4.784
crystal size	0.09 x 0.08 x 0.075	0.21 x 0.07 x 0.03	0.27 x 0.11 x 0.08
range of indices	-11 → 11 -12 → 12 -14 → 14	-9 → 9 -15 → 15 -16 → 16	-11 → 11 -11 → 11 -14 → 14
no. of refl. measured	7416	9168	5929
unique refl.	3857	4781	3462
no. parameters	277	312	224
refl. with ($I > 2\sigma(I)$)	3506	4270	3277
R_{int}	0.0150	0.0214	0.0188
R_1 ($I > 2\sigma(I)$)	0.0242	0.0243	0.0219
$wR(F^2)$ ($I > 2\sigma(I)$)	0.0564	0.0598	0.0810
R_1 (all data)	0.0282	0.0294	0.0260
$wR(F^2)$ (all data)	0.0582	0.0618	0.1019
GooF on F^2	1.184	1.036	1.271
Δ_r (max., min.) eÅ^{-3}	0.944, -0.779	1.319, -0.673	0.672, -0.965

Table A13 Crystallographic data for **IPA2** and **IPA3** (Chapter 5).

	IPA2	**IPA3**
molecular formula	$(C_{11}H_{14}I_3NO_2)$• $0.5(C_{12}H_8N_2)$	$(C_{11}H_{14}I_3NO_2)$• $0.5(C_{16}H_{14}N_2)$
M_r	662.99	688.06
Crystal system	monoclinic	triclinic
a/Å	11.4432(12)	6.2998(7)
b/Å	18.0624(19)	10.1437(11)
c/Å	9.6274(11)	17.0911(18)
α/°	90.00	104.466(5)
β/°	104.263(5)	95.079(5)
γ/°	90.00	90.854(5)
V/Å^3	986.27(19)	1052.6(2)
T/K	190(2)	190(2)
Space group	$P2_1/c$	$P\bar{1}$
Z	2	2
D_c/gcm^{-3}	2.277	2.540
F(000)	1228	768
Radiation type	MoK_α	MoK_α
θ range	1.8 to 24.99	1.24 to 24.99
μ/mm^{-1}	4.874	4.492
crystal size	0.22 x 0.17 x 0.15	0.17 x 0.10 x 0.085
range of indices	-13 → 13 -21 → 21 -11 → 11	-7 → 7 -12 → 12 -20 → 20
no. of refl. measured	12933	6989
unique refl.	3404	3711
no. parameters	218	236
refl. with ($I > 2\sigma(I)$)	3058	3382
R_{int}	0.0226	0.0280
R_1 ($I > 2\sigma(I)$)	0.0365	0.0815
$wR(F^2)$ ($I > 2\sigma(I)$)	0.0851	0.0790
R_1 (all data)	0.0416	0.0330
$wR(F^2)$ (all data)	0.0892	0.0945
GooF on F^2	1.068	1.189
Δ_r (max., min.) eÅ^{-3}	2.176, -1.553	2.771, -1.590